Doctoral Dissertation
Doctoral Program in Civil and Environmental Engineering (39nd Cycle)

Stability of tunnels in water saturated shale under cyclic stresses: investigation on the coupling between mechanical and seepage characteristics

Chongyang Wang

Supervisor

Prof. Dongming Zhang Prof. Marco Barla

Co-supervisor

Prof. Alessandra Insana

Doctoral Examination Committee:

Prof. Marilena Cardu
Prof. Monica Barbero
Prof. Guido Musso
Prof. Beichen Yu
Prof. Weijing Xiao

Chongqing University
Politecnico di Torino
June 25, 2025

Abstract

Under the coupled effect of water and cyclic stress, the mechanical properties of mine surrounding rock deteriorate, and its permeability changes, posing challenges to tunnel excavation support and mine stability control. The interaction between water infiltration into the rock mass and externally applied cyclic stress may lead to significant degradation of the rock's mechanical properties, further affecting its deformation, strength, and permeability. Based on this, this study investigates a water-rich tunnel in a phosphate mine in Yunnan, employing in-situ experiments, laboratory tests, model construction, numerical simulations, and field monitoring.

In-situ hydraulic pressure and geostress tests were conducted, and shale samples were retrieved and processed into standard cylindrical and cubic specimens in the laboratory. Considering the stress and hydrogeological conditions during tunnel excavation, the study systematically examined the damage characteristics of water-saturated shale under cyclic stress disturbances and its mechanical-seepage coupling properties. The effects of water saturation, hydraulic pressure, and cyclic stress on the mechanical properties and permeability of the specimens were analyzed, leading to an understanding of the degradation mechanism of mechanical properties and the evolution of permeability under water-mechanical coupling. Furthermore, FLAC^{3D} software was used to simulate the excavation process of a water-saturated tunnel under cyclic stress disturbances. The deformation and pore water pressure evolution of the excavated tunnel under different support schemes after drainage were analyzed, and field monitoring and verification were carried out.

Main Research Conclusions:

1) Engineering Geological Characteristics of the Water-Saturated Tunnel Surrounding Rock. Based on field geological surveys, core sampling, and laboratory tests, it was determined that the rock mass in the mining area mainly consists of Class IV–V hard to moderately hard rock layers, with interbedded soluble salt rocks contributing to a medium complexity hydrogeological environment. Transient electromagnetic detection revealed an anomalous water-rich zone within 0–8 m ahead of the working face and two sets of water-conducting fractures between 25–40 m, providing insight into the spatial distribution of groundwater migration pathways. Geostress testing results indicated that the maximum principal stress at the tunnel location is σ_1 = 15.68 MPa, the intermediate principal stress is σ_2 = 7.32 MPa, and the minimum principal stress is σ_3 = 4.98 MPa, confirming a geostress regime dominated by tectonic stress. Pore water pressure monitoring showed that water pressure stabilized at 1.42 MPa (fluctuation <4.2%) on the 14th day after tunnel excavation. These geostress and water pressure test results provided boundary conditions for subsequent cyclic stress and hydraulic pressure loading experiments.

2) Damage Mechanism of Water-Saturated Shale under Cyclic Stress Disturbances. Conventional triaxial compression and cyclic loading tests revealed the regulatory mechanism of water saturation duration on shale's mechanical properties. The experiments showed that the compressive strength of the specimens gradually decreased with increasing saturation time. Cyclic stress altered the internal crack distribution (closure of pre-existing cracks and initiation of new cracks), thereby changing the mechanical properties of the specimens. Water infiltration weakened the specimen's strength through both physical softening and chemical corrosion, resulting in multiple post-peak fluctuations in the stress-strain curve under cyclic loading and saturated conditions, with significantly enhanced plasticity. Acoustic emission (AE) monitoring indicated that water molecules suppressed the rapid expansion of newly formed cracks, leading to a gradual decrease in AE response during the loading process of saturated specimens. A complex-plane fatigue damage model was established, correlating AE parameters with plastic strain rate to predict mechanical parameter degradation, and a critical saturation threshold of tw = 24 h was determined, providing a quantitative basis for engineering damage assessment.

3) Mechanical-Seepage Coupling Characteristics and Model Construction of Water-Saturated Shale under Cyclic Stress Disturbances. Through cyclic loading and seepage experiments, the reconstruction mechanism of seepage pathways under the synergistic action of hydraulic pressure and stress was elucidated. The results showed that water-saturated specimens exhibited enhanced stress-strain curve fluctuations due to local expansion effects, while post-failure compressive conditions restricted the instantaneous increase in water flow. Increased hydraulic pressure elevated the effective stress in the σ_1 direction, promoting the main crack's expansion along the maximum principal stress direction while reducing crack density in the σ_2 direction. The permeability critical point gradually disappeared with prolonged saturation, indicating that water infiltration altered the fracture network's flow-conducting characteristics. A complex-plane damage model (real part representing fatigue damage and imaginary part representing post-disturbance mechanical properties) was developed, integrating a neural network algorithm to dynamically predict permeability and strength parameters under different hydraulic pressure conditions. A visualization software tool was also incorporated to support engineering support design.

4) Surrounding Rock Control and Stability Analysis of Water-Saturated Tunnel under Cyclic Stress Disturbances. Through numerical simulation and parameter sensitivity analysis, an optimized "long-anchor + dense support" scheme was proposed for water-saturated tunnels. Simulation results showed that this scheme significantly reduced roof subsidence and substantially decreased the extent of the plastic zone. The pre-drainage measures reduced the pore water pressure from 1.5 MPa to 0.5 MPa (a 66.7% reduction), and when combined with dynamic support sequencing (pre-drainage → long-anchor support), effectively mitigated secondary damage induced by hydraulic pressure redistribution. During excavation, pore water pressure evolution exhibited a "convergence to the excavation face → gradient diffusion"

pattern, while roof subsidence followed a three-stage dynamic response: an initial slow increase phase, a rapid increase phase during excavation, and a stress adjustment stabilization phase. The central area of the second excavation stage experienced the largest proportion of subsidence, necessitating targeted monitoring and reinforcement.

5) Mine Pressure Monitoring and Engineering Application in the Water-Saturated Tunnel. After implementing the new support scheme in a tunnel of the Yunnan phosphate mine, joint monitoring using multipoint displacement meters, roof separation instruments, and pore water pressure gauges verified the engineering effectiveness of the support system. The monitoring data showed that the deformation of the tunnel sidewalls decreased with depth in a gradient manner (from 0.173 mm at 1 m depth to 0.157 mm at 1.5 m depth), and the deformation rate tended to converge after the 10th day of monitoring. Roof subsidence stabilized at 0.45 mm within 16 days, entering a stable phase after the 14th day. The coordinated effect of support and drainage significantly alleviated pore water pressure concentration, providing theoretical references for the excavation and support of deep water-rich tunnels.

Keywords: Water-Saturated Tunnel, Cyclic Stress, Mechanical-Seepage Coupling, Surrounding Rock Control, Numerical Simulation

Acknowledgments

I am naturally introverted, with average academic performance. During my undergraduate studies, due to unsatisfactory grades, I was transferred from the popular field of electronic information to the less sought-after mining engineering. With a weak foundation in mechanics, a lack of professional interest, and poor research capabilities, this was the reality I faced at the beginning of my graduate studies. Though my supervisor's meticulous guidance prevented any delays in my graduation, by the time I was nearing completion, I had only one SCI paper published in a fourth-tier open-access journal.

At that time, I could almost predict my future — becoming a technician in a coal mine in Henan or Shanxi, operating the winch or cage, living a monotonous life, waking with the dawn bell, and passing the years away. While the role of technician is respectable, it was far from my original aspiration when I started my graduate studies.

(I)

During uncertainty and hopelessness, I met my doctoral supervisor, Professor *Dongming Zhang*. After a single meeting and several phone calls, we had engaging discussions, and he never dismissed me because of my different academic background or my "non-prestigious" origin. Instead, he gave me the opportunity to continue my studies. At that moment, I didn't yet know that receiving the admission letter from Chongqing University in July 2021 would mark the greatest turning point in my life.

After joining the university, under Professor Zhang's guidance, I began participating in various projects within the research group, gaining an initial understanding of new research directions. However, as a student from a different field, I knew little about underground tunnel excavation, support, and coal mining. Aware of my shortcomings, Professor Zhang repeatedly invited me to his office and personally guided me through the principles and methods of in-situ and laboratory experiments. He also bought me books like Engineering Geology and Strength Theory and Numerical Limit Analysis, teaching me to conduct mechanical theoretical analysis. He even spent hours in front of the computer, reviewing my papers, making detailed revisions. His seriousness and attention to detail greatly enhanced my research capabilities.

Professor Zhang is disciplined, eager to learn, and sets a role model for us. While urging us to study, he himself was constantly learning new knowledge and exploring new software. I still remember one night during a business trip, at 2 a.m. in a hotel room, he was discussing methods for plotting multidimensional graphs with us. Through his exemplary diligence and self-discipline, he set a model for scientific research. Thanks to his guidance and support, I have completed many research topics, and the knowledge I lacked in mining has been gradually filled. In November 2022, I published my first top paper, and in January and September 2023, my second and third top papers were published, with several more under review or revision. With Professor Zhang's careful nurturing, I gradually developed the ability to independently conduct laboratory experiments and write high-level papers.

Professor Zhang is warm-hearted and responsible, embodying the virtues of a teacher. Beyond research, he has always cared for my personal development. He strongly supported my participation in various volunteer services and practical activities, teaching me to remember the original intention of pursuing a PhD, to maintain purity and positivity in my thoughts, and to never forget the spirit of contribution and service. Inspired by his philosophy, I have actively participated in volunteer services and social practice activities organized by the university's student organizations: I have volunteered at oncology hospitals, senior care centers, and assisted in pandemic prevention work during holidays, contributing to grassroots efforts. I was even awarded a letter of appreciation from the pandemic prevention command center. During these volunteer activities, Professor Zhang often called me to remind me to take safety precautions. Thanks to his support and concern, from 2021 to 2024, while participating in both campus and off-campus volunteer services, I completed four social practice activities during holidays, earning recognition as one of Chongqing University's Top 10 Young Volunteers and as an Outstanding Individual in Chongqing's Volunteer Service.

Professor Zhang is a seeker of truth and a man of practice. He not only guided me in writing research papers but also supported us in social and literary creation. He always emphasized that articles should reflect the lives of working people and honor laborers and contributors, just as research papers should focus on solving real engineering problems. Encouraged and supported by him, I participated in various writing and art competitions, creating works that praised the dedication of traffic police and researchers during the pandemic, among other subjects. I also created a comic on the theme of "anti-bullying on campus." Through these efforts, I aimed to highlight admirable people and events encountered in volunteer service, using words and images to promote excellent socialist culture. This led to awards such as the Ministry of Education

"Understanding China" Excellent Micro-Video Award, first prize in Chongqing's Graduate Essay Contest, and recognition as one of Chongqing University's Top 10 Cultural and Artistic Students.

As the ancient saying goes, 'A harmonious sound produces a clear echo, and a straight form casts a direct shadow.' Thanks to Professor Zhang's education, role modeling, and support, I have made significant progress in research, political thought, volunteer service, and literary creation. Looking back, I am amazed at the transformation that has occurred since I began my doctoral studies. In terms of both research and life, I have changed drastically, almost becoming a different person from before.

(II)

However, I dare not take all the credit. Even these modest achievements are the result of collective effort. Here, I must also mention another stroke of luck—meeting Senior Brother *Beichen Yu*.

Senior Brother Yu is diligent, enthusiastic, and always willing to help. I still remember the first time I came to Chongqing to work on a roof cutting and pressure relief project. At that time, I knew nothing about the 3DEC software, and there was no one around who could help. I spent several sleepless nights trying to perfect the code, but the task seemed insurmountable. As the project deadline approached, anxiety and frustration grew. At that time, while my family and friends were all praising my future prospects as a '985 doctoral student,' I could not find anyone to confide in. The office was bustling, the days and nights passing by outside the window, but I never imagined that beyond the thorns and hardships, the research path could be so lonely. Fortunately, Senior Brother Yu noticed my situation and offered help. He shared his solutions and comforted me by inviting me to dinner. I will always remember that meal, which included the first grilled fish I had in Chongqing—truly the most delicious one.

Senior Brother Yu's care for my personal life and his support in research have brought light and hope to my long, endless journey in academia. He gave me the courage to keep going.

(III)

I would like to express my heartfelt thanks to my research group colleagues: *Yushun Yang, Shujian Li, Chen Ye, Weijing Xiao, Han Yang, Chenyu Wang, Xiaolei Wang, Xiao Zhou, Fake Ren, Yu Chen, Kunzhong He, Yun Lin, Qinglin Li, Boxue Fu, Tongfang Yue, Kangde Ren, Weihang Du, Ziyang Xiong, Chenxi Liu, Yu Zhang, Wenzhuo Li, Hongzhi Deng, Chaoyang Gong, Tianxing Chen, Yang Gu, Panpan Wang, Linxiong Chen, Shunfa Zhang, Lei Yang, Lantu Wang, Tianhao Lei, Yan Liu,* and others for their guidance and help.

(IV)

Since my third year of doctoral studies, I have been fortunate to pursue joint training at Politecnico di Torino in Italy. During my time at PoliTo, I had the privilege of being mentored by Professors *Marco Barla* and *Alessandra Insana*. I am grateful for their guidance in research and assistance with my English paper writing. They put forward many meaningful comments and suggestions to my graduation thesis, which played a great help for me to revise and improve my thesis.

(V)

I would like to thank my Iranian classmate *Amirreza Pourfatollah*. Whenever I was confused by language barriers or cultural differences, he was always there to help. I will forever remember the times we made dumplings and ate Chinese food together, the countless evenings spent walking and hiking. These moments filled my otherwise lonely days abroad. I also want to thank *Ward Alarab Safarani*, *Dukang Huang, Xunjian Hu, Malo Brancho*, *Da Shi, Renkang Hu, Yuming Guo, Miao Zhang, Xiao Hu, Qinghua Ou*, *Martina Scerbo, Juliana Lopez Ochoa*, *Maria Romana Alvi, Francesco Campana*, and others. I am deeply grateful for their help and support during my time in Italy.

(VI)

I would like to thank Professor *Sijiang Wei* and classmate *Sheng Zhang*, *Dahua Ren*, for their support in my laboratory experiments! I also want to thank my counselor, Ms. *Jingmeng Dong*, for her concern and help in my personal life!

(VII)

I would like to thank the China Scholarship Council, the Ministry of Education, PRC, Baosteel Education Foundation and other organizations for supporting me during my doctoral study.

(VIII)

I am deeply grateful to my family, relatives, and friends for their unwavering support throughout my doctoral journey!

(IX)

Finally, I want to thank myself.

In truth, I don't particularly like mining, and I don't have a great interest in research. Initially, I was influenced by films and admired the title of "doctor." After all, that is the highest academic degree, and it allows one to conduct groundbreaking scientific research! As a child, I often thought how proud I would feel if one day I could be called "Doctor Wang."

When I was adjusted to the field of mining engineering for my graduate studies, I was extremely disappointed. If it weren't for my obsession with the title of "doctor," I might have chosen to drop out and work long ago. At the beginning of my graduate studies, I even schemed to switch back to electronic information and seriously bought many books on communications and signal processing. However, as I continued my studies, I gradually discovered that I didn't seem to have much talent in the field of electronic information, nor did I despise mining and geology as much as I thought. My insistence was merely due to others' opinions—"Electronic information is more popular; mining is a declining industry." Therefore, after graduating with my master's degree, I chose to "walk the same path to the end," continuing my doctoral studies in mining and geology.

Pursuing a doctorate, like graduate studies, initially brings disappointment… I had to go underground to place sensors in coal mining or excavation work faces, stay in the laboratory waiting for a potential experimental phenomenon to occur, and toil day and night writing experimental reports and research papers. This was a far cry from the "groundbreaking scientific achievements" and "benefits to humanity" I had envisioned as a child.

I don't know how long I endured the psychological pressure, but I ultimately persevered.

I am fortunate to have chosen to keep my feet on the ground rather than merely gazing at the stars, taking one solid step after another in my doctoral journey. Finally, I have emitted a bit of my own light. Rumor has it that in the West, there is an immortal firebird named Phoenix. At 500 years old, it burns itself in incense wood, seeking rebirth from the flames and a new life. I have experienced regret from not preparing adequately for my entrance exams, the pain of not having a strong foundation in my field, and the agony of submitting a paper dozens of times only to be rejected for years. But how fortunate I am, to have met a mentor who is both virtuous and talented, and who gave me the opportunity to grow.

I remember reading a story on Zhihu:

> There was a person who, envious of the knights in stories since childhood, spent a lifetime in the deep mountains learning the skills of dragon-slaying and tiger-hunting. When he was finally ready to come down from the mountain, he discovered that there weren't many dragons and tigers in the world; when one did appear, everyone rushed forward to deal with it. So, he began to envy the wealthy merchants and influential officials, complaining about his useless dragon-slaying skills.
>
> In the end, those who learned to slay dragons and subdue tigers either relied on the strength gained from their mountain training to earn a living, or wandered the streets telling thrilling tales to children, or perhaps turned to shady dealings, deceiving a few coins; or maybe a handful would spend their lives trying to catch a dragon or subdue a rampaging tiger.
>
> After all, it's about subduing dragons and tigers! That sounds cool, doesn't it?

In this world, how many things go as desired?

I don't want to rely on brute strength to survive, I don't want to be a storyteller on the streets, and I certainly don't want to be a con artist…

I aspire to be like my mentor and senior classmates, who diligently traverse the mountains and lakes, dedicating their lives to catching a dragon and subduing a ferocious tiger.

After all, research always "sounds cool", doesn't it?

Chongyang Wang
February 21, 2025

Contents

Chapter 1
Introduction

1.1 Framework

The mechanism of mechanical degradation, seepage, and stability control of shale under coupled saturation-cycle stress is critical for understanding its behavior in various geotechnical engineering. The understanding of how shale responds to water saturation and cyclic loading is essential for addressing challenges in resource extraction, infrastructure stability, and environmental safety. Shale's mechanical and permeability behavior under these conditions must be fully understood to manage risks associated with subsurface operations.

This thesis addresses these challenges by investigating the coupled effects of water saturation and cycle stress on shale's mechanical integrity and permeability evolution. The rock's degradation under these influences is linked to significant issues such as wellbore stability in gas extraction, stability in underground mining, and fluid seepage control in engineering projects. Given the pressing need for solutions in these fields, this research aims to explore the underlying mechanisms and provide insights into stability control methods for shale rock mass formations.

Shale, as a layered and anisotropic material, exhibits unique behavior when subjected to water saturation and cycle stress. The combination of cyclic mechanical loading and exposure to water infiltrating the rock's microstructure can lead to pronounced mechanical degradation, reducing the rock's strength and altering its permeability. This deterioration poses significant risks in engineering applications, where maintaining the stability and controlling seepage is of paramount importance. Despite the relevance of this issue, research on the degradation mechanisms and the interplay of these factors remains limited.

Thus, this thesis focuses on the following core aspects:

1) the coupled mechanisms of water saturation, water pressure, and fatigue stress on the mechanical properties and permeability evolution of shale are analyzed by means of laboratory experiments and numerical simulations.

2) the stability of excavated tunnel tunnels under different conditions is analyzed, and a support scheme suitable for cycle-saturated shale tunnels is developed by using both in-situ experiments and numerical simulations.

3) field monitoring is used to assess the effectiveness of the proposed support scheme.

To achieve these objectives, a multi-disciplinary approach combining laboratory experiments, theoretical analysis, and numerical simulations is employed. This thesis aims to reveal the degradation mechanisms of shale under the combined effects of saturation and cycle stress while providing effective strategies for the support of water-saturated shale tunnels and water pressure control.

1.2 Problem statement

The Kun'yang phosphate mine in Yunnan (Fig. 1.1), located in the southwestern phosphate-rich region of Dian'chi Lake, faces significant challenges due to the accumulation of groundwater in its tunnel tunnels. Severe water inrush accidents occurred in 2022 have left sections of the mine submerged for extended periods, leading to the deterioration of the mechanical properties of the surrounding rock (mostly shale) and increasing the need for tunnel support measures (Fig. 1.2). Additionally, the mine is situated within the Xiao'jiang Fault Zone, where mining-induced stresses during excavation causes cycle disturbances to the rock mass, leading to changes in rock permeability.

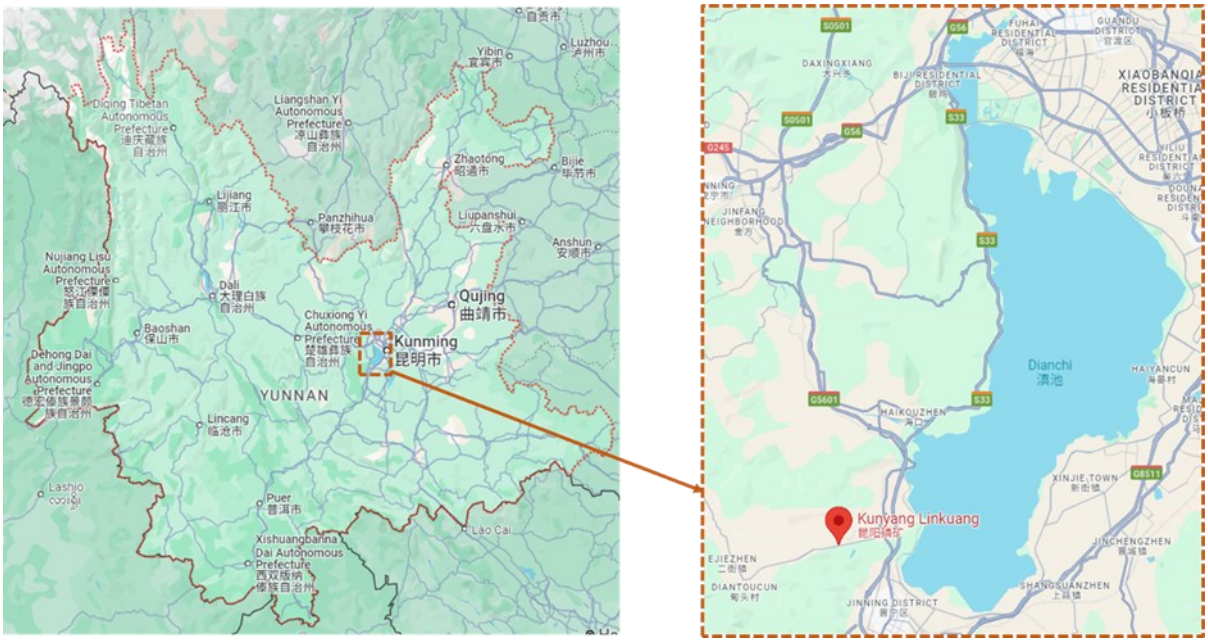

Fig.1.1 Location of Kunyang phosphate mine in Yunnan Province

Fig. 1.2 A water-rich tunnel in Kunyang mine

The combined effects of water saturation, water pressure, and cycle stress create a complex fluid-solid coupling environment in the surrounding rock, which results in degradation of its mechanical integrity and evolution of its permeability. This poses significant risks to the excavation and support of tunnels, as the weakened rock mass becomes less stable and more prone to failure under these conditions.

Despite the critical nature of these issues, the mechanisms of mechanical degradation and permeability changes in shale under the influence of coupled saturation and cycle stress remain poorly understood. There is a pressing need for research that investigates the relationship between saturation damage and fatigue damage, as well as the effects of these combined factors on rock properties and seepage behavior.

This thesis seeks to address this knowledge gap by conducting in-situ experiments, laboratory tests, theoretical analysis, numerical simulations, and field monitoring to explore the degradation mechanisms and permeability evolution of shale under coupled saturation and cycle stress. The research aims to develop a mathematical model that captures these processes, providing critical insights into the stability control of tunnels in the Kunyang phosphate mine and similar water-filled mining environments.

1.3 Thesis scope and objectives

The scope of the present Thesis is to investigate the mechanisms of mechanical degradation, permeability evolution, and stability control of shale under complex conditions of saturation and cyclic loading. This thesis primarily investigates the mechanical degradation, permeability evolution, and stability control of shale under the combined effects of water saturation and cycle stress. The research focuses on addressing the significant impact of water inrush and mining-induced stress on the surrounding rock during tunnel excavation in the Kunyang phosphate mine in Yunnan. The scope of the research includes the following:

1) In-situ experiments: Geological radar was used to detect the development of fractures and the presence of water bodies in front of the tunnel working face. A hollow inclusion stress meter was used to measure the in-situ stress of the tunnel to be tested.

2) Laboratory experiments: Various tests were conducted on shale under different water saturation conditions, including conventional triaxial tests, uniaxial cycle loading tests, true triaxial loading and unloading tests, and true triaxial seepage tests. During the experiments, acoustic emission signals and water flow of the samples were monitored to evaluate the mechanical properties and permeability evolution of the shale under the coupled effects of water pressure, saturation, and cycle stress.

3) Numerical simulations: Numerical simulation software was used to model the deformation and pore water pressure evolution of excavated tunnels under different conditions. A support scheme suitable for water-saturated and cycle-stressed shale tunnels was proposed.

4) Field monitoring: The deformation and pore water pressure in the excavated tunnels were monitored using roof separation instruments, multi-point displacement meters, and pore water pressure gauges to verify the feasibility of the support scheme.

The results of this study will provide important insights into shale's response to complex fluid-solid coupling environments and will contribute to the development of strategies to ensure the stability of tunnels excavated in similar geological conditions.

1.4 Organization of the thesis

The Thesis is divided into 8 chapters. Following the present chapter, which has the purpose to provide a general introduction to the work carried out, *Chapter two* will give a brief overview on the mechanical properties and permeability evolution mechanism of rocks under cycle loading and water saturation, to introduce the shortcomings of previous studies and the innovation of this thesis.

Chapter*s three* to *seven* represent the core work of the thesis, as shown in Figure 1.3.

Chapter *three* analyzes the engineering geological characteristics of a specific mine in the Kun'yang region of the Yunnan phosphate mine through field investigation and engineering geological surveys. An engineering geological evaluation and an estimation of the height of the water-conducting fracture zone were conducted. On this basis, a hollow inclusion stress meter was used to measure the in-situ stress of the tunnel to be tested at the Kun'yang phosphate mine in Yun'nan.

Chapter *four* discusses the effects of saturation duration on the mechanical properties of shale samples through conventional triaxial compression tests and cycle loading tests on water-saturated shale. It analyzes the degradation mechanism of mechanical properties under the influence of water saturation and cycle stress.

Chapter *five* investigates the influence of water saturation and water pressure on the cycle loading characteristics and mechanical properties of shale samples through true triaxial cycle

loading tests and true triaxial seepage tests. It explores the mechanical properties and permeability evolution of samples before and after cycle loading.

Chapter *six* conducts a stability analysis of excavated tunnels under natural and water-saturated conditions using numerical simulations. It simulates the deformation and pore water pressure evolution of tunnels under different support schemes in cycle stess-saturated conditions and proposes a suitable support scheme for such tunnels.

Chapter *seven* monitors the deformation of tunnel sidewalls and roof subsidence in excavated tunnels using multi-point displacement meters and roof separation instruments. Pore water pressure monitoring is also conducted to assess the pore water pressure in the roof of the excavated tunnel, verifying the feasibility of the support scheme.

In conclusion, the results obtained are summarized. Chapter *eight* discusses the innovation of these results and describes the limitations of the thesis, as well as future developments and new prospects.

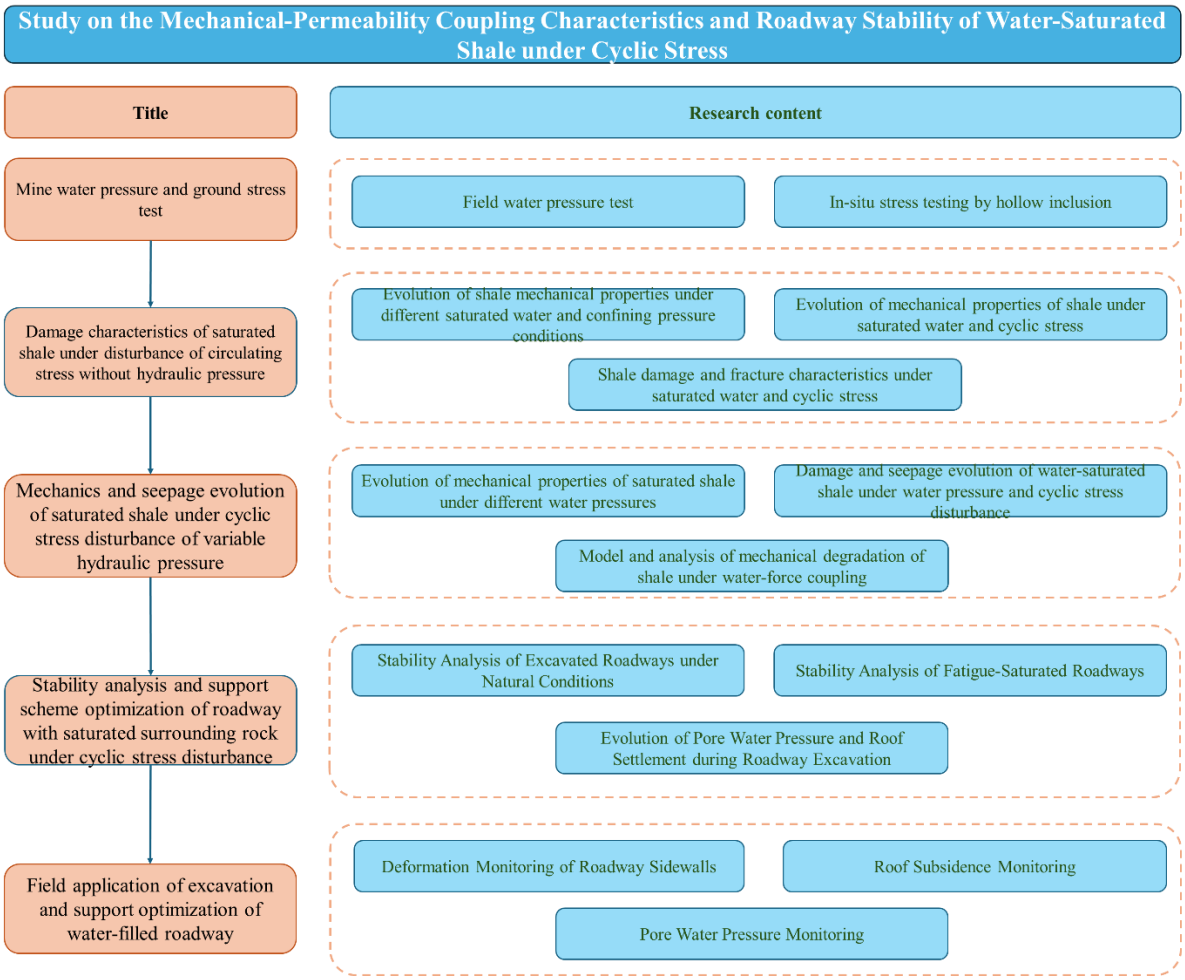

Fig.1.3 Technical roadmap of mechanical degradation, seepage mechanism and stability control of phosphate rock shale under the coupling effect of saturated water- cycle stress

Chapter 2.
Mechanical deterioration and degradation of rocks under fatigue cycle stress and water saturation

2.1 Deterioration mechanism of rock mechanical properties under cycle stress action

During the excavation of underground tunnels, mining-induced stresses can cause the surrounding rock to experience cycle stress disturbances (Li et al., 2023a; Li et al., 2023b). Under the influence of groundwater, the rock surrounding the excavation is subjected to various saturation conditions, water pressure, and cyclic loads, resulting in significant differences in the mechanisms of mechanical degradation (Ghanbarzadeh et al., 2016; Wang et al., 2020; Li et al., 2018). Therefore, studying the mechanical properties of water-rich tunnels is crucial for ensuring the safety of underground engineering.

Numerous scholars have conducted extensive research on the water saturation characteristics of rocks over the years, with experimental methods becoming increasingly sophisticated (Cao et al., 2022; Chen et al., 2014; Ma et al., 2020; Cai et al., 2020; Liu et al., 2023). In laboratory experiments, water treatment of samples can simulate the engineering environment of real rocks under varying water content, allowing for a better understanding of the mechanical behavior of rocks in saturated conditions. Such simulation experiments aid in the study of rock stability, deformation characteristics, and responses to groundwater (Grab et al., 2017). Moreover, the use of cyclic testing machines can evaluate the durability and fatigue resistance of rocks under long-term cyclic loading, providing a scientific basis and reference for engineering design and construction in relevant fields. By examining the mechanical properties and fatigue characteristics of samples, a comprehensive understanding of rock mechanical properties can be achieved, which can then be better applied to practical engineering (Moore & Lockner, 2004; Priest et al., 2021).

In the study of rock fatigue characteristics, the strength of samples, the evolution of deformation parameters, and the damage evolution laws based on formulas and acoustic emission characteristics are key focal points for researchers (Chen et al., 2012; Xu et al., 2021; Sun et al., 2017; Li et al., 2020). To investigate the evolution of deformation and damage parameters of marble under cycle loading, Song et al. (2021) conducted freeze-thaw fatigue tests involving multiple freeze-thaw cycles and multi-level cyclic loading, discovering that the maximum axial strain and strain rate of the samples increased with the number of freeze-thaw

cycles, resulting in shorter fatigue lifespans for the marble specimens as the number of freeze-thaw cycles increased (see Figure 1.2). He et al. (2019) found that in exploring the damage evolution laws of salt rock under fatigue loading, higher amplitudes of fatigue stress, increased loading frequency, and faster loading rates all contributed to reduced fatigue lifespans for salt rock samples (Li et al., 2023; Zhao et al., 2021). Furthermore, the fatigue lifespan exhibited an exponential negative correlation with both stress amplitude and loading rate (see Figure 1.3). Dai et al. (2022) performed shear and compression coupling loading tests under different loading conditions, systematically revealing the effects of cyclic loading parameters on rock deformation characteristics, energy evolution, damage variables, and failure mechanisms under coupled shear and compression loading. Zhong et al. (2022) conducted indoor tests on anchored jointed rock masses under different fatigue shear loads, showing that the loss of prestress caused by fatigue loads increased in a wave-like manner, with the increment and rate of prestress loss increasing with the increase in fatigue load. Given that the load amplitude remained constant, the average cyclic stress of the tested samples increased with the maximum stress, leading to an increase in fatigue energy density. This is similar to the effect of maximum stress, where higher amplitudes resulted in larger areas of individual cyclic hysteresis loops, consuming more energy during loading and unloading processes. In fatigue loading tests, the accumulation of damage during the cyclic loading phase can affect the failure and energy conversion modes of the samples, with significant differences in friction strength, mechanical behavior, elastic wave velocity, uniaxial compressive strength, elastic modulus, and elastic energy storage capacity between saturated and dry rock samples under cyclic stress (Wang et al., 2022b; Gu et al., 2023).

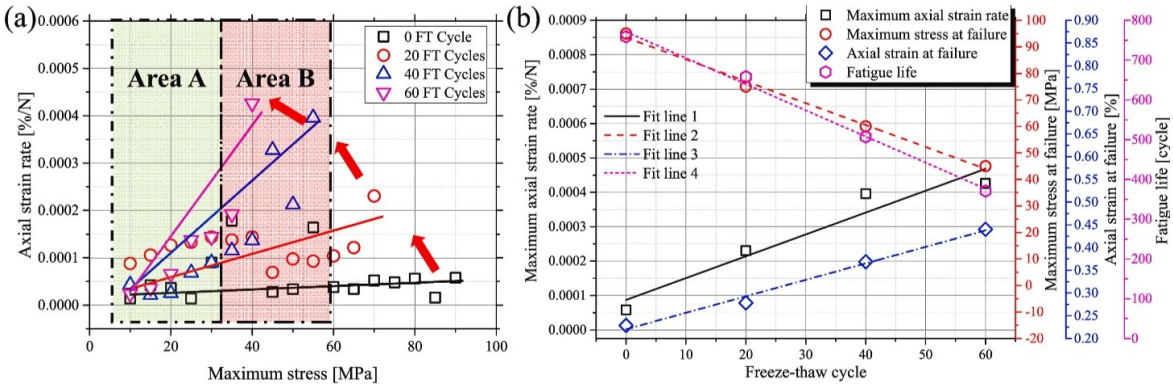

(a) (b)

Fig.1.2 Evolution of axial strain rate of marble samples in freeze-thaw cycle test. (a) The axial strain rate of the sample. (b) the relationship between the deformation parameters and the freeze-thaw cycle (Song et al., 2021).

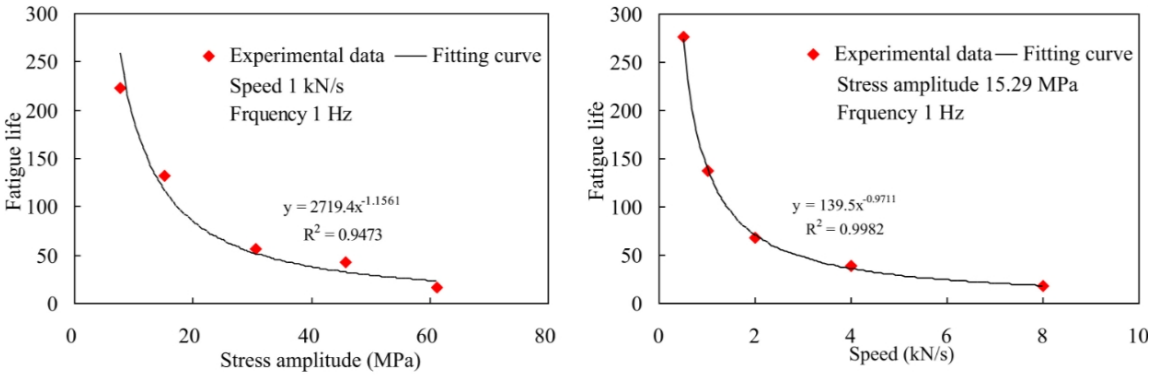

(a) (b)

Fig. 1.3 Fatigue life of salt rock under different test conditions. (a) Fatigue life of salt rock under different stress amplitudes. (b) fatigue life of salt rock under different loading speeds (He et al., 2019).

In basic physical mechanics experiments conducted in laboratories, shale has consistently been a primary subject of mechanical exploration (Zhai et al., 2022; Dou et al., 2021; He et al., 2020). The inherent low porosity and permeability characteristics of shale can significantly influence the hydraulic fracturing process. Therefore, a thorough investigation of the deformation and seepage characteristics of shale under fatigue loading and water saturation coupling is crucial for the advancement of shale tunnel excavation support and the utilization of shale gas (Tang et al., 2023; Li et al., 2016; Chen et al., 2022). Wei et al. (2020) studied the variation of mechanical parameters of shale from deformation to failure under different stress paths and water content through triaxial compression, numerical simulations, and physical-mechanical cyclic loading experiments. Peng et al. (2018) employed triaxial compression and alternating loading rate tests to investigate the effect of loading rate on the post-failure characteristics of three types of saturated rocks, as well as the influence of confining pressure on the post-failure loading rate effects. Tang et al. (2018) analyzed the influence of layering and water on the creep characteristics of shale based on uniaxial compression creep tests. They developed a creep model that replaces the instantaneous elastic modulus and viscosity coefficient in the model with functions of layering angle and water content, reflecting these parameters. To explore the degradation of mechanical properties of rock masses at reservoir slopes under the action of water and gas drying cycles, Song et al. (2023) conducted triaxial compression tests on sandstone at varying water levels of reservoir slopes to determine the rock degradation mechanism. Feng et al. (2022) utilized true triaxial unloading-dynamic disturbance tests to examine the instability and rupture characteristics of red sandstone samples under different water saturation conditions in dynamic-static combined scenarios, revealing the weak water rock explosion mechanism under true triaxial unloading-dynamic disturbance. Luo et al. (2019) conducted rock burst tests on red granite under varying water saturation conditions using a true triaxial rock burst test system, exploring the quantitative relationship between rock saturation and the kinetic energy of rock bursts, as well as the influence of water on rock bursts.

In practical engineering, issues such as rock cycle loading and water saturation are frequently encountered (Xu et al., 2022; Cheng et al., 2021; Song et al., 2023; Wang et al., 2021; Chen et al., 2023). Consequently, various forms of indoor experiments are vital for scientifically evaluating the long-term stability of geotechnical engineering (Huang et al., 2023). The FCI loading tests on rocks with pre-fabricated cracks at different angles can be used to study the damage and failure characteristics of rocks under the interaction of fatigue and creep (Wang et al., 2022a; Wang et al., 2022b). In studies on the dynamic tensile fatigue characteristics of rocks, the peak stress of samples decreases while the peak strain increases with the number of impacts (Li et al., 2022). Based on the characteristics of rock failure under uniaxial cyclic loading and unloading, Cao et al. (2021) developed a new method that can serve as a precursor to severe rock failure. Shi et al. (2023) proposed a new constitutive model for rocks under multi-layer fatigue loads based on the Lemaitre strain equivalence hypothesis. Ma et al. (2021) investigated the combined effects of creep and fatigue on the mechanical properties of rock salt, finding that the stress hold time reduces the cyclic life of rock salt, and the rate of acoustic emission is related to the formation of microcracks. They also noted a linear correlation between the deformation rate during the steady-state phase and the life expectancy and observed different fracture patterns in joint experiments. Although scholars at home and abroad have studied the effects of saturated water and fatigue loads on the mechanical properties of rocks, there are still some issues that need to be addressed (Wang et al., 2023). First, the mechanical properties of different types of rocks under water saturation and fatigue load conditions may vary, making further research on the mechanical properties of phosphorite necessary. Secondly, the coupling effect of water saturation and fatigue load is unclear and requires further investigation through specific experiments.

Under fatigue loading, the stress experienced by the rock undergoes significant changes from static to dynamic stress, significantly impacting the strength, fracture, and deformation characteristics of the rock (Du et al., 2020; Du et al., 2021). For instance, the deformation and rupture behavior of rocks under seismic stress exhibits nonlinear and dynamic characteristics, affecting the propagation velocity, amplitude, and frequency of seismic waves (Wang et al., 2022a). Zhao et al. (2021) pointed out through experiments that under fatigue loading, the damage-failure curve of the rock exhibits a “loose-dense-loose” type of hysteresis loop. The crack development curve initially shows a convex shape during loading, slows down, stabilizes, and then presents a concave shape with an increased loading rate until failure, demonstrating an overall stepwise increase. Sui et al. (2020) established a true triaxial numerical model of core samples using the discrete element method to study the fatigue damage of reservoir rocks during the cyclic injection and extraction process. Based on laboratory experiments, they calibrated the numerical model parameters to examine the effects of cyclic stress on the microstructure and mechanical properties of the rocks. Li et al. (2023) conducted uniaxial and triaxial gradient creep fatigue tests on rock salt, analyzing its mechanical and acoustic emission characteristics

in conjunction with the actual gas pressure during the operation of compressed air energy storage (CAES) facilities. Liu et al. (2022) performed multi-axial multi-stage cyclic loading and unloading tests to investigate the impact of unloading rate on the deformation behavior, energy evolution, and damage characteristics of rock-like materials. They found that during the evolution of various energy density parameters under different unloading rates, both the total energy density and elastic energy density increased with rising unloading rates, while the dissipated energy density decreased. As the unloading rate increased, the nonlinearity of the energy density and relative cycle number curve became more pronounced (See Fig. 1.4). Wang et al. (2022b) conducted multi-stage intermittent cyclic loading tests on red sandstone with cracks at different angles, finding that the deformation parameters increased initially before stabilizing. As the rock sample approached failure, the plastic strain accumulated rapidly, and both the elastic modulus and deformation modulus decreased. Fatigue damage exhibited characteristics of initially slowing, followed by stable accumulation, and eventually accelerating development.

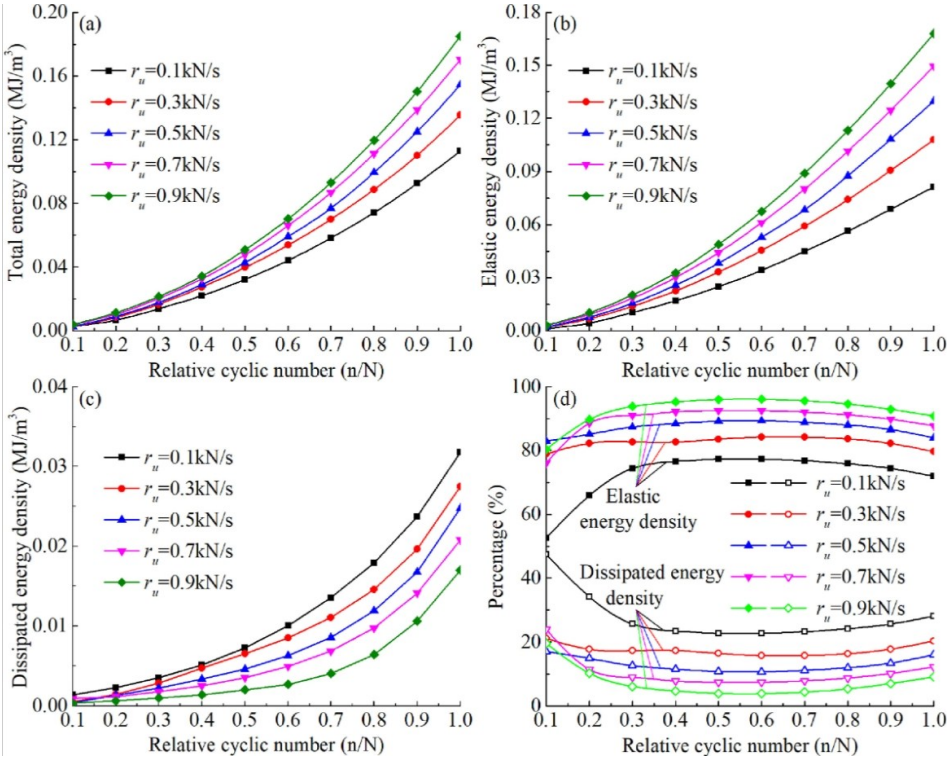

Fig. 1.4 Energy density evolution of rock-like materials at different unloading rates. (a) Total energy density; (b) Elastic energy density; (c) Dissipated energy density; (d) Percentage of elastic energy density and dissipated energy density in total energy density (Liu et al., 2022).

2.2 Degradation mechanism of rock mechanical properties under water saturation

The presence of water significantly affects the mechanical properties and failure behavior of rock samples. Relevant experiments have revealed that the strength of the intact rock is primarily influenced by the duration of water exposure rather than water saturation itself (Siddiqui and Roshan, 2022). Numerous scholars have conducted laboratory studies on the mechanical properties and failure behavior of dry and water-saturated anisotropic rock specimens, highlighting that the presence of water markedly reduces the strength, elastic modulus, and strength anisotropy of rocks (Liu et al., 2019; Wen et al., 2022; Alishaev et al., 2012; Wu et al., 2023). In studies focusing on the water saturation characteristics of rocks, many researchers have concluded through experiments that when rocks are in a saturated state, the presence of water fills the internal cracks, thereby altering the pore structure of the rock and changing the interactions between cracks, which leads to significant changes in the stress transfer characteristics of the rock (Wang et al., 2020; Liu et al., 2023).

In water-rich tunnels, the influx of groundwater can lead to prolonged immersion of rocks, altering their mechanical properties. Additionally, the fatigue loads induced by fatigue stress and mining-induced stress can cause fatigue damage to rocks, increasing the difficulty of mining support. Therefore, studying the fatigue damage characteristics of rocks under varying durations of water saturation is of significant importance. The impact of saturation conditions on rock mechanical properties has garnered considerable attention in geological research (Li et al., 2012; Liang et al., 2019; Sang et al., 2019). Under water-saturated conditions, the strength, deformation, and rupture characteristics of rocks exhibit significant changes (Yin et al., 2022; Luo, 2020). Zheng et al. (2017) examined the strength and strain rates of rocks under four different saturation conditions from the perspectives of rock strength, peak strain, peak modulus, and strain rate. Previous studies have shown that there are notable differences in the mechanical properties, acoustic emission characteristics, and crack evolution features of rocks in dry, natural, and saturated water states. The presence of water considerably decreases the compressive strength, elastic modulus, and peak strain of fractured rocks (Zhu et al., 2023). As illustrated in the stress-strain curve evolution of fractured sandstone under different water content conditions (see Fig. 1.5), with an increase in water content, the slope of the stress-strain curve of fractured sandstone gradually decreases, indicating a linear reduction in its compressive strength, elastic modulus, and peak strain. This demonstrates that water has a significant deteriorating effect on the strength and stiffness of fractured sandstone, with the tensile strength, uniaxial compressive strength, and triaxial compressive strength of samples showing varying degrees of reduction after saturation (Tan et al., 2019).

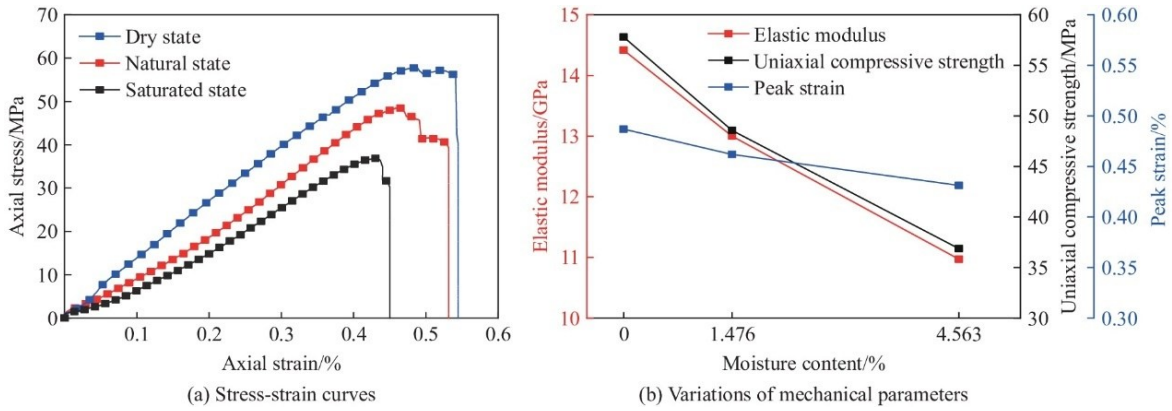

(a) (b)

Fig. 1.5 Stress-strain curve and mechanical parameter change of fractured sandstone under different water state. (a) Stress-strain curve (b). Evolution of mechanical parameters (Zhu et al., 2023).

The mechanical properties of rocks are not only related to the number of interlayer water molecules but also to their arrangement (Meng et al., 2023). As shown in Figure 1.6, coal of different grades exhibits cyclic hardening under cyclic loading. Compared to low-rank coal, high-rank coal has smaller internal pore sizes and a more stable structure. During the first cycle, high-rank coal shows higher hardness and elastic modulus. Under continuous cyclic loading, as the coal rank increases, changes in hardness and elastic modulus decrease, and cyclic hardening weakens. Additionally, the higher the coal rank, the less energy dissipation occurs under cyclic loading, and the change in energy dissipation rate is smaller. In studies of the mechanical and acoustic emission characteristics of water-saturated rocks, experimental results indicate that water content alters the mechanical strength, acoustic emission signals, and failure modes of samples. The presence of water in rocks reduces their strength, the number of secondary cracks, and acoustic emission counts (Zhuang et al., 2020; Zhao et al., 2022). Various laboratory studies have employed different experimental methods to investigate the mechanical properties of water-saturated rocks, such as water absorption measurements, Brazilian splitting tests, uniaxial and triaxial compression tests, and molecular dynamics (MD) simulations (Liu et al., 2022; Zhu et al., 2022). Luo et al. (2022) pointed out that the duration of water saturation significantly affects the strength and acoustic emission parameters of clay mineral-bearing rocks. The impact of water saturation on the mechanical properties of rocks is a widely studied topic in geology. Rocks with high water saturation have increased porosity and permeability due to the presence of a large amount of water, and water content significantly influences the strength, deformation, and fracturing behavior of rocks (Zhu et al., 2022).

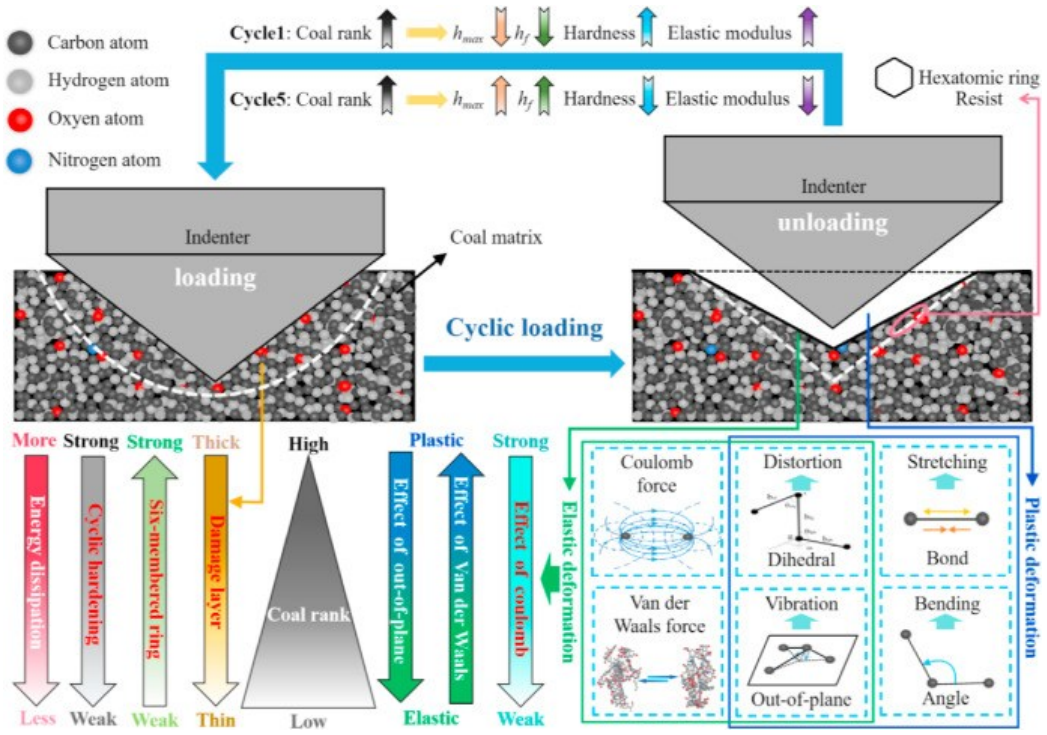

Fig. 1.6 Effect of cyclic loading on mechanical properties and failure mechanism of different grades of coal (Meng et al., 2023)

Numerous scholars have conducted both dynamic and static compression experiments on rock samples under different water content conditions to study the effects of water saturation on rock strength, peak strain, peak modulus, and strain rate (Zheng et al., 2017; Liu et al., 2022; Luo et al., 2022). Li et al. (2023) characterized the pore characteristics of sandstone using low-field nuclear magnetic resonance and scanning electron microscopy, investigating the effect of water on the mechanical properties of rock materials. Caselle et al. (2022) conducted experiments on dry, oil-saturated, and water-saturated samples to quantify the weakening effect of water on gypsum. Uniaxial and conventional triaxial tests revealed a significant weakening effect of water on gypsum; however, the weakening effect in the water-saturated state was not as pronounced compared to other rocks.

In the excavation of mine tunnels, water inrush often occurs, and immersion and saturation lead to the deterioration of rock mass mechanical properties, increasing the difficulty of excavation and support. Therefore, it is of great significance to explore the degradation mechanisms of rock mechanical properties under different saturation durations (Liu and Li, 2023a; Liu et al., 2023b; Liu et al., 2023c). Many scholars at home and abroad have conducted extensive research on the water-induced deterioration mechanisms of rocks (Ni et al., 2005; Wood, 2015; Wang et al., 2023; Ma et al., 2020). Feng et al. (2022) explored the instability and fracture characteristics of red sandstone samples at different water saturation states through laboratory tests. They concluded that the mechanical response of natural sandstone samples exhibits typical rockburst characteristics, while the mechanical response of saturated sandstone samples is mainly reflected in the degree of fragmentation. Zhao (2022) in studying the changes in the mechanical

properties and microstructure of rocks under saturation, performed triaxial compression and scanning electron microscopy (SEM) experiments under different confining pressures and saturation conditions, concluding that as the degree of saturation increases, the mechanical properties of sandstone continuously decline, and the water-induced deterioration effect is significant. Wang et al. (2019) found through experiments that the elastic modulus and deformation modulus of sandstone are negatively correlated with sample volume, with the Poisson's ratio of dry sandstone increasing with volume, while the Poisson's ratio of saturated sandstone first increases and then stabilizes with increasing volume. The presence of water has no significant impact on the failure mode of rock samples under uniaxial compression. Jia et al. (2023) in studying the deformation characteristics of saturated rock masses in cold regions, pointed out that the freeze-thaw strain characteristics of water-saturated rock masses are related to fracture length, width, and lithology, with freeze-thaw failure of fractured rock masses being a process of gradual accumulation of residual strain. The water environment (moisture content, seepage pressure), loading rate, and generalized stress relaxation significantly affect the aging characteristics of rock, and these aging characteristics in the presence of water have important implications for the long-term stability of tunnel surrounding rocks (Chen, 2021); Wang et al. (2020) through research on the tensile strength and failure mechanisms of thermally-hydro-coupled damaged rocks at different loading rates, noted that the indirect tensile strength of saturated sandstone specimens is lower than that of dry specimens, and the strain rate dependence of saturated rock samples is stronger than that of dry rocks. A large amount of electromagnetic radiation signals is released during the loading failure process of water-bearing fractured rock masses, providing guidance for monitoring and early warning of related geological disasters. Shen et al. (2021) studied the effects of water on the electromagnetic radiation characteristics of fractured sandstone under stress loads. The results showed that, compared to dry rock samples, saturated rock samples have lower compressive strength, earlier cracking times, and more complex failure modes. Additionally, the damage evolution characteristics of samples based on acoustic emission localization indicated that more crack sources are generated inside the saturated samples in the early stages of loading, and their electromagnetic radiation signals are stronger than those of dry samples. However, in the mid to late stages of loading, the number of internal crack sources in dry samples increases sharply, and the intensity of their electromagnetic radiation signals gradually surpasses that of saturated rock samples (Figure 1.7).

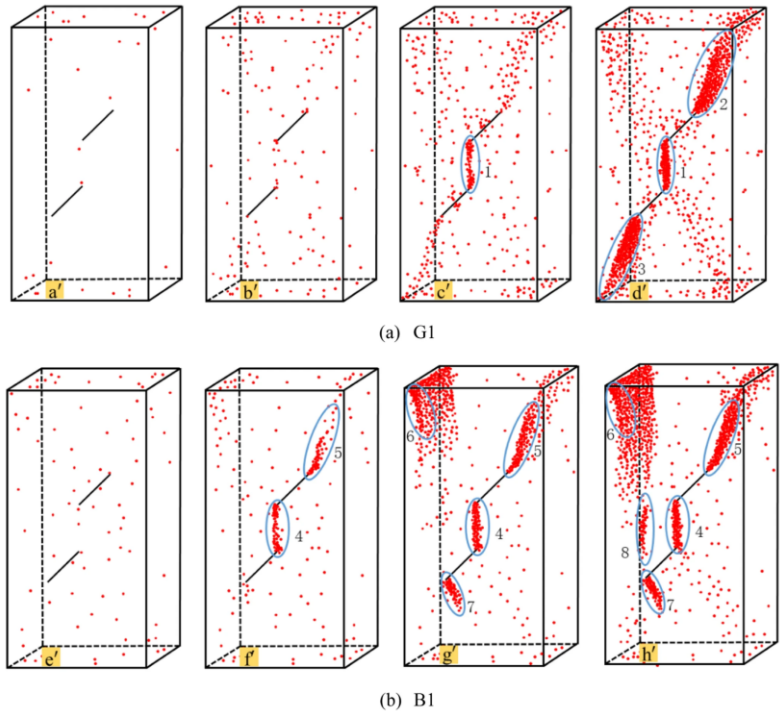

Fig. 1.7 Acoustic emission localization and spatiotemporal evolution of samples. (a) dry samples. (b) saturated samples (Shen et al., 2021)

Permeability is a key parameter affecting shale gas development (Hu, 2022; Zhang et al., 2023; Liu et al., 2019). To study the seepage capacity of shale matrix, Hu (2023) simulated gas seepage in different shale facies matrices, calculated permeability, and modified the results based on the slip and diffusion effects of shale gas, establishing a permeability calculation model for shale reservoirs considering different shale facies. Yang et al. (2021) studied the permeability of intact and fractured shale samples under effective stress and proposed a new model to describe the anisotropy of rock permeability characteristics, pointing out that the permeability of both types of shale samples decreases exponentially with increasing effective stress. Shale expansion, water blockage, and NaCl crystals make shale permeability more sensitive to pore pressure, and the original structure affects the mechanical behavior and permeability of shale (Lyu et al., 2022; Liang et al., 2021). Tan et al. (2021) proposed a comprehensive permeability model considering the impact of water saturation on stress-related gas permeability, with experiments showing that water content has a significant impact on the effective permeability of low-permeability samples. Li et al. (2023) characterized the surface morphology, internal moisture, pore-fracture structure, and molecular structure changes in coal, revealing the effect of steam on coalbed methane extraction. Extensive research on the deformation and permeability characteristics of shale by many scholars provides theoretical references for supporting water-rich tunnels and shale gas extraction under complex conditions (Jiang et al., 2016; Yang et al., 2022; Cheng & Yu, 2019; Zhang et al., 2022).

In the study of the mechanical properties and permeability of water-saturated shale, many scholars have explored the factors affecting the evolution of fractures and permeability in

saturated shale through a series of experiments (Chen et al., 2019; Zhang & Sheng, 2018; Zuo et al., 2018; Roshan et al., 2015). Zeng et al. (2020) through nuclear magnetic resonance (NMR) experiments on shale samples, pointed out that the wettability index is related to the gas production capacity of wells, aiding in the study of shale pore types and wettability. As the main pathway for gas flow, microfractures may exhibit mixed wettability, potentially allowing oil to enter the fractures. NMR signals only reflect hydrogen-containing substances, making it difficult to drive all bound water out of shale samples, and at high pressure, it is much harder for oil to enter inorganic pores. Chen et al. (2019) studied the mechanical properties of fractures in two different compositional shales using saturated water, ambient air, and dry CO_2 gas, showing that water has a significant impact on the fracture development characteristics of shale, with a competitive relationship between the mechanical extension of fractures and the physico-chemical interactions between water and rock. These studies are of great significance for understanding the mechanical properties and permeability evolution of water-saturated shale under complex conditions.

2.3 Summary

This thesis examines the changes in the mechanical properties of intact rocks resulting from groundwater accumulation in the Kunyang phosphate mine, China. Due to mining stress and engineering activities, the rock mass in this area experience the combined effects of water saturation and cycle stress. Understanding the deterioration of intact rock properties and the evolution of permeability under these conditions is essential for tunnel excavation and support strategies.

This chapter provides a detailed review of recent advancements, focusing on key case studies that assess the effects of water saturation, water pressure, and cycle stress on intact rock mechanics and permeability. With more refined research methods, mathematical models based on field monitoring data can now simulate rock mass behavior under various conditions. Extensive studies have investigated the deterioration mechanisms induced by cycle stress, including failure, deformation, acoustic emission characteristics, and fatigue life. Saturation significantly increases permeability while affecting rock strength, elastic modulus, and acoustic emissions.

Despite ongoing research, there has been limited progress in understanding the mechanical behavior of shale under the combined effects of water saturation, water pressure, and cycle stress. This study, centered on the Kunyang phosphate mine, explores the complex interactions between these factors in shale during mining operations.

The research integrates field monitoring, experimental analysis, and numerical simulations to summarize the fatigue characteristics and permeability evolution of shale under varying saturation and pressure conditions. It proposes effective support strategies for the mine, offering

valuable insights for excavation and support in water-filled tunnels and similar mining environments.

Chapter 3
Mine water pressure and ground stress test

Yunnan Phosphate Chemical Group Co., Ltd. is a modern phosphate mining and beneficiation enterprise, as well as a key national phosphate chemical company. The company has a raw phosphate ore production capacity of approximately 11.5 million tonnes per year and a flotation processing capacity of 7.5 million tonnes per year. Its phosphate products hold a market share of about 15% nationwide. The Yunnan phosphate mining area under investigation was established in 1965. As of the end of September 2019, a total stripping volume of 35.45 million cubic meters and an extracted ore volume of 6.00 million tonnes had been completed. The mining area is in the southwest of the Dianchi phosphate enrichment zone, bordered by the Xiaojiaying phosphate mine to the west and the Haikou phosphate mine to the north. It enjoys convenient transportation, and the specific mining area boundaries are shown in Fig. 3.1.

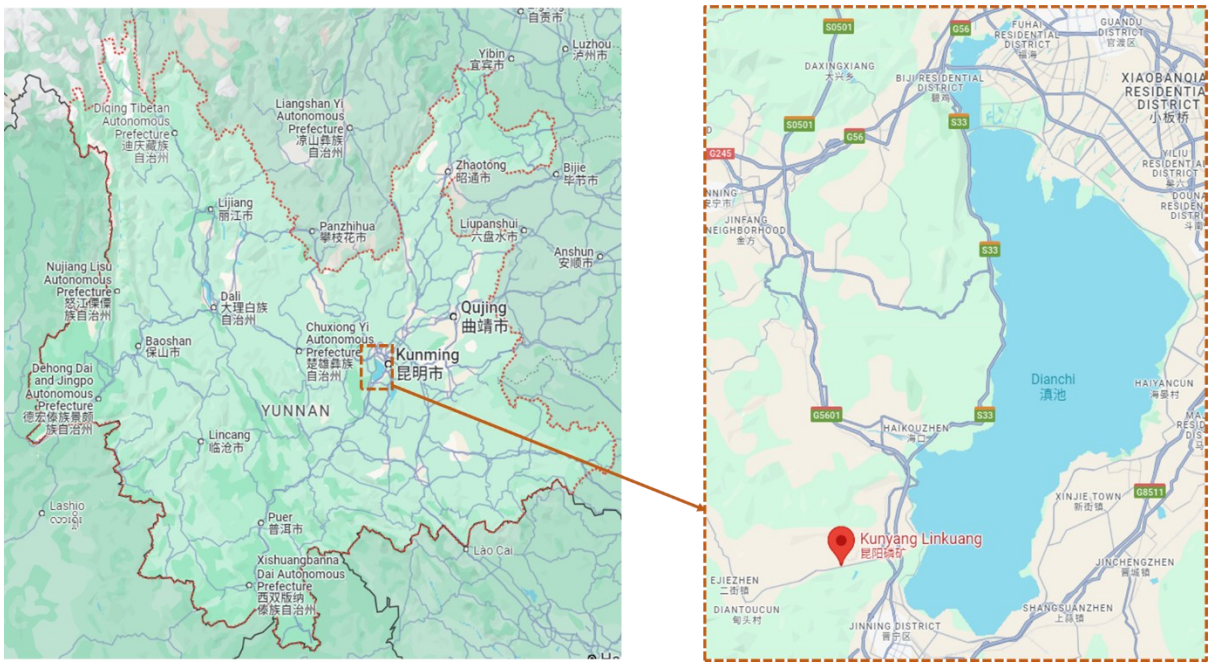

Fig. 3.1 Mining area and scope of mining rights of Kunyang phosphate mine in Yunnan Province

The Yunnan phosphate mining area has abundant groundwater, and water saturation and water pressure lead to the deterioration of the mechanical properties of surrounding rock mass and changes in permeability, which in turn affect the stability of excavated tunnels. Based on

field monitoring and data collection, the excavation plan for the targeted mining area was obtained, and the excavation layout and roof water pressure distribution of the selected tunnel were mapped, as shown in Fig. 3.2.

As shown in Fig. 3.2, the roof loading process during tunnel excavation can be divided into two stages. The first stage involves horizontal excavation, where the roof is relatively far from the water-rich zone and remains unaffected by water pressure disturbances. The second stage involves inclined upward excavation, which is located beneath the water-rich zone. In this stage, the roof is not only influenced by mining-induced stress but also disturbed by water pressure. Therefore, it is necessary to analyze the geological conditions on site and conduct water pressure and in-situ stress tests to provide references for subsequent laboratory experiments and numerical simulation designs.

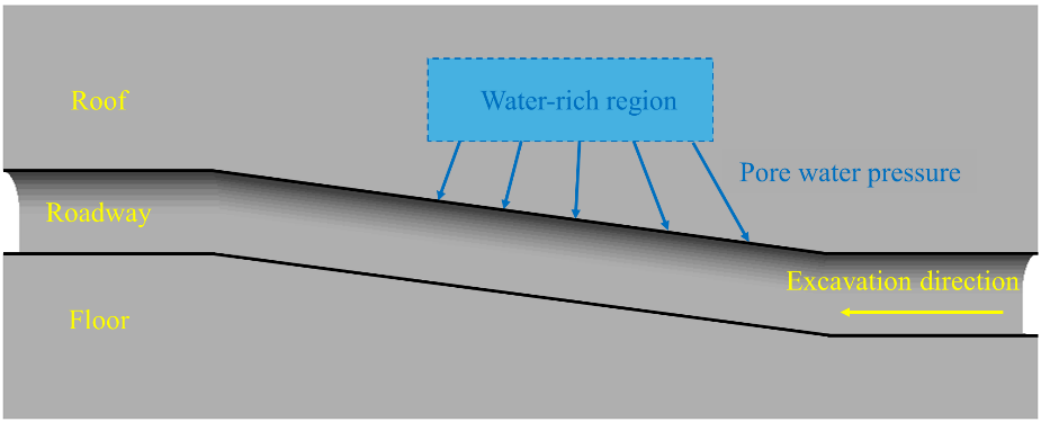

Fig. 3.2 Distribution of tunnel excavation and roof water pressure

3.1 Engineering geological condition

3.1.1 Engineering geological characteristics

3.1.1.1 Subdivision into Engineering Geological Rock Groups

The phosphate ore layer in a certain mine in Kunyang, Yunnan, is hosted in the first section of the Lower Cambrian Zhongyicun Formation. The ore bodies are distributed continuously and have a relatively simple structure, mainly consisting of dense massive phosphorite, striped and banded clastic phosphorite. Based on the structure and composition of the rocks and ores, the degree of weathering of the rock masses, and the development of fractures and karst features, the rock and ore bodies in this mining area are divided into four engineering geological rock units:

(1) Loose rock formations: The lithology is composed of Quaternary sands, gravels, and clays, mainly distributed in the southwestern part of the mining area, with a thickness of 3 to 44 meters. The structure is loose.

(2) Layered clastic rock unit (hard to semi-hard): The thickness ranges from 136.88 to 368.27 meters, and it is continuously distributed throughout the entire mining area. Surface fractures are well-developed, with a spacing of 5 to 60 cm, mostly closed.

(3) Soluble salt rock unit (hard to semi-hard): - Upper Devonian Zhaige Formation: Thickness of 76 to 422 meters, with well-developed fractures and karst features; the rocks are hard. - Lower Cambrian Yuhucun Formation: Thickness of 272.1 to 517.29 meters, with well-developed surface fractures, fracture widths of 0 to 5 mm, filled with mud, and spacing of 5 to 45 cm, up to a maximum of 70 cm.

(4) Weak rock unit: Lower section of the Lower Cambrian Zhongyicun Formation, with a thickness of 0 to 2 meters. This rock layer is hard-plastic in its natural state and becomes plastic to soft-plastic when saturated with water, which is unfavorable for mining operations.

The physical and mechanical properties of layered clastic rock unit and soluble salt rock unit are shown in Table 3.1.

Table. 3.1 Physical and mechanical properties of rock strata in mining area

	Physical and mechanical parameters	Layered clastic rock unit (hard to semi-hard)		Upper Devonian Zhaige Formation		Lower Cambrian Yuhucun Formation	
		Value range	Mean value	Value range	Mean value	Value range	Mean value
Physical property	Drilling RQD value (%)	12～96	37	10～85	45.5	0～59	17.7
	Rock specific gravity	2.73～2.8	2.76	2.78～2.78	2.72	2.81～3	2.88
	Wet density (g/cm^3)	2.66～2.71	2.69	2.65～2.71	2.69	2.81～2.85	2.84
	Water absorption (%)	1.15～2.79	1.68	1.18～3.16	2.17	0.3～2.53	0.88
	Porosity (%)	3.06～7.22	4.42	3.22～8.06	5.64	0.83～6.94	2.40
Mechanical parameters under dry conditions	Uniaxial compressive strength (MPa)	2.88～127.9	62.29	34.5～47.8	40.63	27.9～65.6	47.2
	Tensile strength (MPa)	2.38～6.54	4.50	2.75～3.78	3.10	3.43～6.17	4.61
	Cohesion (MPa)	3.64～5.78	4.96	6.43～7.38	6.91	——	4.51
	Internal friction Angle (°)	39.2～42.6	41.13	42.2～43.	42.75	——	42.1
Mechanical parameters under	Uniaxial compressive strength (MPa)	1.27～113	40	23.6～44.9	32.85	21.9～56.3	37.11

saturated water condition	Tensile strength (MPa)	1.52～4.09	2.54	1.77～2.40	2.00	2.63～4.23	3.29
	Cohesion (MPa)	2.75～5.01	4.03	5.95～6.44	6.20	4.31～6.17	5.01
	Internal friction Angle (°)	38.6～41.2	40.07	41.7～42.4	42.05	38.8～42.1	40.65

In summary, except for the Quaternary loose rocks, which have poor engineering properties due to their loose structure, the ore bodies and surrounding rocks are generally categorized as hard to semi-hard rock units with high rock mechanical strength, making them favorable for tunnel excavation. However, the weak rock layers interbedded in the ore layer exhibit a fragmented, short-columnar structure with low mechanical strength, making them prone to collapse during the later stages of lower-layer mining.

3.1.1.2 Structural plane characteristics

The structural surfaces in the mining area are primarily composed of faults, bedding planes, and joint fractures. After a comprehensive analysis of the types, orientations, extensions, dips, and impacts on rock mass stability of the faults, joints, and fractures, three main structural surface levels are identified within the area: Level II and Level III structural surfaces, as follows:

(1) Level II structural surface

The Level II structural surface is represented by the Sanjiacun Fault, which runs near east-west and is in the southern part of the mining area. This fault is a north-dipping normal fault and is the largest regional fault in the area. The fault has a strike of 70°–75°, which is roughly parallel to the lower boundary of the orebody, with a dip direction of 345° and a dip angle of 73°. Although the fault exerts regional control over the orebody's shape, it has no direct impact on the stability of underground mining operations.

(2) Level III structural surface

Two normal faults are developed within the mining area, both trending southeast to northwest with dip angles of approximately 70°. Detailed parameters are provided in Table 3.2:

F1 Fault: Located on the western side of the sixth mining section of Kunyang mine, the F1 fault has a general strike of 154° with a dip angle of about 80° and a fault displacement of 68 meters. As this fault lies within the open-pit mining boundary, it has no direct impact on the stability of underground mining operations.

F2 Fault: Located in the northwest part of the mining area, the F2 fault is 410 meters long with a general strike of 137° and a dip angle of 75°, and a fault displacement of 10–20 meters. Due to surface phosphate mining and dumping, the fault is covered by Quaternary deposits. Since part of this fault lies within the scope of this evaluation, it has a certain impact on the stability of local engineering works. When the tunnel passes through this fault, appropriate support measures should be implemented.

Table. 3.2 Fault structure of a mine in Kunyang

Name of fault	Attitude				Statement
	Length (m)	Strike (°)	Dip Direction (°)	Dip Angle (°)	Displacement (m)	
F1	330	154	64	80	68	The eastern block has subsided, and the western block has risen.
F2	410	137	227	70～80	10～20	The southwestern block has subsided, and the northeastern block has risen.

3.1.2 Engineering geological evaluation

3.1.2.1 Stability evaluation of orebody and roof and floor rock layers

The quality of the orebody, surrounding rock, and the stability of surrounding rock in shafts and tunnels are evaluated using the rock mass quality evaluation method (Z) (Liu et al., 2021) and the rock quality designation method (RQD). The calculation formulas for the rock mass quality coefficient are as follows:

$$\begin{cases} Z = I \times S \times tan\varphi \\ M = \frac{\sigma_c}{300} \cdot RQD \end{cases} \tag{3.1}$$

where Z is the rock mass quality coefficient, I is the integrity coefficient (i.e. RQD value), S is the rock hardness coefficient ($\sigma_c/100$), φ is the internal friction angle of rock mass (°), M is the rock mass quality index, σ_c is the uniaxial compressive strength of rock mass (MPa), RQD is the Rock Quality Designation. Using Equation (3.1), the rock mass quality coefficient Z and the rock mass quality index M are calculated. The results are shown in Table 3.3.

Table. 3.3 Calculation results of rock mass quality coefficient Z and rock mass quality index M

Rock group	Rock mass quality evaluation coefficient method (Z)				Rock quality designation method (RQD)			
	I	S	Z	Rock Mass Quality Classification	σ_c	RQD	M	Rock Mass Quality Classification
Ore body roof	0.13	0.37	0.04	Very poor	37.11	0.13	0.02	Poor
Overburden rock	0.37	0.40	0.13	Poor	40	0.37	0.05	Poor
Ore body	0.16	0.35	0.05	Very poor	34.8	0.16	0.02	Poor
Ore body floor	0.20	0.37	0.07	Poor	20.3	0.20	0.01	Poor

Based on the analysis of Table 3.3, it can be concluded that the fracture development in the roof of the ore body is highly pronounced, with brittle and fragile characteristics. The average uniaxial compressive strength of the rock mass is 37.11 MPa, and the rock mass quality index (M) is 0.02, indicating poor rock mass quality and stability. The average RQD (Rock Quality Designation) value of the overlying strata from boreholes is 37%, with an average uniaxial compressive strength of 40 MPa, signifying high mechanical strength but poor rock mass quality. The average RQD value of boreholes in the ore body strata is 16.3%, showing a fractured rock mass, with an average uniaxial compressive strength of 34.8 MPa and a rock

mass quality index (M) of 0.02, again indicating poor rock mass quality. The average RQD value of the floor strata from boreholes is 20.3%, indicating a fractured rock mass, with an average uniaxial compressive strength of 20.3 MPa and a rock mass quality index (M) of 0.01, demonstrating poor rock mass quality.

Through the stability evaluation of the ore body and the roof and floor strata, it is found that the surrounding rock of the ore body's roof and floor, as well as the surrounding rock of the mine tunnels, is mainly hard to relatively hard (Class IV–V). The rock mass quality is poor.

3.1.2.2 Estimation of the height of water-conducting fracture zone

In underground mining engineering, the creation of goafs (mined-out areas) leads to stress concentration on the roof, which subsequently forms secondary fractures. Calculating the height of the water-conducting fracture zone during underground mining is of great significance for studying the stability of the aquiclude and the aquifer in the indirect roof. Based on the engineering geological conditions of the mining area, the ore body is mainly located in the Zhongyicun Formation, with the Haikou, Canglangpu, and Qiongzhusi Formations above it, predominantly consisting of sandstone and shale. The dip angle of the ore body is roughly consistent with that of the strata, approximately 15°. The average uniaxial saturated compressive strength of the upper sandstone and shale is 40 MPa. According to the mining method, the calculation formula for the water-conducting fracture zone in gently dipping strata is as follows:

$$H_{\mathrm{f}} = \frac{100\mathrm{D}}{3.3\mathrm{n}+3.8} + 5.1 \tag{3.2}$$

where D represents the cumulative mining thickness (m), with the total thickness of the upper and lower ore layers being 12.53 m, and n is the number of stratified layers, which is set to 2.

Using Equation (3.2), the calculated height of the water-conducting fracture zone is 125.58 m, which is less than the thickness of the aquiclude. Under the protective effect of the aquiclude, the hydraulic connection between the indirect roof aquifer and the direct water-bearing aquifer of the ore deposit is relatively weak.

In summary, the mining area is located in a watershed to gentle slope terrain, with the topography higher in the north and lower in the south, and higher in the northeast and lower in the southwest, which favors natural drainage. The mining area is situated on the southern flank of the Xiangtiao Village anticline, and the strata form a southward-inclined monocline. The surface layers expose strata from the Sinian, Cambrian, Devonian, Carboniferous, and Quaternary periods, indicating a simple geological structure. Surface karst fractures are well-developed, while deeper fractures are less developed. The shallow part of the mining area contains heavily weathered strata, and the dip angle of the rock layers is relatively gentle. The rock mass is locally fractured, which affects its stability. The pit slope is relatively stable, and a discontinuous weak interlayer exists between the upper and lower ore bodies. Therefore, the

complexity of the engineering geological conditions in this mining area can be classified as moderate, dominated by hard to semi-hard soluble salt rocks and clastic rocks.

3.2 Field water pressure test

3.2.1 Geophysical testing results of the tunnel face under examination

To investigate the fracture development and water distribution in the rock mass ahead of the tunnel face, a geophysical survey was conducted using the transient electromagnetic method. The survey lines were arranged 1.5 meters above the tunnel face. First, survey line A was laid horizontally from left to right, followed by survey line B laid in the opposite direction, and finally, survey line C was placed vertically from the bottom to the top in the center of the tunnel face. Survey line A used an advanced probing method with angular measurements, while survey lines B and C employed continuous measurements using the roof and floor method. The layout of the survey lines on the working face is shown in Fig. 3.3.

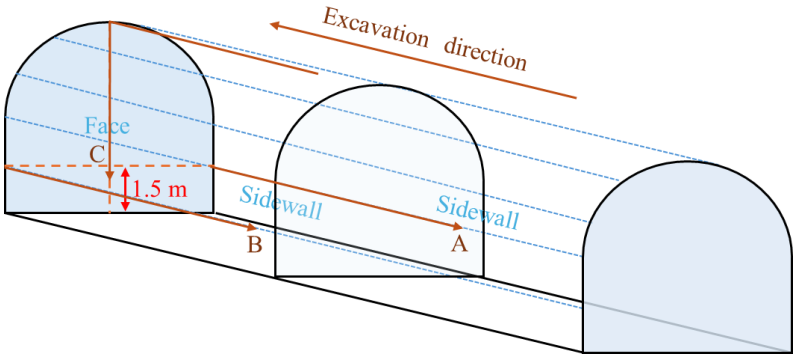

Fig. 3.3 Layout sketch of Transient Electromagnetic Survey Lines

Fig. 3.4 provides a photograph of the tunnel face under examination. As shown in Fig. 3.4, joints and fractures are well developed on the tunnel face and roof, with fractures extending along the bedding planes. Localized water inflow is observed along the fractures, with a flow rate of approximately 0.2 to 0.4 L/s. The rock strata are relatively hard, and the walls and roof of the tunnel face are damp. Water inflow is also visible in the blast hole on the right side of the tunnel face, with a flow rate of about 0.2 to 0.5 L/s. The water quality in the blast hole is clear.

Fig. 3.4 Photo of a palm face in the tunnel to be tested

Based on the layout method shown in Fig. 3.3, the transient electromagnetic survey results of the tunnel face under examination were obtained, as shown in Fig. 3.5.

From Fig. 3.5, a low-resistivity anomaly zone, YC-1#, can be observed, which developed within the 0–8 m range in front of the tunnel face. Two additional low-resistivity anomaly zones, YC-2# and YC-3#, were identified in the 25–40 m range on both sides of the tunnel face. From the apparent resistivity image, YC-1# appears as a relatively isolated low-resistivity anomaly, indicating the presence of water-filled fractures within the 0–8 m range, but with a low water content. The two anomaly zones, YC-2# and YC-3#, exhibit high-frequency resistivity anomalies, suggesting that these areas have well-developed fractures, though with a low water saturation.

During the tunneling process, the balance between existing rock fractures and groundwater is likely to be disrupted, causing water from the low-frequency anomaly zone to flow through the fracture channels of the high-frequency anomaly zone into the tunnel. Therefore, it is essential to further investigate the impact of water (such as water saturation duration and water pressure) on the stability of the surrounding rock mass in the tunnel. This would provide theoretical guidance for the support and excavation of the tunnel.

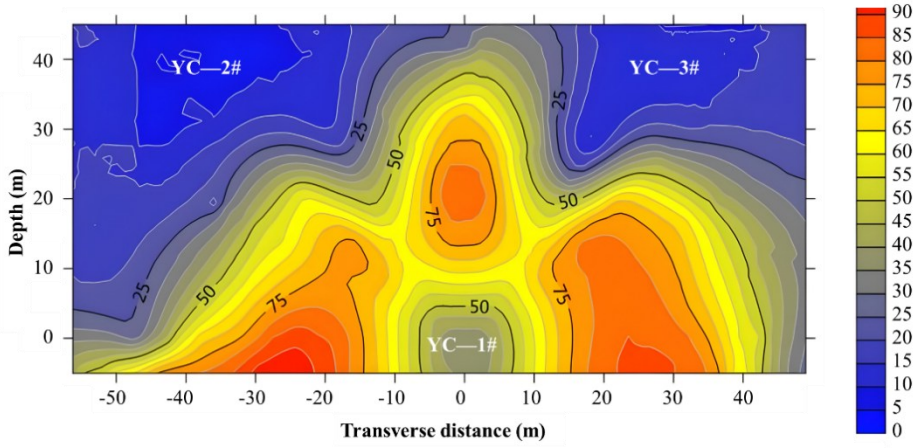

(a)

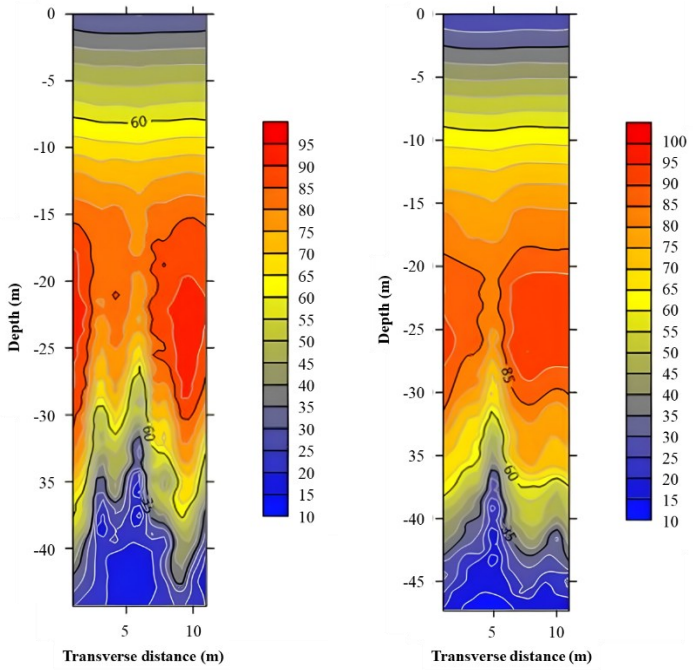

(b) (c)

Fig. 3.5 Transient Electromagnetic Survey Results. (a) Survey Line A (Left Side → Right Side). (b) Survey Line B (Right Side → Left Side). (c) Survey Line C (Bottom → Top)

3.2.2 Water pressure test results of the tunnel

Based on the geophysical testing in Section 3.2.1, JM series vibrating string pore water pressure is used to monitor the water pressure in front of the testing tunnel's palm face, as shown in Fig. 3.6. Four monitoring points, designated as S1, S2, S3, and S4, were arranged along the tunnel face, and the monitoring results are shown in Fig. 3.7.

(a) (b)

Fig.3.6 Layout and field monitoring of pore water pressure gauges. (a) Sensor layout. (b) Data monitoring.

As observed in Fig. 3.7, the water pressure at all four monitoring points gradually increased over time, but the rate of increase progressively slowed. After the 14th day, the water pressure at each monitoring point tended to stabilize, with an average variation of less than 4.2%. Therefore, the average monitored water pressure on the 16th day, 1.42 MPa, was selected as the pore water pressure of the target tunnel. This value serves as a reference for designing the cyclic loading experiment on water-saturated samples under the influence of water pressure.

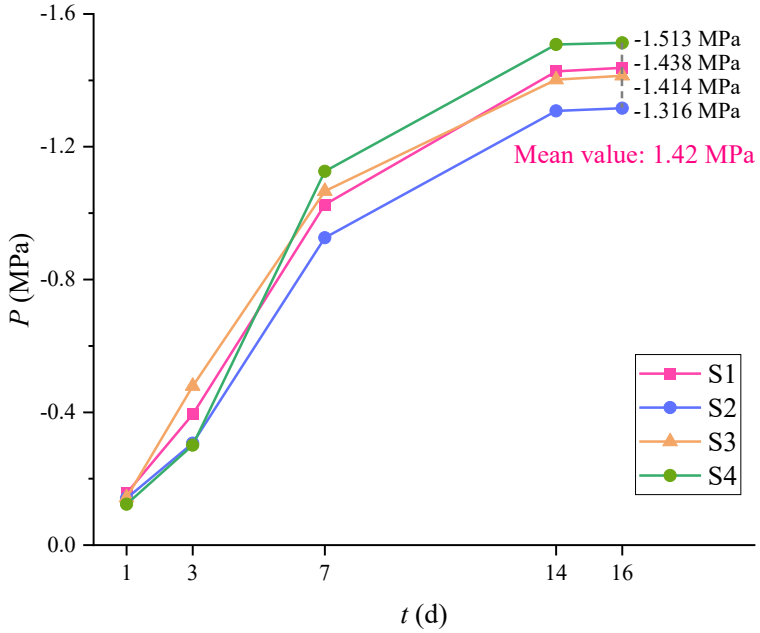

Fig. 3.7 Water pressure monitoring results of the tunnel

3.3 In-situ stress testing

In-situ stress is the fundamental driving force behind tunnel excavation deformation and failure, and it is a necessary prerequisite for analyzing surrounding rock stability and designing rock engineering excavations. Obtaining the in-situ stress data at the study site provides critical

reference points for developing laboratory experimental plans and establishing numerical simulation models. The location of the in-situ stress test in this study is shown in Fig. 3.8.

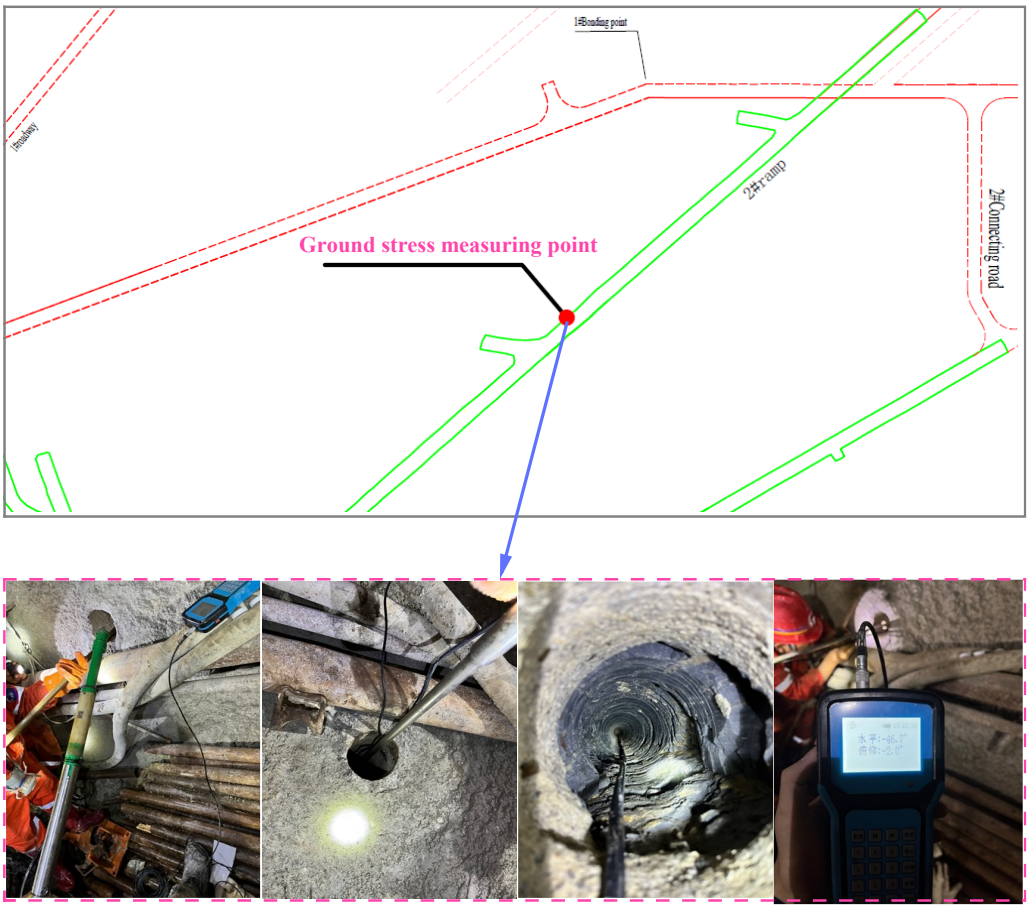

Fig. 3.8 Test site of in-situ stress

The in-situ stress of the tunnel under examination was measured using the overcoring stress relief method. The basic principle of this method involves installing deformation or strain measurement elements in a borehole. By measuring changes in borehole diameter, strain at the borehole bottom, or strain on the borehole wall surface before and after stress relief, the magnitude and direction of the in-situ stress can be determined (Qin et al., 2018; Zhao et al., 2021). The overcoring stress relief method is one of the longest-established and most reliable techniques for in-situ stress testing. The in-situ stress testing equipment (Fig. 3.9) is listed in Table 3.4.

Table 3.4 Test equipment characteristics

Instrument Name	Model	Specifications and Performance
Hollow Body Strain Gauge	KX-81	Accuracy: 0.1 μs
Mine Pressure Monitoring System Station	KJ327-F	Accuracy: ±0.1% of measured value

(a)

(b)

Fig. 3.9 In-situ stress test. (a) KX-81 Hollow Body Strain Gauge. (b) Stress Relief Drilling Process.

3.3.1 In-situ stress measurement

The key indicators, the structure, installation and testing methods of Hollow Body Strain Gauge are as follows:

(1) Key Indicators: The strain gauge has a total length of 290 mm, a diameter of 36 mm, and a lead cable length of 15 m. The sensitivity coefficient of each strain gauge is 3.3.

(2) Structure and Installation of the Strain Gauge: The strain gauge consists of 12 resistance strain gauges embedded in an epoxy resin cylinder. Three strain rosettes are bonded around the epoxy resin cylinder, spaced 120° apart. An outer layer of epoxy resin is then poured to encase the strain gauges within the cylinder wall. After a certain period, when the adhesive has cured, the overcoring procedure can be initiated.

(3) Overcoring for Stress Relief: A borehole with a diameter of 130 mm is drilled at the testing location. A smaller hole, with a diameter of 36–36.5 mm, is drilled at the center of this borehole to install the probe and measure the initial strain value. Next, a drill bit with a diameter of 130 mm is used to drill concentrically, excavating the stress relief cavity. As the cavity deepens, the rock core becomes isolated from the external stress field, leading to elastic recovery of the rock core. The instrument readings change accordingly until the readings stabilize, at which point drilling is stopped, and the rock core is extracted. Fig. 3.9(b) illustrates the stress relief drilling process.

3.3.2 Test results and analysis

Based on the data obtained from the measurements at the drilling points, the stress relief curve was plotted, as shown in Fig. 3.10.

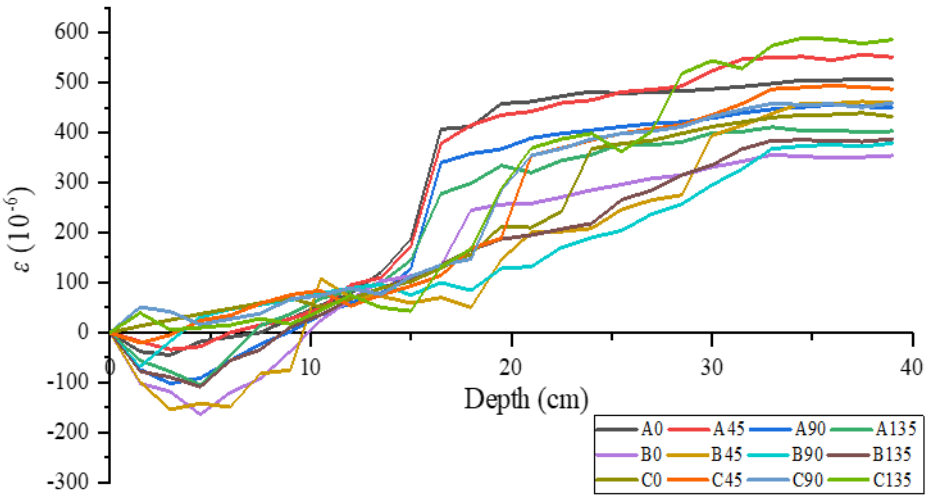

Fig. 3.10 Borehole stress relief curve

The stabilized strain values from the 12 strain gauges listed in Fig.3.10 were used to calculate the three-dimensional principal stresses using the following equation (Wang et al., 2022):

$$\begin{cases} \varepsilon_\theta = \frac{1}{E}\{(\sigma_x+\sigma_y)+2(1-v^2)[(\sigma_x-\sigma_y)cos2\theta-2\tau_{xy}sin2\theta]-v\sigma_z\} \\ \varepsilon_z = \frac{1}{E}[\sigma_z-v(\sigma_x+\sigma_y)c] \\ \gamma_{\theta z} = \frac{4}{E}(1+v)(\tau_{yz}cos\theta-\tau_{zx}sin\theta) \\ \varepsilon_{\pm 45^\circ} = \frac{1}{2}(\varepsilon_\theta+\varepsilon_z+\gamma_{\theta z}) \end{cases}$$

(3.3)

where ε_θ, ε_z, $\gamma_{\theta z}$ represent the circumferential strain, axial strain, and shear strain, respectively. $\varepsilon_{\pm 45^\circ}$ indicates the strain in directions ±45° relative to the borehole axis (Z-axis). σ_x, σ_y, σ_z, τ_{xy}, τ_{yz}, and τ_{zx} are the six components of the in-situ rock stress.

The formulas for calculating the rock's Poisson's ratio and elastic modulus are given by:

$$\begin{cases} E = K_1 \dfrac{P_0}{\varepsilon_\theta} \dfrac{2R^2}{R^2 - r^2} \\ \upsilon = \dfrac{\varepsilon_z}{\varepsilon_\theta} \end{cases} \tag{3.4}$$

where P_0 is the confining pressure; ε_z is the average axial strain; ε_θ is the average radial strain; R and r are the outer and inner diameters of the overcored rock core, respectively. K_1 is a correction factor for the bonding degree of the strain gauge to the borehole wall.

From the experiment, the elastic modulus E and Poisson's ratio ν of the rock at the testing location were determined. After correcting the laboratory data to account for geological structure and overburden stress, the reference values obtained were: E=22 GPa, υ=0.2.

The iterative method was used to solve equation (3.3), and the results are presented in Table 3.5. In the table, the directions of in-situ stress are referenced to the geographic coordinate system, as shown in Fig. 3.11. The direction of the three-dimensional principal stresses is calculated clockwise from true north, with upward dip angles considered positive and downward dip angles considered negative.

Table 3.5 Three-dimensional principal stress test results

Project	Maximum Principal Stress (MPa)	Intermediate Principal Stress (MPa)	Minimum Principal Stress (MPa)
Principal Stress Value (MPa)	15.68	7.32	4.98
Dip Angle (°)	4.98	-9.64	65.84
Azimuth Angle (°)	224.55	-7.21	131.65

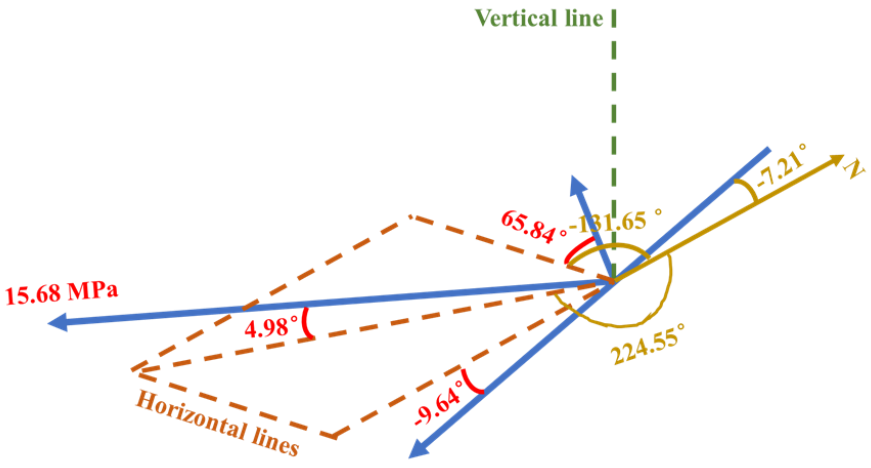

Fig. 3.11 Schematic diagram of in-situ stress test results

From Table 3.5, it can be observed that the maximum principal stress and intermediate principal stress are close to the horizontal direction, while the minimum principal stress is oriented near the vertical direction. The results of the lateral pressure coefficient indicate that the initial in-situ stress of the surrounding rock in the area under investigation is primarily influenced by tectonic stresses.

3.4 Source of in-situ cyclic stress

The Yunnan phosphate mining area is located in the Xiaojiang Fault Zone, where frequent microseismic activity creates a complex stress environment for advancing tunnels. The surrounding rock mass of the target tunnel exhibits well-developed joints, poor integrity, and long-term water saturation, resulting in intricate stress conditions in the roof. To investigate the stress evolution of the tunnel roof during excavation, a GZY60 intrinsic safety borehole stress sensor (see Fig. 2.11) was deployed to measure roof stress.

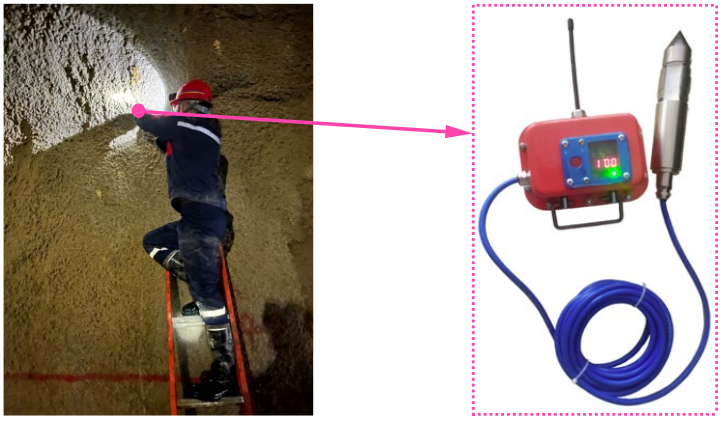

Fig.2.11 GZY60 intrinsic safety borehole stress sensor for mining

The GZY60 sensor consists of a force-measuring unit and a transmitter, rigidly connected via stainless steel tubing. It infers stress changes by measuring internal rock deformation, with an error margin of ±2.5%. A borehole was drilled into the roof strata of the target tunnel, and the sensor was installed inside. Using an external rod, the sensor was pushed to the designated position within the borehole, and data were recorded periodically. The test results are shown in Fig. 2.12.

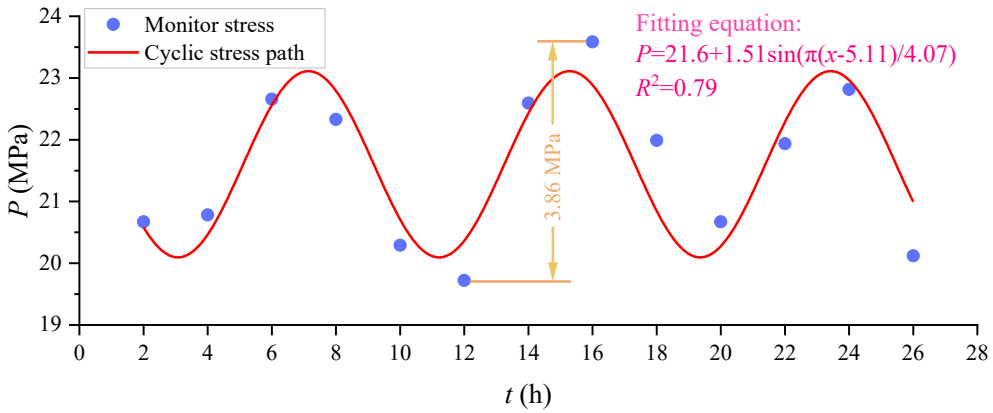

Fig. 2.12 Evolution trend of borehole stress in tunnel roof strata

Monitoring data from Fig. 2.12 reveal that under the combined effects of tectonic stress in the Xiaojiang Fault Zone and frequent microseismic activity, the roof pressure of the target tunnel exhibits significant dynamic non-steady-state characteristics. The dense joint network and long-term water-induced softening of the surrounding rock further intensify stress fluctuations, with the amplitude (ΔPmax = 3.86 MPa) showing strong correlations with excavation disturbances and microseismic energy release. To quantitatively characterize roof stress under such complex conditions, a sinusoidal function model was applied for fitting, achieving a coefficient of determination ($R^2 = 0.79$). This validates the model's applicability to roof stress fluctuations, revealing a cyclic sinusoidal-like stress pattern. These stress measurements provide a basis for designing cyclic loading experimental protocols.

3.5 The coupling effect of water saturated, water pressure and circulating stress in tunnel excavation

The evolution of stress state and water environment is critical for stability analysis during tunnel excavation. Fig. 3.12 illustrates the water pressure evolution in the studied tunnel during excavation and its coupling effect with cyclic stress (Fang et al., 2021).

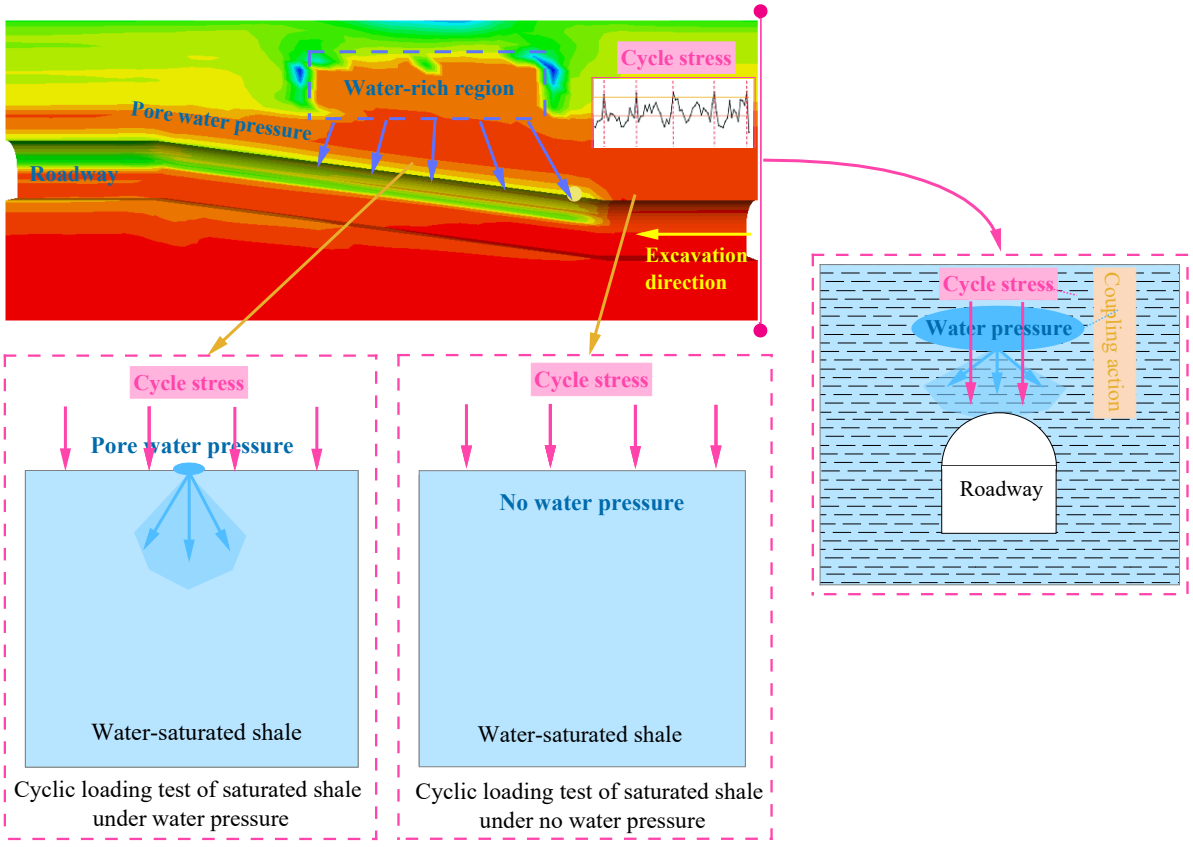

Fig. 3.12 Coupling effect of saturated water, water pressure and cyclic stress during tunnel excavation

As shown in Fig. 3.12, in the initial stage of tunnel excavation, due to the distance from the water-rich area, the water pressure is small, and the roof is subjected only to the effects of water saturation and cyclic stress. However, in the second excavation segment, due to the infiltration of water from the overlying water-rich zone, the roof experiences the combined effects of cyclic stress and water pressure. Therefore, to investigate the stability of surrounding rock and the evolution of roof water pressure during tunnel excavation, it is necessary to conduct research on the mechanical deterioration and seepage evolution of water-saturated shale under cyclic loading conditions with and without water pressure.

3.6 Summary

Based on field investigations, engineering geological surveys, and hollow inclusion stress gauge tests, this chapter systematically reveals the engineering geological characteristics and in-situ stress field distribution patterns of the targeted mining area in the Yunnan phosphate mine. The main conclusions are as follows:

1. Engineering Geological Evaluation of the Mining Area: The roof and floor of the ore body, as well as the surrounding rock of tunnels, are primarily composed of hard to relatively hard rock (Class IV–V), with moderate to poor rock mass quality. The complexity of the engineering geological conditions in the mining area is classified as moderate, predominantly consisting of soluble salt rocks and clastic hard to semi-hard rocks.

2. Transient Electromagnetic Detection: The results reveal the presence of three low-resistivity anomaly zones ahead of the excavation face. A water-rich anomalous body is developed within the 0–8 m range, while fracture water channel anomaly signals appear on both sides within the 25–40 m range. Pore water pressure monitoring indicates that 14 days after tunnel excavation, the pore water pressure stabilizes at an average of 1.42 MPa with fluctuations of less than 4.2%. The on-site measured data provide a basis for the design of water pressure and cyclic disturbance experiments.

3. In-Situ Stress Test Data: The maximum principal stress (σ_1 = 15.68 MPa) and the intermediate principal stress (σ_2 = 7.32 MPa) are nearly horizontal, while the minimum principal stress (σ_3 = 4.98 MPa) is close to the vertical direction. The lateral pressure coefficient is λ = 0.46, indicating that the initial in-situ stress field is primarily governed by tectonic stress. The in-situ stress test results serve as a reference for designing true triaxial experimental schemes.

4. Effects of Excavation on Surrounding Rock Stability: In the early stage of tunnel excavation, the roof is mainly subjected to water saturation and cyclic stress. In the second excavation phase, due to water infiltration from the overlying water-rich area, the roof is influenced by both cyclic stress and water pressure. To investigate the stability of surrounding rock and the evolution of roof water pressure during the excavation of water-rich tunnels, it is necessary to conduct research on the mechanical degradation and seepage evolution

characteristics of water-saturated shale under cyclic loading conditions with and without water pressure variation.

Chapter 4
Damage characteristics of saturated shale under disturbance of circulating stress without hydraulic pressure

As indicated in Section 3.4, during the initial stage of tunnel excavation (first segment), the roof is subjected to the combined effects of water saturation and cyclic stress. This water-mechanical coupling alters the shale structure, leading to the deterioration of its physical and mechanical properties (as shown in Fig. 4.1), which in turn significantly affects the long-term stability and safety of the shale tunnel.

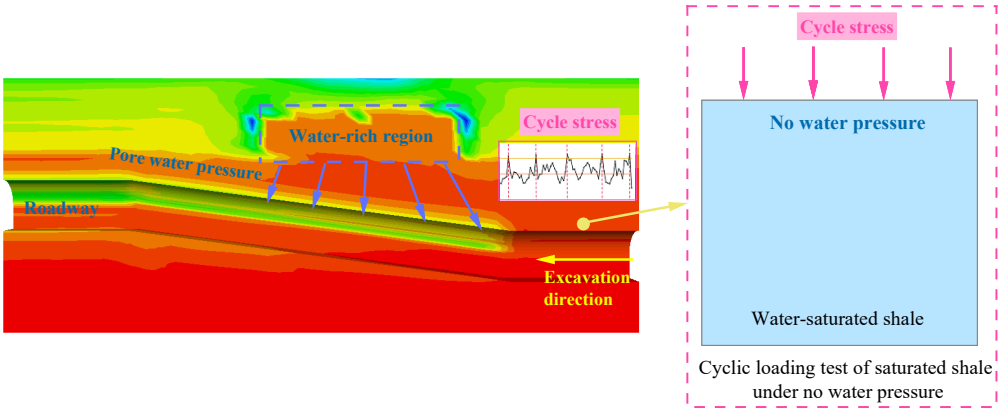

Fig. 4.1 The stress environment of surrounding rock during the excavation of the first section of tunnel

Therefore, this chapter focuses on investigating the damage characteristics of water-saturated shale under cyclic stress disturbance. First, the static mechanical properties of shale under different water saturation durations are examined to explore the influence of saturation time on shale's mechanical behavior. Then, under a constant water saturation duration, the evolution of the mechanical properties of water-saturated shale under cyclic stress is analyzed. Based on this, the combined effects of water saturation duration and cyclic stress are studied to reveal the damage failure characteristics and mechanical deterioration mechanism of shale under coupled water saturation and cyclic stress conditions. The specific research framework is shown in Fig. 4.2, and the findings can provide references for excavation support in similar water-rich tunnels.

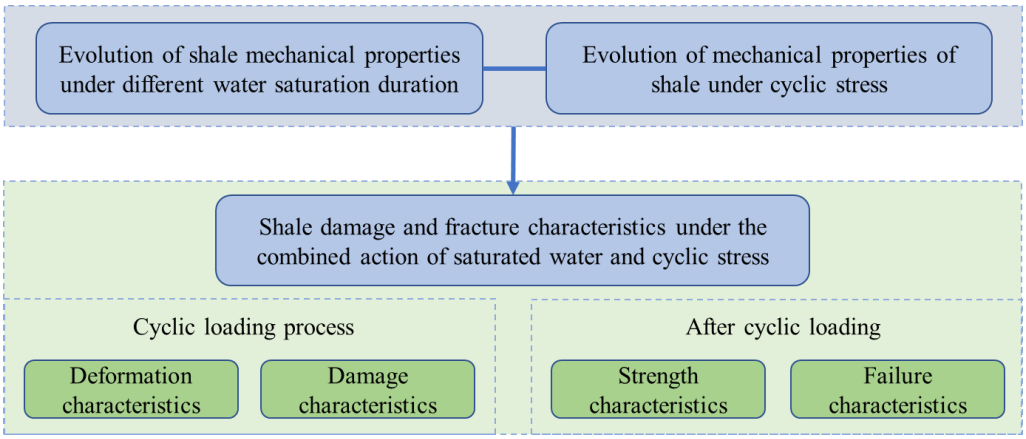

Fig. 4.2 Research roadmap of damage characteristics of saturated shale under cyclic stress disturbance

4.1 Evolution of shale mechanical properties under different saturated water and confining pressure conditions

4.1.1 Sample characteristics and testing methods

4.1.1.1 Sample preparation

To study the degradation mechanism of mechanical properties of shale during saturated water duration, water saturation test and conventional triaxial loading test were carried out on shale samples. Samples were taken from the test tunnel and processed in the laboratory into standard cylindrical samples with a diameter of 50 mm and a height of 100 mm. To avoid the effects of end friction on the test, the flatness of the end surfaces was controlled within 0.02 mm. The sample surfaces were smooth, with no visible joints or cracks, as shown in Fig. 4.3.

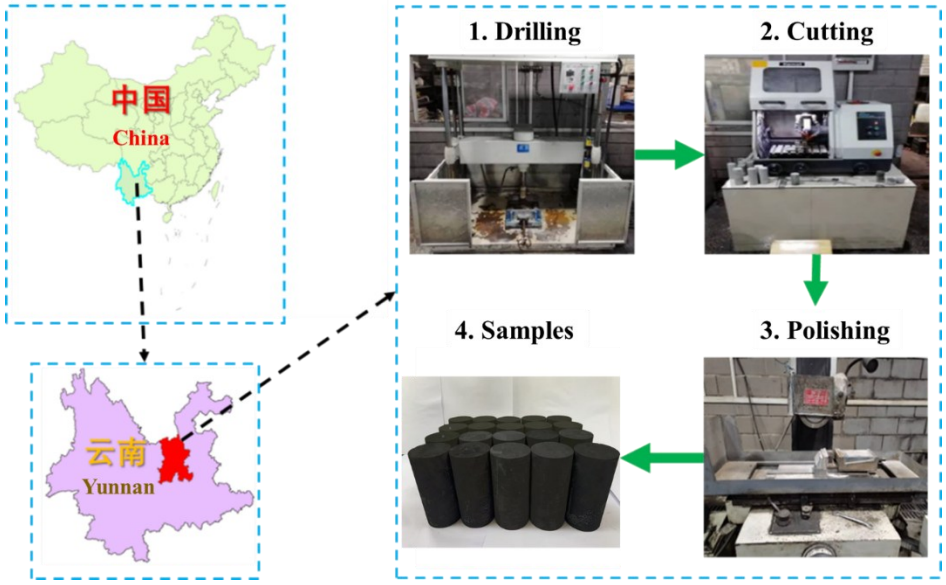

Fig. 4.3 Standard cylindrical samples after processing

4.1.1.2 Testing equipment

The testing equipment adopted included:

1) Vacuum saturation apparatus. The NJ-BSJ concrete vacuum saturation instrument (see Fig. 4.4(a)) was used for the water saturation treatment of the samples. The main unit of the instrument has dimensions of 750 × 680 × 400 mm^3, a vacuum capacity of 10 L, and a pressure transmitter equipped with a 2 L oil pump. The water level sensor can control automatic water injection, and the digital display shows the vacuum values and saturation time for each channel, with a timing function.
2) Ultrasonic testing apparatus. The longitudinal wave velocity was measured using the UTA-2000A intelligent ultrasonic monitoring instrument, as shown in Fig. 4.4(b). The equipment has a sampling frequency of 10 MHz, a sensor frequency of 35 kHz, and an accuracy of 0.1 μs. Vaseline cream was used as a coupling agent between the sample and the sensor.
3) Mechanical testing apparatus. Mechanical tests were conducted using the RMT-150B electro-hydraulic servo rock testing system, as shown in Fig. 4.4(c). The system has a maximum axial load of 1000 kN, a maximum horizontal load of 500 kN, and a maximum confining pressure of 50 MPa. It can perform various tests, including uniaxial compression, indirect (direct) tension, compression-shear, and triaxial compression. The system allows control through load, displacement, and stroke, and the computer automatically collects and displays real-time data on load and deformation during testing.

(a) (b)

(c)

Fig. 4.4 Physical and mechanical property testing equipment. (a) NJ-BSJ Concrete Vacuum Saturation Apparatus. (b) UTA2001A Ultrasonic Testing Device. (c) RMT-150B Electro-hydraulic Servo Rock Testing System.

4.1.1.3 Testing methods

To analyze the effects of different saturation durations on the fatigue characteristics of the samples, it is necessary to first test the degradation mechanism of the mechanical properties of shale under varying saturation conditions. The sample preparation plan is as follows:

1) Grouping: The samples were divided into four groups (A, B, C, D), with 8 samples in each group. Group A samples were left untreated and labeled as natural samples. Samples in groups B, C, and D were saturated in the vacuum saturation instrument for 12, 24, and 36 hours, respectively, and then sealed with plastic wrap.

2) Physical Property Testing: The density of each group of samples were tested. Samples with better homogeneity were selected for mechanical testing. The average physical parameters of the samples from each group are shown in Table 4.1.

Table 4.1 Physical and mechanical properties of samples under different water saturation duration

Type	Group	Saturation Duration (h)	Density (g/cm³)
Natural Sample	A	0	2.772
Saturated Sample	B	12	2.791
	C	24	2.810
	D	36	2.814

3) Conventional Triaxial Tests: Conventional triaxial tests were conducted on the four groups of samples to measure mechanical parameters such as peak strength (σ_1), peak strain (ε_c), elastic modulus (E), cohesion (c), and internal friction angle (f). The confining pressures for this test were set at 4, 6, 8, 10, and 12 MPa.

4.1.2 Experimental results and analysis

Fig.4.5 and Table 4.2 show the results of conventional triaxial compression tests for each group of samples. From the table, it can be observed that for the natural sample (Group A), when the confining pressure is 4 MPa, the peak strength is 84.9 MPa. As the confining pressure increases, the peak strength of the sample gradually increases, reaching 138.9 MPa at 12 MPa, which represents a 63.6% increase. However, as the saturation time extends, the peak strength of the samples decreases under all confining pressures. For instance, when the confining pressure is 4 MPa, the peak strength of the samples saturated for 12, 24, and 36 hours are 75.6 MPa, 65.2 MPa, and 45.7 MPa, respectively. This corresponds to a reduction of 11.0%, 23.3%, and 46.1% compared to the natural sample, indicating that the longer the saturation time, the greater the degradation of the sample.

Moreover, the degradation effect of water saturation is not only reflected in the decrease in peak strength but also in the effect of confining pressure on the samples. Observing the degree of influence of confining pressure under different saturation durations reveals that when the saturation times are 12, 24, and 36 hours, as the confining pressure increases from 4 MPa to 12 MPa, the peak strength of the samples increases by 63.6%, 67.1%, and 111.0%, respectively. The longer the saturation time, the more pronounced the effect of confining pressure on increasing the peak strength (i.e., the greater the confining pressure influence coefficient).

Analyzing the impact of confining pressure on the saturation effect, the overall strength of the saturated samples shows a downward trend. In other words, the greater the confining pressure, the weaker the degradation effect of water saturation on the sample strength. This result is like previous uniaxial and triaxial tests on gypsum samples (Wei et al., 2020; Wang et al., 2023). In the earlier study on gypsum rock, it was found that water saturation significantly degrades the strength of gypsum rock, with the most notable effect observed under uniaxial compression: the uniaxial strength of the saturated sample was 44.4% lower than that of the natural sample. However, under confining pressure, the average strength of the saturated samples across all confining pressures was only 32.7% lower than that of the natural samples. The test results of both samples indicate that the effect of water saturation is closely related to confining pressure.

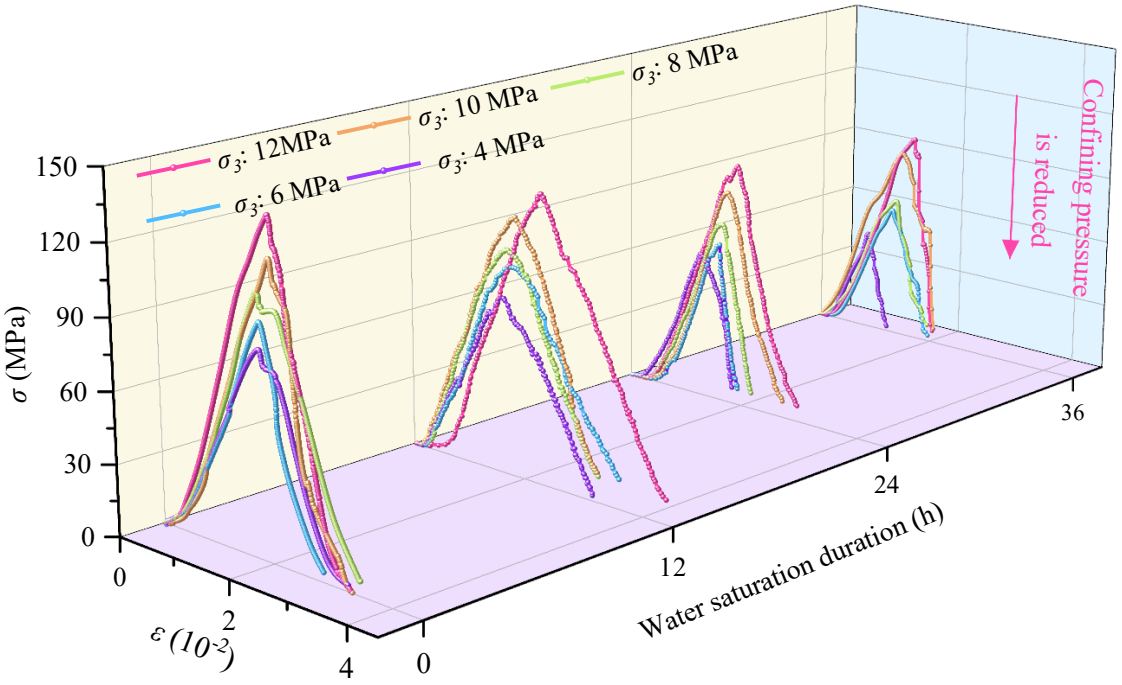

Fig. 4.5 Stress-strain curves of samples under conventional triaxial compression with different saturated water duration

Table 4.2 The mechanical properties of each group of samples

Group	σ_3 (MPa)	σ_1 (MPa)	ε_c (10^{-2})	c (MPa)	φ (°)
Group A: Natural Sample	4	84.94	1.77	10.98	47.43
	6	95.85	1.79		
	8	107.27	1.78		
	10	121.7	1.99		
	12	138.92	2.12		
Group B: Saturated Sample T = 12 h	4	75.62	1.62	15.65	28.27
	6	89.87	1.71		
	8	96.68	1.72		
	10	111.27	1.83		
	12	123.69	2.01		
Group C: Saturated Sample T = 24 h	4	65.17	1.34	8.41	44.15
	6	71.63	1.57		
	8	81.04	1.62		
	10	95.87	1.72		
	12	108.92	1.89		

Group D: Saturated Sample T = 36 h	4	45.75	0.88	3.45	47.23
	6	59.93	1.31		
	8	64.7	1.24		
	10	88.83	1.41		
	12	96.51	1.65		

This phenomenon occurs because, under uniaxial compression, where there is no lateral confinement, water escapes from the sides of the sample during loading. In contrast, in conventional triaxial tests, confining pressure restrains the sample, causing water to fill the fractures and bedding planes inside the sample, which leads to an increase in peak strength. The greater the confining pressure, the more significant this strengthening effect becomes. This has engineering significance: for rock masses subjected to long-term water erosion, increasing the confining pressure can mitigate the degradation effect of water on their strength.

At the same time, a cross-comparison of the groups revealed that the average peak strength of Group A samples (109.7 MPa) was the highest. The average peak strengths of Group B (99.4 MPa), Group C (84.5 MPa), and Group D (71.1 MPa) were 9.4%, 23.0%, and 35.2% lower than that of Group A, respectively. This indicates that water saturation has a significant degrading effect on the samples.

According to the Mohr-Coulomb strength criterion, the maximum shear stress that a sample can withstand is determined by cohesion and the internal friction angle, which can be expressed as:

$$\tau=c+\mu\sigma \tag{4.1}$$

where c represents the cohesion, μ is the friction coefficient ($\mu = tan\varphi$), φ is the internal friction angle, and σ is the normal stress on the failure plane. If expressed in terms of principal stress, it can be written as:

$$\sigma_1 = k\sigma_3 + Q \tag{4.2}$$

where σ_1 is the peak strength, and k and Q are material strength parameters, where the values relate to the material strength parameters (c, f) as follows:

$$\varphi = arcsin\frac{(k-1)}{(k+1)} \tag{4.3}$$

$$c = Q\frac{(1-sin\,\varphi)}{(2\,cos\,\varphi)} \tag{4.4}$$

Based on Equations (4.1)-(4.2), the relationship between the peak strength of the samples and confining pressure is obtained through regression, as shown in Fig. 4.6. The mechanical parameters of the samples in each group, calculated using the Mohr-Coulomb criterion, are presented in Table 4.2.

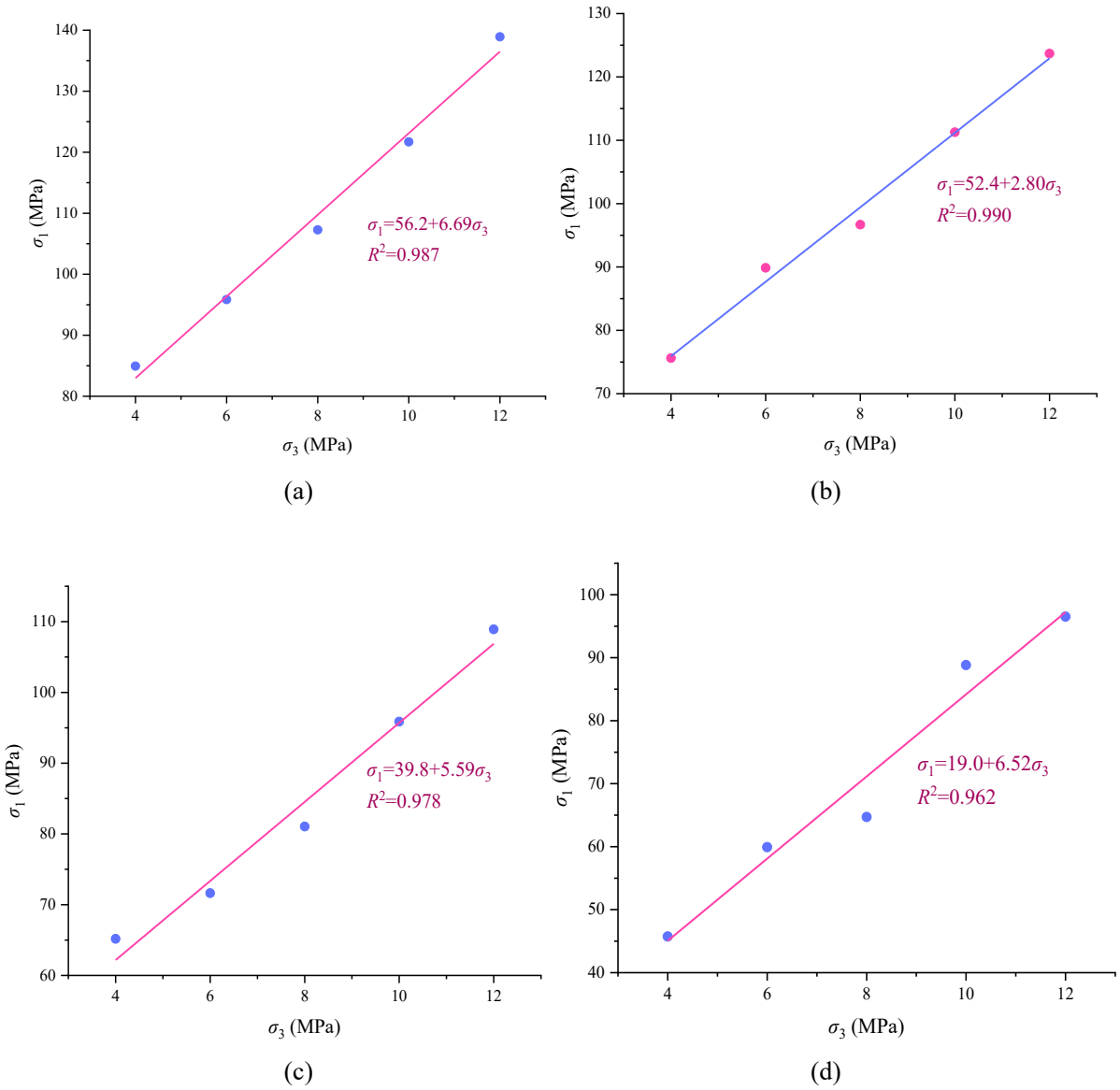

Fig. 4.6 Relationship between peak strength and confining pressure of each group of samples under triaxial compression. (a) Group A (0 hours). (b) Group B (12 hours). (c) Group C (24 hours). (d) Group D (36 hours).

4.2 Evolution of mechanical properties of shale under saturated water and cyclic stress

4.2.1 Testing methods

(1) Sample Grouping

The samples were divided into three groups: A, B, and C, with eight samples in each group. Group A (Natural Group): This group received no treatment. Group B (Saturated Group): Samples were placed in a vacuum saturation device for 48 hours and then sealed with plastic wrap. Group C (Fatigue Saturated Group): Samples underwent fatigue loading (as detailed in step 3) before being placed in the vacuum saturation device for 48 hours, followed by sealing with plastic wrap.

(2) Physical Properties Testing

The dimensions and masses of the samples were measured using calipers and an electronic scale to calculate density. The UTA-2000A intelligent ultrasonic monitoring instrument was used to perform ultrasonic tests on the samples. Based on the density and ultrasonic testing results, samples with uniform texture were selected for further testing.

Physical property testing serves as the foundation for mechanical testing, assisting in the formulation of the mechanical testing plan. Wave speed is one of the important parameters reflecting rock joint and crack characteristics. By utilizing the test results of density and wave speed, a preliminary judgment can be made regarding the crack development in the samples, allowing for the exclusion of those with poor uniformity, thereby enhancing the accuracy of the test results.

(3) Fatigue Loading Test

Group C samples underwent fatigue loading. The loading parameters were set as follows: Minimum stress, $\sigma_{\min} = 0.1\sigma_{cw}$ (Uniaxial compressive strength of specimens saturated with water for 48 h). Maximum stress, $\sigma_{\max} = 0.9\sigma_{c}$ (covering the elastic and yield stages). The fatigue frequency is 1 Hz, the number of cycles = 10, and the waveform is Sine wave.

(4) Conventional Triaxial Testing

Conventional triaxial tests were performed on Groups A, B, and C. The displacement loading method was employed with a loading rate of 0.005 mm/s. Mechanical parameters such as peak strength (σ_1), peak strain (ε_c), elastic modulus (E), cohesion (c), and internal friction angle (φ) were measured under different confining pressure conditions. The confining pressures for this experiment were set at 4, 6, 8, 10, and 12 MPa.

4.2.2 Test results and analysis

Fig. 4.7 and Table 4.3 show the results of conventional triaxial compression tests for each group of samples. From the observation of the peak stress of each sample group in Table 4.3, as the confining pressure increases, the peak strength of the samples gradually rises. However, the impact of confining pressure on the peak strength of samples under different conditions varies significantly. The natural samples and saturated samples are more affected by confining pressure, with influence coefficients ranging from 6.37 to 6.69. In contrast, after undergoing fatigue saturation treatment, the influence coefficient for the samples decreases to 2.81. This indicates that fatigue loading alters the mechanical properties of the samples, diminishing the strengthening effect of confining pressure to their strength.

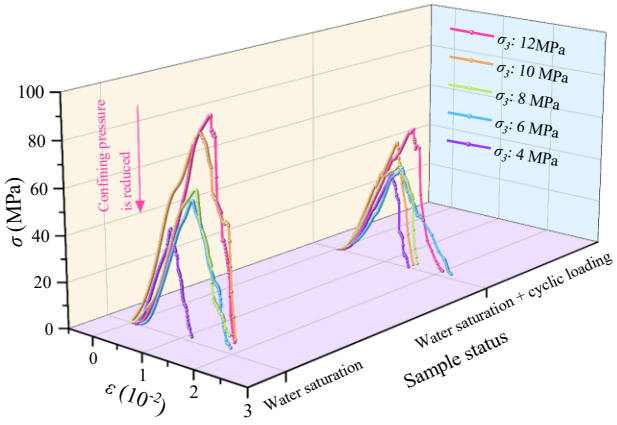

Fig. 4.7 Stress-strain curve of samples after cycle stress loadind

Table 4.3 Triaxial compression test results of each group of samples

	σ_3 (MPa)	σ_1 (MPa)	ε_c (10^{-2})	E (GPa)	c (MPa)	φ (°)
Natural Group	4	84.94	1.77	6.48	10.98	47.43
	6	95.85	1.79	9.76		
	8	107.27	1.78	8.43		
	10	121.70	1.99	9.00		
	12	138.92	2.12	11.15		
Saturated Group	4	45.75	0.88	4.76	3.87	46.77
	6	59.93	1.31	8.58		
	8	64.70	1.24	7.02		
	10	85.83	1.41	8.48		
	12	96.51	1.65	7.76		
"Fatigue-Saturated" Group	4	42.09	0.98	7.06	8.61	28.34
	6	45.79	1.39	7.98		
	8	47.17	1.18	4.63		
	10	56.85	1.23	7.72		
	12	64.62	1.57	8.07		

A ~~lateral~~ horizontal comparison among the sample groups reveals that the natural samples exhibit the highest peak strength. The average peak strengths of the saturated and fatigue-saturated samples under various confining pressure conditions are 35.7% and 53.3% lower, respectively, than that of the natural samples, demonstrating a significant degrading effect of both saturation and fatigue loading on the samples. The strength of the samples after fatigue stress disturbance is the lowest, attributed to prolonged fatigue loading that promotes the propagation of inherent cracks and the initiation of new ones. Additionally, the saturation treatment following fatigue loading facilitates the infiltration of water molecules into these

cracks, causing secondary damage to the samples and leading to a substantial deterioration in their mechanical properties.

Based on Equations (4.1)-(4.2), the relationship between the peak strength of the samples and confining pressure is obtained through regression, as shown in Fig. 4.8.

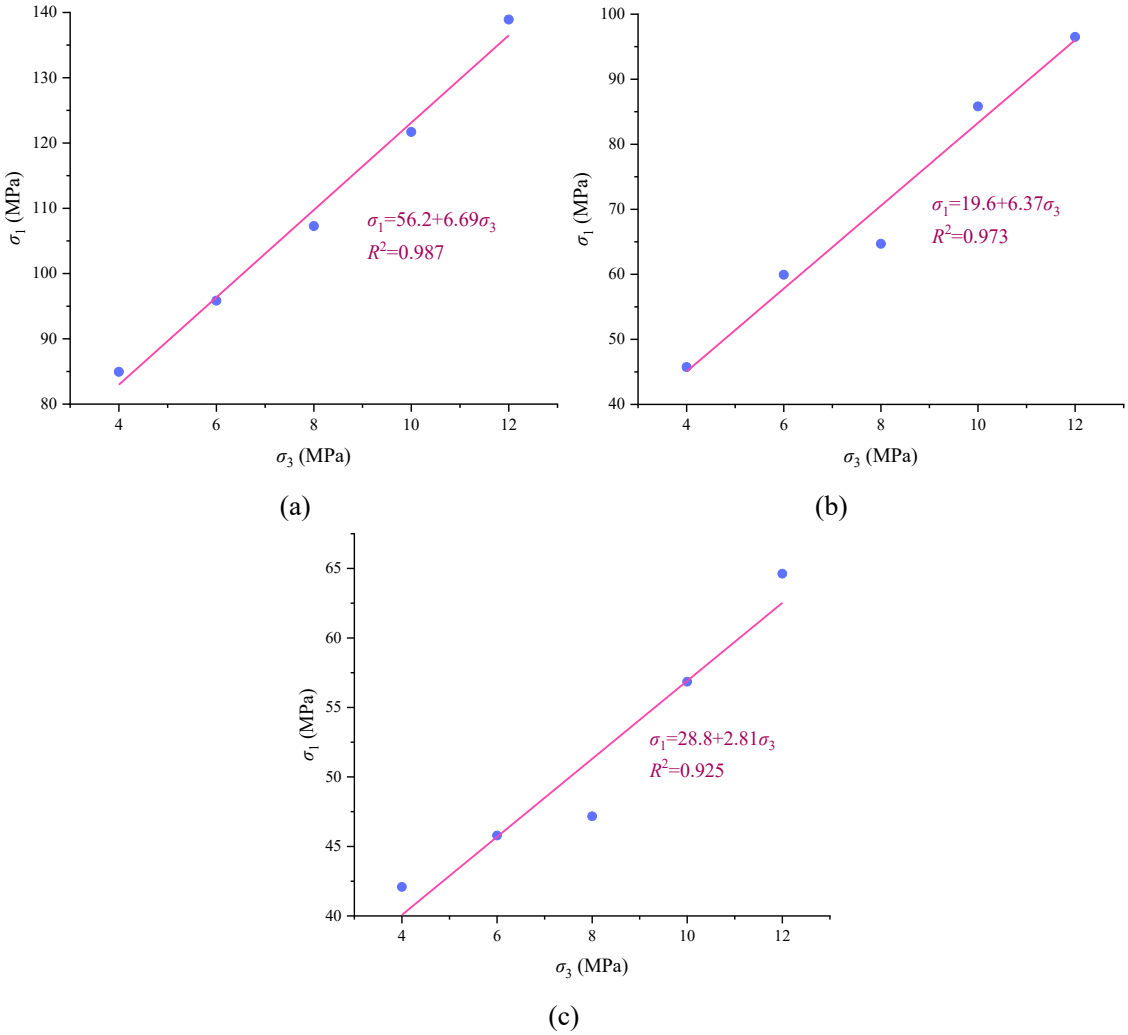

Fig. 4.8 Relationship between peak strength and confining pressure of each group of samples under triaxial compression. (a) Natural Group (b) Saturated Group (c) "Fatigue-Saturated" Group

From Figure 4.8, it can be observed that the influence coefficient of confining pressure on the samples ranges approximately from 2.81 to 6.69, with correlation coefficients greater than 0.92. This indicates that the peak triaxial compressive strength of each sample group has a strong correlation with confining pressure, consistent with the Mohr-Coulomb strength criterion. Using Equations (4.16) and (4.17), the cohesion and internal friction angle for each sample group can be derived, as shown in Table 4.3.

To monitor the evolution of damage characteristics in samples under different conditions during the loading process, a DS5-8B holographic acoustic emission signal analyzer was used to track the acoustic emission signals of the samples. Taking the samples under a confining

pressure of σ_3 = 4 MPa as an example, the stress/acoustic emission parameter versus time curve was plotted, as shown in Figure 4.9.

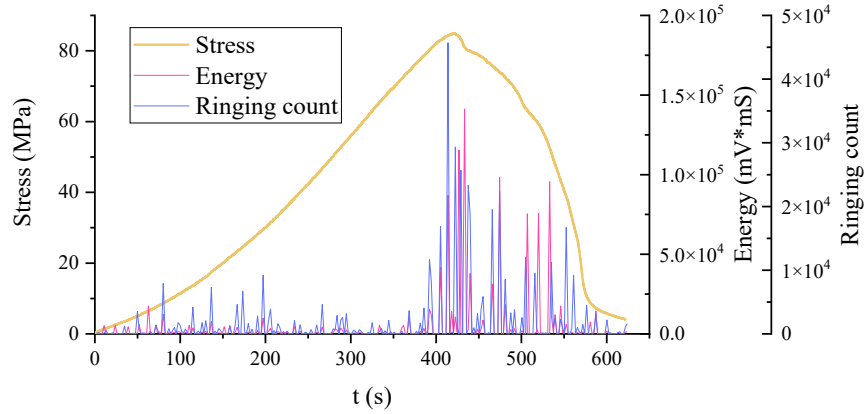

(a)

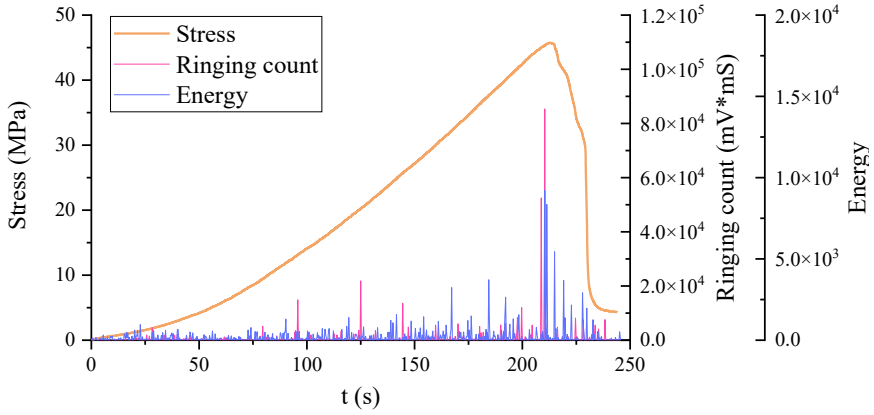

(b)

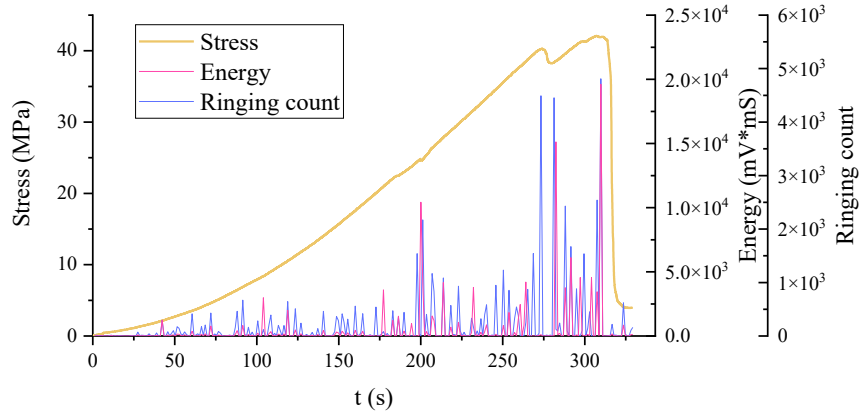

(c)

Fig. 4.9 Stress/acoustic emission parameters-time curve of sample. (a) Natural Group (b) Saturated Group (c) "Fatigue-Saturated" Group

From Figure 4.9, it can be observed that when t∈[0, 200] , the natural samples are in the compaction stage, showing a certain level of acoustic emission signals. However, as the stress increases, the samples enter the elastic stage (t = 200~400 s), and the acoustic emission response level gradually decreases. At t = 400 s, the natural samples begin to fracture, resulting in a

significant increase in the acoustic emission response level. After fracture, due to the presence of confining pressure, the stress of the samples does not drop rapidly to zero, and the acoustic emission signals remain at a high level.

In contrast, the acoustic emission signal peaks of the saturated samples are concentrated in the failure stage. During the compaction and elastic stages of loading, there are no significant differences in the intensity of the acoustic emission signals. In the post-peak stage, the intensity of the acoustic emission signals is also relatively low. This is because saturation causes some damage to the samples, with a large number of water molecules entering the samples, which reduces the acoustic emission signals generated due to crack closure during the initial compaction phase and decreases the load-bearing capacity after the peak.

The fatigue-saturated samples, compared to the first two groups, exhibit an increase in damage due to crack closure before the peak and a further decrease in load-bearing capacity after the peak. Before the stress reaches its peak, significant crack closure occurs, resulting in a large number of acoustic emission signals (t=200 s). This indicates that prolonged fatigue loading has caused secondary damage to the samples, leading to significant deterioration in their mechanical properties and a substantial reduction in both load-bearing capacity and stability.

4.3 Shale damage and fracture characteristics following water saturation and cyclic stress

Sections 4.1 and 4.2 utilized conventional triaxial tests to evaluate the mechanical properties of samples under fatigue loading and varying saturation conditions, exploring the impact of different saturation durations on the mechanical characteristics of the samples. Building on Sections 4.1 and 4.2, this section investigates the deterioration mechanism of the mechanical properties of samples under the coupled effects of saturation and fatigue loading, specifically under uniaxial loading conditions.

4.3.1 Test device and test method

4.3.1.1 Test device

1) Mechanical testing device

The QKX-YD-1000 electro-hydraulic servo rock dynamic fatigue testing machine was jointly developed by Henan Polytechnic University and Shandong Qiankun Xing Intelligent Technology Co., Ltd., as shown in Figure 4.10(a). This testing machine has both static and dynamic modes and is capable of performing uniaxial compression, conventional triaxial compression, and tensile tests. The maximum loading speed is 800 mm/min, and the maximum confining pressure is 50 MPa. In dynamic mode, the maximum axial load is 800 kN, the maximum displacement is 50 mm, and the maximum cyclic frequency is 50 Hz; in static mode, the maximum axial load is 1000 kN, and the maximum displacement is 100 mm.

(a)

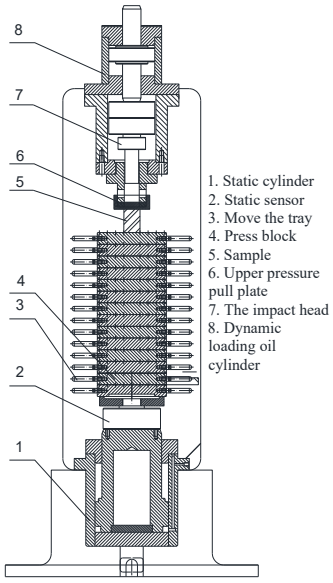

(b)

(c)

Fig. 4.10 Mechanical and acoustic emission test equipment. (a) QKX-YD-1000 Electro-Hydraulic Servo Rock Dynamic Fatigue Testing Machine. (b) Schematic Diagram of the Testing Machine. (c) DS5-8B Holographic Acoustic Emission Signal Analyzer.

2) Acoustic emission testing equipment

The DS5-8B holographic acoustic emission signal analyzer, shown in Figure 4.10(c), is capable of utilizing 2 to 8 channels via a USB 3.0 interface for multi-channel synchronous data acquisition. The sampling trigger modes include signal threshold triggering and external triggering. The continuous data throughput is 65.5 MB/s, with a maximum capacity of up to 393 MB/s.

4.3.1.2 Test method

Fatigue loading tests were conducted on four groups of samples with different water saturation durations (0, 12, 24, and 36 hours) using the dynamic fatigue testing machine. The fatigue loading parameters were as follows: minimum stress $\sigma_{\min} = 0.15\sigma_c$,; maximum stress $\sigma_{\max} = 0.95\sigma_c$; loading rate = $0.1\sigma_c$/s (1/16 Hz); waveform = sine wave; and the number of cycles = 10. During the fatigue loading process, two acoustic emission probes were placed at the bottom of the samples to monitor damage and fracture information. Since the uniaxial compressive strength of the samples varies under different water saturation conditions, the

stress cycle scheme for this test was developed based on the test results in Section 4.1.1, as shown in Table 4.4.

Table 4.4 Fatigue loading test method for each group of samples

Group	σ_c (MPa)	σ_{min} (MPa)	σ_{max} (MPa)	Loading Rate
Natural Sample	52.8	7.92	50.16	$0.1\sigma_c$/s
Sample after 12 h Saturation	25.5	3.83	24.23	
Sample after 24 h Saturation	14.8	2.22	14.06	
Sample after 36 h Saturation	12.9	1.94	12.26	

Uniaxial compression tests were conducted on the samples after fatigue loading to obtain the complete stress-strain curves. The mechanical properties of the samples were compared before and after fatigue loading to investigate the degradation mechanism of the mechanical properties under the combined effects of water saturation and fatigue loading. The technical roadmap for this experiment is illustrated in Figure 4.11.

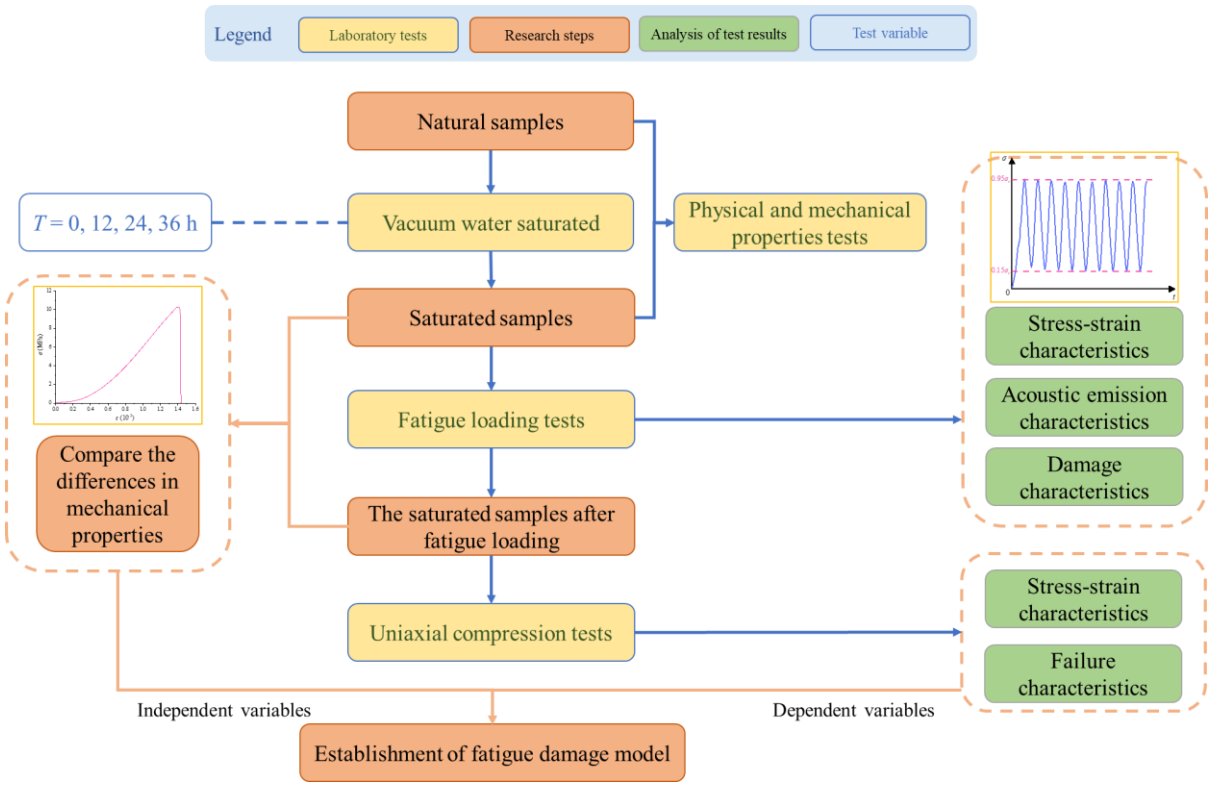

Fig. 4.11 Technical roadmap for research on fatigue damage characteristics of shale

4.3.2 Test results and analysis

4.3.2.1 Stress-strain characteristics of samples during fatigue loading

Figure 4.12 presents the stress-axial/radial/volumetric strain curves of each group of samples during the fatigue loading process. It can be observed from Figure 4.12 that the stress-strain characteristics of the samples exhibit significant differences under varying water saturation durations during fatigue loading.

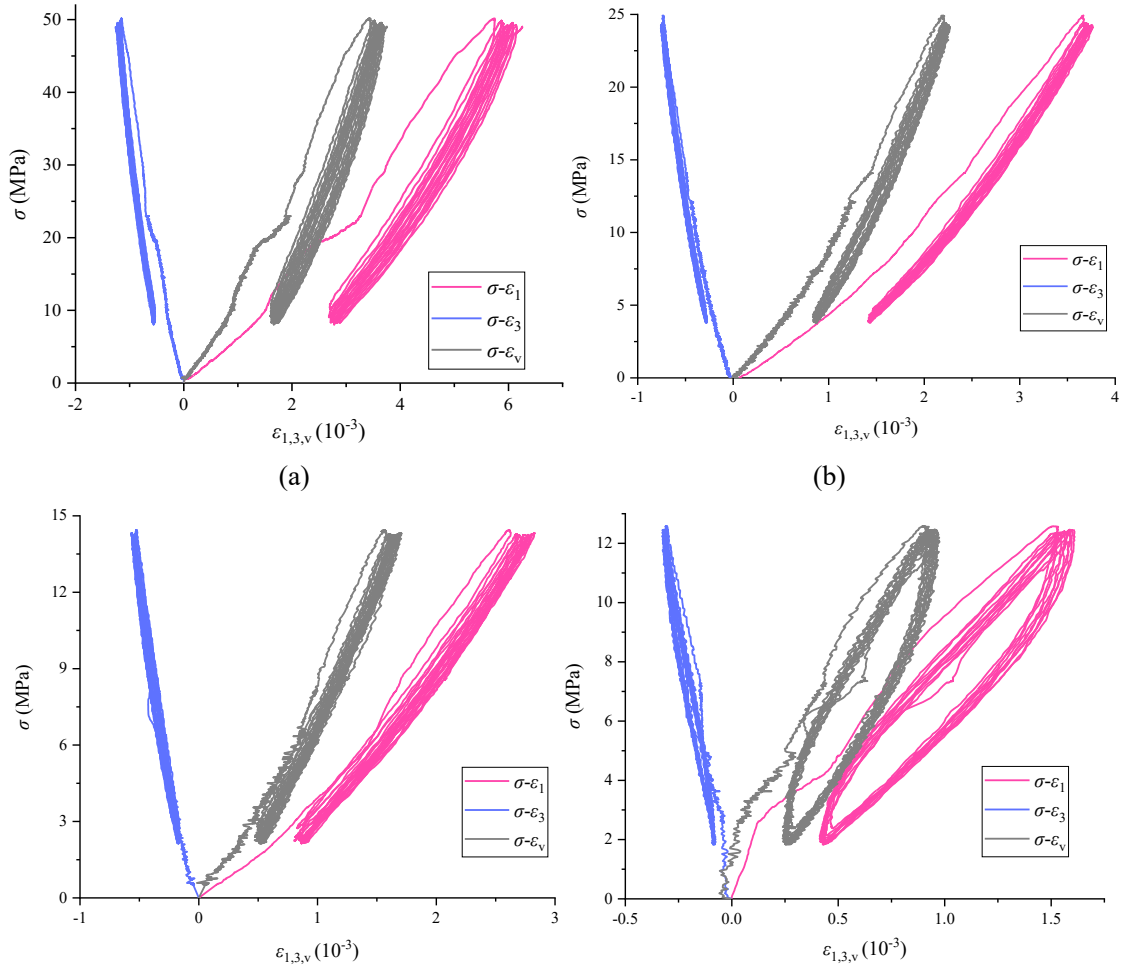

Fig. 4.12 Stress- strain curves of each group of samples during fatigue loading. (a) Water Saturation Time: 0 h (Natural Sample). (b) Water Saturation Time: 12 h. (c) Water Saturation Time: 24 h. (d) Water Saturation Time: 36 h.

In terms of stress characteristics, the uniaxial strength of the samples decreases with increasing water saturation time (see Table 4.4), leading to a corresponding reduction in the fatigue cycle stress. The stress cycle range for the natural samples is 7.9 to 51.1 MPa, while that for the 36-hour saturated samples is 1.9 to 12.3 MPa. Regarding strain characteristics, the maximum strain of the samples during fatigue loading gradually decreases with longer water saturation times. The natural sample has a maximum axial strain of 6.26×10^{-3}, which is

greater than the maximum strains of the samples after 12 hours (maximum strain 3.76×10^{-2}), 24 hours (maximum strain 2.83×10^{-2}), and 36 hours (maximum strain 1.61×10^{-2}), by 66.5%, 121.2%, and 288.9%, respectively.

Upon examining the shapes of the stress-strain curves of the various groups, it is found that as the water saturation time increases, the stress-strain curves of the samples become increasingly irregular. Notably, for the samples saturated for 24 hours and 36 hours, the stress-circumferential strain curves display more undulations and steps, leading to a pronounced jittering trend in the stress-volumetric strain curves of the samples.

In addition, upon examining the stress-strain shapes of each group of samples, it was observed that the hysteresis loop openings for samples with water saturation times of 0, 12, and 24 hours predominantly developed in a long strip shape in the direction of stress loading and unloading. However, the hysteresis loop opening for the sample with a saturation time of 36 hours significantly increased and appeared elliptical, with a notable difference in the loading and unloading paths of a single hysteresis loop. This indicates that the sample with a saturation time of 36 hours exhibits greater fatigue damage within a single hysteresis loop.

Observing the movement state of the stress-strain hysteresis loops for each group of samples, the hysteresis loop of the natural sample shifted notably to the right, while the rightward shift gradually decreased as the water saturation time increased. This suggests that during the fatigue loading process, the fatigue damage between each loading-unloading cycle of the sample decreases with increasing water saturation time.

The results indicate that as the water saturation time increases, the damage within a single stress-strain hysteresis loop of the sample gradually intensifies, while the damage between different hysteresis loops diminishes. This seemingly contradictory phenomenon is not isolated; in our previous study on the fatigue characteristics of gypsum rock, we found that the damage of samples during fatigue loading is closely related to frequency. However, the damage within a single hysteresis loop increases with frequency, while the damage between loops decreases with frequency (Wang 2021).

The reason for this phenomenon lies in the fact that natural samples, which have not undergone water saturation treatment, exhibit minimal initial damage before fatigue loading, allowing for a greater degree of strain recovery during unloading (the plastic strain during a single loading-unloading process is small). However, because they experience less initial damage, the rightward shift of their stress-strain curve during subsequent loading-unloading cycles is more significant. This principle is similar to the rapid growth of fatigue strain during the early stages of fatigue loading, which stabilizes in the later stages. In contrast, water-saturated samples experience prior water-induced damage, leading to increased plasticity. Consequently, the difference between the strain recovery path and the loading path during the same loading-unloading cycle becomes more pronounced, resulting in a larger hysteresis loop. Additionally, due to the prior water-induced damage, their sensitivity to fatigue loading

decreases, leading to reduced strain variation between different fatigue loading-unloading cycles.

4.3.2.2 Acoustic emission characteristics of samples during fatigue loading

To investigate the damage characteristics of each group of samples during the fatigue loading process, acoustic emission (AE) monitoring was conducted on the samples, recording the acoustic emission energy, ringing count, and cumulative values throughout the loading process, as shown in Figure 4.13.

The acoustic emission system can capture the initiation, propagation, and damage of cracks during compression through the rapid release of energy in rocks and AE counts. Under the influence of fatigue stress, the AE parameters of the samples (ringing count and energy) show a significant correlation with the stress-time curve. The damage process can be divided into three stages: the initial loading stage, the initial fatigue loading stage, and the later fatigue loading stage.

1) Initial Loading Stage (stress loading from zero to the fatigue stage, encompassing the compaction and elastic phases): in this stage, the stress of the samples increases relatively steadily. Most samples exhibit low ringing count and energy values, as shown in Figures 4.13(a) and (b). This indicates that the samples are in a linear crack propagation phase, where some cracks undergo compaction and closure, generating only a small amount of acoustic emission signals. However, for the samples with a saturation time of 36 hours, the stress-time curve displays many inflection points, indicative of nonlinear crack development and propagation. Compared with other groups, the proportion of the corresponding ringing counts and energy values of this group of samples in this stage to the total ringing counts and total energy values is also higher. This suggests that this group experienced greater saturation-induced damage, resulting in a higher level of damage during the initial loading phase than the other groups.

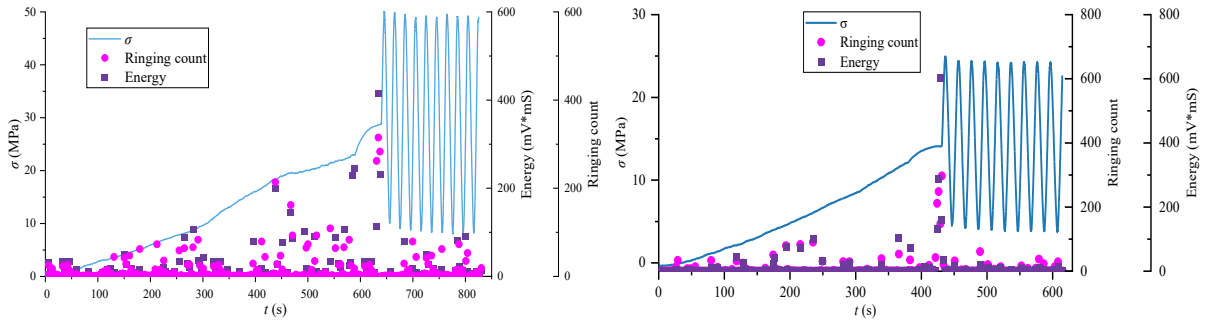

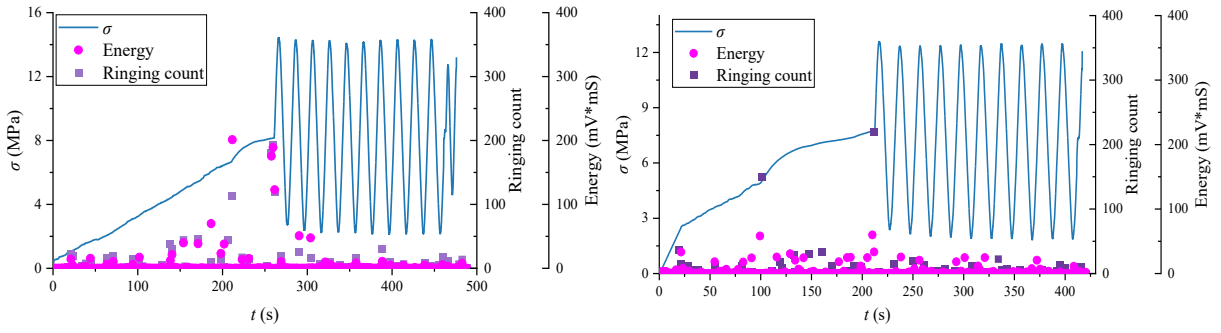

Fig. 4.13 Stress-time curve of the sample during fatigue loading and acoustic emission parameters (ringing count, energy) -time curve. (a) Water Saturation Time: 0 h (Natural Sample). (b) Water Saturation Time: 12 h. (c) Water Saturation Time: 24 h. (d) Water Saturation Time: 36 h.

2) Initial Stage of Fatigue Loading (the first and second cycles of fatigue loading): this stage represents the critical point between the initial loading phase and the fatigue loading phase. During this phase, the stress loading method for the samples suddenly shifts from a slow displacement loading (0.002 to 0.005 mm/s) to a rapid stress loading (0.1σ_c/s: 1.29 to 5.28 MPa/s). As the loading rate increases abruptly, the stress-strain curves of the samples begin to cyclically oscillate between the elastic and yielding phases, causing the crack development characteristics to alternate between nonlinear and linear propagation. The change in crack development status leads to a sudden increase in the acoustic emission parameters (ringing count and energy). Taking the water saturation duration of 12 h as an example, both the ringing count and energy peaks rising to over 300% of the levels observed before fatigue loading.

3) Later Stage of Fatigue Loading (from the third cycle of fatigue loading until the end of fatigue loading): compared to the initial stage of fatigue loading, the acoustic emission response levels of the samples in this phase show a marked decrease, particularly in the saturated samples. This indicates that under the continuous loading of stable sinusoidal fatigue stress, the development of internal cracks within the samples tends to stabilize, resulting in a deceleration in the rate of damage accumulation and a corresponding reduction in acoustic emission response levels.

To further analyze the differences in the variations of acoustic emission characteristics among the groups of samples, the cumulative values of ringing counts and energy under different saturation durations were statistically recorded and represented in a bar chart, as shown in Figure 4.14.

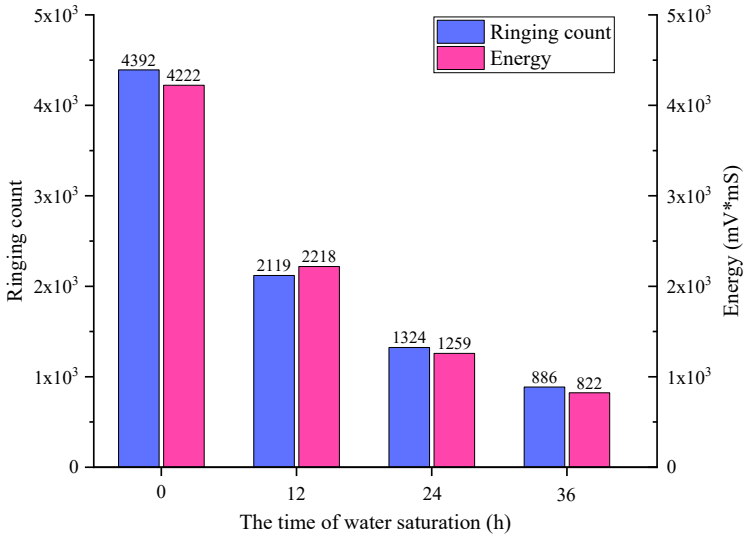

Fig. 4.14 The ringing count and energy accumulation value of samples with different water saturation duration during fatigue loading

From Figure 4.14, it can be observed that as the saturation time increases, both the cumulative values of the ringing count and energy of the samples show a decreasing trend. The samples with saturation times of 12, 24, and 36 hours exhibit reductions in ringing count cumulative values of 51.8%, 69.9%, and 79.8%, respectively, compared to the natural samples, while their energy cumulative values decrease by 47.5%, 70.2%, and 80.5%, respectively. As the saturation time extends, the acoustic emission levels during the fatigue loading process gradually diminish. This phenomenon preliminarily indicates that the saturation damage and fatigue damage of the samples are not independent; the former interferes with the latter's effects. The longer the saturation time, the lower the degree of damage to the samples during the fatigue loading process.

4.3.2.3 Damage characteristics of the samples during fatigue loading

The damage variable represents the degradation level of the samples and reflects the irreversible changes in their structure during the loading process. Calculating the changes in the damage variable *D* under fatigue loading is crucial for investigating the damage characteristics of the samples. The expression for the damage variable *D* is given by (Mazars 1986)：

$$D = 1 - \frac{1}{exp(mY)+nY} \tag{4.5}$$

where *m* and *n* are material parameters determined experimentally, and *Y* is the generalized shear strain, expressed as:

$$Y = \sqrt{\frac{2}{9}[(\varepsilon_1 - \varepsilon_2)^2 + (\varepsilon_2 - \varepsilon_3)^2 + (\varepsilon_3 - \varepsilon_1)^2]} = \frac{2}{3}(\varepsilon_1 - \varepsilon_3) \tag{4.6}$$

Based on the damage evolution formula, the stress-strain curves obtained from the fatigue loading tests were fitted to determine the material parameters as follows:

$$\begin{cases} m = 0.85 \\ n = 0.02 \end{cases} \tag{4.7}$$

Substituting equation (4.7) into equation (4.5), the damage evolution curves of the samples during the fatigue loading process are obtained, as shown in Figure 4.15.

From Figure 4.15, it can be observed that the damage variable-time curves of the various samples show a trend similar to that of the stress-time curves during the compaction and elastic phases. In the initial stage of fatigue loading, as the stress increases rapidly, the fatigue damage of the samples also increases accordingly. Moreover, with the increase in the number of fatigue loading cycles, the maximum fatigue damage also gradually increases, but the trend of increase slows down. This indicates that the majority of the damage to the samples occurs in the initial phase of fatigue loading.

A horizontal comparison in Figure 4.15 shows that as the saturation time increases, the maximum damage variable (D_{max}) in the fatigue loading cycles gradually decreases. A scatter plot of D_{max} versus saturation time is presented in Figure 4.16. From Figure 4.16, it can be seen that D_{max} exhibits a roughly linear negative correlation with saturation time. When the saturation time is 36 hours, the D_{max} value of the sample is 0.54, which is 43.8% lower than that of the natural sample (0.96). This indicates that the longer the saturation time, the less damage the sample experiences during the fatigue loading process.

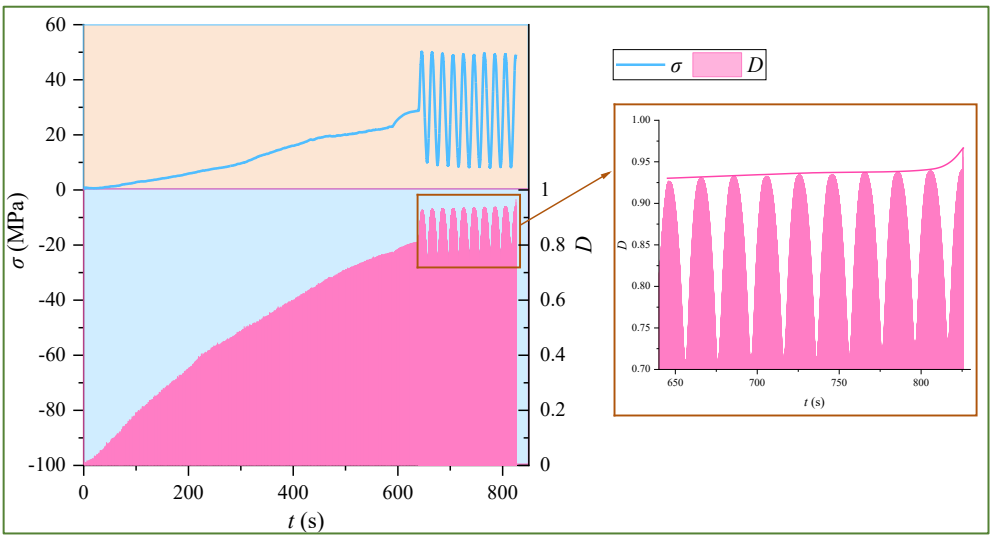

(a)

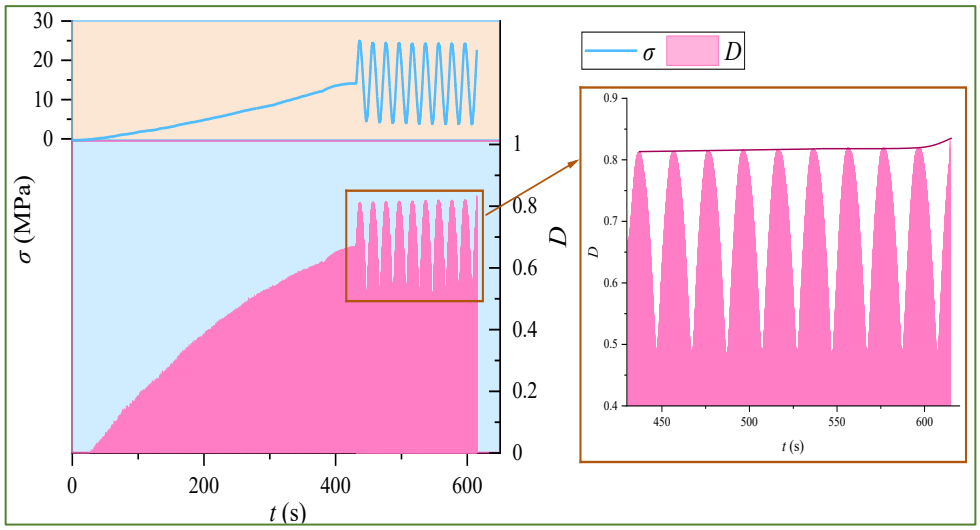

(b)

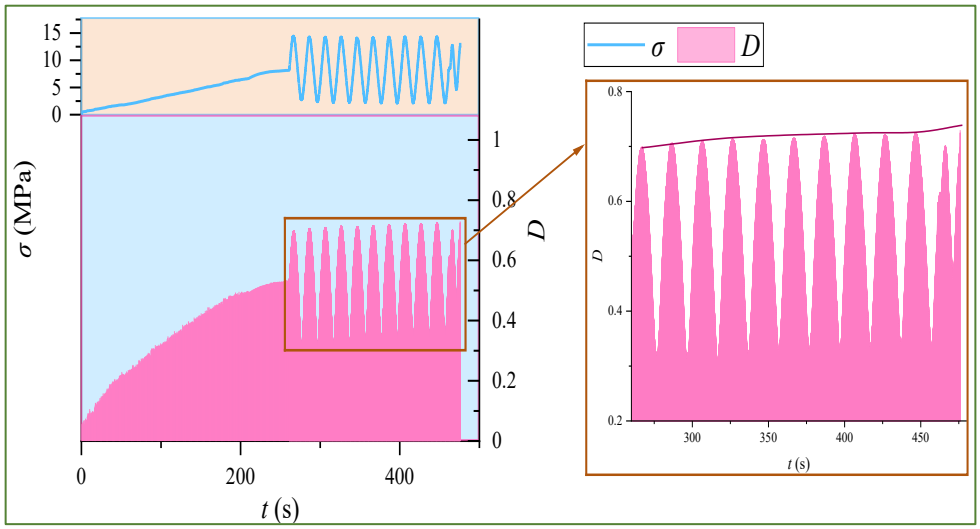

(c)

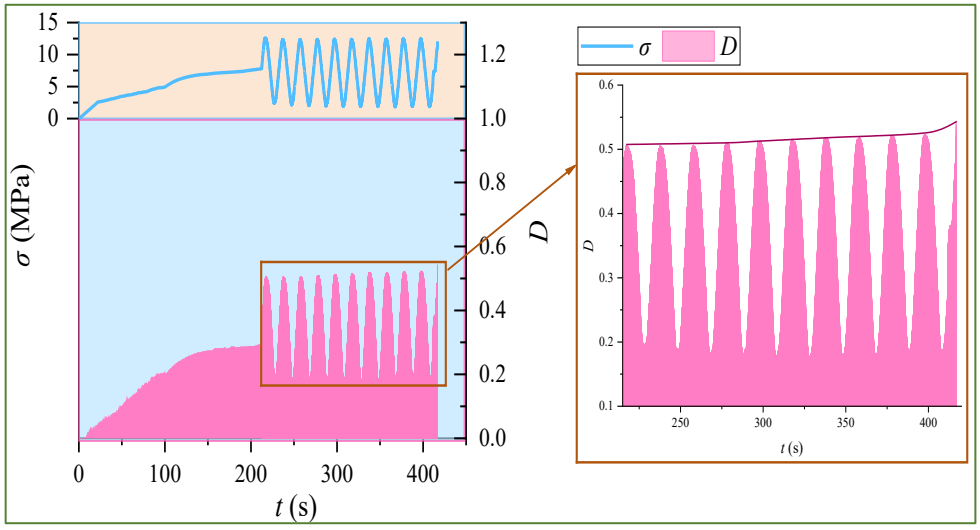

(d)

Fig. 4.15 Damage evolution curve of sample during fatigue loading. (a) Water Saturation Time: 0 h (Natural Sample). (b) Water Saturation Time: 12 h. (c) Water Saturation Time: 24 h. (d) Water Saturation Time: 36 h.

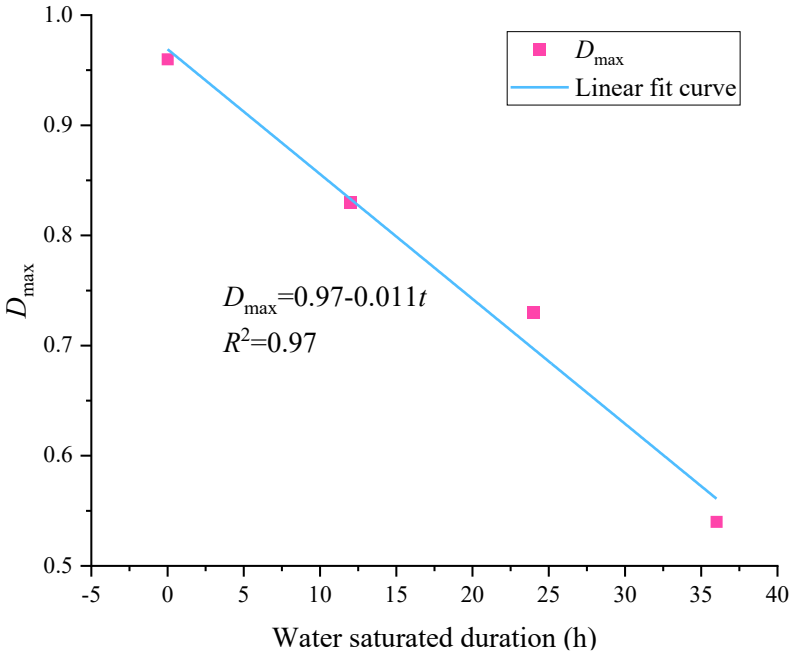

Fig. 4.16 Relationship between maximum damage variable (Dmax) and water saturation duration.

4.3.2.4 Mechanical characteristics of samples after fatigue loading

After the fatigue loading, uniaxial compression tests were conducted on the samples. Figure 4.17(a) shows the complete stress-strain curves from the uniaxial compression tests, while Figure 4.17(b) presents the fitted curve of uniaxial compressive strength versus saturation time for the samples subjected to both saturation and fatigue loading.

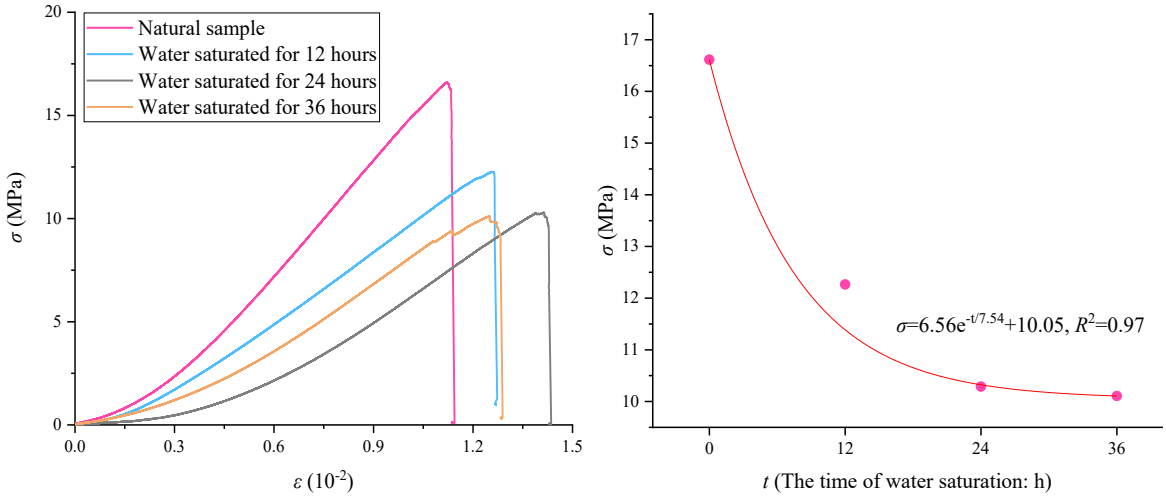

(a) (b)

Fig. 4.17 Uniaxial compression test results of samples under fatigue loading. (a) Full Stress-Strain Curve. (b) Fitted Curve of Uniaxial Compressive Strength with Saturation Duration.

From the observation of the deformation characteristics of each group of samples in Figure 4.17(a), it can be seen that the peak strain of the natural sample (the strain value corresponding to the peak strength) is the smallest. In contrast, after varying durations of water saturation, the peak strain of each sample increases to different extents. This is opposite to the deformation

characteristics of the samples during the fatigue loading process. This discrepancy arises because the natural sample experiences significant fatigue damage during the loading process, resulting in a substantial rightward shift of the stress-strain hysteresis loop and greater fatigue deformation. Consequently, the internal damage from crack development, closure, and fracture in the natural sample is greater than that in the water-saturated samples. This leads to a reduction in the deformation amount caused by crack closure and misalignment in the uniaxial compression test after fatigue loading, subsequently resulting in a decrease in the corresponding peak strain at failure.

From the observation of the strength characteristics of each group of samples in Figures 4.17(a) and (b), it is evident that after water saturation and fatigue loading, the uniaxial compressive strength of the natural sample is 16.6 MPa, which is 35.0%, 61.2%, and 64.4% higher than the strength of the samples saturated for 12, 24, and 36 hours, respectively. Comparing the strength characteristics before and after fatigue loading reveals that the strength of the samples with saturation times of 0, 12, 24, and 36 hours decreases by 68.6%, 51.8%, 30.4%, and 21.7%, respectively, after fatigue loading. Although the strength of the natural sample remains the highest, the strength difference between the natural sample and the water-saturated samples has significantly decreased. Notably, the strengths of the samples saturated for 24 hours and 36 hours are nearly identical (with a strength difference of 14.8% before fatigue loading). This indicates that the impact of fatigue loading on the strength of the samples gradually diminishes with the extension of water saturation time.

4.3.2.5 Failure characteristics of samples after fatigue loading

The failure characteristics of rocks and the evolution of cracks are key to analyzing the degradation mechanism of rocks under fatigue loading [140,141]. Figure 4.18 shows the uniaxial compression failure characteristics of each group of samples after water saturation and fatigue loading.

In Figure 4.18, the upper circular cross-section displays the actual CT scan image, while the left circular image is the reconstructed three-dimensional view. The rectangular images in the middle and on the right represent the front and side views of the middle section of the sample after three-dimensional reconstruction.

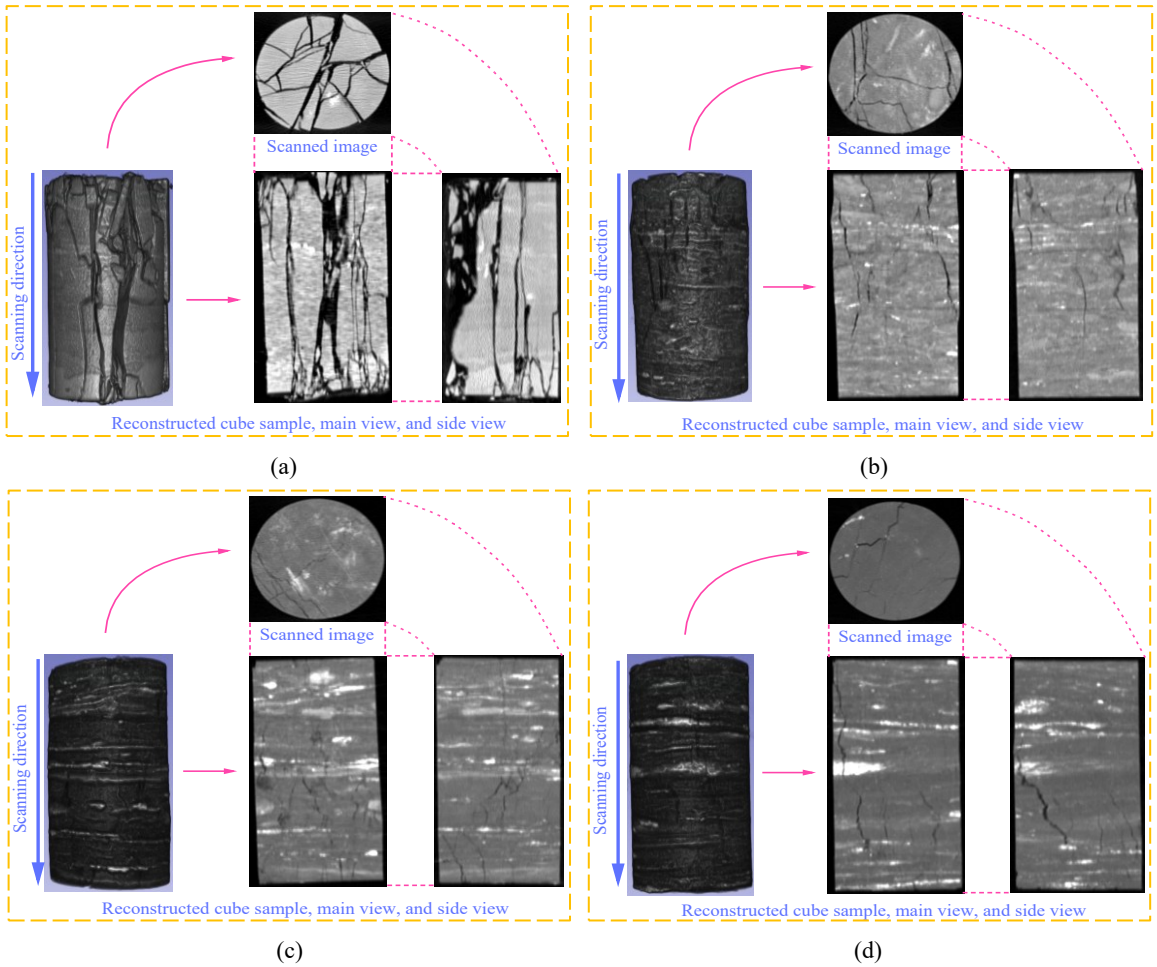

Fig. 4.18 Uniaxial compression failure characteristics of samples with different water saturation duration after fatigue loading. (a) Water Saturation Time: 0 h (Natural Sample). (b) Water Saturation Time: 12 h. (c) Water Saturation Time: 24 h. (d) Water Saturation Time: 36 h.

It can be observed from Figure 4.18 that the failure characteristics of the natural sample are the most pronounced, with multiple cracks penetrating through the upper and lower surfaces of the sample, indicating typical heavy shear failure. This suggests that the natural sample experiences significant damage during the fatigue loading process. In contrast, the failure characteristics of the water-saturated samples differ markedly from those of the natural sample, primarily characterized by a reduction in visible cracks and the disappearance of through-fracture zones. As the water saturation time increases, the density of internal cracks in the samples decreases gradually after uniaxial compression failure, leading to less pronounced failure characteristics.

This indicates that water saturation alters the mechanical properties of the samples, resulting in reduced brittleness and increased plasticity, thereby changing the failure modes of the samples post-saturation. This finding is consistent with previous analyses, which suggest that the longer the water saturation time, the greater the water-induced damage to the samples, leading to reduced fatigue damage during the loading process. In other words, under the same fatigue stress loading conditions of time and proportional stress, the level of damage to the

samples is influenced by another factor: the saturation time. The degree of fatigue damage and the extent of uniaxial compression failure in the samples are negatively correlated with the degree of water-induced damage.

4.3.3 Numerical simulation of the sample failure characteristics

The laboratory experiment can only analyze the fracture evolution of the samples before and after the experiment, and cannot obtain the fracture evolution characteristics of the samples during the experimental loading process. Therefore, a 3D discrete element software can be used to build a model to simulate the loading of the sample.

(1) Model Establishment

Using 3D discrete element software, a model was built to simulate the uniaxial compressive failure characteristics of samples after fatigue loading, as shown in Figure 4.19(a). The model consists of three parts: one sample and two loading plates. The dimensions of the loading plates are 70×70×20 mm³, and they are set as linear elastic constitutive models that do not cause shear or tensile damage. The dimensions of the sample match those of the actual samples and are set as Mohr-Coulomb constitutive models. In the laboratory experiments, the loading directions for both fatigue and uniaxial compression are parallel to the bedding direction. To better replicate the actual loading conditions, bedding parallel to the loading direction is also incorporated into the numerical model, as shown in Figure 4.19(b).

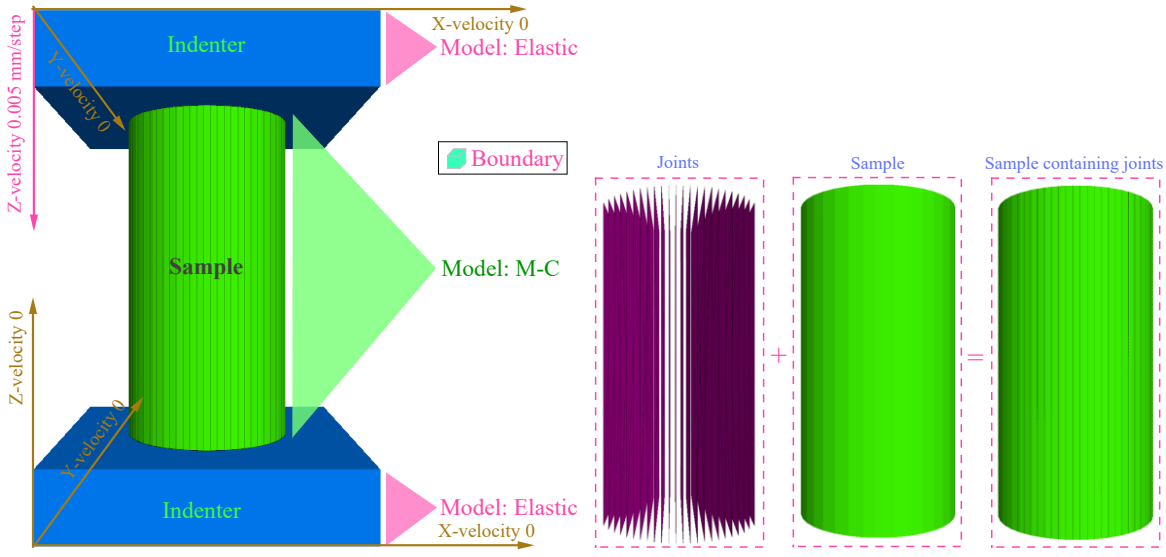

(a) (b)

Figure 4.19 Uniaxial compression test model based on 3DEC. (a) Samples and indenters. (b) Samples containing bedding.

(2) Model Boundary Conditions

The normal displacement (rate) and tangential displacement (rate) of the lower loading plate are set to 0 to prevent displacement during the test. The tangential displacement (rate) of the upper loading plate is set to 0. The normal displacement (rate) of the upper loading plate is

set to -0.005 mm/step, consistent with the laboratory test results. A monitoring point is set at the middle position on the top of the sample to observe the trend of axial stress changes during loading. If an irreversible decreasing trend occurs, loading is to be halted.

(3) Model Parameters

Conventional triaxial tests were conducted on each group of samples after fatigue loading to obtain their mechanical parameters under different conditions, as shown in Table 4.5. The parameters from Table 4.5 are adopted in the model to perform uniaxial compression tests on samples under different saturation durations.

Table 4.5 The mechanical properties of each group of samples after fatigue loading

Group	E (GPa)	c (MPa)	φ (°)	σ_t (MPa)
A (Natural Sample)	8.25	10.98	47.4	8.56
B (Saturation Duration: 12 h)	7.29	4.31	18.1	6.25
C (Saturation Duration: 24 h)	7.15	3.87	16.1	5.82
D (Saturation Duration: 36 h)	6.95	4.00	13.3	6.33

(4) Analysis of Model Calculation Results

Fig. 4.20 illustrates the deformation evolution distribution of each group of specimens after failure under loading. As observed in Fig. 4.20, specimens in their natural state exhibit the most significant deformation at the top, which gradually extends downward as loading intensifies. This phenomenon is closely related to the initial structural state of the specimen, the distribution of microcracks, and the brittle characteristics of the rock. In the unsaturated condition, the specimen structure is relatively compact, and the initial crack propagation is mainly concentrated at the top or surface region. As loading progresses, cracks gradually extend downward, eventually leading to overall specimen failure. After water saturation, the deformation distribution tends to be more uniform, with a smaller difference in deformation between the top and bottom. This indicates that the presence of water may alter the stress distribution characteristics of the specimen, slow down rapid crack propagation, and result in a more uniform deformation distribution across the entire specimen. The cracks predominantly develop along several parallel bedding planes, suggesting that water lubrication reduces transverse crack propagation while promoting crack extension along the bedding direction, thereby increasing deformation uniformity.

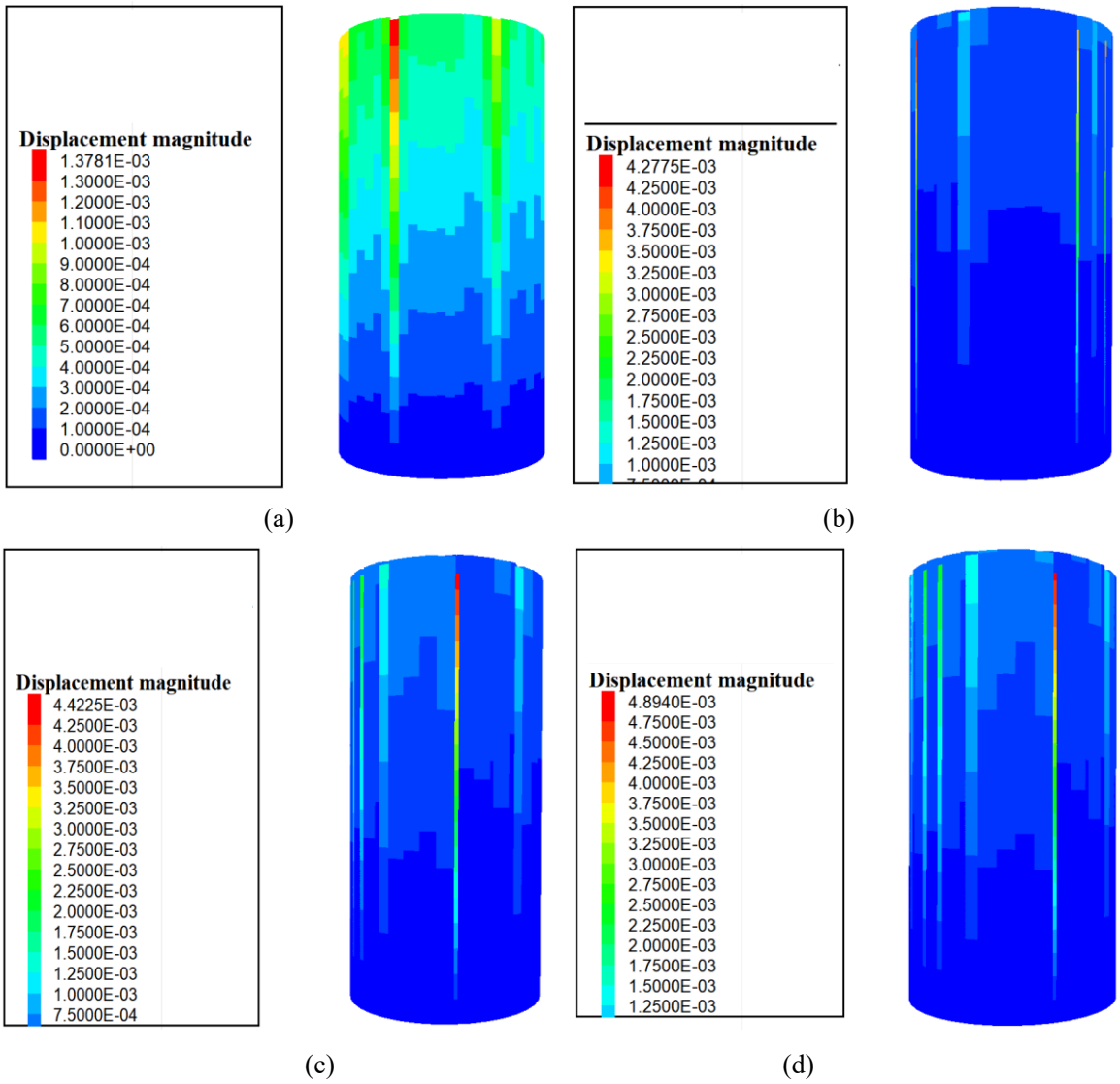

Fig. 4.20 Deformation evolution distribution characteristics of samples in each group after failure. (a) Water Saturation Time: 0 h (Natural Sample). (b) Water Saturation Time: 12 h. (c) Water Saturation Time: 24 h. (d) Water Saturation Time: 36 h.

When the water saturation time is 0 h (natural specimen), the maximum strain at failure is the lowest, at only 1.38% (corresponding to a deformation of 1.38 mm). As the water saturation duration increases, the maximum strain rises to 4.28% (12 h), 4.42% (24 h), and 4.89% (36 h), which is consistent with laboratory experimental results. This indicates that water saturation induces structural softening in the specimen, where water infiltration weakens the cohesive forces between mineral particles, leading to a reduction in overall strength and deformation resistance.

Table 4.6 presents the plastic zone distribution characteristics of each group of specimens after failure. As shown in Table 4.6, in the natural state, multiple parallel shear failure bands along the bedding direction appear on the specimen's lateral surface, manifesting as intense shear failure, which is similar to the results in Fig. 4.17(a). This occurs because, in a dry state, the rock exhibits higher brittleness, with rapid stress concentration and microcrack propagation,

leading to localized plastic deformation. These shear failure bands are closely related to the specimen's bedding planes and mineral composition, forming multiple failure zones along the bedding direction.

With increasing water saturation duration, the number of shear plastic bands on the specimen surface gradually decreases, indicating that the presence of water slows crack propagation, making microcrack extension more gradual, failure more dispersed, and plastic deformation more uniform. As water saturation time increases, the specimen’s strength decreases, plastic deformation capacity improves, the number of visible surface cracks reduces, and the failure mode becomes less distinct. In terms of the relationship between energy release and failure characteristics, water saturation reduces the energy released during uniaxial compression failure. Water infiltration alters the rock’s microstructure, making stress distribution within the specimen more uniform and reducing localized energy accumulation. This suggests that in a saturated state, stress release in the specimen becomes more stable, energy release decreases, and crack propagation slows.

Table 4.6 the distribution characteristics of the plastic zone of each group of samples after failure

Water Saturation Time: 0 h (Natural Sample)	Water Saturation Time: 12 h	Water Saturation Time: 24 h	Water Saturation Time: 36 h
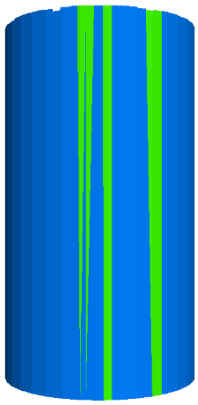	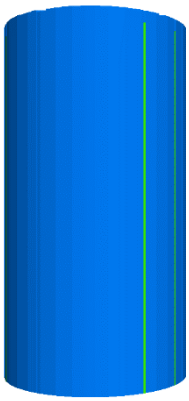	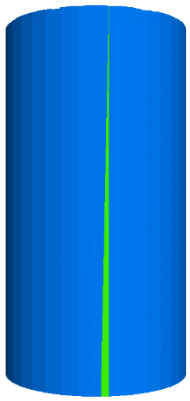	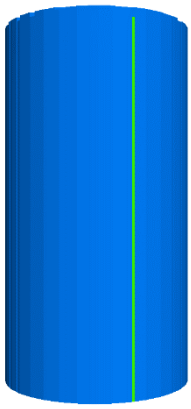

The above results indicate that the extension of water saturation time not only alters the mechanical strength of the rock but also influences its plasticity and brittleness by modifying stress distribution and microcrack propagation patterns. Furthermore, although prolonged water saturation reduces rock brittleness and enhances plasticity, it also makes the rock more prone to uniform deformation during loading, thereby preventing excessive damage accumulation caused by localised stress concentration. Therefore, in engineering applications, hydrological conditions and water saturation duration are critical factors affecting the mechanical behaviour of rocks.

4.3.4 Analysis and modeling of saturated fatigue damage mechanism

4.3.4.1 Analysis of saturated fatigue damage characteristics

The cause of rock fatigue failure is the accumulation of plastic strain. Fatigue failure occurs when the accumulated plastic strain reaches a level sufficient to induce rock failure. To further analyze the damage characteristics of the samples during the fatigue loading process, it is essential to calculate the variation of plastic strain in the samples throughout the fatigue loading.

Figure 4.21 illustrates the evolution of the stress-strain hysteresis loops of the samples during fatigue loading. The stress range of the fatigue loading in this experiment encompasses both the elastic and yield stages of the samples. The elastic strain in the elastic stage is recoverable, while the plastic strain generated in the yield stage is non-recoverable. Therefore, by calculating the difference between the peak strain of the hysteresis loop for each loading cycle and the initial point strain, the total strain of the samples under fatigue loading conditions can be determined. Similarly, the plastic strain under fatigue loading conditions can be obtained by calculating the difference between the strain at the trough of each hysteresis loop and the initial point strain. By calculating the incremental values of the strain at the troughs of the hysteresis loops, the incremental plastic strain for each loading cycle in the samples can be determined.

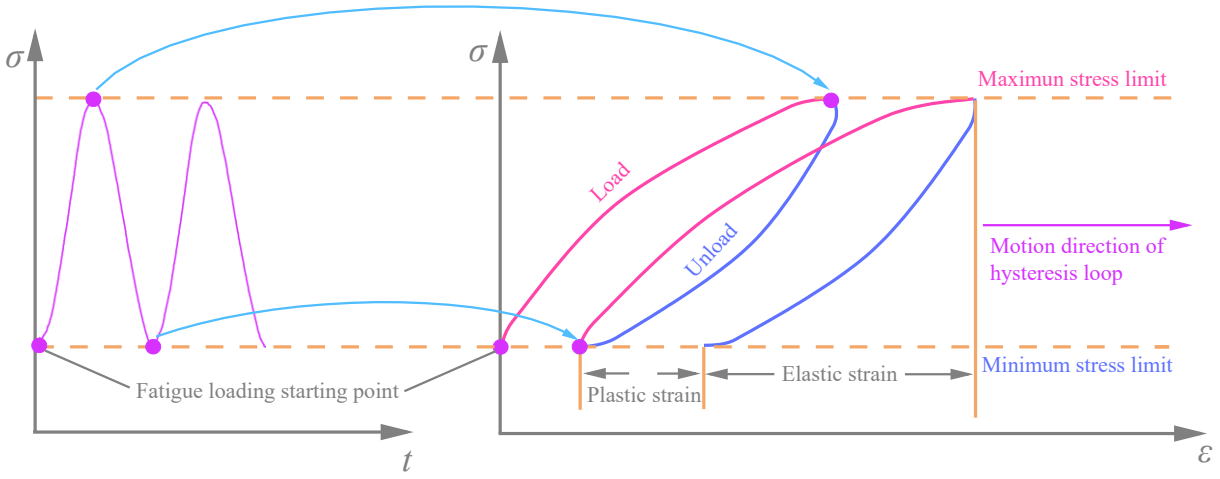

Fig. 4.21 Evolution diagram of stress-strain hysteresis loop of samples during fatigue loading

In each group of samples during the fatigue loading cycles, an average of five points were extracted as typical points, with the strain at the beginning of the fatigue loading set to zero. The variation in peak strain (total strain) of the samples during the fatigue loading process is calculated and presented in Table 4.7.

As indicated in Table 4.7, with the increase in the number of fatigue loading cycles, the total fatigue axial strain of the samples shows an overall increasing trend, while the total fatigue circumferential strain remains relatively stable. To fully consider the effects of axial strain and circumferential strain, the volumetric strain of the samples is calculated as follows:

$$\varepsilon_v = \varepsilon_1 + 2\varepsilon_3 \tag{4.8}$$

where ε_v represents the volumetric strain, ε_1 is the axial strain, and ε_3 is the circumferential strain.

The overall volumetric strain of the samples is computed using Equation (4.8), and the fitted curve of the overall volumetric strain against the number of fatigue cycles is shown in Figure 4.22(a), with the fitting formula given in Equation (4.9).

$$\begin{cases} \tau_{\varepsilon v} = 2.49 + 0.031n, R^2 = 0.95 \\ \tau_{\varepsilon v} = 2.47 + 0.0032n, R^2 = 0.87 \\ \tau_{\varepsilon v} = 1.16 + 0.0085n, R^2 = 0.80 \\ \tau_{\varepsilon v} = 0.89 + 0.0036n, R^2 = 0.95 \end{cases} \tag{4.9}$$

where $\tau_{\varepsilon v}$ represents the overall volumetric strain of the samples.

By calculating the increments of the valley strain values from the stress-strain hysteresis loops, the evolution of the plastic strain of the samples during the fatigue loading process can be obtained, as shown in Table 4.7. A polynomial fitting of the plastic volumetric strain of the samples against the number of fatigue loading cycles is illustrated in Figure 4.22(b). The fitting formula is given in Equation (4.10).

$$\begin{cases} D_{\varepsilon v} = 0.72 - 0.025n + 0.0037n^2, R^2 = 0.99 \\ D_{\varepsilon v} = 0.58 - 0.026n + 0.0024n^2, R^2 = 0.80 \\ D_{\varepsilon v} = 0.28 - 0.0024n, R^2 = 0.75 \\ D_{\varepsilon v} = 0.095 - 0.000069n, R^2 = 0.72 \end{cases} \tag{4.10}$$

where $D_{\varepsilon v}$ represents the plastic volumetric strain of the samples during the fatigue loading process.

Based on Table 4.7 and Figure 4.22, considering the effect of saturation time on the total strain and plastic strain of the samples under fatigue loading, a scatter plot of total strain/plastic strain against the number of hysteresis loops and saturation time was created. The scatter plot was fitted using the Parabola^{2D} function, as shown in Figure 4.23.

From Figure 4.23, it can be observed that the total strain of the samples under fatigue loading generally shows an increasing trend, particularly for the natural samples, where the slope of the fitted line is 3.1×10^{-2}. The total strain represents the overall displacement of the hysteresis loops to the right during the fatigue loading process, which is the sum of the elastic and plastic strains of the samples. The natural samples exhibit the highest volumetric strain values and the fastest rate of increase, indicating that they are most significantly affected by the fatigue stress.

Table 4.7 The change rule of the peak strain (total strain) and the valley strain (plastic strain) of samples

	Peak Strain (Total Strain)	Valley Strain (Plastic Strain)

A (Natural Sample)	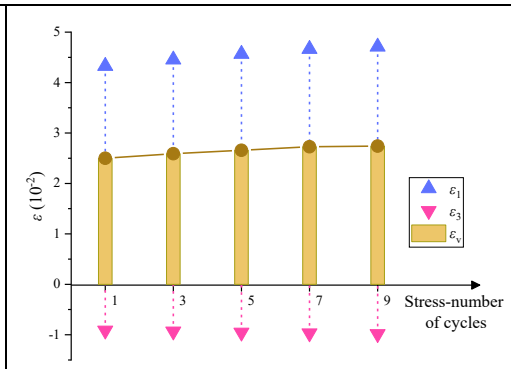	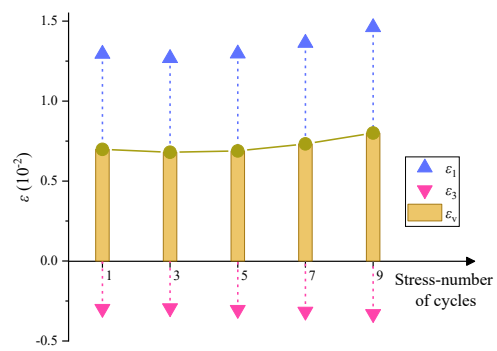
B (Saturation Duration: 12 h)	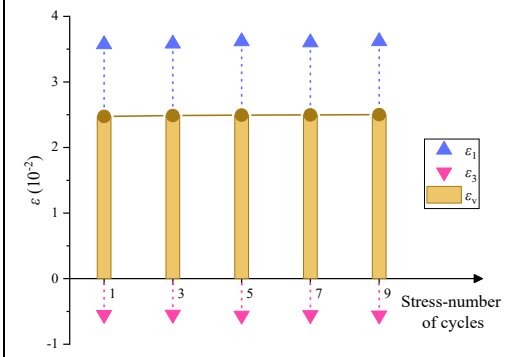	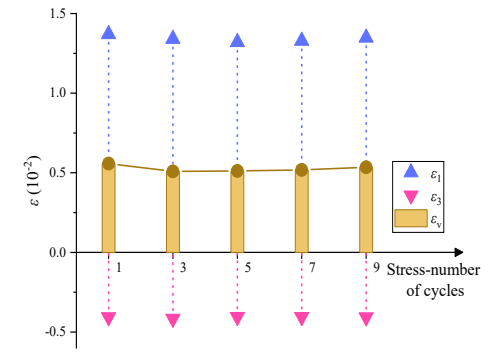
C (Saturation Duration: 24 h)	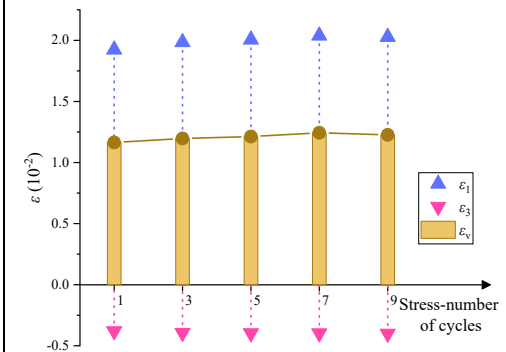	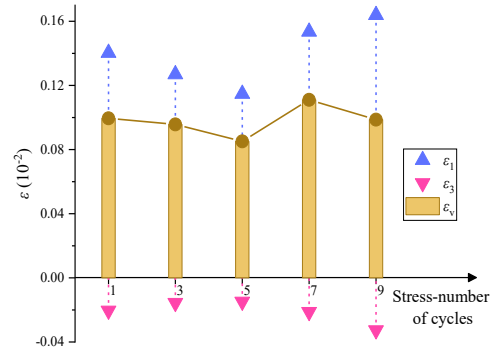
D (Saturation Duration: 36 h)	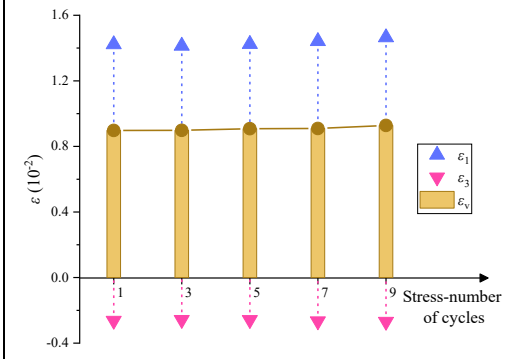	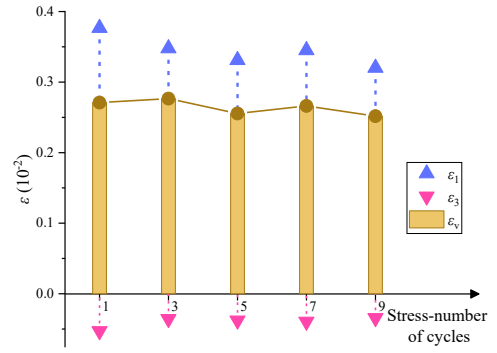

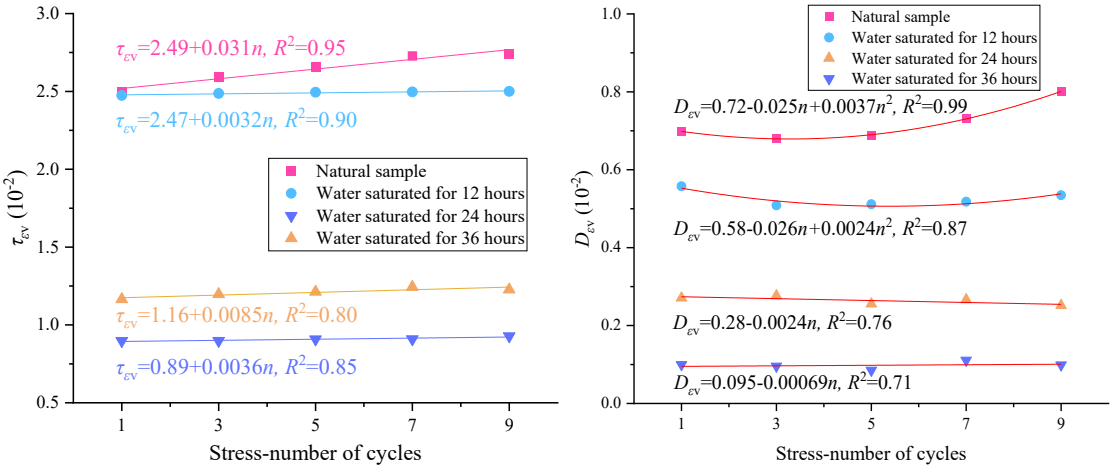

(a) (b)

Fig. 4.22 The relationship between the volume strain of samples and the number of fatigue cycles during fatigue loading. (a) Total Strain. (b) Plastic Strain.

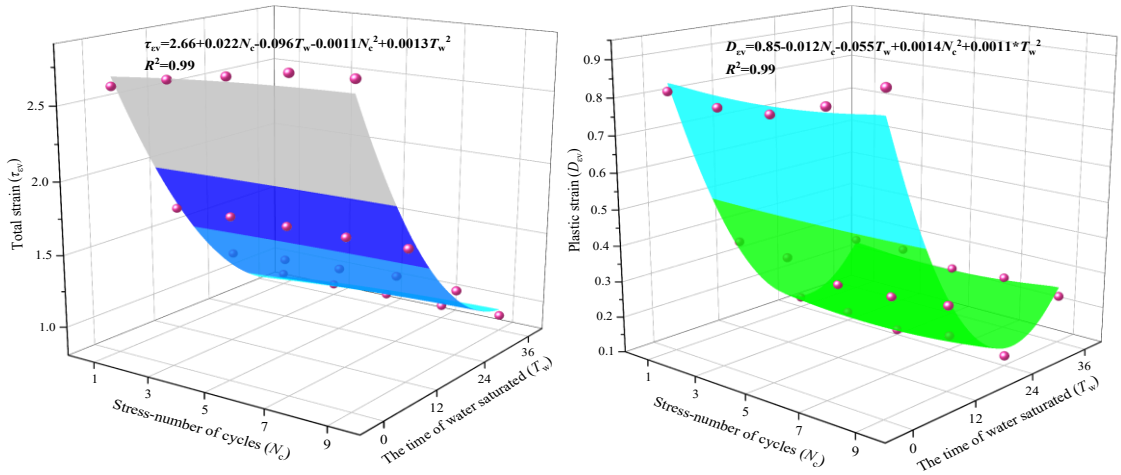

(a) (b)

Fig. 4.23 Strain Scatter Plot and Fitting Surface. (a) Total Strain - Fatigue Cycle Count - Water Saturation Duration. (b) Plastic Strain - Fatigue Cycle Count - Water Saturation Duration.

Simultaneously, observing the strain variation trend of the specimens reveals a significant difference between the trends of plastic strain and total strain under fatigue loading, as the latter no longer follows a simple linear trend. The plastic strain of natural specimens shows little change during the initial phase of fatigue loading but begins to increase rapidly after the fifth cycle. In contrast, the plastic strain of water-saturated specimens exhibits a stable or slightly decreasing trend with increasing stress cycle counts. Natural specimens are more significantly affected by the number of fatigue loading cycles, as greater loading cycles lead to increased plastic damage. The fatigue damage in water-saturated specimens is lower than that in natural specimens and is less influenced by the number of fatigue loading cycles.

The above results indicate that the degradation effects of water saturation and fatigue loading on the mechanical properties of the specimens do not exhibit a simple additive effect of "1 + 1 = 2." Instead, water saturation and fatigue stress interact with each other while

influencing the mechanical performance of the specimens, thus altering each other's degradation effects.

4.3.4.2 Establishment of water saturation and fatigue damage model

To quantitatively analyze the deterioration mechanism of samples under fatigue loading, the water saturation and fatigue damage deterioration index λ was introduced to characterize the deterioration rule of the sample strength. At the same time, considering the water saturation duration (0-36 h), fatigue damage characteristics (plastic strain) and Acoustic Emission parameters (Ringing count, Energy), the fatigue damage model of samples was established as follows:

$$\begin{cases} |\lambda| = \triangle \sigma/\sigma \\ \lambda \propto \{S_E, S_R, D_{\varepsilon v}\} \end{cases} \tag{4.11}$$

where $\triangle \sigma$ is the value of the uniaxial strength reduction, S_E is the cumulative value of Energy parameter, and S_R is the cumulative value of Ringing count parameter.

Acoustic Emission parameters represent the crack development of samples under fatigue loading, and fatigue damage characteristics represent the strain variation law. The two parameters were not of the same type. To make the formula more scientific, imaginary part *j* is introduced, namely:

$$\lambda \propto \{f(S_E, S_R) + j \cdot g(D_{\varepsilon v})\} \tag{4.12}$$

In Equation (4.12), the introduction of the imaginary part is motivated by the ability of complex functions to represent the degradation degree of the specimen's mechanical properties through both real and imaginary components. This dual-dimensional representation ensures that even when the two components are combined, they remain distinct and do not become mixed. Additionally, when necessary, the complex function can be used to compute the modulus $|\lambda|$ to integrate the effects of the real and imaginary parts. Utilizing complex functions to establish the model facilitates a clear representation of the degradation effects of each component while also allowing for a quick assessment of the overall degradation effect of the specimen under the combined influence of multiple factors.

Among Acoustic Emission parameters, Ringing count is the number of times that the signal exceeds the threshold value, and Energy is the area surrounded by the signal envelope and the *X*-axis. To unify the dimensions of each parameter, set:

$$f(S_E, S_R) \propto \sqrt{S_E} + S_R = \sqrt{S_E(t_w)} + S_R(t_w) \tag{4.13}$$

where t_w is water saturation duration.

The fatigue loading plastic deformation was also closely related to the water saturation duration, so:

$$g(D_{\varepsilon v}) \propto D_{\varepsilon v} = D_{\varepsilon v}(t_w) \tag{4.14}$$

Then,

$$\lambda = a\left[\sqrt{S_E(t_w)} + S_R(t_w)\right] + j \cdot D_{\varepsilon v}(t_w) \tag{4.15}$$

where a is a constant. The purpose of introducing the constant a is to make the real part and the imaginary part close to facilitate calculation and drawing.

The relationship between the cumulative value of Energy parameter $S_E(t_w)$, the cumulative value of Ringing count parameter $S_R(t_w)$, and the plastic deformation $D_{\varepsilon v}(t_w)$ of samples and the water saturation duration during fatigue loading was drawn, and the curves of each group were fitted, as shown in Figure 4.24. See Formula (4.16) for the fitting curve.

$$\begin{cases} S_E = 5030 - 1171 \cdot ln(t_w) \\ S_R = 5181 - 1206 \cdot ln(t_w) \\ D_{\varepsilon v} = 0.76 - 0.17 \cdot ln(t_w) \end{cases} \tag{4.16}$$

By substituting Formula (4.27) into Formula (4.26):

$$\lambda = a\sqrt{5030 - 1171ln(t_w)} + a[5181 - 1206ln(t_w)] + j \cdot [0.76 - 0.17ln(t_w)] \tag{4.17}$$

Then：

$$|\lambda|^2 = a^2\left[\sqrt{5030 - 1171\ln(t_w)} + 5181 - 1206ln(t_w)\right]^2 + [0.76 - 0.17ln(t_w)]^2 \tag{4.18}$$

Substituting $|\lambda| = \triangle\sigma/\sigma$ into Formula (4.28), we get: a=2.67×10^{-4}. By combining Formulas (4.9) and (4.10) with Formulas (4.17) and (4.18), the relationship between λ and the fatigue loading times and the water saturation duration can be obtained. The water saturation fatigue damage model of samples was drawn by Formulas (4.17) and (4.18), as shown in Figure 4.25.

As can be seen from Figure 4.25, the water saturation and fatigue damage of samples was closely related to the Acoustic Emission response characteristic and the development of plastic deformation during fatigue loading. There was also a strong positive correlation between acoustic emission response characteristic and plastic deformation. According to the model, the strength variation of samples can be inferred from the response characteristic of Acoustic Emission and the variation of plastic strain during fatigue loading.

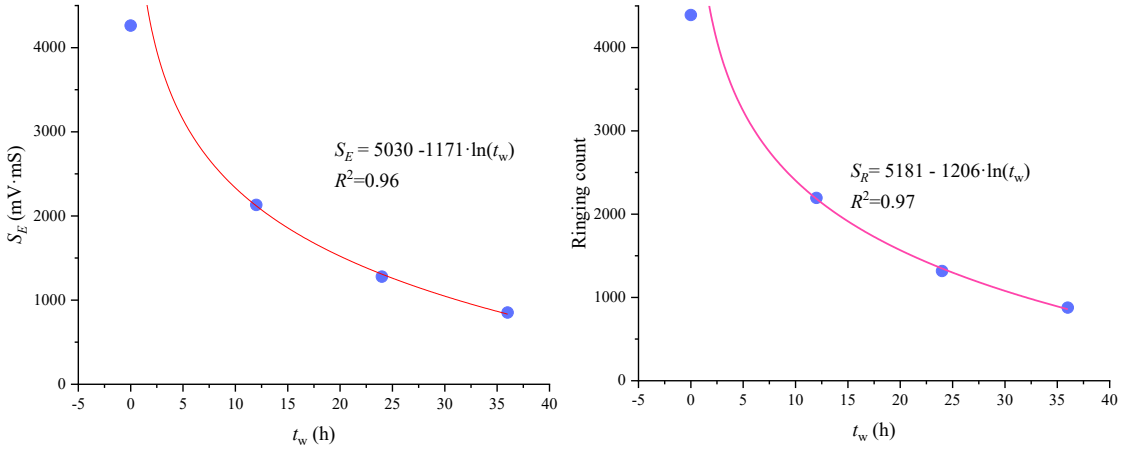

(a) (b)

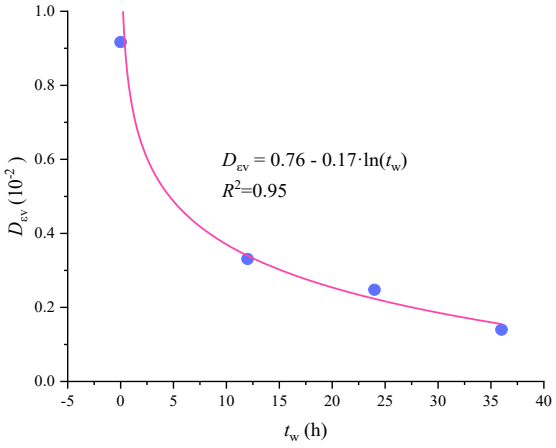

(c)

Fig. 4.24 The fitting curve of each parameter of the deterioration index of the mechanical properties and the water saturation duration. (a) S_E. (b) S_R. (c) $D_{\varepsilon v}$.

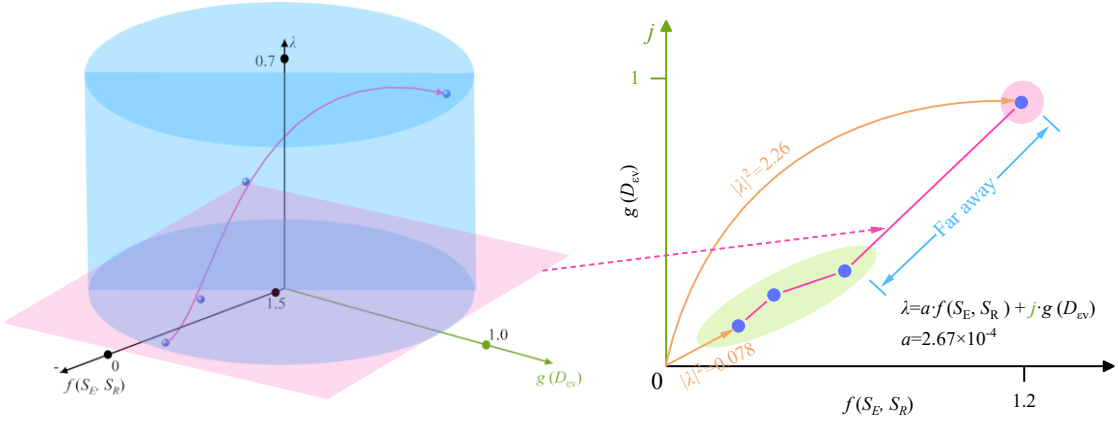

Fig. 4.25 Degradation model of samples mechanical properties

Combining the mechanical property degradation model in Fig. 4.25 with the damage characteristics of samples in Section 4.3 during fatigue loading, then:

$$D_{max}(t_w = 0, 12, 24, 36\ \text{h}) = 0.96, 0.83, 0.73, 0.54 \tag{4.27}$$

The maximum damage quantity $D_{\max}$ of Equation (4.27) is combined with the cumulative acoustic emission energy parameter in Section 4.3.2.2, to draw the variation rule of damage factors of samples under different water saturation duration, as shown in Figure 4.26.

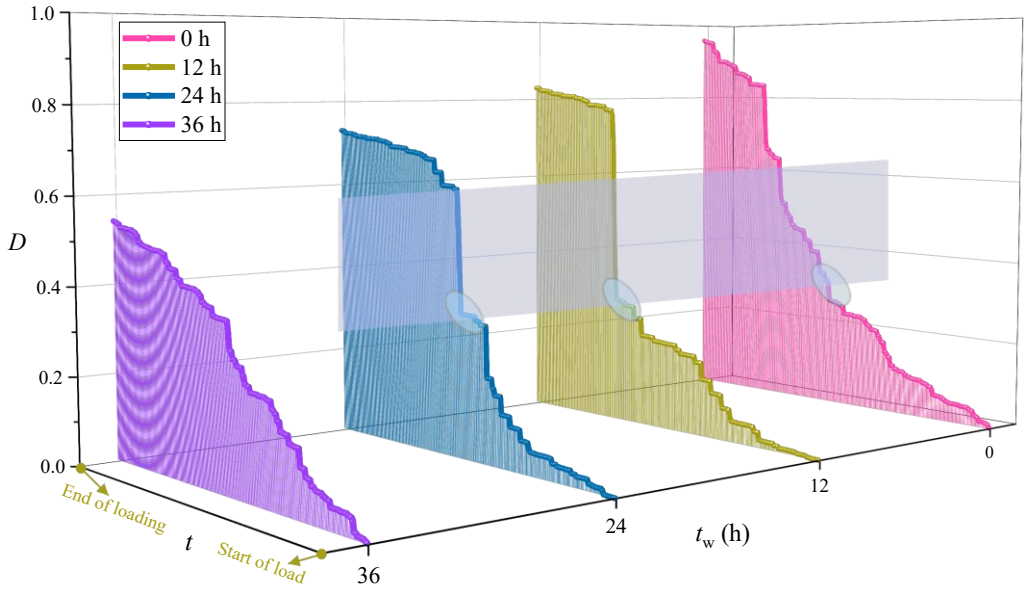

Fig. 4.26 The variation of damage factors during fatigue loading of samples under different water saturation duration.

As can be seen from Figure 4.26, when the water saturation duration is less than 24 h, the damage curves of samples tend to be similar, that is, they all begin to increase rapidly at the starting point of fatigue loading, and the changes are relatively stable after entering the fatigue loading stage. However, the damage curve of samples with water saturation duration of 36 h has no obvious threshold value, and there is no obvious initial loading stage and fatigue loading stage. This indicates that the influence of fatigue loading on samples has been greatly reduced when the water saturation duration is 36 h. Therefore, the threshold point of the interaction between water saturation and fatigue coupling damage is t_w=24 h. When t_w<24 h, the damage of fatigue loading on samples is greater. When t_w>24 h, the susceptibility to fatigue damage was lower.

4.3.4.3 Discussion on the water saturation-fatigue damage model

In this study, water saturation duration was used as the main basis for determining water saturation damage of samples. As can be seen from Table 1, with the increase of water saturation duration, the water content of samples will increase to different degrees (manifested as an increase in density), as shown in Figure 4.27.

In Figure 4.27, "a" is a constant and "a%" is the water content of natural samples (w_g). It can be seen from Figure 4.27 that the w_g of samples is approximately quadratic correlated with water saturation duration (the size of "a" only changes the intercept and does not affect the curve change trend). In the modeling analysis, we have once considered water content as an independent variable to measure saturated water damage. Many laboratory tests results also show that the water content is closely related to the internal friction Angle and cohesion of rock mass, and is a potentially useful parameter to estimate the mechanical properties of rock mass (Yun et al., 2022; Liu et al., 2017). However, through many tests, we found that the influence

of water saturation on samples is not only reflected in the water content, but the process of water saturation also causes damage to samples (Wang et al., 2021; Zheng et al., 2023). In our previous study on gypsum-like rock (Wang 2021), we also found that natural samples have the highest strength, and dehydration at high temperature and vacuum water saturation will both reduce the mechanical properties of samples. The mechanical properties of samples are not only related to water content, but also the process of dehydration and water saturation will also cause damage to samples. Therefore, through comprehensive consideration, we finally chose to use the water saturation duration rather than the water content as the independent variable (input) to determine the damage degree of samples, to establish a more scientific deterioration model of the mechanical properties of the sample, and then provide theoretical reference for the mining of phosphate rock and tunnel support.

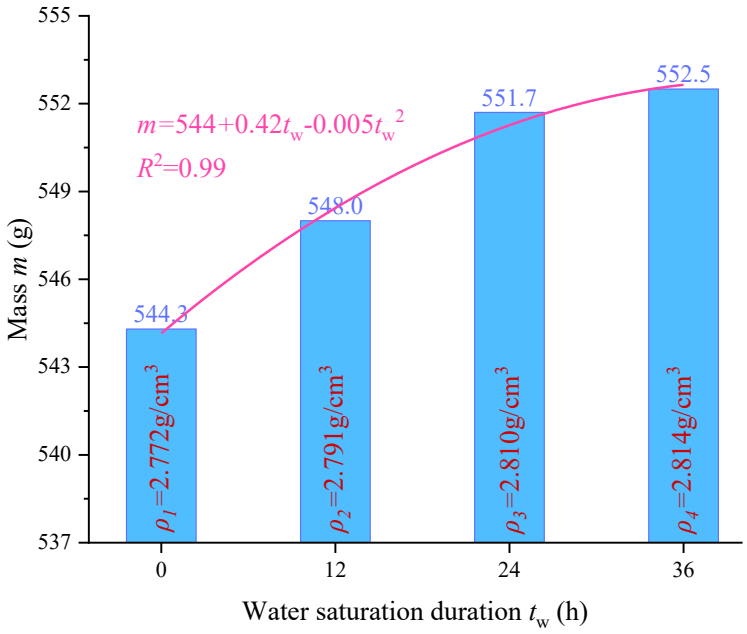

Fig. 4.27 The relationship between Mass m (g), Density ρ (%), and water saturation duration t_w

4.4 Summary

This chapter systematically investigates the mechanical response characteristics of shale under the coupled effects of water saturation duration and cyclic stress through conventional triaxial compression tests and cyclic loading experiments. By integrating acoustic emission monitoring and damage variable analysis, the study reveals the synergistic deterioration mechanism of water-rock interaction and fatigue damage, providing a theoretical basis for assessing the stability of deep shale engineering. The main conclusions are as follows:

1. Synergistic Water-Rock Damage Characteristics: Cyclic loading promotes the expansion of pre-existing fractures and the initiation of new cracks, while long-term vacuum water saturation exacerbates crack softening effects through water infiltration. Consequently, the stress-strain curves of the "cyclic loading + water saturation" group exhibit multiple

fluctuations after the peak, with significantly enhanced plasticity. The failure mode transitions from oblique shear failure in the natural state to intensive shear failure or through-going failure, with the fracture surfaces displaying multi-stage fracture zone expansion characteristics.

2. Time-Dependent Degradation Patterns: As the water saturation duration increases, the compressive strength of the specimens decreases by 11.0%–46.1%, and the stress-strain curve transitions from a smooth elastic-brittle form to a stepped plastic form. The degradation effect of cyclic stress exhibits a nonlinear attenuation trend with increasing water saturation time, indicating a significant dynamic coupling relationship between the two factors.

3. Damage Evolution Mechanism: The damage variable-time curve is highly correlated with stress evolution during the compaction and elastic stages, with a higher contribution of damage in the initial cyclic loading phase. The acoustic emission response level is positively correlated with the cumulative plastic strain, while the acoustic emission activity of the water-saturated specimens gradually decreases during loading. This suggests that water molecule infiltration inhibits the rapid propagation of newly formed cracks.

4. Threshold Effects and Model Development: A complex-plane water saturation fatigue damage model is established, revealing a coupling threshold point at $t_w = 24$ h. When $t_w < 24$ h, fatigue damage dominates mechanical degradation; when t $t_w > 24$ h, water-rock chemical interactions become the primary controlling factor, reducing the specimen's sensitivity to cyclic stress. The model incorporates a dual-index correlation of acoustic emission parameters and plastic strain, enabling the prediction of mechanical parameter variations in water-saturated specimens after cyclic loading.

Chapter 5
Mechanics and seepage evolution of saturated shale under cyclic stress disturbance of variable hydraulic pressure

Chapter 4 analyzed the damage characteristics of surrounding rock (shale) under the combined effect of water saturation and cyclic stress during the first stage of tunnel excavation. However, as excavation progresses into the second inclined mining stage, the surrounding rock is subjected not only to water saturation and cyclic stress but also to additional water pressure from the roof, as shown in Figure 5.1. The presence of water pressure further complicates the stress environment of the surrounding rock.

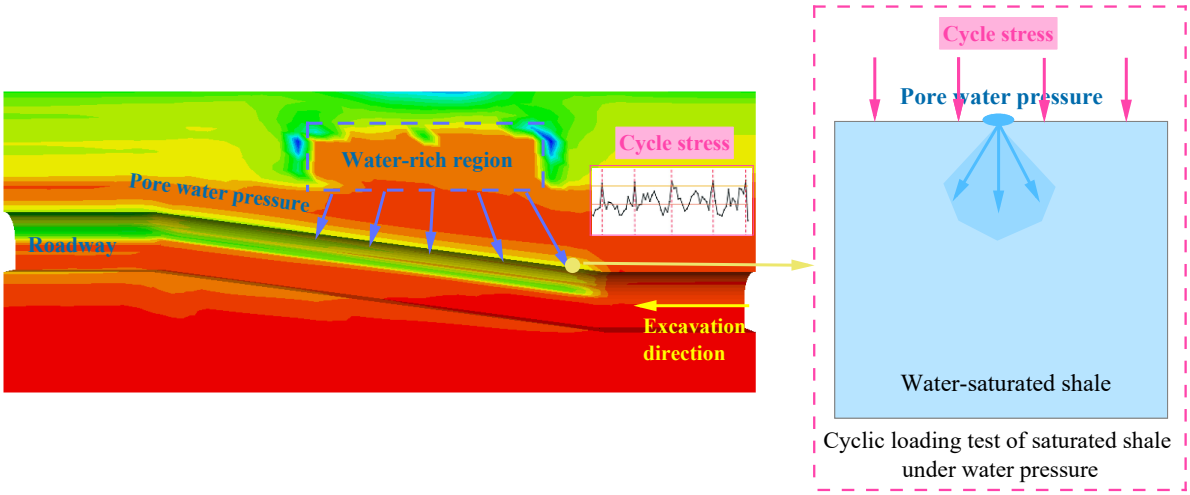

Fig. 5.1 Stress environment of surrounding rock during excavation of the second section of tunnel

To further investigate the mechanical and seepage characteristics of the surrounding rock under water pressure during excavation, pore water pressure gauges and hollow inclusion stress meters were first used to monitor in-situ water pressure and geostress. Based on the field monitoring results, an experimental methodology was developed. A multifunctional true triaxial fluid-solid coupling experimental system was used to conduct cyclic loading tests on water-saturated shale specimens under different water pressures and saturation durations. This study aims to explore the mechanical deterioration and seepage evolution mechanism of water-

saturated shale under cyclic loading with variable water pressure conditions. The research roadmap is illustrated in Figure 5.2, and the findings provide guidance for the excavation support of water-rich tunnels under water pressure effects.

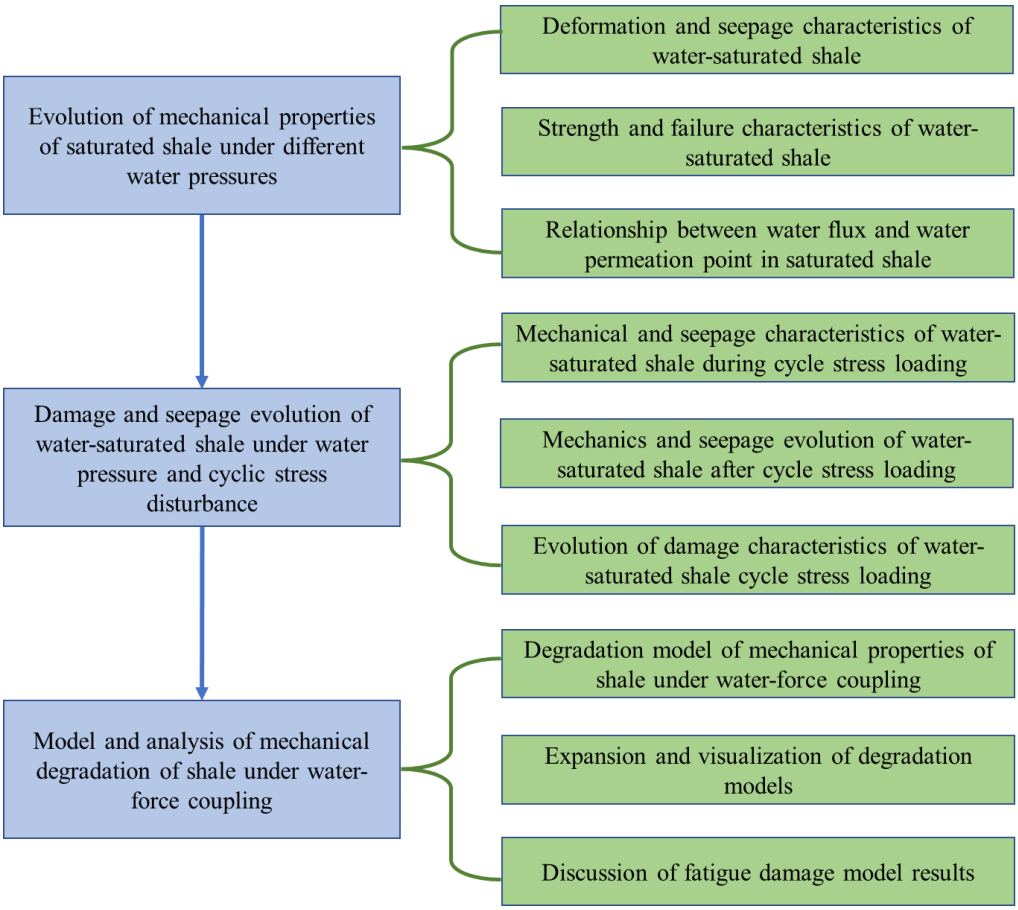

Fig. 5.2 Research roadmap of mechanics and seepage evolution of saturated shale under cyclic stress disturbance of variable hydraulic pressure

5.1 Evolution of mechanical properties of saturated shale under different water pressures

5.1.1 Sample characteristics and experimental methods

5.1.1.1 Sample preparation

The shale samples were cut and polished to form cubic samples with side lengths of 100 mm. To avoid the effects of end friction during the test, the flatness of the end faces was controlled within 0.02 mm. The surface of the samples was smooth, without visible joints or cracks, and was prepared strictly in accordance with the standards set by the International Society for Rock Mechanics. The prepared samples are shown in Figure 5.3. During sample selection, rigorous tests on mass, dimensions, and longitudinal wave velocity were conducted. Six samples with density differences less than 0.02 g/cm³ and longitudinal wave velocity differences less than 50

m/s were selected for the subsequent experiments to minimize the impact of sample heterogeneity on the experimental results.

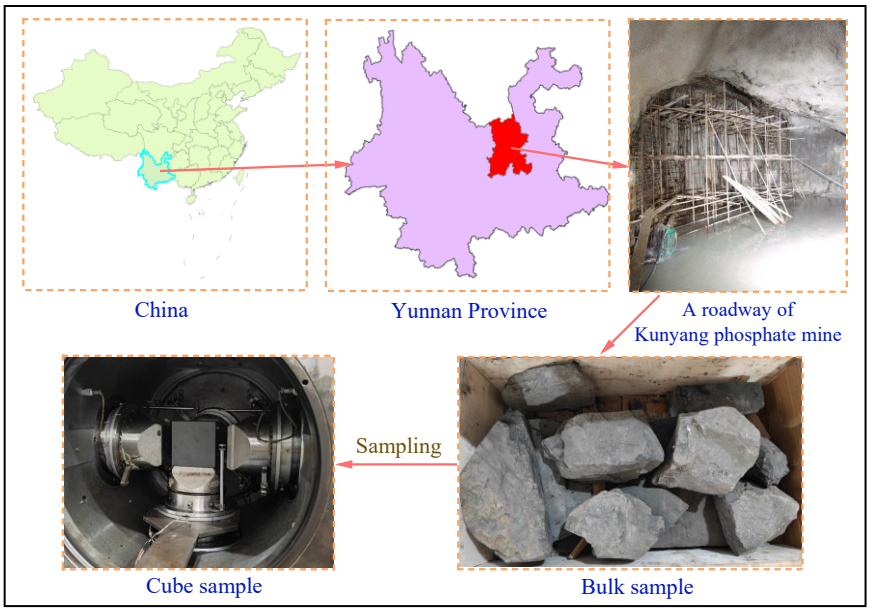

Fig 5.3 Sampling and processing of cube samples

The prepared samples were divided into two groups: Group A consisted of natural samples, while Group B was placed in a vacuum water saturation device for forced saturation for 48 hours. After saturation, the samples were wrapped in plastic wrap, representing the water-saturated samples. The physical properties of the samples before and after water saturation are shown in Table 5.1. It can be seen from Table 5.1 that after water saturation, the sample density and wave velocity increased by 4.0% and 1.6%, respectively.

Table 5.1 Physical property of samples

Group	m (g)	ρ (g/cm^3)	v (m/s)
A: Natural group	2,678.6	2.68	2,854
B: Water-saturated group	2,786.4	2.79	2,901

5.1.1.2 Experimental equipment

The seepage experiments under true triaxial stress were conducted using the "Multifunctional True Triaxial Fluid-Solid Coupling Experimental System," independently developed by Chongqing University, as shown in Figure 5.4 (Li et al., 2016a, 2016b). This experimental system consists of a true triaxial pressure chamber, a hydraulic oil pressure system, and a water-gas permeability system. The pressure control mechanism of the experimental setup ensures that the center point of the sample remains unchanged during true triaxial loading. The maximum load capacity of the testing machine in the x, y, and z directions is 6×10^3, 6×10^3, and 4×10^3 kN, respectively. This system can be used for mechanical, seepage, water retention, and

hydraulic fracturing experiments on coal and rock samples under various true triaxial stress paths.

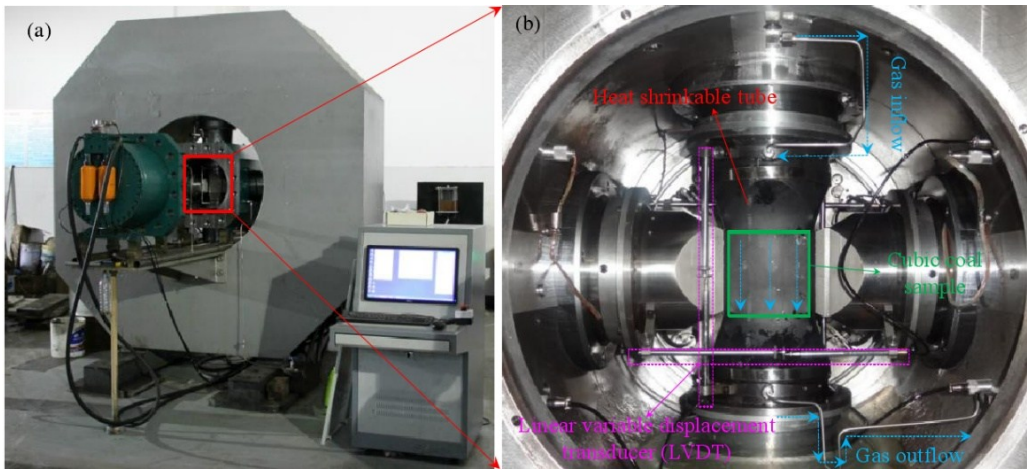

Fig. 5.4 Multifunctional true triaxial fluid-structure coupling experimental system

5.1.1.3 Experimental method

To more accurately study the true triaxial mechanical properties of the samples under different simulated depths and stress paths, the experimental plan was developed based on the in-situ stress conditions measured in Section 3.3 (σ_1=15.5 MPa，σ_2=7.5 MPa，σ_3=5.0 MPa) as follows:

1) The sample was placed in the test chamber, and the three principal stresses were loaded at a rate of 0.5 kN/s until reaching the in-situ stress state.

2) While keeping the three principal stresses constant, water pressures of P = 1, 2, and 3 MPa were applied in the direction of the maximum principal stress.

3) σ_1 was increased at a rate of 0.002 mm/s, while σ_3 was unloaded at a rate of 0.5 kN/s until the sample fractured.

Six sets of true triaxial water retention tests were conducted using this method. The test parameters for each group are shown in Table 5.2. The stress loading path is illustrated in Figure 5.5a. During the tests, both the maximum principal stress and the seepage direction were aligned parallel to the bedding planes (Figure 5.5b) to minimize the impact of sample anisotropy on the experimental results. Figure 5.6 provides the technical workflow of this experiment.

Table 5.2 Experimental parameters of group samples

Tests	Group	p (MPa)	Conditions
1/4	Natural / Water-saturated group	1	σ_1= 15.5 MPa, σ_2= 7.5 MPa, σ_3= 5.0 MPa
2/5		2	
3/6		3	

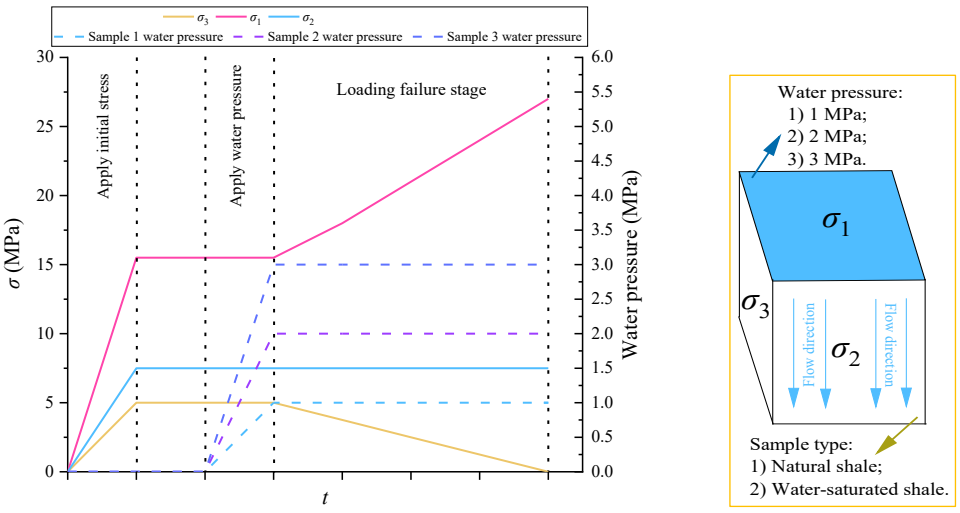

(a) (b)

Fig. 5.5 Stress loading path and seepage direction of true triaxial seepage test. (a) stress loading path (b) seepage direction.

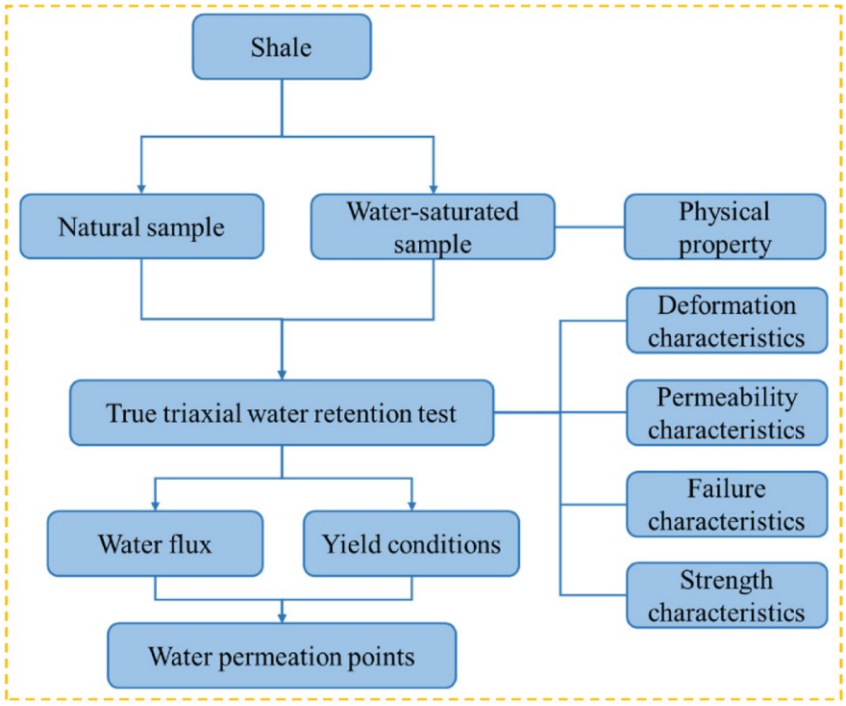

Fig. 5.6 Technical roadmap of true triaxial seepage tests on natural and water saturated samples

5.1.2 Test results and analysis

5.1.2.1 Deformation characteristics of natural and saturated samples under different water pressure conditions

The stress-strain curves of natural and saturated samples under different water pressure conditions are shown in Fig. 5.7. In the figure, τ_{oct} represents the octahedral shear stress, defined as $\frac{1}{3}\sqrt{(\sigma_1-\sigma_3)^2+(\sigma_1-\sigma_2)^2+(\sigma_2-\sigma_3)^2}$, while $\varepsilon_1, \varepsilon_2, \varepsilon_3$ denote the strains in the three principal stress directions. As shown in Fig. 5.7, during the loading process, the absolute

values of ε_1 and ε_3 for each sample group are greater than that of ε_2. The increase in ε_1 primarily occurs during the compaction and elastic stages of the stress-strain curve, while the increase in ε_3 is concentrated after the sample fractures. Initially, ε_2 is greater than 0, indicating that under the action of true triaxial stress, the sample first exhibits compression in the σ_2 direction. As σ_1 increases during the loading process, ε_2 gradually decreases to negative values, at which point the σ_2 direction begins to transition from compression to expansion. After sample failure, as the bearing capacity in the σ_1 direction decreases and σ_3 is unloaded, the difference between σ_2 and σ_3 for some samples gradually diminishes, eventually becoming less than the difference between σ_1 and σ_2. This results in the σ_2 direction transitioning back to compression, which explains the observed process of compression—expansion—recompression in some samples in theσ_2 direction (Fig. 5.7b and 5.7c).

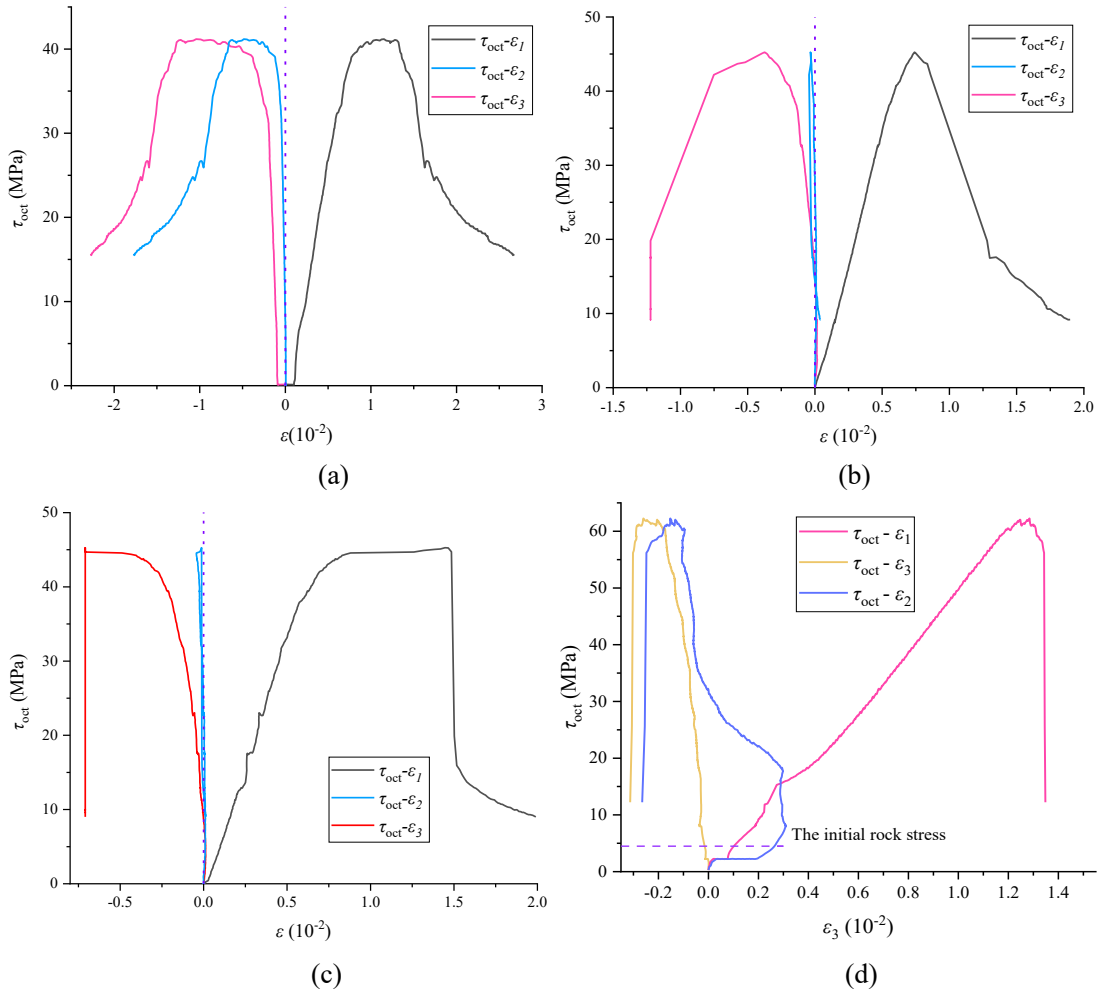

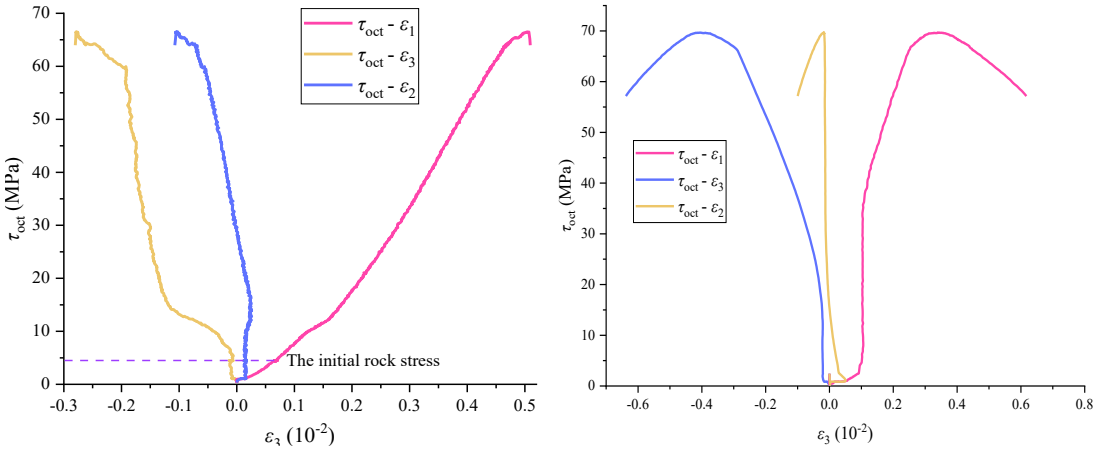

Fig. 5.7 Shear stress-strain curves of shale samples under different water pressure. (a) Group A; Water pressure :1 MPa. (b) Group A; Water pressure :2 MPa. (c) Group A; Water pressure :3 MPa. (d) Group B; Water pressure :1 MPa. (e) Group B; Water pressure :2 MPa. (f) Group B; Water pressure :3 MPa.

From the shape of the stress-strain curves in Fig. 5.7, it is evident that the stress-strain curve for natural samples is smooth and regular, with $\tau_{oct} - \varepsilon_1$和$\tau_{oct} - \varepsilon_3$ curves being approximately symmetrical along the *x*=0axis. In contrast, the stress-strain curve for saturated samples shows significant variability, lacking smoothness and symmetry. In Fig. 5.7c, during the initial loading, the rate of compression in the σ_2 direction is greater than that in the $\sigma_1$direction. As σ_1 increases, the shear stress begins to rise, causing ε_2 to decrease rapidly and gradually transition to expansion. The deformation characteristics of the samples before and after saturation under different water pressure conditions are summarized as ε (*P*=1 MPa) > ε (*P*=2, 3 MPa) and ε (natural) > ε (saturated). These results indicate that both water pressure and water saturation alter the deformation characteristics of the samples, leading to a reduction in ductility.

5.1.2.2 Permeability characteristics of natural and saturated samples under different water pressure conditions

To analyze the changes in permeability characteristics of shale samples before and after water saturation under different water pressure conditions, the variation of the volumetric strain ε_v during the loading of the samples is calculated as follows:

$$\varepsilon_{\mathrm{v}} = \varepsilon_1 + \varepsilon_2 + \varepsilon_3 \tag{5.1}$$

Using Equation (5.1), the $\varepsilon_{\mathrm{v}} - t$ curves for samples under 1 MPa and 2 MPa water pressure are computed, while simultaneously recording the water flow data *V* from above the samples during loading. The *V*−*t* curves are presented in Figure 5.8.

From Fig. 5.8(a) and 5.8(b), it can be observed that the average water flow rate for the saturated samples is 1.16 L, which is 10.5% higher than the average flow rate of the natural samples (1.05 L). Within the same group of samples, there is a positive correlation between water flow and water pressure. The volumetric strain curves show that with the extension of

time, the volumetric strain of all four groups of samples first increases, then decreases, and subsequently stabilizes or continues to increase. The changes in water flow velocity are closely related to the volumetric strain.

For the natural samples at P=1 MPa, the $\varepsilon_v - t$ curve is overall smooth, showing a pattern of first increasing and then decreasing, with a relatively consistent trend. Specifically, during $t\in[0,235]$, the samples are gradually compacted under the action of the triaxial principal stress, and the rate of increase in water flow gradually decreases. At t=235 s, the samples fail, new cracks develop and quickly propagate, leading to a rapid decrease in volumetric strain followed by negative growth, indicating a transition from compression to expansion, with the water flow rate beginning to increase sharply. At P=2 and 3 MPa, the $\varepsilon_v - t$ curves for natural samples can be divided into three stages: increase, decrease, and then increase again. This phenomenon occurs because, after the samples fractured, although crack propagation and penetration result in an increase in sample volume, the closure of dislocations in the cracks leads to a return to a compressed state, which in turn decreases the rate of water flow increase.

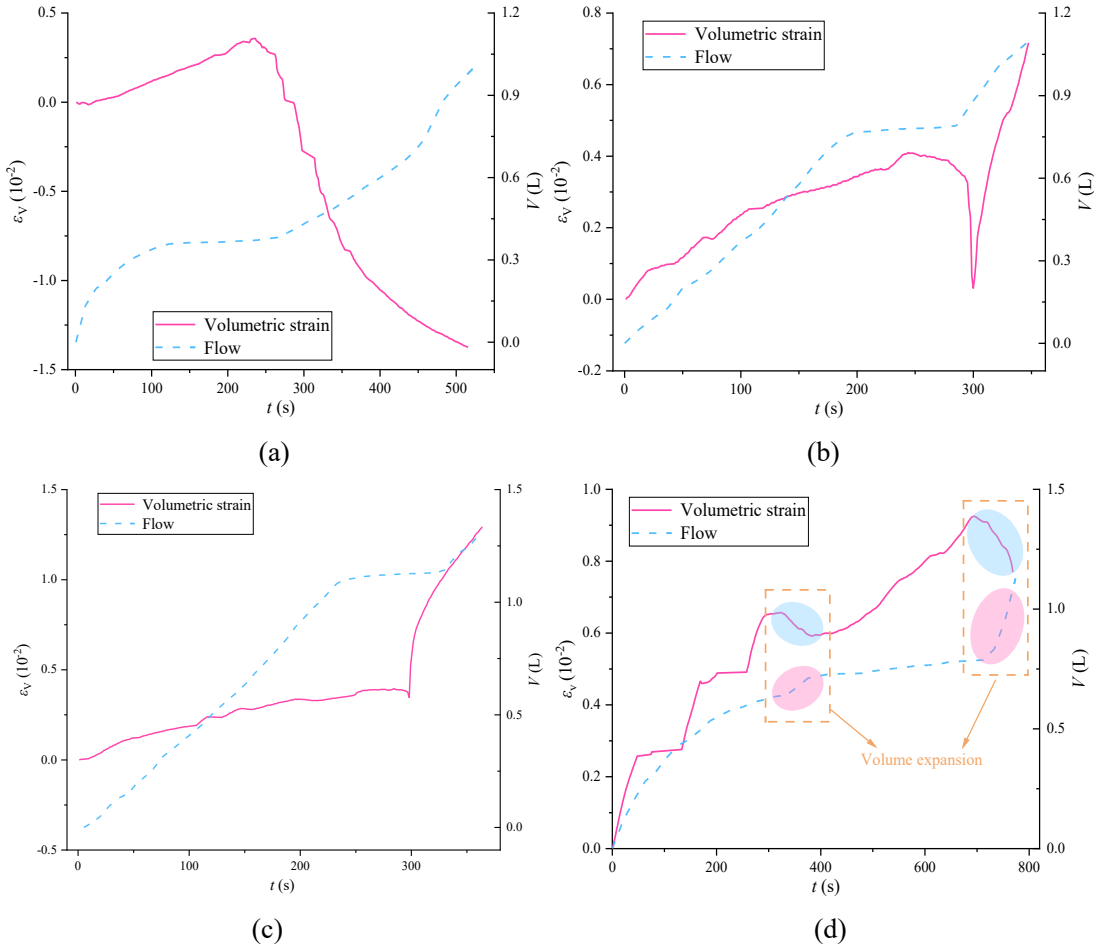

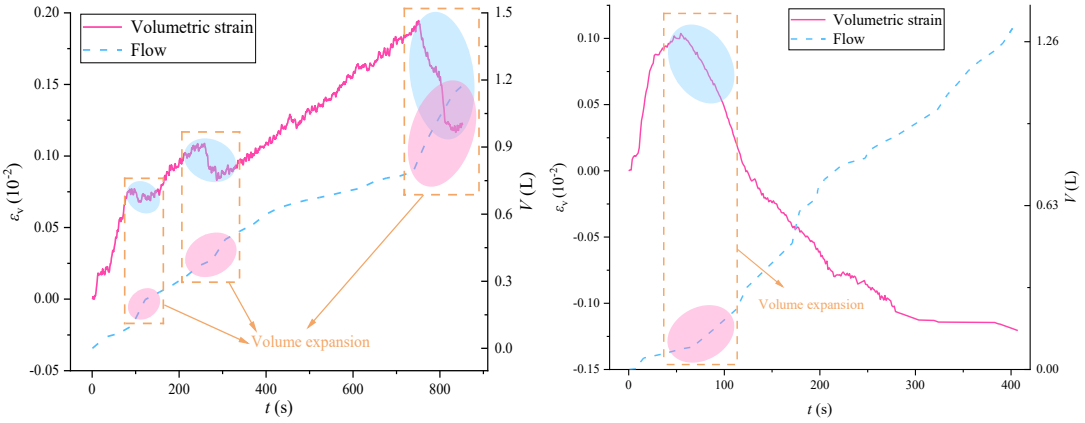

Fig 5.8 The relationship between water flow and volume strain. (a) Group A; Water pressure :1 MPa. (b) Group A; Water pressure :2 MPa. (c) Group A; Water pressure :3 MPa. (d) Group B; Water pressure :1 MPa. (e) Group B; Water pressure :2 MPa. (f) Group B; Water pressure :3 MPa.

The $\varepsilon_v - t$ curves for saturated samples exhibit significant differences compared to those of natural samples, primarily characterized by multiple inflection points and steps. As shown in Fig 5.8(d)-(f), the volumetric strain of the samples increases in a peak-like manner, indicating that the deformation characteristics change due to saturation. The reduction in volumetric strain corresponds with the expansion of the samples, and the increase in water flow velocity is amplified with each expansion of the samples. Unlike natural samples, the volumetric expansion of the saturated samples occurs not only after failure but also during various stages of the loading process. After failure, the expansion of the saturated samples is constrained, and the entire sample remains in a compressed state, which results in the instantaneous growth rate of water flow being lower than that of the natural samples.

5.1.2.3 Strength characteristics of natural and saturated samples under different water pressure conditions

To analyze the effect of water pressure on the strength characteristics of the samples and verify the differences in mechanical parameters under various water pressure conditions, the Mogi-Coulomb criterion is employed to compare the strength parameters of shale before and after saturation [34-35]. The Mogi-Coulomb criterion describes the monotonic relationship between the octahedral shear stress τ_{oct} and the effective mean normal stress $\sigma_{m,2}$ as follows:

$$\tau_{oct} = a + b\sigma_{m,2} \tag{5.2}$$

where $\tau_{oct} = \frac{1}{3}\sqrt{(\sigma_1 - \sigma_3)^2 + (\sigma_1 - \sigma_2)^2 + (\sigma_2 - \sigma_3)^2}$, and $\sigma_{m,2} = \frac{\sigma_1 + \sigma_3}{2}$. Here, a represents the intercept of the fitted Mogi-Coulomb line, and b is the slope of the line.

Substituting the experimental data into Equation (5.2), the mechanical parameters for the natural and saturated samples are obtained, as illustrated in Fig. 5.9.

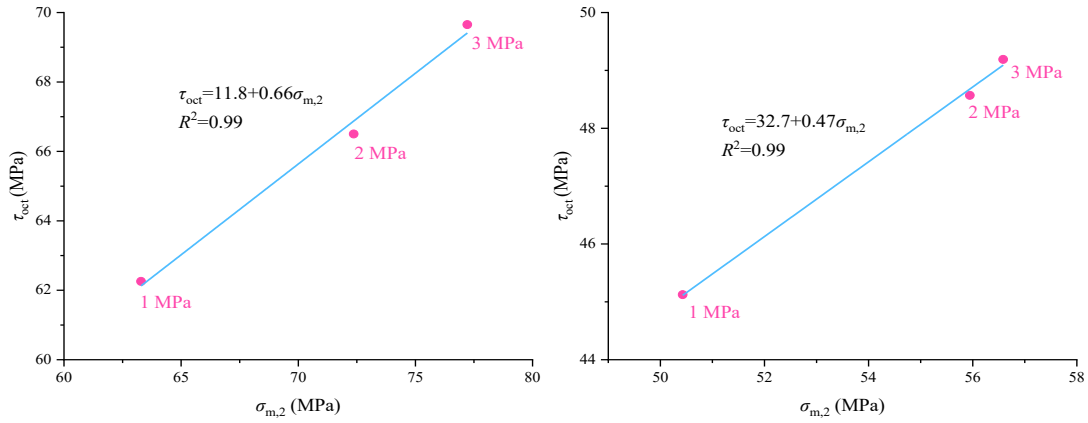

(a) (b)

Fig. 5.9 Mohr-Coulomb mechanical parameters of natural and water-saturated samples. (a) Group A. (b) Group B.

From Figure 5.9, it can be seen that the mechanical parameters $\{\tau_{oct}, \sigma_{m,2}\}$ for both natural and saturated samples exhibit a roughly linear correlation. A linear regression analysis of these parameters yields a correlation coefficient (R^2) of 0.99, indicating that the samples used in this study conform to the Mogi-Coulomb criterion. The resulting criterion equations are as follows:

$$\begin{cases} \tau_{oct} = 11.8 + 0.66\sigma_{m,2}\ (Group\ A) \\ \tau_{oct} = 32.7 + 0.47\sigma_{m,2}\ (Group\ B) \end{cases} \tag{5.3}$$

The relationship between the Mogi-Coulomb parameters (a, b) and the Mohr-Coulomb criterion parameters (c,φ) is given by:

$$\begin{cases} \mathrm{a} = \frac{2\sqrt{2}}{3} c\ cos\varphi \\ \mathrm{b} = \frac{2\sqrt{3}}{3} sin\varphi \end{cases} \tag{5.4}$$

From Equations (5.4) and (5.3), the Mohr-Coulomb model strength parameters for the natural and saturated samples are determined as follows:

$$\begin{cases} c = 15.3MPa, \varphi = 34.9°\ (Group\ A) \\ c = 31.0MPa, \varphi = 24.0°\ (Group\ B) \end{cases} \tag{5.5}$$

3.3.2.4 Effect of saturation on sample failure characteristics

The evolution characteristics of rock fractures are crucial for analyzing the mechanisms of rock failure. To investigate the impact of saturation on the failure characteristics of the samples, CT scans were performed on samples subjected to a water pressure of 1 MPa. Both natural and saturated samples were scanned, and slices were extracted from the surface and interior of the samples for three-dimensional reconstruction, as shown in Table 5.3.

Table 5.3 CT scans and reconstructed images of natural and saturated specimens

Group A: P = 1 MPa	Group B: P = 1 MPa

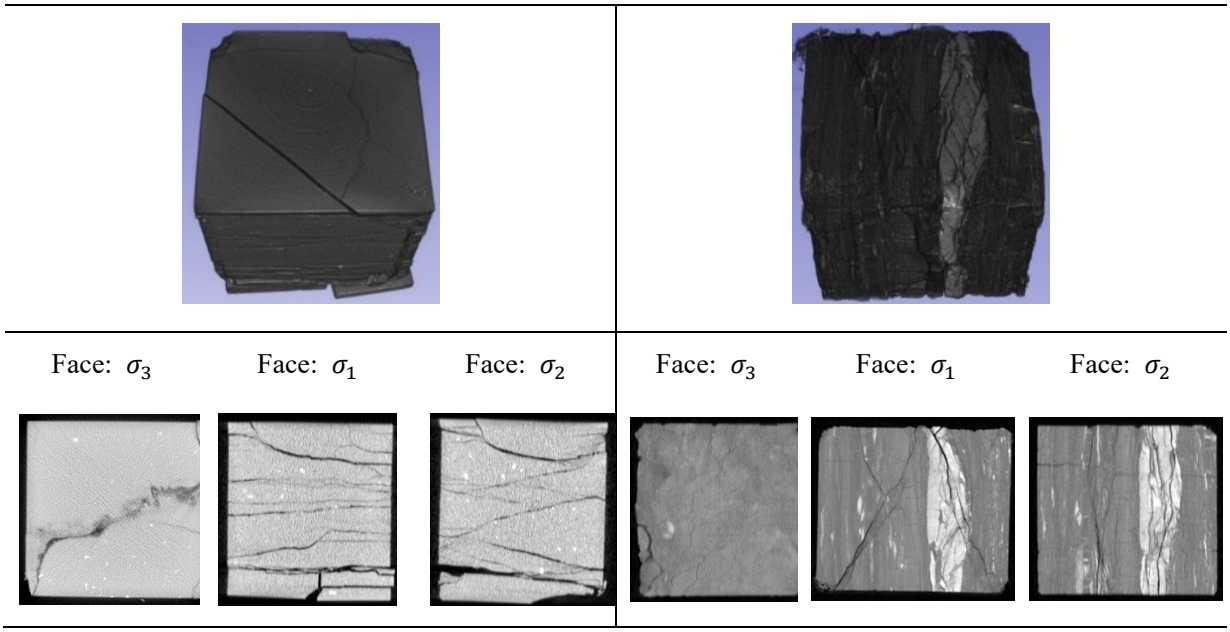

From Table 5.3, it can be observed that the length of the slices in theσ_1 direction is the greatest, while the length in the σ_3 direction is the smallest. This indicates that the loading failure process of the samples involves compression in the σ_1 direction and expansion in the σ_3 direction. The failure process of the rock includes the propagation and through-going of existing cracks and the initiation and development of new cracks.

In this experiment, the differences in crack morphology are primarily influenced by saturation and the upper water pressure. The failure characteristics of natural samples are more pronounced, displaying distinct vertical and inclined cracks in the σ_1 and σ_2 directions, along with a crack that extends diagonally in the σ_3 direction, indicating conventional shear and tensile failure. Conversely, the failure characteristics of the saturated samples are relatively less apparent; the density of vertical and inclined cracks in the σ_1 and σ_2 directional cross-sections is significantly lower than in the natural samples, and there are no distinct fracture zones observed in the σ_3 direction.

This phenomenon aligns with the previous analytical results, suggesting that saturation leads to a deterioration of the mechanical properties of the samples, promoting a transition from brittle to plastic behavior. The failure mode of the samples also shifts from sudden fracture upon reaching peak strength to a more continuous failure process during loading, which corresponds to the change in the volume strain-time curve from smooth to fluctuating.

Consequently, the flow rate curve for the natural samples appears smooth, characterized by a decrease in flow velocity before failure and an increase after failure. In contrast, the flow rate curve for the saturated samples fluctuates continuously throughout the test, indicating a more complex interaction between water flow and the evolving fracture network within the samples. This continuous fluctuation suggests that the saturation not only affects the integrity of the rock but also alters how fluid dynamics interact with structural changes, further complicating the failure mechanisms observed.

5.1.3 Relationship between water flux at the sample top and permeability points during loading

5.1.3.1 Calculation of water flux on the sample surface

Fig. 5.10 illustrates the variation trend of the total water flow V above the sample with respect to time during the loading process. To further understand the flow mechanism of water within the sample, the changes in water flux on the sample surface can be calculated. A schematic diagram for calculating the water flux on this surface is shown in Figure 5.8.

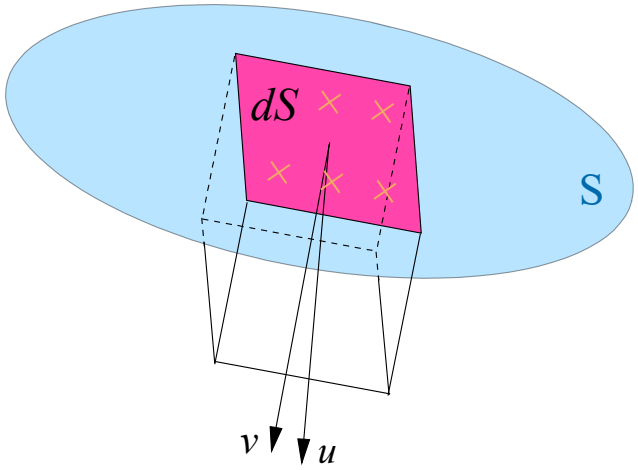

Fig. 5.10 Concept of water flux at the top of the sample

Taking Fig. 5.10 as an example, the flux of water flowing through a closed surface is given by:

$$\varphi = \oiint_S v(x,y,z)\,dS = \iint_S v_x(x,y,z)dydz + v_y(x,y,z)dxdz + v_z(x,y,z)dxdy \quad (5.6)$$

In this experiment, the direction of water flow is constant, but the magnitude of the water flow velocity varies with time. Let the z direction be the direction of seepage, which is also the direction of the maximum principal stress. Therefore,

$$v_x(x,y,z)dydz = v_y(x,y,z)dxdz = 0 \quad (5.7)$$

Thus,

$$\varphi = \iint_S \ v_z(x,y,z)dxdy \quad (5.8)$$

where

$$v_z(x,y,z) = v(t)|_{t=t_0} \quad (5.9)$$

In Equation (5.9), $v(t)$ is the flow velocity of water passing through the upper surface of the sample during loading, which is the derivative of the water flow V(t):

$$v(t) = \frac{dV(t)}{dt} \quad (5.10)$$

To calculate the surface integral in Equation (5.6), we need to know the expression for dS. In a true triaxial test, the area of the sample in the direction of the maximum principal stress is

influenced by the deformations in the directions of the intermediate and minimum principal stresses, as shown in Fig. 5.11.

According to Figure 5.11, the formula for the change in the top surface area of the sample during loading is:

$$S = d^2[1 + \varepsilon_2(t)][1 + \varepsilon_3(t)]|_{t=t_0} \tag{5.11}$$

where d is the initial edge length of the sample, and t is the loading duration.

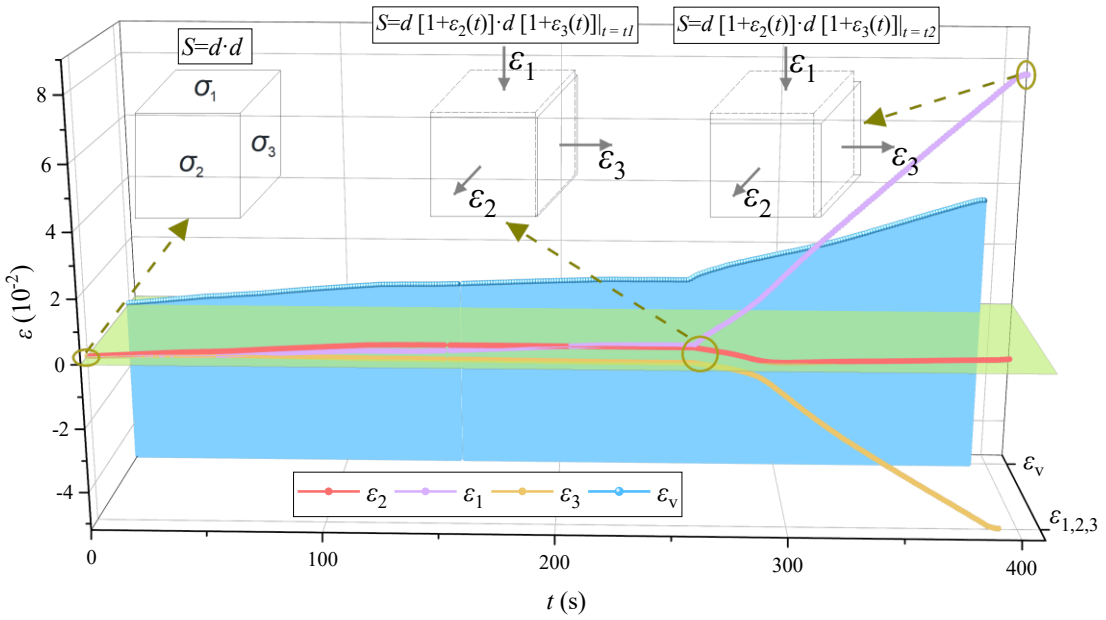

Fig. 5.11 Change diagram of dS under true triaxial loading

By combining Equations (3.35) to (3.38), the changes in water flux at the upper surface of the sample during the triaxial loading and unloading process can be determined. This allows for the plotting of the water flux-time curves for both natural and saturated samples, as shown in Figure 5.12.

As illustrated in Figure 5.12, the water flow velocity of the sample is relatively high during the initial compaction and failure stages, with average flow velocities of 0.0019 L/s and 0.0020 L/s, respectively. These velocities are 58.3% to 66.7% higher than the average flow velocity during the experimental process (0.0012 L/s). This is attributed to the presence of numerous primary cracks within the sample during the initial loading stage, which allow a significant amount of water molecules to penetrate from the upper surface of the sample as the water pressure increases.

Subsequently, as the triaxial pressure rises, the primary cracks within the sample gradually compress, leading to an elastic stage (the linear evolution of cracks). During this phase, as the sample compacts, the water flow velocity gradually decreases until it approaches zero (for example, at t=300 s in Figure 5.12(a) and at t=400 s in Figure 5.12(b)).

In the later part of the elastic stage, as the maximum principal stress continues to be applied while the minimum principal stress is continuously released, the maximum shear stress within

the sample gradually reaches the yield condition (the elastic limit). The sample begins to enter the yield stage (the nonlinear crack propagation phase), where the existing cracks cannot propagate further, and new cracks continuously emerge. As the difference between the maximum and minimum principal stresses increases, the cracks within the sample gradually link up and misalign, leading to sample failure and the formation of seepage pathways, which results in a rapid increase in water flow velocity within the sample.

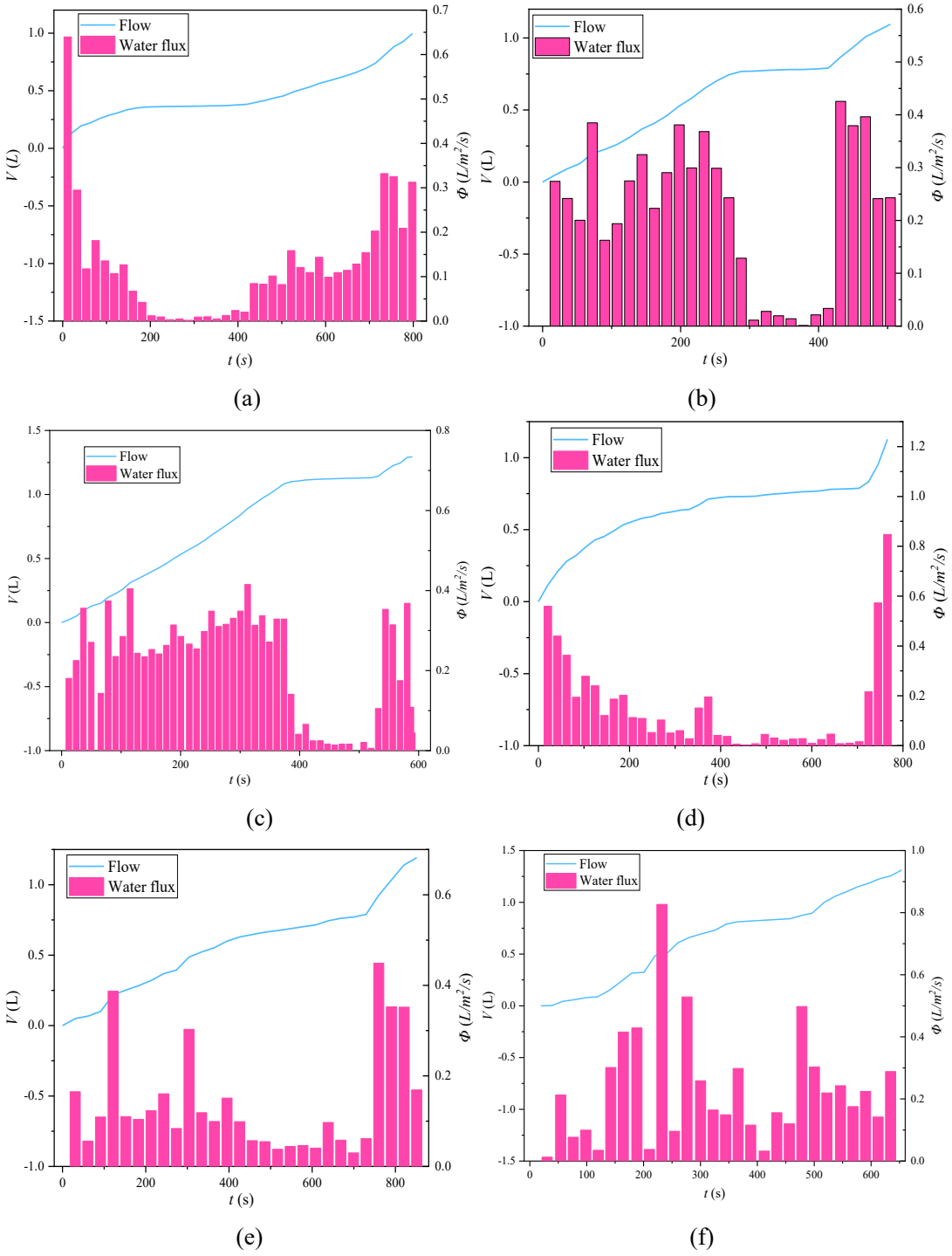

Fig. 5.12 Flux-time curves of natural and saturated samples. (a) Group A; Water pressure :1 MPa. (b) Group A; Water pressure :2 MPa. (c) Group A; Water pressure :3 MPa. (d) Group B; Water pressure :1 MPa. (e) Group B; Water pressure :2 MPa. (f) Group B; Water pressure :3 MPa.

5.1.3.2 Yield conditions of the sample and seepage points

In the stress-strain curve of the sample, the yield condition represents the limit of the elastic stage and serves as the boundary between linear and nonlinear crack propagation. Calculating the yield conditions of samples under natural and saturated conditions is significant for further analyzing the mechanical properties and the evolution of permeability rates.

Academician Zheng Yingren proposed a three-dimensional energy yield condition based on the traditional three-dimensional Mohr stress circle [148]:

$$psin\varphi + \frac{q}{3}\left(\sqrt{3}cos\theta_\sigma - sin\theta_\sigma sin\varphi\right) = c \cdot cos\varphi \tag{5.12}$$

where p, q, and $\theta_\sigma$represent the stress state of the sample during triaxial loading and unloading:

$$\begin{cases} p = \frac{\sigma_1+\sigma_2+\sigma_3}{3} \\ q = \frac{\sqrt{(\sigma_1-\sigma_2)^2+(\sigma_1-\sigma_3)^2+(\sigma_2-\sigma_3)^2}}{\sqrt{2}} \\ \theta_\sigma = \arctan\left[\frac{2\sigma_2-\sigma_1-\sigma_3}{\sqrt{3}(\sigma_1-\sigma_3)}\right] \end{cases} \tag{5.13}$$

During the loading process, the internal stress state of the sample can be expressed as a function $y = f(p, q, \theta_\sigma)$:

$$y = f(p, q, \theta_\sigma) = psin\varphi + \frac{q}{3}\left(\sqrt{3}cos\theta_\sigma - sin\theta_\sigma sin\varphi\right) \tag{5.14}$$

At the point of yield:

$$\begin{cases} y_n|_{Yield} = f_n(p, q, \theta_\sigma)|_{Yield} = c \cdot cos\varphi = 12.52 \\ y_w|_{Yield} = f_w(p, q, \theta_\sigma)|_{Yield} = c \cdot cos\varphi = 28.32 \end{cases} \tag{5.15}$$

where y_n and $f_n(p, q, \theta_\sigma)$ denote the yield conditions of the natural sample, while y_w and $f_w(p, q, \theta_\sigma)$ represent those of the saturated sample. Based on Equation (3.42), the variations of the yield conditions of natural and saturated samples under different water pressures over time can be calculated, leading to the construction of three-dimensional graphs, as shown in Figure 5.13. In Figure 5.13, the three dotted lines represent the relationships between the yield conditions $f\{y, p, q\}$ and p, q under three different water pressures. The blue planes represent the horizontal cross-sections at y=12.52， 28.32. The intersection points of the curve $y = f(p, q, \theta_\sigma)$ with these sections indicate the yield conditions of the samples. Once the curve crosses these planes, the sample enters the yield stage.

In Figure 5.13, the horizontal axis ppp represents the average of the three principal stresses, while the vertical axis qqq is a multiple of the octahedral shear stress τ_{oct} (where $q = \frac{3\sqrt{2}}{2}\tau_{\mathrm{oct}}$). As observed in Figure 5.13(a), water pressure significantly affects the yield conditions of the natural sample. When the water pressure increases from 1 MPa to 2 MPa, the values of

p and *q* for the natural sample increase by 0.8% and 12.8%, respectively, indicating that higher water pressure results in greater shear stress at which the sample enters the yield state. However, there is no obvious linear relationship between the average of the three principal stresses *p* and the water pressure.

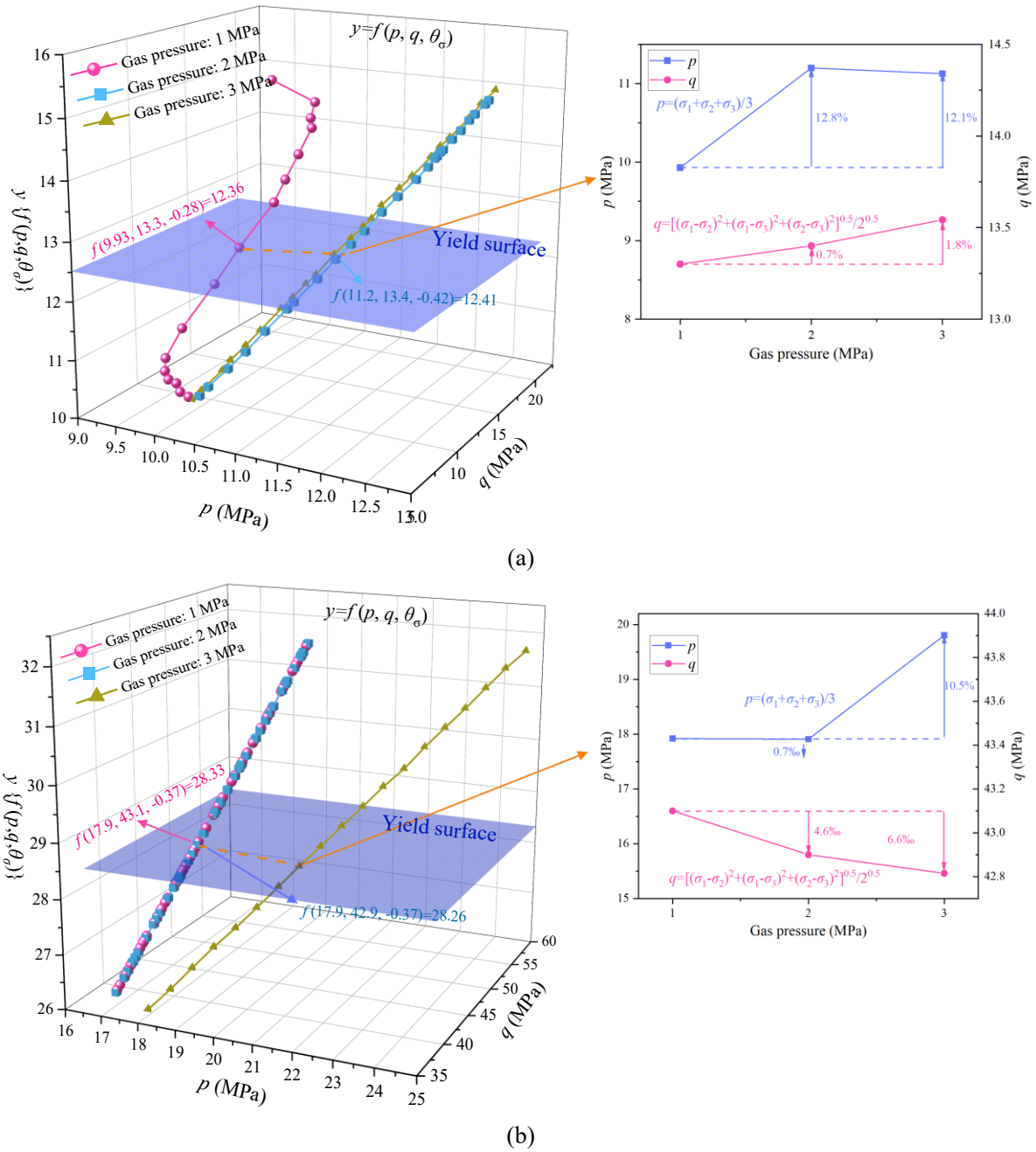

Fig. 5.13 Yield conditions of natural and saturated samples under different water pressure conditions. (a) Natural samples. (b) Water saturated samples.

From Figure 5.13(b), it can be seen that the impact of water pressure on the yield conditions of the saturated samples is minimal. As the water pressure varies, the difference in shear stress required for the saturated samples to reach yield conditions is less than 1%. The

trend of the yield function $y = f(p, q, \theta_\sigma)$ is also similar, indicating that the influence of water pressure on the yield state of the saturated samples is limited.

This is because the natural samples contain numerous natural joints and pores. During the early stages of loading, the high water pressure facilitates the rapid influx of water molecules into the sample, thereby affecting its mechanical properties. However, after being fully saturated for 48 hours, the internal fractures of the saturated samples become filled with water molecules, limiting the ability of the upper water pressure to drive additional water into the sample. At this point, changes in water pressure have a significantly reduced effect on the internal state of the sample's fractures, effectively only altering the pre-stress applied to the upper part of the sample. As shown in Figure 5.7, the peak internal shear stress of the saturated sample during failure is around 70 MPa, which is much higher than the applied water pressure (1-3 MPa). Therefore, the impact of changing water pressure on the mechanical properties of saturated samples is minimal.

To further analyze the variation patterns of water flow and yield conditions in natural and saturated samples, a comparison chart of yield conditions and water flow for natural and saturated samples is drawn by combining the water flow from Figure 5.12 with the yield condition calculations from Figure 5.13. This is illustrated at a water pressure of 1 MPa, as shown in Figure 5.14.

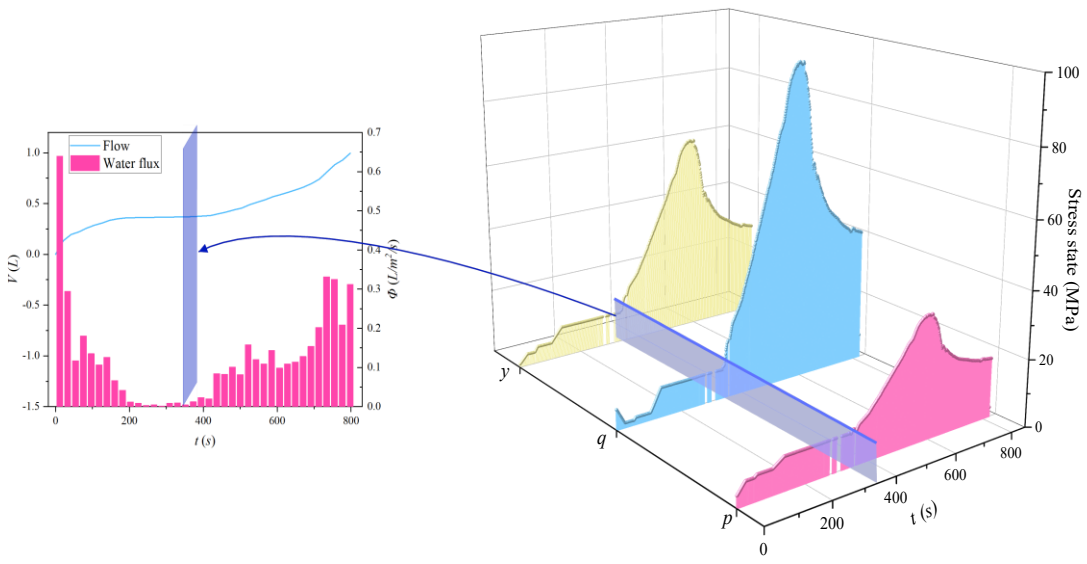

(a)

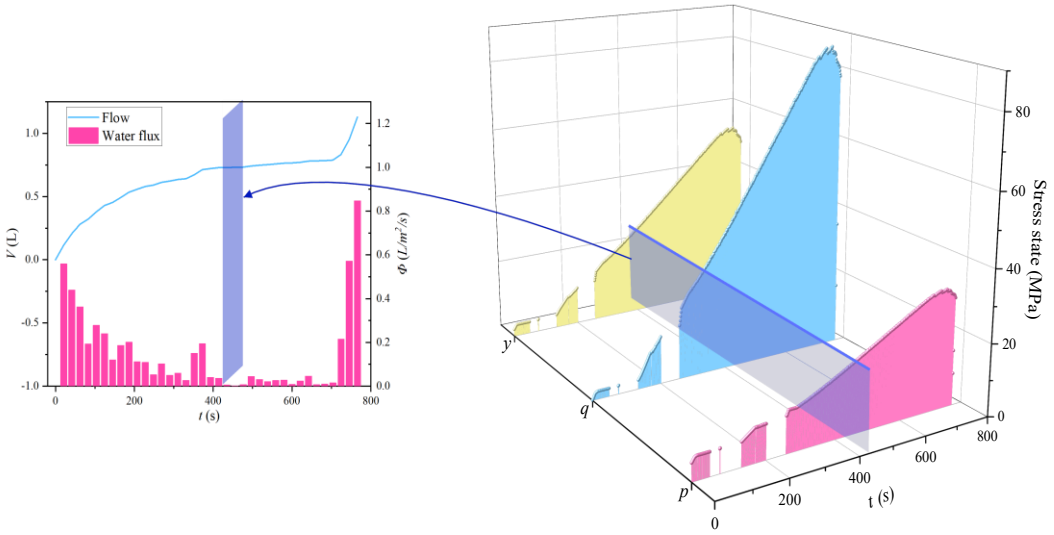

(b)

Fig. 5.14 The relationship between yield conditions and water flux. (a) Natural samples. (b) Water saturated samples.

As depicted in Figure 5.14(a), the yield condition of the natural sample serves as a relatively distinct boundary. Before reaching the yield condition, the stress state function $[y = f(p, q, \theta_\sigma)]$ of the natural sample changes little. However, once the yield limit is exceeded, the stress state function of the sample begins to increase rapidly. Moreover, before reaching the yield condition, the water flow above the sample drops almost to zero after passing through the compaction and elastic stages. Once the yield condition is achieved, the water flow at the upper part of the sample starts to rise sharply due to the nonlinear extension of cracks (increasing from 0.0018 L/m²/s to 0.101 L/m²/s), and the total water flow also experiences a rapid increase (from 0.36 L to 0.44 L). Given the significant differences in the internal stress state and water flow before and after reaching the yield condition, the yield condition in the true triaxial loading-unloading test can be referred to as the seepage point of the natural sample.

Additionally, as shown in Figure 5.14(b), the stress state of the saturated sample at the yield point does not exhibit significant changes, and there is no notable increase in water flow or total water flow after yielding. This indicates that saturation alters the mechanical properties of the sample, resulting in enhanced plasticity and causing the boundary between the elastic and yield stages to become less distinct. Furthermore, as illustrated in Figure 5.8(d), the volume strain-time curve of the saturated sample shows multiple fluctuations and "steps" during loading, with the sample's volume repeatedly changing between expansion and compression. The increase in water flow above the sample also lags behind the yield condition, leading to an increase in total water flow above the sample occurring after failure rather than after yielding.

5.2 Damage and seepage evolution of water-saturated shale under water pressure and cyclic stress disturbance

5.2.1 Experimental method

The cubic samples were divided into four groups: A, B, C, and D. Group A consisted of natural samples, while Groups B, C, and D included samples saturated for 12, 24, and 36 hours, respectively. The treated samples underwent true triaxial loading and fatigue loading tests, conducted as follows:

1) Initially, the three principal stresses of the sample were loaded to the original rock stress state at a rate of 0.5 kN/s. Subsequently, the three principal stresses were held constant while water pressure was applied in the σ_1 direction. After the water pressure was applied, σ_2 remained unchanged, and σ_1 was loaded at a rate of 0.002 mm/s while σ_3 was unloaded at a rate of 0.5 kN/s until the sample failed. The peak strengths of the four groups of samples were recorded, and the corresponding shear stress values were calculated, as shown in Table 5.4. In Table 5.4, P represents the water pressure; T indicates the saturation duration; and τ_{oct} denotes the peak value of the octahedral shear stress during the loading process, calculated as $\tau_{oct} = \frac{1}{3}\sqrt{(\sigma_1-\sigma_2)^2+(\sigma_1-\sigma_3)^2+(\sigma_2-\sigma_3)^2}$。

Table 5.4 Peak shear stress of three groups samples before fatigue loading (MPa)

Water pressure	Group A (T=0 h)	Group B (T=12 h)	Group C (T=24 h)	Group D (T=36 h)
P=1 MPa	41.5	51.2	59.0	52.5
P=2 MPa	46.1	55.1	56.3	55.9
P=3 MPa	45.5	56.1	60.1	59.2

2) Each group of samples underwent fatigue loading tests. First, the three principal stresses of the samples were loaded to the original rock stress state, after which fatigue loading was applied in the σ_1 direction of the samples. The fatigue stress range was set at $0.1\sigma_c$ to $-0.9\sigma_c$ (where σ_c is the maximum value of σ_1 at failure), with a loading rate of $1.6\sigma_c$/s, a loading frequency of 1 Hz, and a loading waveform of a sine wave, repeated for 200 cycles. During the loading process, the fatigue characteristics of the samples were observed. The stress path for fatigue loading and the direction of seepage are illustrated in Figure 5.15.

3) Following the fatigue loading, the samples underwent true triaxial loading-unloading tests. The loading scheme and steps were consistent with those in Step 1, allowing for the assessment of the mechanical properties of the samples after fatigue loading.

A technical flowchart summarizing the experimental procedures is illustrated in Figure 5.16.

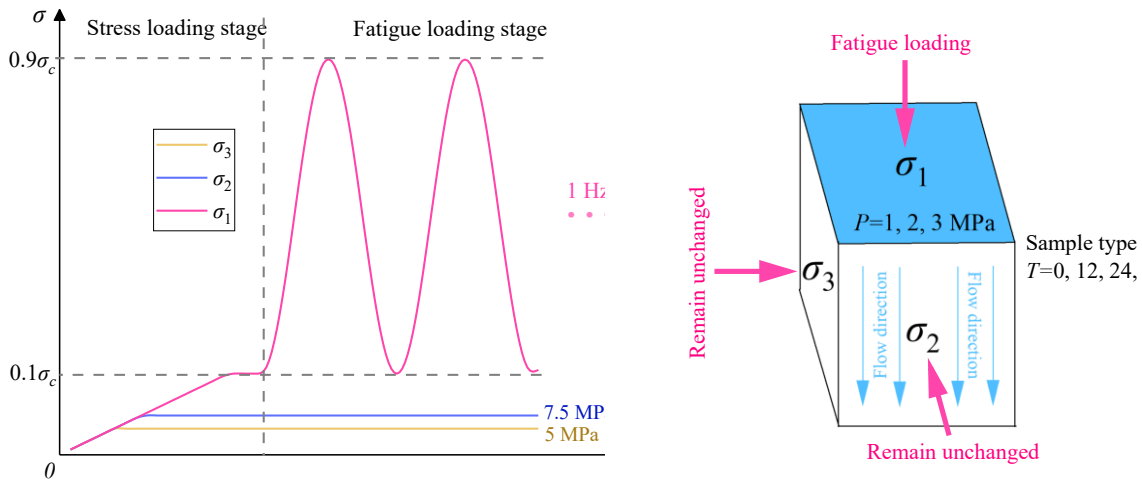

(a) (b)

Fig 5.15 True triaxial fatigue loading stress path of samples under different water saturation duration and water pressure. (a) Stress path (b) seepage direction.

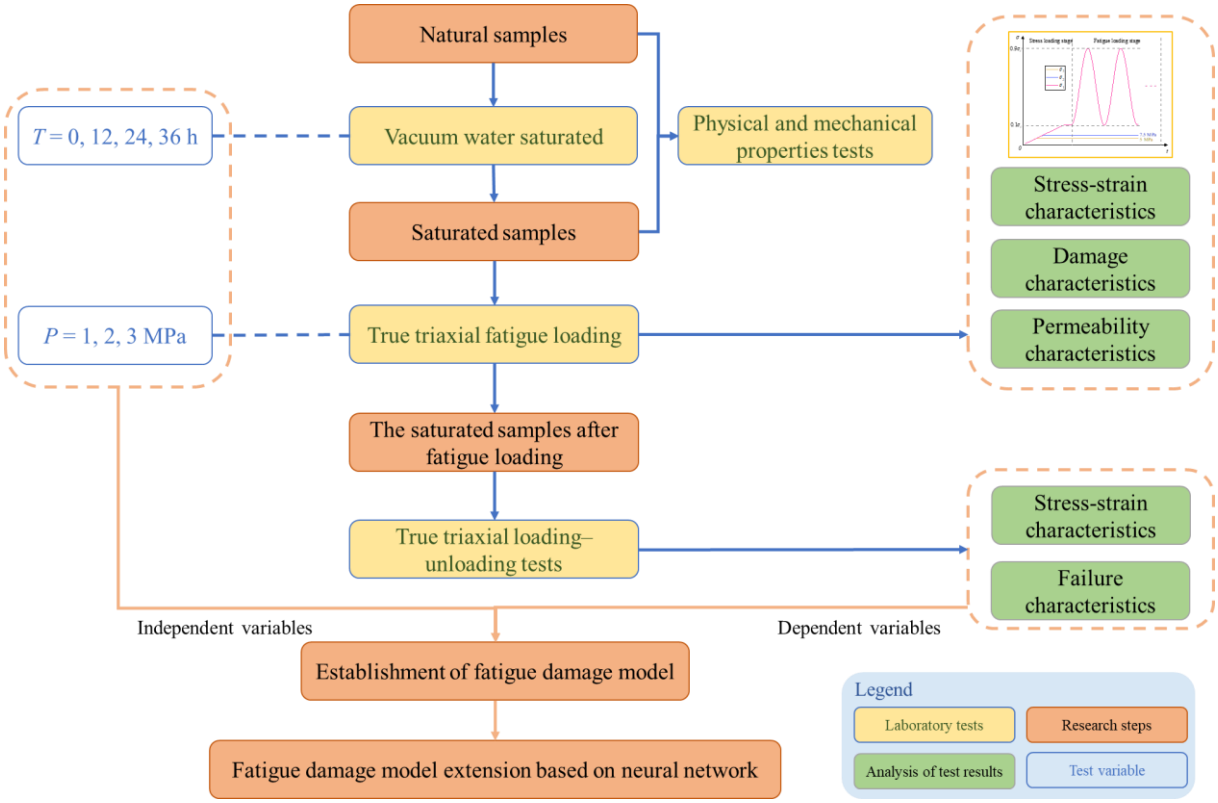

Fig. 5.16 Technical roadmap of deterioration of mechanical properties and seepage mechanism of samples under the coupling of saturated water, water pressure, and fatigue stress

5.2.2 Experimental results and analysis

5.2.2.1 Stress-strain characteristics of samples under true triaxial fatigue load

Tables 5.5 and 5.6 present the stress-strain curves for each group of samples under true triaxial fatigue loading. The first aspect to analyze is the effect of saturation duration on the fatigue characteristics of the samples. As the saturation duration increases, the rightward shift of the

hysteresis loop in the stress-strain curve during fatigue loading gradually increases. Taking the samples with a water pressure of 1 MPa as an example, the maximum rightward shift of the stress-strain hysteresis loop in the direction of maximum principal stress increased from 0.0029 to 0.026 as the saturation duration increased from 0 hours to 36 hours. This indicates that saturation significantly affects the deformation characteristics of the samples. With longer saturation times, the fatigue deformation of the samples under true triaxial stress significantly increases.

Water pressure also has a substantial impact on the shift of the fatigue loading stress-strain hysteresis loop. As the water pressure increases, the total movement of the hysteresis loop to the right gradually increases. Using the fatigue loading curve of natural samples as an example, when the water pressure is 1 MPa, the strain rate of the samples during the initial stage of fatigue loading increases significantly, with a high growth rate of ε_1. As the water pressure increases, the proportion of the rightward shift of the hysteresis loop during the initial stage of fatigue loading relative to the total shift of the sample gradually decreases. At the same time, the proportion of the changes in the three-dimensional strains of the samples also varies with the increase in water pressure. When the water pressure increases from 1 MPa to 3 MPa, the ratio of the maximum ε_3 to the maximum ε_1 increases from 57.0% to 85.7%, while the ratio of the maximum ε_2 to the maximum ε_1 decreases from 3.36% to 2.68%. This indicates that with changes in water pressure, the deformation characteristics of the samples during the fatigue loading process undergo significant changes, shifting from "compression in the ε_1 direction and expansion in the ε_2 direction" to "compression in the ε_1 direction, reduction in ε_2, and accelerated expansion in the ε_3 direction." The water pressure in the σ_1 direction can reduce the influence of σ_2 on the fatigue deformation characteristics of the samples. This may be because the water pressure in the σ_1 direction increases the effective stress at the top of the sample, thereby increasing the value of the $\{\sigma_1\text{-}\sigma_3\}$ term in the distribution of internal shear stress in the sample, which reduces the influence of the intermediate principal stress.

Taking natural samples as an example, the peak strains of each hysteresis loop during the fatigue loading process were statistically analyzed, allowing the fatigue loading process to be divided into two stages: the initial strain growth stage and the stable strain growth stage, as shown in Figure 5.17.

Table 5.5 The stress-strain curve of sample under true triaxial fatigue stress subject to different water saturation duration and water pressure (T=0, 12 h)

	T=0 h	T=12 h
P=1 MPa	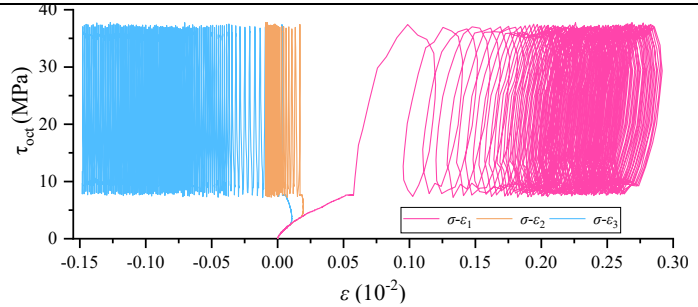	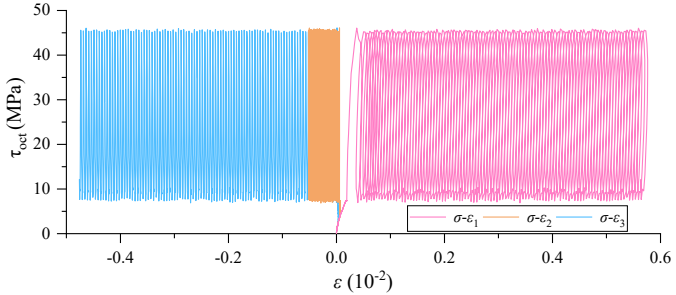
P=2 MPa	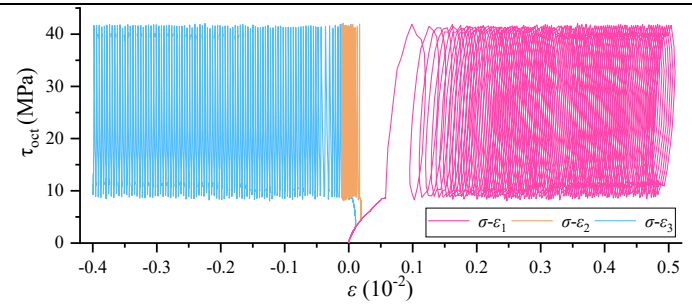	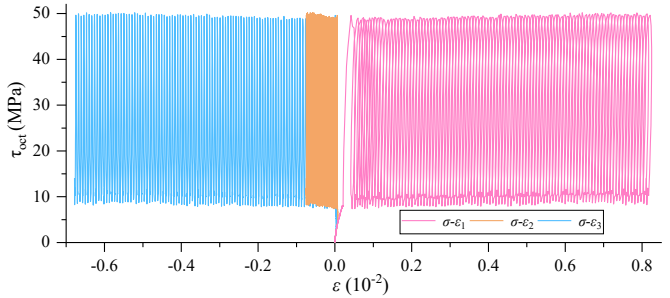
P=3 MPa	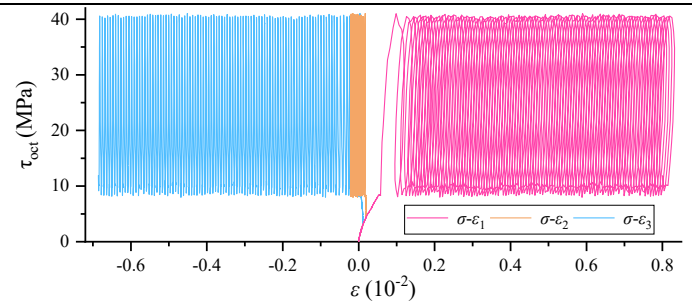	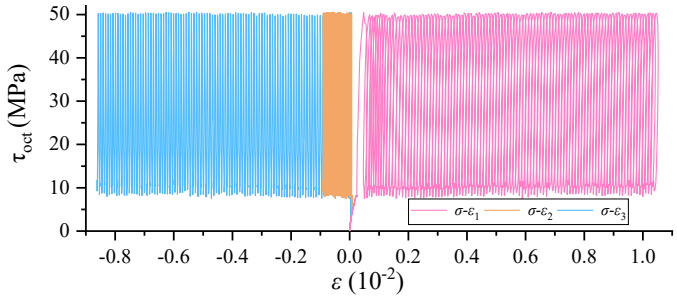

Table 5.6 The stress-strain curve of sample under true triaxial fatigue stress subject to different water saturation duration and water pressure (T=24, 36 h)

	T=24 h	T=36 h
P=1 MPa	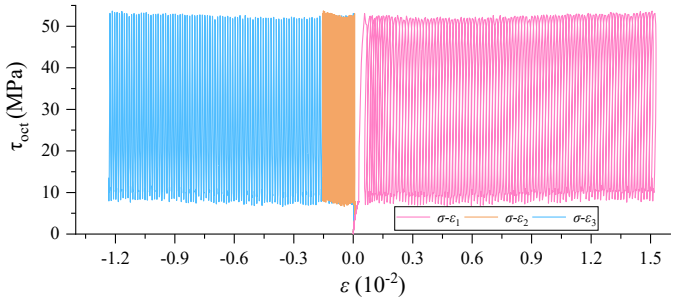	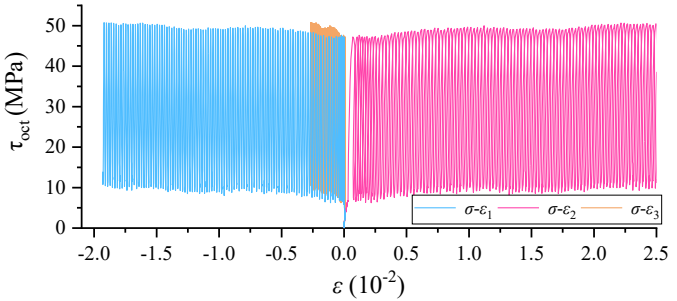
P=2 MPa	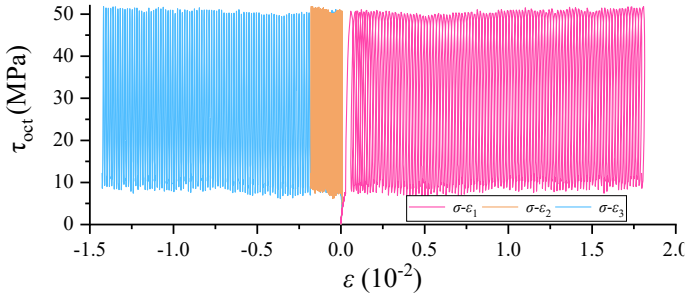	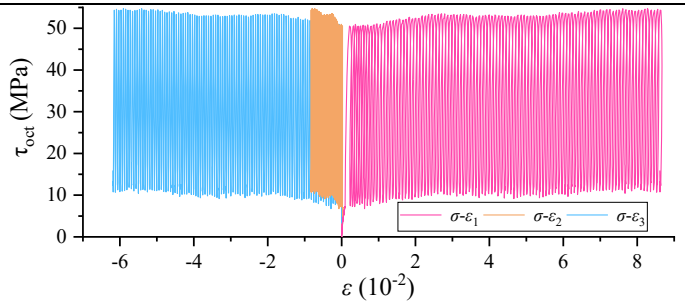
P=3 MPa	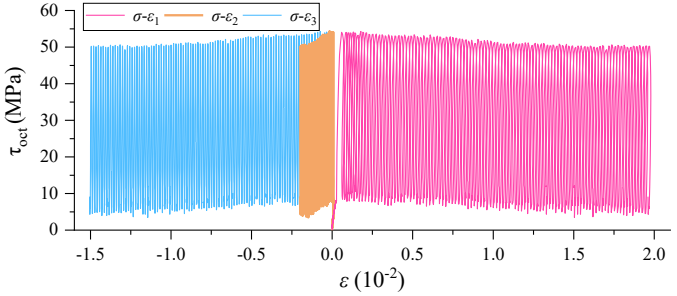	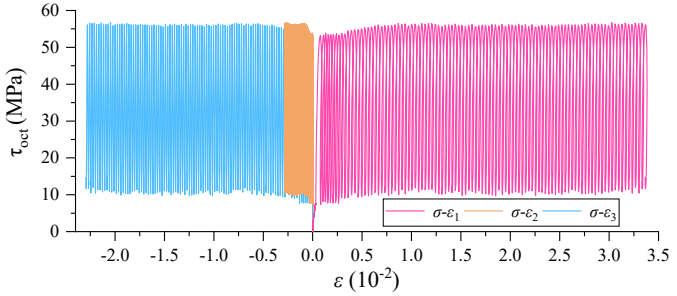

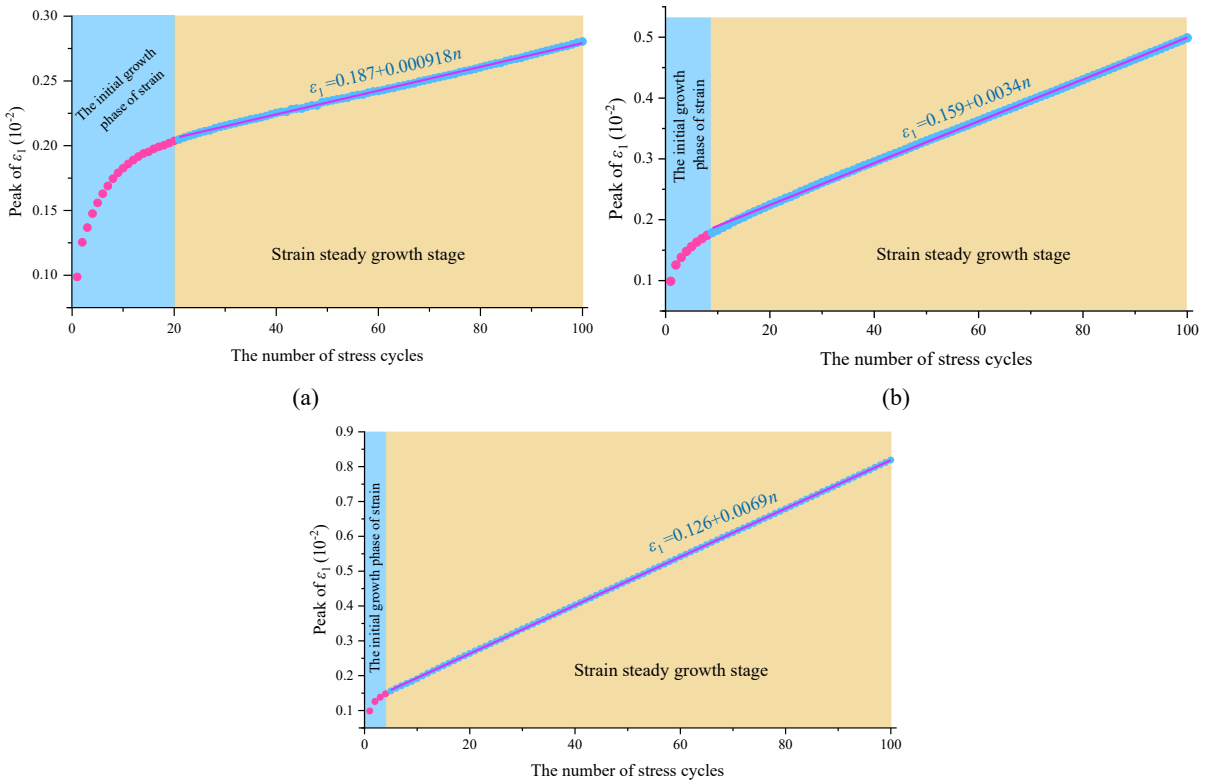

Fig. 5.17 Curve of hysteretic ring strain peak and fatigue cycle number under true triaxial condition. (a) P=1 MPa. (b) P=2 MPa. (c) P= 3 MPa.

From Figure 5.17, it can be observed that in the initial strain growth stage, the loading mode in the σ_1 direction transitions suddenly from relatively slow displacement loading to relatively fast stress loading, with the upper limit of the cyclic stress exceeding the elastic limit of the sample. This causes the sample to rapidly transition from the elastic stage to the yield stage. The cyclic stress forces the sample to alternate between the elastic and yield stages, further developing internal cracks, leading to rapid increases in plastic deformation and total strain of the sample.

After a certain period of fatigue loading, the rate of increase in sample strain gradually decreases, entering the stable strain growth stage. This is because although the upper limit of the fatigue loading stress exceeds the elastic limit, it remains below the peak strength of the sample. Consequently, while the sample experiences significant plastic strain due to sudden yielding in the initial stage of fatigue, the growth rate of axial strain gradually decreases and stabilizes as the upper limit of the stress no longer changes.

By observing the differences in strain changes of the samples under various water pressure conditions, it can be concluded that as the water pressure increases, the initial strain growth stage of the samples gradually shortens.

First, we analyze the impact of water pressure on the initial strain growth stage. At a water pressure of P=1 MPa, the samples exhibit 20 stress-strain hysteresis loops within the initial

strain growth stage during fatigue loading. As the water pressure increases, the number of hysteresis loops in this stage decreases to 8 at P=2 MPa and further reduces to 4 at P=3 MPa.

Next, we examine the effects of water pressure on the stable strain growth stage. At P=1 MPa, the strain growth rate during the stable strain growth phase is 9.18×10^{-4} (the slope of the fitted line for strain versus fatigue cycle number). As the water pressure increases, this strain growth rate in the stable stage gradually rises to 3.4×10^{-3} at P=2 MPa and 6.9×10^{-3} at P=3 MPa.

These findings indicate that water pressure significantly alters the fatigue strain evolution characteristics of the samples. Specifically, higher water pressures facilitate a quicker transition to the strain stability growth stage, and during this stable phase, the samples exhibit a faster rate of strain increase.

5.2.2.2 Damage characteristics of samples based on acoustic emission response levels

The acoustic emission system can capture the initiation, propagation, and damage of cracks at different stages during compression by utilizing acoustic emission counts and the rapid release of energy within the rock. To investigate the damage characteristics of the samples during true triaxial fatigue loading, acoustic emission monitoring was conducted, recording the acoustic emission energy, ringing counts, and their cumulative values throughout the loading process, as shown in Figure 5.18. It can be observed from Figure 5.18 that the damage process of the samples under true triaxial fatigue stress can be divided into three stages: the initial loading stage, the early fatigue loading stage, and the late fatigue loading stage.

1) Initial Loading Stage: During this stage, the loading method is displacement-based, with stress slowly increasing from zero to the fatigue loading starting point. Most samples are in the initial compaction stage and the linear elastic stage. The slow loading rate and low stress levels cause the internal cracks to develop slowly, resulting in minimal damage to the samples, with overall low levels of acoustic emission response. The generation of some acoustic emission signals is primarily due to the closure and compaction of micropores within the samples.

2) Early Fatigue Loading Stage: In this stage, with the onset of fatigue loading, the stress in the σ_1 direction suddenly increases. The fatigue stress, capped at $0.9\sigma_c$, rapidly increases the internal shear stress and surpasses the elastic limit (yield condition), causing the samples to enter the nonlinear crack propagation phase, where the strain rate begins to increase. Additionally, since the lower limit of the fatigue loading ($0.1\sigma_c$) is below the yield condition, the loading stress continuously cycles between the elastic and yield stages, leading to a significant amount of irreversible plastic deformation during stress unloading (after unloading to the stress lower limit, ε_1 cannot recover to its level prior to loading). This results in a substantial increase in fatigue damage, which in turn causes the acoustic emission levels to rise sharply.

3) Late Fatigue Loading Stage: As the number of fatigue cycles increases, the increment in plastic strain gradually decreases and stabilizes, signaling the samples' transition into the

stable strain growth stage. In this stage, the samples experience more regular fatigue stress, and the internal crack development rate stabilizes, leading to a gradual decrease in acoustic emission response levels.

The cumulative ringing counts and energy values of the acoustic emissions during the fatigue loading of each sample are statistically analyzed, as shown in Figure 5.17. To ensure the cumulative acoustic emission parameters among the sample groups are comparable, the acoustic emission probe was placed on the spacer between the sample and the loading cap. When changing the test samples, care was taken not to touch the acoustic emission probe, thereby maintaining the contact coupling between the probe and the spacer. Additionally, the amplification factor of the amplifier and the threshold for signal acquisition were not altered, ensuring that the acoustic emission signal intensity of all test samples remained at the same collection and amplification level.

From Figure 5.19, it can be seen that the growth rate of the cumulative ringing counts and cumulative energy values is substantial during the early fatigue loading stage but slows down during the late fatigue loading stage. By utilizing cumulative acoustic emission parameters to determine the damage characteristics of the samples during fatigue loading, it is evident that as water pressure increases, both the cumulative ringing counts and cumulative energy values during the loading process show an increasing trend. For instance, in the case of the natural sample at a water pressure of 3 MPa, the cumulative ringing count is 3204, and the cumulative energy value is 5438 mV·mS, which is an increase of 14.8% (2790) and 10.1% (4940 mV·mS) compared to the values at 2 MPa, and an increase of 45.0% (2210) and 44.6% (3762 mV·mS) compared to those at 1 MPa. This indicates that water pressure significantly affects the overall damage of the samples during fatigue loading; as water pressure increases, the effective stress above the samples also gradually increases. The difference between the maximum and minimum principal stress directions also increases, leading to greater internal shear stress within the samples. Consequently, the total damage incurred during fatigue loading at the same stress level is greater, which corresponds to an increase in acoustic emission response levels.

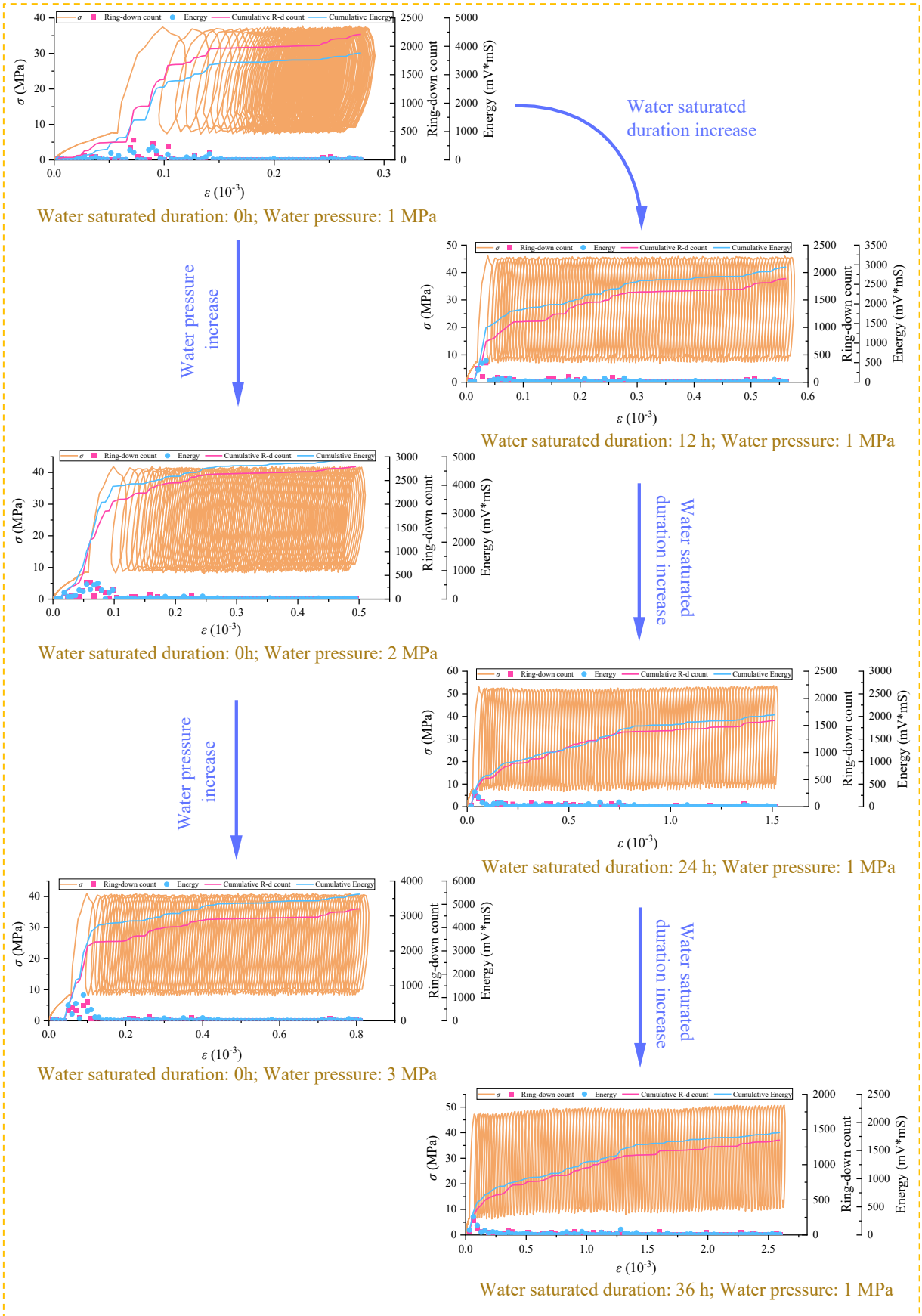

Fig. 5.18 Effects of water saturation duration and water pressure on acoustic emission characteristics of samples under true triaxial fatigue stress

The effect of saturation on the damage characteristics of the samples is contrary to that of water pressure. As the saturation time increases, the acoustic emission response levels of the samples during the loading process gradually decrease. For instance, at a water pressure of 1 MPa, when the saturation time is 36 hours, the cumulative ringing count is 1348, and the cumulative energy value is 1822 mV·mS, which represents decreases of 15.3% (from 1592) and 10.6% (from 2037), respectively, compared to the saturation time of 24 hours. When compared to the saturation time of 12 hours, the decreases are 28.7% (from 1890) and 38.1% (from 2942 mV·mS), and compared to a saturation time of 0 hours, the reductions are 39.0% (from 2210) and 51.6% (from 3762 mV·mS). This finding is consistent with the analysis results from uniaxial fatigue tests, indicating that saturation leads to the deterioration of the mechanical properties of the samples while also weakening the effect of fatigue on those properties. Higher water pressure and shorter saturation times result in greater damage due to crack development, dislocation, and penetration during fatigue loading.

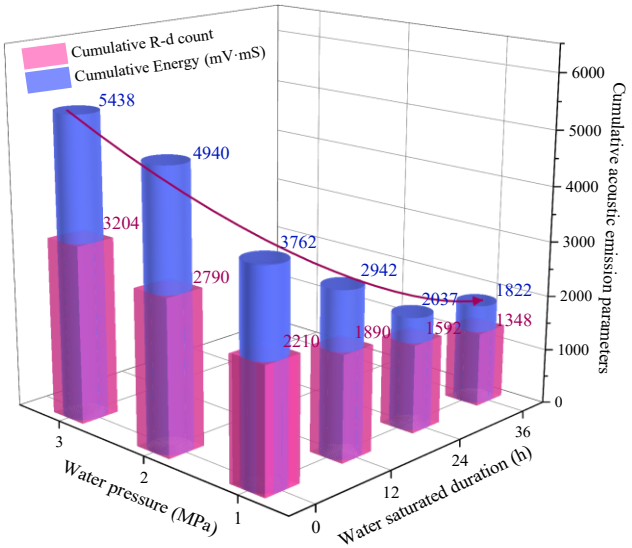

Fig .5.19 Variation of cumulative acoustic emission parameters of samples under true triaxial fatigue loading under different saturation time and water pressure

5.2.2.3 Evolution of damage variables under different saturation durations and water pressure conditions

The damage variable is a parameter that indicates the degree of deterioration of the sample, which can be intuitively understood as the percentage of microcracks or pore volume relative to the total volume of the sample. In damage mechanics, the damage variable acts as a "deterioration operator"; from a thermodynamic perspective, it reflects the irreversible changes in the structure of the sample. Therefore, calculating the variation of the damage variable D under true triaxial loading and unloading conditions is significant for exploring the damage characteristics of the sample.

The expression for the damage variable D is based on the damage evolution formula proposed by Mazars for concrete materials under compressive loading. Its expression is given by:

$$D = 1 - \frac{1}{exp(mY)+nY} \tag{5.16}$$

where m and n are material parameters determined experimentally; Y is the generalized shear strain, expressed as:

$$Y = \sqrt{\frac{2}{9}[(\varepsilon_1 - \varepsilon_2)^2 + (\varepsilon_2 - \varepsilon_3)^2 + (\varepsilon_3 - \varepsilon_1)^2]} \tag{5.17}$$

Based on the damage evolution formula, the stress-strain curves of the samples during fatigue loading are fitted to determine the material parameters as follows:

$$\begin{cases} m = 11.2 \\ n = -9.5 \end{cases} \tag{5.18}$$

By substituting equation (5.18) into equation (5.16), the damage evolution curve of the sample during fatigue loading is obtained. The damage curve derived from formula (5.16) is compared with the damage coefficient curve based on cumulative acoustic emission parameters, as shown in Figure 5.20.

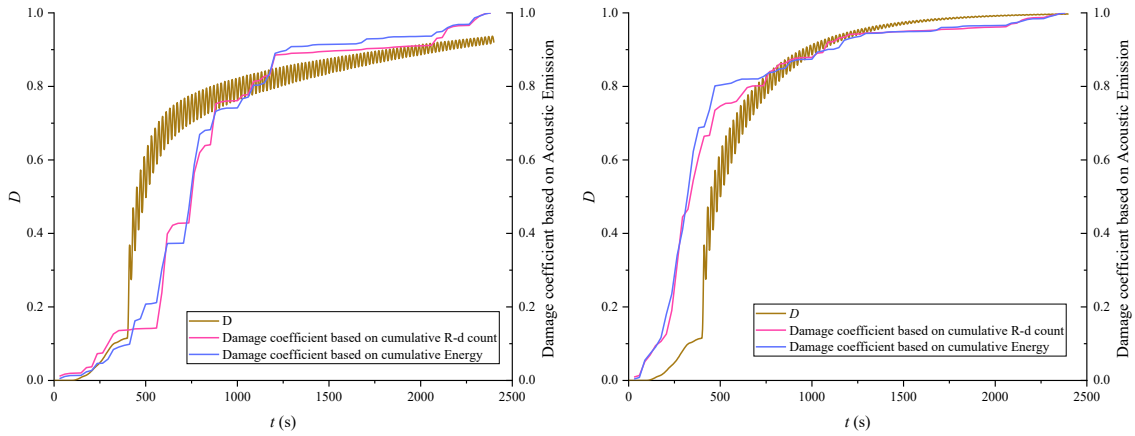

(a)

(b)

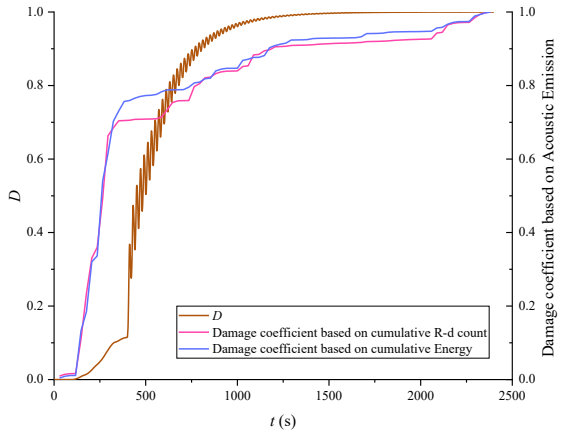

(c)

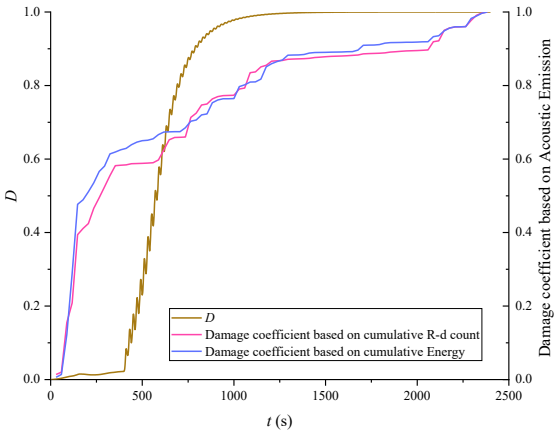

(d)

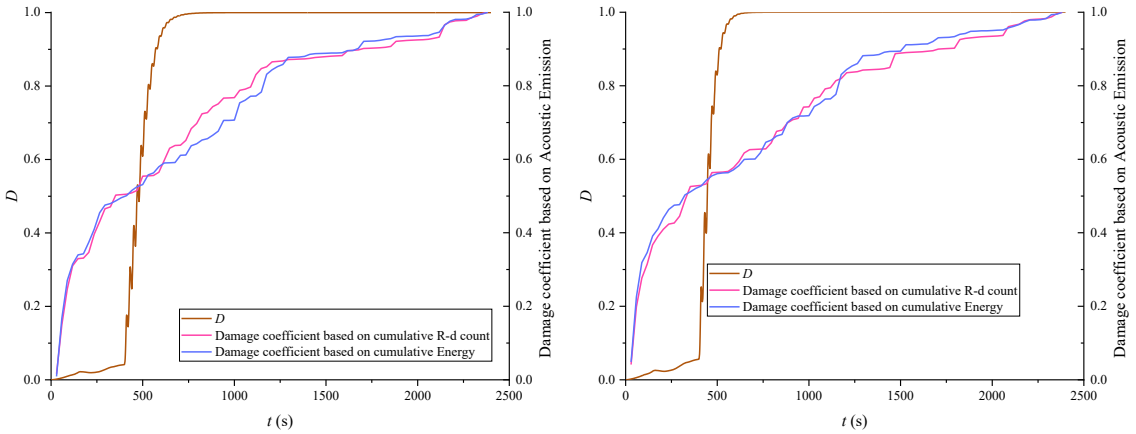

(e) (f)

Fig.5.20 Damage evolution curve of samples under true triaxial fatigue loading. (a) T=0 h; P= 1 MPa. (b) T=0 h; P= 2 MPa. (c) T=0 h; P= 3 MPa. (d) T=12 h; P= 1 MPa. (e) T=24 h; P= 1 MPa. (f) T=36 h; P= 1 MPa.

From Figure 5.20, it can be observed that the advantage of the damage variable curve based on the formula method is its ability to better reflect the damage characteristics within each fatigue loading cycle. The trend of the damage factor D is similar to that of the fatigue stress loading, effectively highlighting the changes in the sample's damage characteristics at the peak and trough of the fatigue stress. Furthermore, when the saturation duration is 0 hours (natural sample), the damage factor D curve closely resembles the trend of the damage curve based on acoustic emission parameters, indicating that the formula adequately reflects the damage evolution of the natural sample during the loading process. In contrast, the damage factor D curve of the saturated water samples shows significant divergence from the damage curve based on acoustic emission, primarily characterized by insufficient damage during the initial loading and late fatigue loading stages, which is clearly inconsistent with the experimental acoustic emission phenomena. Thus, compared to saturated samples, the damage variable curve based on the formula method is more suitable for describing the damage characteristics of natural samples during the loading process.

5.2.2.4 Permeability characteristics of samples under true triaxial fatigue loading

The permeability characteristics are crucial for analyzing the development of internal cracks in the samples. By analyzing the seepage mechanism of samples under different conditions, one can determine the degree of true triaxial fatigue damage under various water pressures or saturation durations. To investigate the permeability characteristics of samples under true triaxial fatigue conditions, the water flow through the samples during the loading process was monitored and recorded. Figure 5.21 illustrates the variation in water flow for a typical sample during fatigue loading. Due to the presence of significant moisture in the saturated samples, and to prevent the internal moisture from overflowing and affecting the test results, the water flow collected in this study was the inflow rate through the sample's inlet. Taking the sample at T=0

h and P= 1 MPa as an example, the evolution of the sample's water flow can be divided into three stages, corresponding to its acoustic emission characteristics during the fatigue loading process:

1) Initial Loading Stage: At low loading stresses, all groups of samples are in the crack closure and linear expansion stage. The water flow rate is relatively low, and the growth rate of the water flow decreases gradually with the densification of the samples. This stage corresponds to the densification and elastic phases of the samples.

2) Early Fatigue Loading Stage: As the fatigue loading begins, the stress in the σ_1 direction suddenly increases, and the larger cyclic stress causes the primary cracks within the sample to gradually develop and connect. New cracks are continuously generated, beginning nonlinear expansion, leading to a rapid increase in water flow rate and a significant rise in water flow volume.

3) Late Fatigue Loading Stage: With the prolonged fatigue loading time, the sample gradually enters the stable strain growth phase. The rate of internal crack development tends to stabilize, resulting in a gradual decrease in the rate of water flow increase, with the total water flow approaching stability.

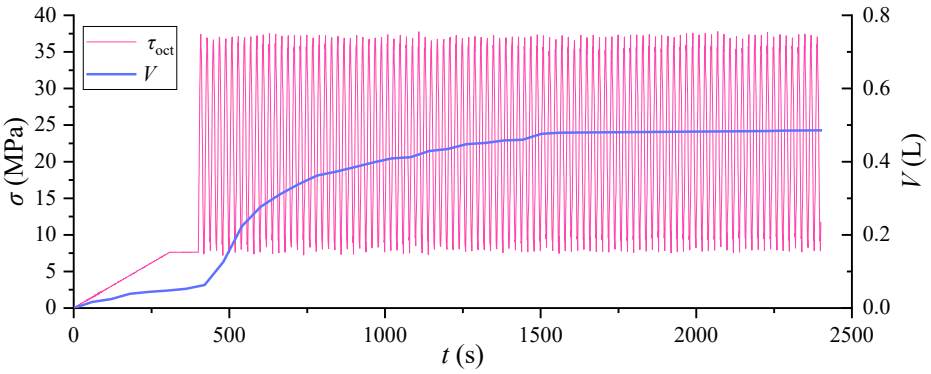

(a)

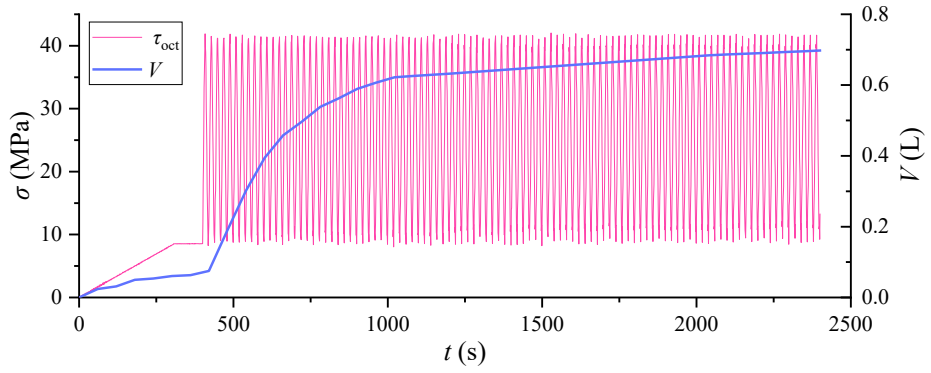

(b)

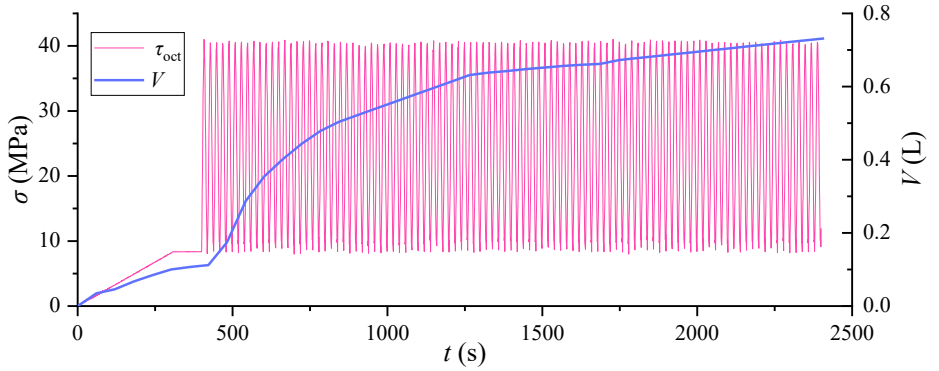

(c)

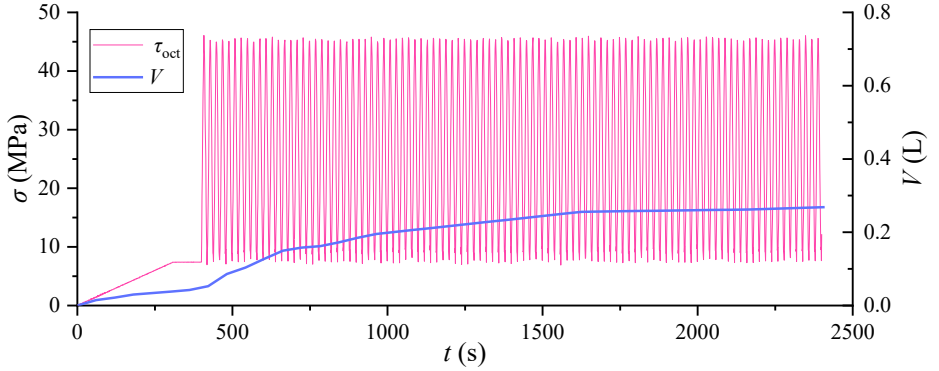

(d)

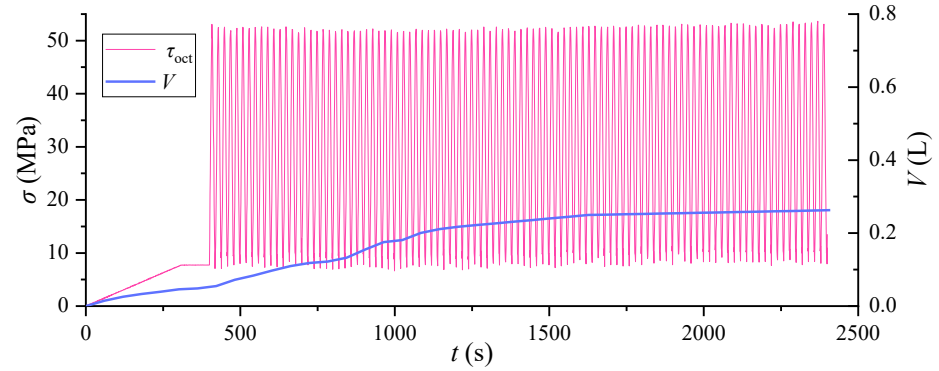

(e)

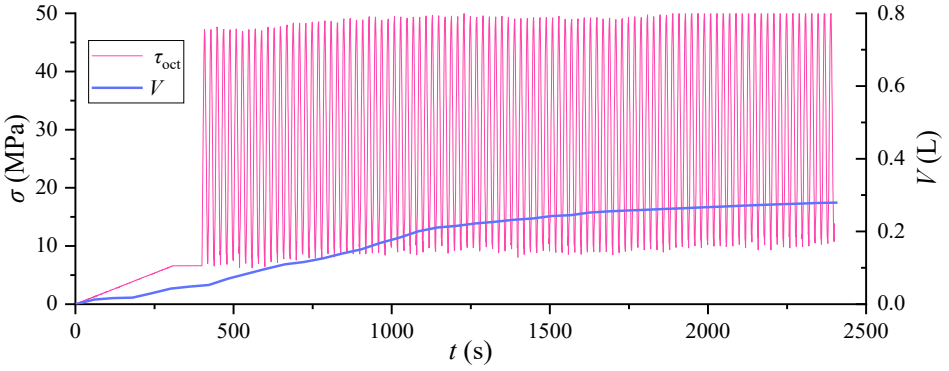

(f)

Fig. 5.21 Water flow curve during true triaxial fatigue loading. (a) T=0 h; P= 1 MPa. (b) T=0 h; P= 2 MPa. (c) T=0 h; P= 3 MPa. (d) T=12 h; P= 1 MPa. (e) T=24 h; P= 1 MPa. (f) T=36 h; P= 1 MPa.

Analysis of the influence of water pressure in the σ1 direction on the flow rate and velocity of water through the samples, as illustrated in Figures 5.19a, b, and c, reveals that when the water pressure is 1 MPa, the total flow rate through the sample is 0.486 L. When the water pressure increases to 2 and 3 MPa, the total flow rates increase by 43.6% (0.698 L) and 50.6% (0.732 L), respectively. This indicates a positive correlation between water pressure and the total water flow rate during fatigue loading. Additionally, the trend of the flow rate curves under different water pressure conditions shows that water pressure is the primary factor affecting the seepage characteristics of the samples in the early stages of fatigue loading. Higher water pressure leads to greater flow velocity and total flow rate during the initial fatigue loading phase.

From the comparative analysis of Figures 5.19a, d, e, and f regarding the impact of saturation duration on the flow rate of the samples, it is observed that the sample with a saturation duration of 0 hours (natural sample) exhibits a higher flow velocity during the loading process. However, when the saturation duration increases from 12 to 36 hours, there is little change in the total flow rate of the samples. The trend of the flow rate curves indicates that saturation duration primarily affects the shape of the flow rate curve rather than the total flow rate. As the saturation duration increases, the slope of the flow rate curve during the early fatigue loading phase gradually decreases, and the inflection point of the flow rate curve during the loading process becomes less distinct. This observation aligns with the results presented in Section 3.3, where true triaxial seepage tests were conducted on natural and saturated samples, revealing a clear "permeability point" in the natural samples, which was absent in the saturated samples. The phenomenon illustrated in Figure 5.7 also indicates that as the saturation duration increases, the critical permeability point of the samples under fatigue loading gradually "disappears."

This can be attributed to the presence of numerous micro-cracks and pores in the natural samples, which allow water to enter the sample more rapidly under water pressure, marking the "water filling" phase. Once the internal pores of the sample are filled with water, the entry of external water requires expelling the internal moisture, which characterizes the "water outflow" phase. During this phase, the flow velocity is suppressed, and the boundary between the "water filling" and "water outflow" phases corresponds to the sample's "permeability point." Conversely, the saturated samples were already filled with substantial water prior to the true triaxial tests, leading to no distinct boundary between the "water filling" and "water outflow" phases during true triaxial loading. Consequently, as the saturation duration increases, the "permeability point" of the saturated samples gradually "disappears.".

5.2.2.5 Stress-strain characteristics of samples after true triaxial fatigue loading

Figure 5.22 presents the shear stress-strain curves of typical samples following true triaxial fatigue loading. The stress curve trends across different samples are quite similar, showing compression in the σ1 direction and expansion in the σ_2 and σ_3 directions. Without analyzing

the mechanical property deterioration mechanisms of the samples after true triaxial fatigue loading, the control variable method is utilized to investigate the effects of water pressure and saturation on the stress-strain characteristics of the samples post-fatigue loading.

First, the influence of water pressure on fatigue damage characteristics is examined. Taking the natural sample as an example, when the water pressure is at 1 MPa, the peak strain (ε_{1max}) in the σ_1 direction corresponding to the peak shear stress intensity is 6.4×10^{-3}, with a peak shear stress of 29.0 MPa. At water pressures of 2 and 3 MPa, the peak strains increase by 6.3% (6.8×10^{-3}) and 28.1% (8.2×10^{-3}), respectively, while the peak shear stresses decrease by 17.6% (23.9 MPa) and 18.3% (23.7 MPa). This indicates that water pressure significantly affects both the strength and deformation characteristics of the samples after fatigue loading. Higher water pressure leads to a greater deterioration of the samples' strength characteristics, resulting in reduced resistance to deformation. This is attributed to the alignment of the water pressure direction with that of the maximum principal stress; thus, greater water pressure results in increased effective stress during fatigue loading, enhancing fatigue damage and further deteriorating the mechanical properties of the samples post-fatigue.

Next, the impact of saturation duration on the mechanical properties of samples after true triaxial fatigue loading is analyzed. When the saturation duration is 12 hours, the peak shear stress decreases from 51.2 MPa before fatigue to 29.5 MPa after fatigue, a reduction of 43.6%. For a saturation duration of 36 hours, the peak shear stress drops from 52.5 MPa to 28.1 MPa, a reduction of 46.5%. This suggests that the saturation duration has a limited effect on the true triaxial strength of the samples. This is the primary distinction between true triaxial loading and uniaxial loading; as noted in Section 3.2, the saturation duration has a significant impact on the uniaxial strength before fatigue loading, where longer saturation times correspond to lower uniaxial strength. However, there is no evident correlation between the true triaxial strength of the samples before fatigue loading and saturation duration, a conclusion that can also be inferred from Tables 5.2 and 5.3. Under true triaxial conditions, although saturation leads to deterioration of the samples' mechanical properties, the presence of confining pressure prevents water from rapidly exiting through cracks from the sample surface, thereby enhancing the mechanical properties to varying degrees. This results in reduced sensitivity of the peak strength of the samples to saturation under true triaxial conditions.

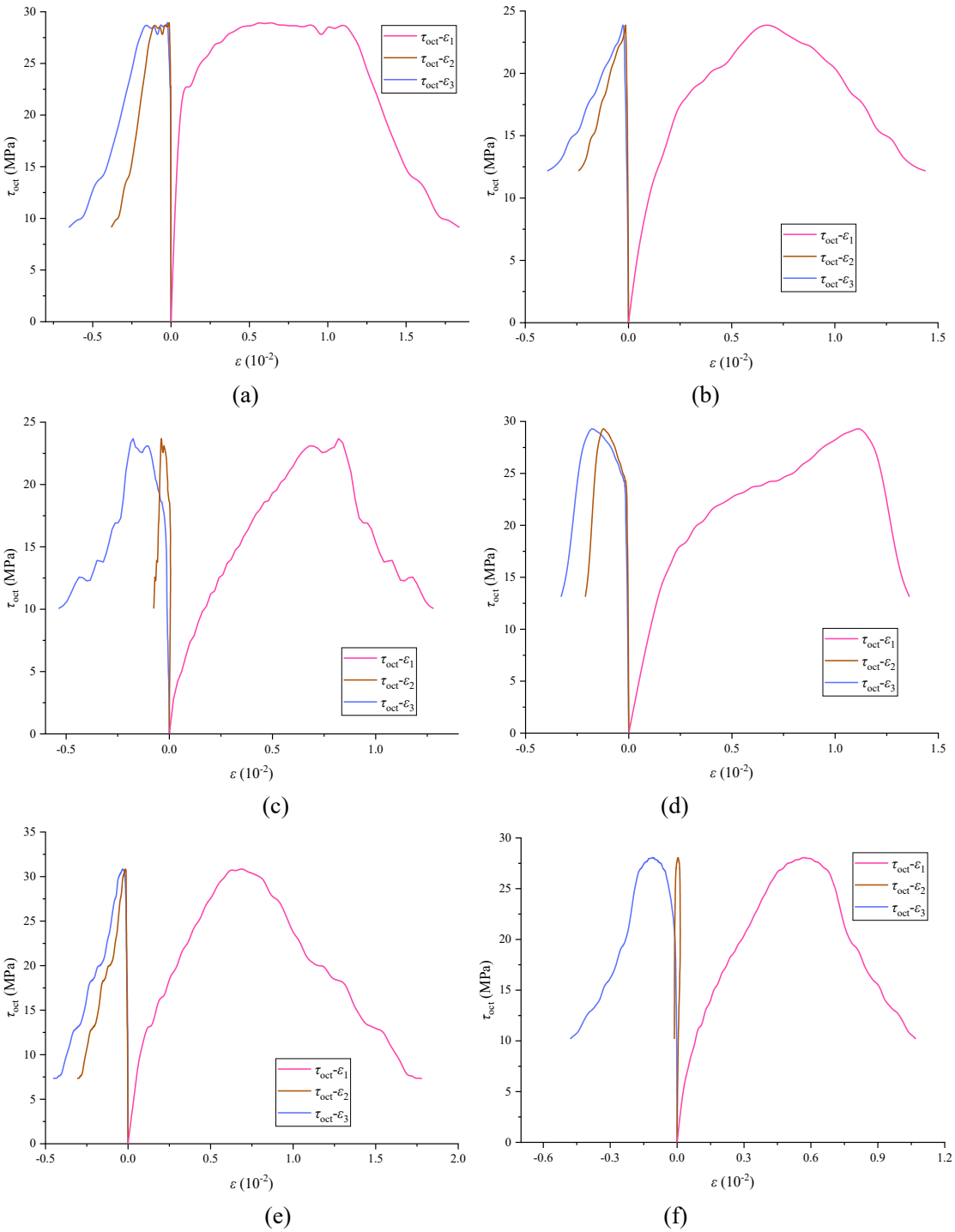

Fig. 5.22 Stress-strain characteristics of samples under true triaxial fatigue loading. (a) T=0 h; P= 1 MPa. (b) T=0 h; P= 2 MPa. (c) T=0 h; P= 3 MPa. (d) T=12 h; P= 1 MPa. (e) T=24 h; P= 1 MPa. (f) T=36 h; P= 1 MPa.

Regarding deformation characteristics, as the saturation duration increases from 12 to 36 hours, ε_{1max} decreases from 11.2 × 10^{-3} to 5.7 × 10^{-3}, a reduction of 49.1%, indicating that saturation duration significantly affects the ductility of the samples before and after fatigue loading. Longer saturation times lead to a decrease in the samples' resistance to deformation following fatigue loading.

5.2.2.6 Failure characteristics of samples after true triaxial fatigue loading

Saturation, true triaxial fatigue loading, and true triaxial loading-unloading all contribute to the deterioration of the mechanical properties of samples. Analyzing the failure characteristics of samples under different conditions is key to understanding the mechanisms behind the degradation of mechanical properties due to true triaxial fatigue loading. CT scans were conducted on the samples after true triaxial loading-unloading failure, and three-dimensional reconstructions were performed to obtain the fracture characteristics of typical samples under varying water pressure and saturation durations, as presented in Table 5.7.

Table 5.7 Failure characteristics of samples under different water pressures and water saturation duration

	T=0 h; *P*= 1 MPa.	*T*=0 h; *P*= 3 MPa.	*T*=36 h; *P*= 1 MPa.
The σ_1 direction	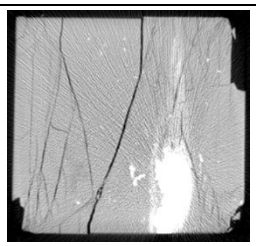	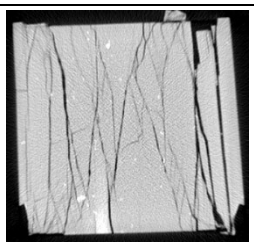	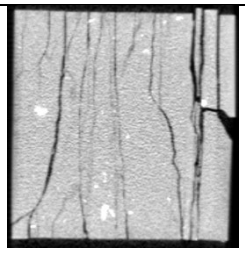
The σ_2 direction	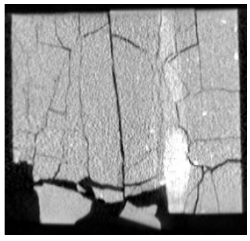	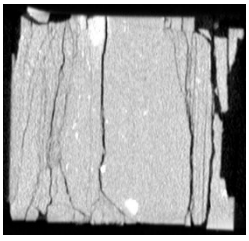	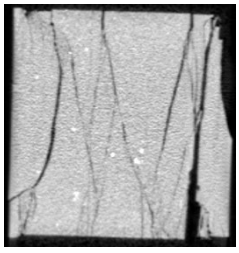
The σ_3 direction	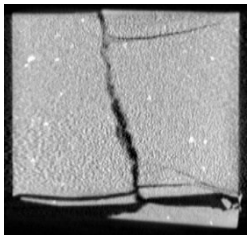	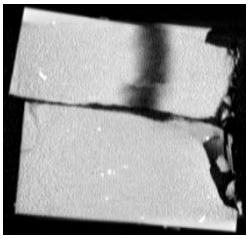	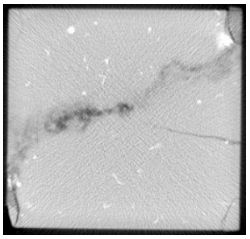
3D reconstruction of the image	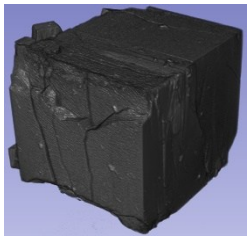	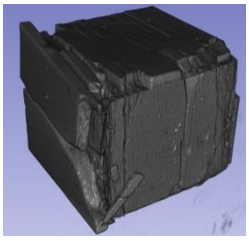	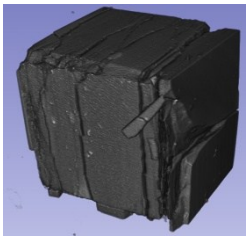

From the analysis in Table 5.7 regarding the influence of saturation duration on the failure characteristics of the samples, it is evident that after true triaxial loading failure, the natural sample (*T*=0 h) exhibits a distinct fracture zone in the σ₃ direction, indicating that the sample experiences multiple fractures under the continuous action of shear stress. In contrast, the saturated sample (*T*=36 h) shows shear cracks in the σ₃ direction but does not form a pronounced

fracture. In the σ_2 direction, the natural sample displays several parallel penetrating cracks, indicating through-going failure, while the saturated sample exhibits inclined cracks at an angle to the vertical direction, indicative of shear failure. This suggests that saturation alters the mechanical properties of the samples, resulting in different fracture characteristics during true triaxial loading failure.

The impact of water pressure on the failure characteristics of the samples is primarily reflected in the density of cracks and the degree of fracture. Taking the natural sample as an example, when the water pressure is at 1 MPa, the distribution of cracks in the σ_1 and σ_2 directions is relatively balanced. However, as the water pressure increases, a denser network of shear cracks gradually forms in the σ_1 direction, while the crack density in the σ_2 direction significantly decreases, with a more pronounced fracture zone in the σ_3 direction. This observation is consistent with the previous analysis of the deformation characteristics of the samples. Increased water pressure elevates the effective stress on the samples, amplifying the difference between σ_1 and σ_2, thereby diminishing the influence of the intermediate principal stress on the mechanical and failure characteristics of the samples.

5.2.3 Damage and seepage evolution of saturated shale after cyclic disturbance during true triaxial loading

5.2.3.1 Development patterns of the plastic zone in samples under different water pressure and saturation duration conditions

The 3D discrete element software was used to conduct true triaxial loading and unloading tests on samples under various conditions to analyze their deformation and failure characteristics. The established model is shown in Figure 5.23 (Wang et al., 2023). This model consists of seven parts: one sample and six loading platens. The loading platens are composed of a rectangular prism and a trapezoidal body, with the dimensions of the rectangular prism being 100 × 100 × 40 mm³. The height of the trapezoidal body is 10 mm, with contact surface dimensions of 100 × 100 mm² with the rectangular prism and 90 × 90 mm² with the sample. The dimensions of the sample are 100 × 100 × 100 mm³. The loading platens are assumed to have linear elastic constitutive behavior and are isotropic, meaning they do not undergo sliding or tensile damage.

The sample dimensions are set at 20 × 20 × 20 mm, maintaining a scale ratio of 1:5 compared to the laboratory sample size. The sample is defined using the Mohr-Coulomb constitutive model.

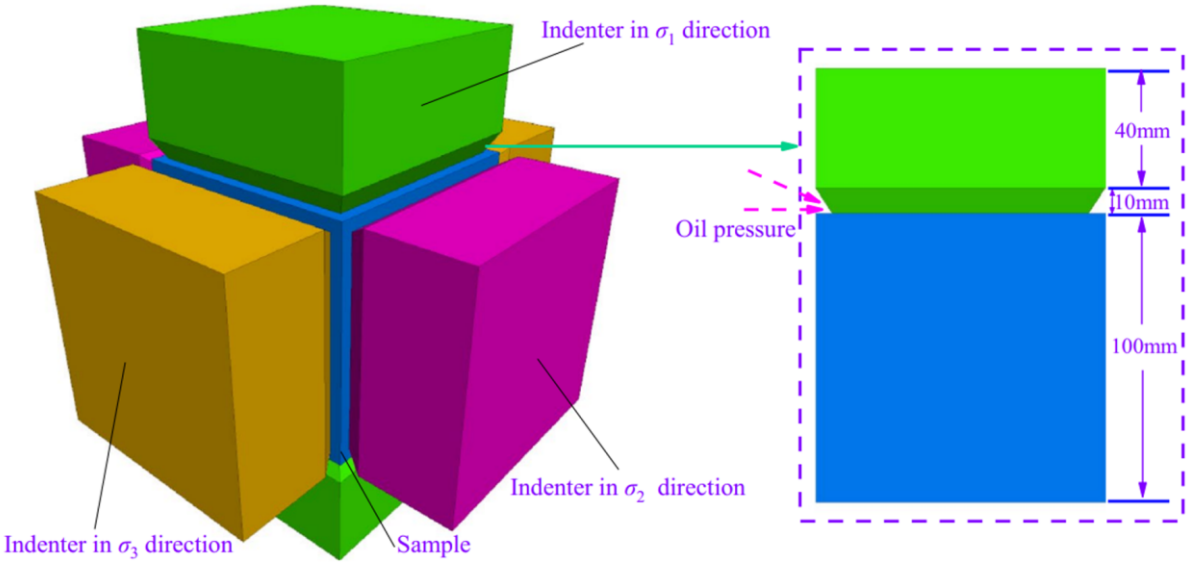

Fig. 5.23 Model diagram based on 3DEC (Wang et al., 2023)

The boundary conditions for the model are set as follows:

1) The tangential displacement of each loading platen is fixed at 0 (to prevent tangential displacement during the loading and unloading process).

2) The normal boundary stress for each loading platen is set according to the in-situ stress state of the rock: σ_1 = 5 MPa, σ_2 = 7.5 MPa, σ_3 = 15.5 MPa.

3) The initial stress within the sample is set to be the same as the normal boundary stresses.

After establishing the boundary conditions, equilibrium is first calculated, and then the loading and unloading tests on the sample are conducted using Fish language. The specific method involves changing the boundary condition in the σ1 direction from stress constraint to displacement (rate) constraint, controlling the loading platen in the σ_1 direction to apply loading at a rate of -0.002 mm/s; simultaneously, unloading in the σ_3 direction is conducted at a rate of 0.2 kN/s (with compression defined as negative). During the loading process, the stress in the σ1 direction is monitored, and loading is stopped when a downward trend is observed.

The physical and mechanical parameters of the samples after fatigue loading under different saturation durations are presented in Table 3.2. By substituting the parameters from Table 3.2 into the aforementioned model and varying the sample parameters and water pressure, the development patterns of the plastic zone under true triaxial conditions are obtained, as shown in Table 5.8.

Table. 5.8 Plastic zone development of samples under different water pressure and water saturation duration

Directions	*T*=0 h; *P*= 1 MPa.	*T*=0 h; *P*= 3 MPa.	*T*=36 h; *P*= 1 MPa.

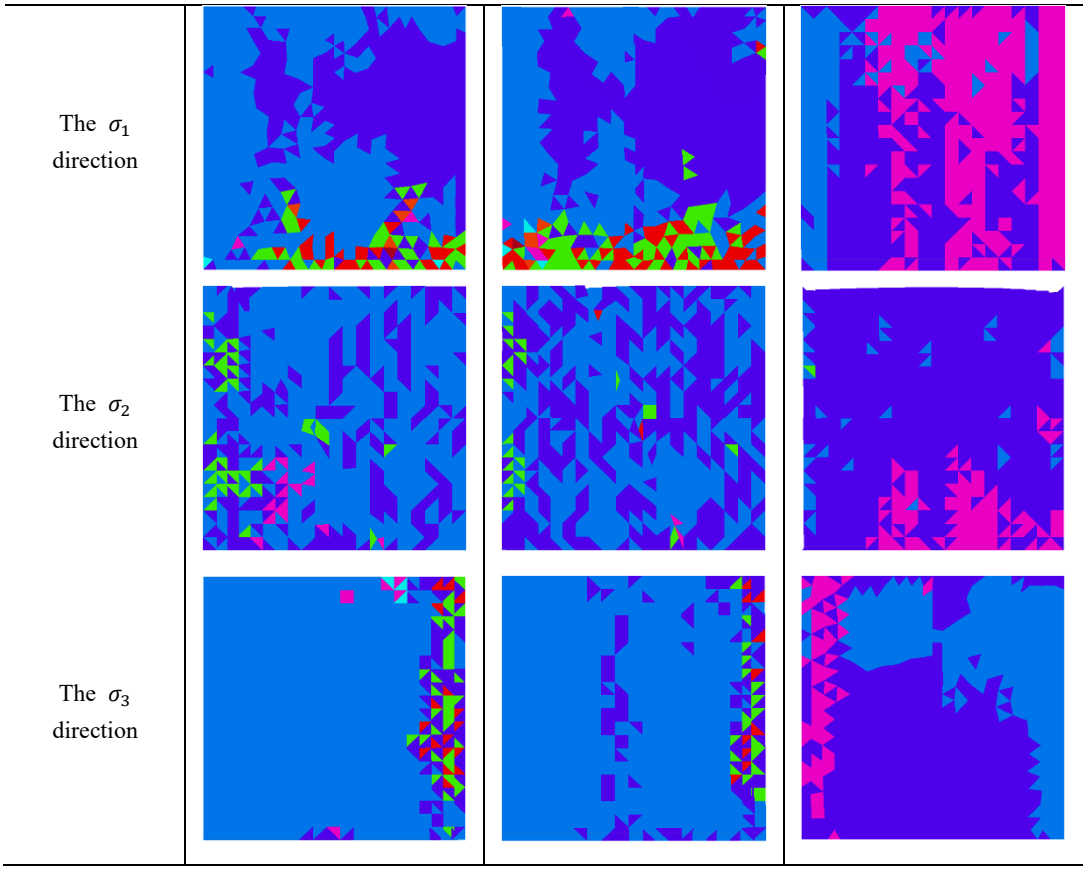

From Table 5.8, it can be observed that the fracture morphology of the samples obtained from numerical simulations differs slightly from that observed in laboratory experiments. However, the evolutionary patterns of the fracture characteristics under different saturation and water pressure conditions are quite similar.

Analyzing the impact of water pressure on the fracture characteristics of the samples, it is evident that at a water pressure of 3 MPa, the surface of the sample in the σ1 direction exhibits multiple parallel fracture zones, with a higher crack density compared to the condition at 1 MPa. The density of cracks in the σ_2 and σ_3 directions is also greater at 3 MPa than at 1 MPa, which is consistent with the results from CT scans. This indicates that higher water pressure results in more pronounced fracture characteristics of the samples under true triaxial loading and unloading conditions.

Regarding the influence of saturation on the fracture characteristics of the samples, it is observed that at a water pressure of 1 MPa, the natural sample has more concentrated cracks on the surface in the σ1 direction, with the plastic zone primarily located on the right side of that surface, forming a distinct through-going fracture zone. In contrast, the cracks on the surface of the saturated sample display a more dispersed characteristic, with the cracks being uniformly distributed across the σ1 direction surface and lacking a significant through-going fracture zone. Additionally, in the σ_2 and σ_3 directions, the distribution range of the plastic zone in the saturated sample is smaller than that in the natural sample. This suggests that saturation reduces

the brittleness of the samples, leading to a transition in the failure mode from brittle fracture to overall plastic failure.

5.2.3.2 Development of plastic zones in samples during loading

Tables 5.9–5.11 present the damage evolution characteristics of specimens under true triaxial loading conditions. As shown in Table 5.9, when T=0 h and P=1 MPa, cracks in the σ_1 direction initially appear sporadically in the lower-middle region of the σ_1 plane. As strain increases, these cracks gradually develop, expand, and eventually coalesce, leading to specimen failure. In the σ_3 direction, cracks are primarily distributed on the right side of the plane, with crack density increasing as the applied stress increases.

Table 5.9 Damage evolution of the sample under true triaxial loading when T=0 h and P= 1 MPa

	ε_1=0.25%	ε_1=0.50%	ε_1=0.75%	ε_1=1.00%	ε_1=1.25%	ε_1=1.50%
The σ_1 direction				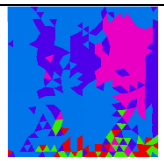	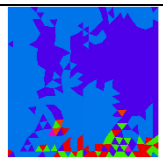	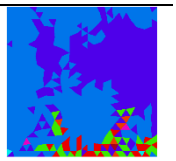
The σ_2 direction	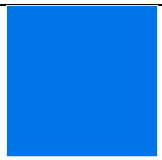	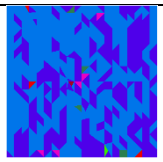	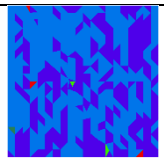	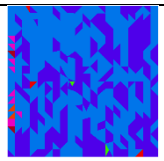	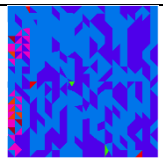	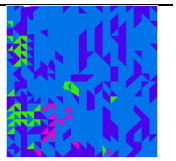
The σ_3 direction	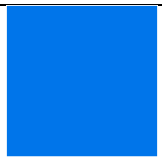	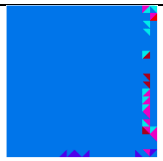		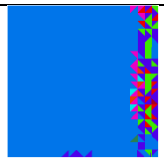	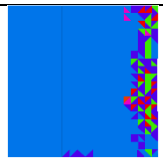	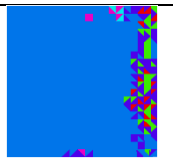

As shown in Table 5.10, when T=0 h and P=3 MPa, the degree of specimen failure during loading is more severe compared to P=1 MPa. In the σ_1 direction, the crack density at the bottom of the plane is higher and more concentrated than that observed at P=1 MPa. After failure, the central crack zone expands further and connects with the bottom cracks, forming a continuous failure region. In the σ_3 direction, in addition to cracks appearing on the right side, dispersed fracture zones also develop in the middle, indicating more pronounced shear failure compared to the case at P=1 MPa.

This phenomenon occurs because the increase in water pressure alters the internal stress state of the rock, particularly affecting crack propagation paths and stress concentration at crack tips. Higher water pressure increases the internal pore water pressure of the rock, thereby changing the effective stress. Elevated water pressure reduces the contact stress between rock grains, decreasing both shear strength and tensile strength, making cracks more likely to initiate and propagate under lower stress conditions. This explains the increased crack density and more severe shear failure observed at P=3 MPa.

Furthermore, crack development is influenced by the stress state. In true triaxial tests, due to the higher stress in the σ_1 direction, the increased water pressure leads to more concentrated

crack propagation along σ_1. Water pressure not only raises the pore water pressure and affects rock strength but also enhances water penetration, altering the rock failure mode by guiding crack propagation along stress concentration zones.

Table 5.10 Damage evolution of the sample under true triaxial loading when T=0 h and P= 3 MPa

The σ_1 direction	ε_1=0.25%	ε_1=0.50%	ε_1=0.75%	ε_1=1.00%	ε_1=1.25%	ε_1=1.50%
The σ_2 direction				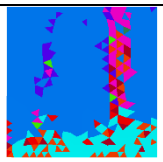	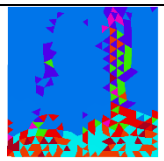	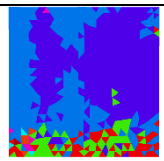
The σ_3 direction	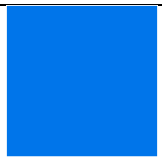	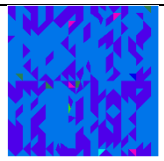	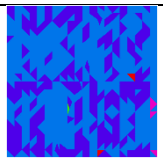	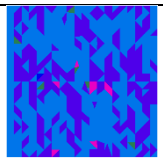	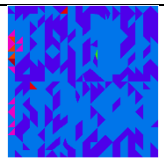	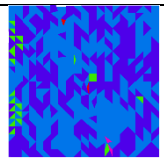
The σ_1 direction	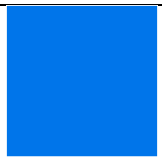			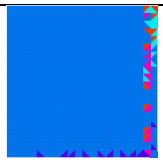	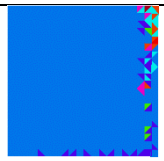	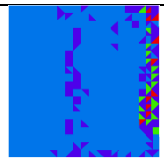

According to Table 5.11, when T=36 h and P=1 MPa, the crack development pattern during loading differs significantly from that of natural specimens as the saturation time increases. Before failure, the damage in the σ_1 and σ_3 directions is minimal, mainly occurring at the tops of both planes. However, after failure, cracks rapidly develop and expand, forming complex shear and tensile failure zones. This indicates that saturation has a significant impact on the crack evolution pattern, altering the timing, nature, and distribution characteristics of crack development during loading.

This phenomenon is closely related to the influence of saturation time on the rock's pore structure and crack propagation mode. The infiltration and accumulation of water inside the rock may lead to further changes in pore pressure, interacting with the mechanical properties of the rock. As the saturation time increases, water gradually penetrates microcracks, causing their progressive expansion. Prolonged saturation may induce a "hydration expansion" effect, where water entering the gaps between mineral grains leads to expansion, increasing the internal cracking pressure. This results in a slower crack development rate during early loading, but once a critical crack propagation threshold is reached, the crack growth rate accelerates sharply, manifesting as rapid crack expansion after failure, forming complex shear and tensile failure zones.

Additionally, saturation affects the strength characteristics of the rock. The presence of water may lead to mineral dissolution, expansion, or slippage, reducing both compressive and tensile strength. When the saturation duration is long, crack propagation during loading is often accompanied by increased permeability and greater complexity in crack interweaving. This

contrasts sharply with the case of shorter saturation times, where cracks are primarily concentrated at the top and remain relatively scattered.

Table 5.11 Damage evolution of the sample under true triaxial loading when *T*=36 h and *P*= 1 MPa

	ε_1=0.25%	ε_1=0.50%	ε_1=0.75%	ε_1=1.00%	ε_1=1.25%	ε_1=1.50%
The σ_1 direction	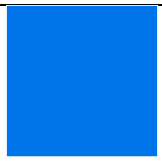		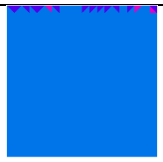			
The σ_2 direction	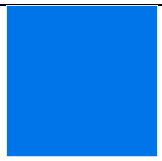			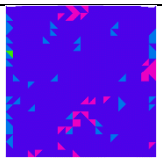	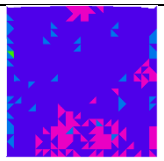	
The σ_3 direction	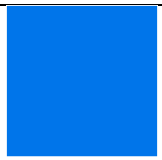					

Furthermore, a comprehensive analysis of Tables 5.9–5.11 reveals that in the σ_2 direction, crack evolution occurs more rapidly, with numerous shear and tensile failure zones forming during the early stages of loading. In contrast, cracks in the σ1\sigma_1 and σ3\sigma_3 directions develop more slowly in the initial loading phase, accelerating only after the specimen yields or fails.

This differs significantly from our previous numerical simulations of true triaxial loading tests on coal specimens. In earlier studies, we found that during loading, damage evolution in coal specimens primarily occurred in the σ_1 and σ_3 directions, while damage in the σ_2 direction was relatively minor (Wang et al., 2023). This discrepancy may stem from the higher plasticity of coal compared to the greater brittleness of shale.

Tables 5.9 and 5.10 also illustrate significant variations in failure characteristics under different water pressure conditions. To further investigate the underlying mechanisms of these variations, we analyzed the distribution patterns of pore water pressure within the specimens at different water pressure levels. Figure 5.24 presents a schematic of the applied water pressure, while Table 5.12 summarizes the evolution of pore water pressure during the true triaxial loading–unloading process.

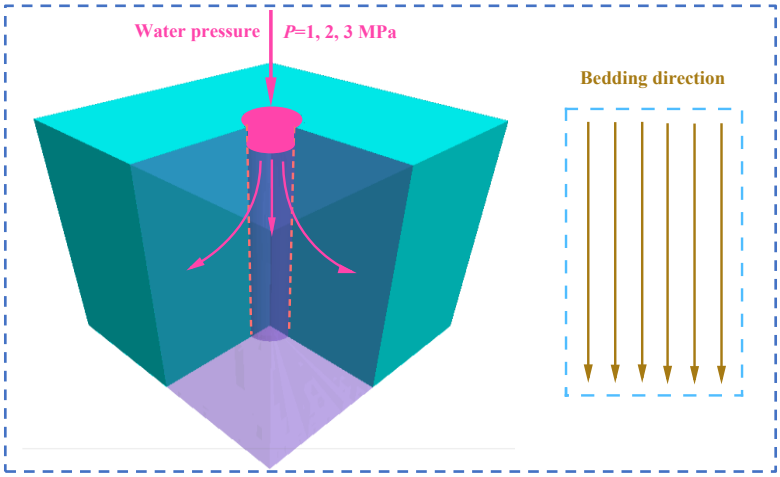

Fig. 5.24 Schematic diagram of water pressure application in true triaxial loading-unloading test

According to Table 5.12, when the water pressure is 1 MPa, the relatively low pressure allows the water to seep primarily along the σ_1 direction while also extending into the σ_2 and σ_3 directions. Since both the applied water pressure and the σ_1 direction are parallel to the bedding planes, the seepage rate is higher along σ_1.

When the water pressure increases to 3 MPa, the higher pressure causes the initial seepage to predominantly propagate along σ_1. After penetrating a certain distance inside the specimen, the water then extends into the σ_2 and σ_3 directions. During the true triaxial loading–unloading process, the increased water pressure raises the effective stress in the σ_1 direction, leading to a higher crack density and more severe damage along σ_1. Additionally, the water pressure alters the internal seepage direction and pressure distribution, which in turn affects the specimen's damage and failure characteristics (Table 5.3).

The coupling effect of water pressure and saturation duration on shale specimens indicates that their influence on crack evolution is not linear but rather interactive. For instance, under T=36 h and P=1 MPa conditions, prolonged water infiltration may generate high hydration pressure inside the rock, further accelerating the expansion of surface and internal cracks. In this case, crack development exhibits nonlinear behavior, especially as long-term hydration enhances the propagation of microcracks, forming complex shear bands and tensile zones. Under such conditions, the combined effect of water pressure and saturation duration significantly alters the distribution and morphology of cracks, shifting from localized expansion to overall connectivity, ultimately leading to the formation of a failure zone.

Table 5.12 Evolution of pore water pressure of samples under loading-unloading test

	Initial compaction stage	Elastic stage	Failure stage

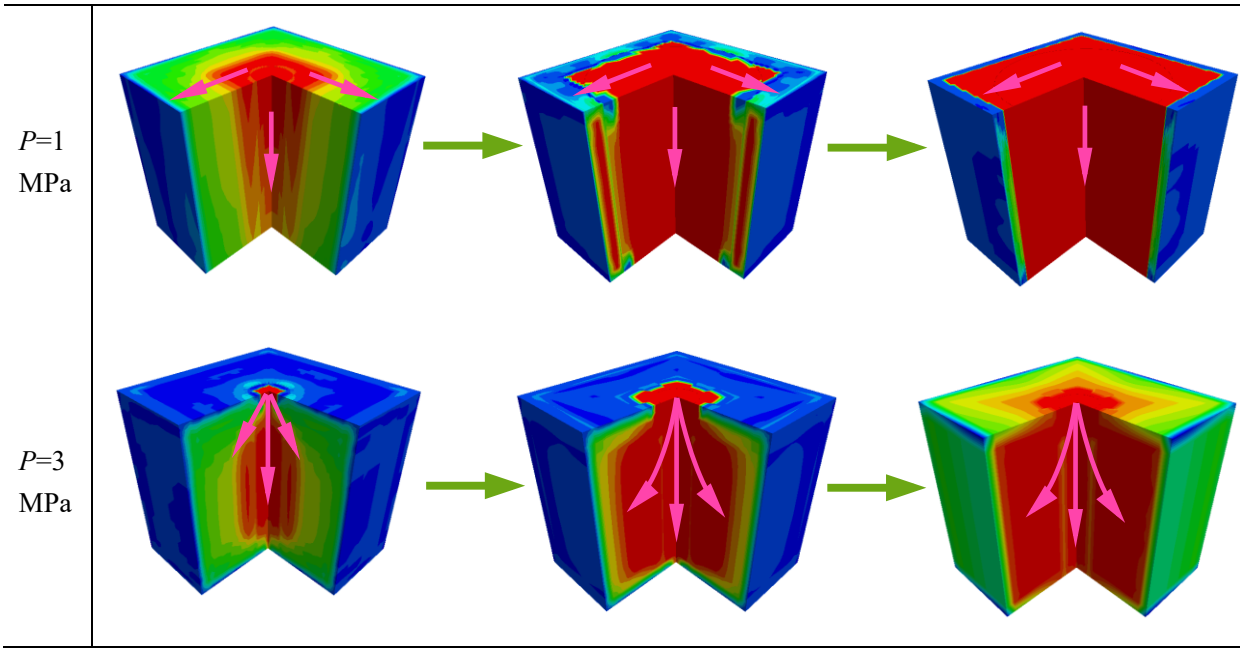

Water pressure and saturation duration also influence the failure characteristics of shale specimens, leading to changes in failure modes. Under short saturation durations and low water pressure, cracks primarily develop locally and exhibit a relatively linear expansion pattern. However, as water pressure increases and saturation time extends, crack propagation becomes more nonlinear, with a pronounced tendency toward shear failure.

Hydration effects and water pressure alter the pore structure of the rock, transforming initially localized microcracks into macroscopic shear bands and tensile zones. This explains the formation of complex failure zones under prolonged saturation. As a typical brittle rock, shale's crack propagation is primarily triggered by stress concentration points. Therefore, water pressure and saturation duration significantly impact the brittle failure of shale.

With increased water infiltration, shale's brittleness decreases, making cracks more likely to propagate in multiple directions, ultimately leading to the formation of macroscopic failure zones. Compared to coal, which exhibits higher plasticity, shale’s inherent brittleness results in more intense crack propagation and failure phenomena under the influence of water pressure and saturation duration.

5.3 Model and analysis of mechanical degradation of shale under water-force coupling

5.3.1 Deterioration model of mechanical properties of samples under the coupling action of water pressure, saturated water and cyclic stress

The mathematical model is a mathematical structure that is generally expressed in mathematical language with reference to the characteristics of a certain system of things. According to our previous research, the degradation mechanism of the mechanical properties of samples after fatigue loading was closely related to the fatigue characteristics during fatigue loading.

Therefore, to further analyze the coupling mechanism of each factor on the mechanical properties of samples under true triaxial loading, the test phenomena (strength characteristics, deformation characteristics, damage characteristics, seepage characteristics, etc.) under the conditions of multiple factors (water saturation duration, water pressure, fatigue loading) can be systematically analyzed by establishing a mathematical model.

First, the mechanical parameters of samples before, during, and after fatigue loading were counted, as shown in Table 5.13. According to Table 5.13, we first analyzed the influence of water saturation duration and water pressure on the damage characteristics and seepage characteristics of the sample during fatigue loading. The scatter diagram between the cumulative Acoustic Emission parameters and total water flow, water saturation duration T and water pressure P was drawn, and the Parabola^{2D} function was used to fit the three spatial functions $\{C'_{R-d}(T,P),\ C'_E(T,P),\ V'(T,P)\}$, as shown in Figure 5.25.

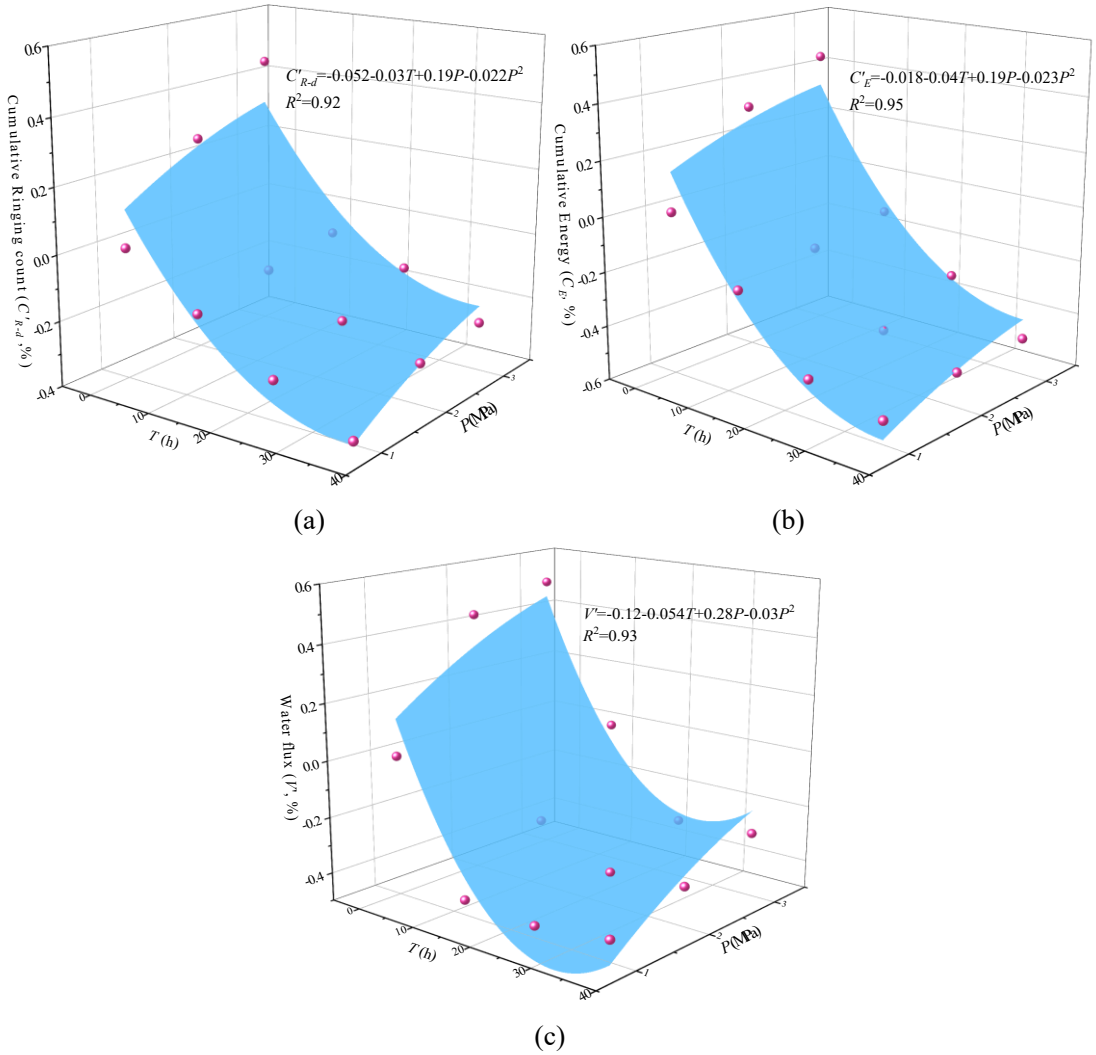

Fig. 5.25 Fitting diagram of fatigue loading parameters subject to different water saturation duration and water pressure. (a) Cumulative Ringing count. (b) Cumulative Energy. (c) Water flux.

Fig. 5.13 Mechanical parameters of samples with different water saturation duration under fatigue stress with different water pressures

T (h)	P (MPa)	Parameters during fatigue loading						Parameters after fatigue loading											
		Cumulative R-d count		Cumulative Energy (mV·mS)		Water flow (L)		τ_{oct} (MPa)			Cumulative R-d count			Cumulative Energy (mV·mS)			$\varepsilon_{3\,max}$ (10^{-3})		
		Actual value	Rate of change	Actual value	Rate of change	Actual value	Rate of change	Before fatigue loading	After fatigue loading	Actual value	Rate of change	After fatigue loading	Rate of change	Actual value	Rate of change	Rate of change	Before fatigue loading	Actual value	Rate of change
0	1	2210	0	3762	0	0.486	0	41.5	29	-30.1%	11.5	6.4	-44.3%	-4.84	-0.14	-97.1%	-10.4	-0.23	-97.8%
0	2	2790	26.2%	4939.7	31.3%	0.698	43.6%	46.1	23.9	-48.2%	7.41	6.8	-8.2%	-0.33	-0.14	-57.6%	-3.74	-0.27	-92.8%
0	3	3204	45.0%	5438.3	44.6%	0.732	50.6%	45.5	23.7	-47.9%	14.5	8.2	-43.4%	-0.13	-0.38	192.3%	-7.1	-1.75	-75.4%
12	1	1890	-14.5%	2941.9	-21.8%	0.269	-44.7%	51.2	29.5	-42.4%	10.4	11.2	7.7%	-3.51	-1.25	-64.4%	-9.21	-1.81	-80.3%
12	2	1985	-10.2%	3156.1	-16.1%	0.359	-26.1%	55.1	30.3	-45.0%	3.64	2.26	-37.9%	-1.56	-0.76	-51.3%	-3.07	-1.51	-50.8%
12	3	2064	-6.6%	3349.5	-11.0%	0.492	1.2%	56.1	29.4	-47.6%	11.2	7.91	-29.4%	-1.21	-0.16	-86.8%	-10.4	-5.94	-42.9%
24	1	1592	-28.0%	2036.9	-45.9%	0.263	-45.9%	59	30.9	-47.6%	7.31	6.8	-7.0%	-3.49	-0.15	-95.7%	-7.23	-0.31	-95.7%
24	2	1756	-20.5%	2264.1	-39.8%	0.301	-38.1%	56.3	28.9	-48.7%	7.16	7.84	9.5%	-0.95	-0.53	-44.2%	-5.64	-4.94	-12.4%
24	3	1921	-13.1%	2648.2	-29.6%	0.345	-29.0%	60.1	28.6	-52.4%	7.64	7.71	0.9%	-2.46	0.041	-102%	-6.12	-5.46	-10.8%
36	1	1348	-39.0%	1821.9	-51.6%	0.28	-42.4%	52.5	28.1	-46.5%	11.1	3.54	-68.1%	-2.64	0.046	-102%	-9.34	-1.1	-88.2%
36	2	1604	-27.4%	1984.3	-47.3%	0.312	-35.8%	55.9	29.5	-47.2%	6.48	2.18	-66.4%	-0.79	-0.15	-81.0%	-5.19	-2.01	-61.3%
36	3	1656	-25.1%	2013.8	-46.5%	0.354	-27.2%	59.2	30.1	-49.2%	6.92	2.31	-66.6%	-0.82	0.097	-112%	-6.24	-1.94	-68.9%

In Figure 5.25, C'_{R-d} (%) indicates the growth rate of the cumulative ringing count of the specimen relative to the natural specimen when {T=[0,36], P=[1,3]}. The same holds for $C'_E(T,P)$ and $V'(T,P)$. The functional expressions of each parameter after fitting are:

$$\begin{cases} C'_{R-d} = -0.052 - 0.03T + 0.19P - 0.022P^2 \\ C'_E = -0.018 - 0.04T + 0.19P - 0.023P^2 \\ V' = -0.12 - 0.054T + 0.28P - 0.03P^2 \end{cases} \tag{5.19}$$

It can be seen from Figure 5.25 that the damage characteristics of the sample represented by Acoustic Emission ringing count and energy parameters are like the variation trend of water pressure and water saturation duration. With the increase of water pressure and water saturation duration, the damage characteristics of the sample during fatigue loading gradually increase. Water flow was positively correlated with water pressure and negatively correlated with water saturation duration. Moreover, the influence of water saturation duration on water flow will gradually decrease with the increase of water saturation duration.

The curve of the mechanical parameters of the sample in the fatigue loading is shown in Figure 5.26. The function expression after fitting is as follows:

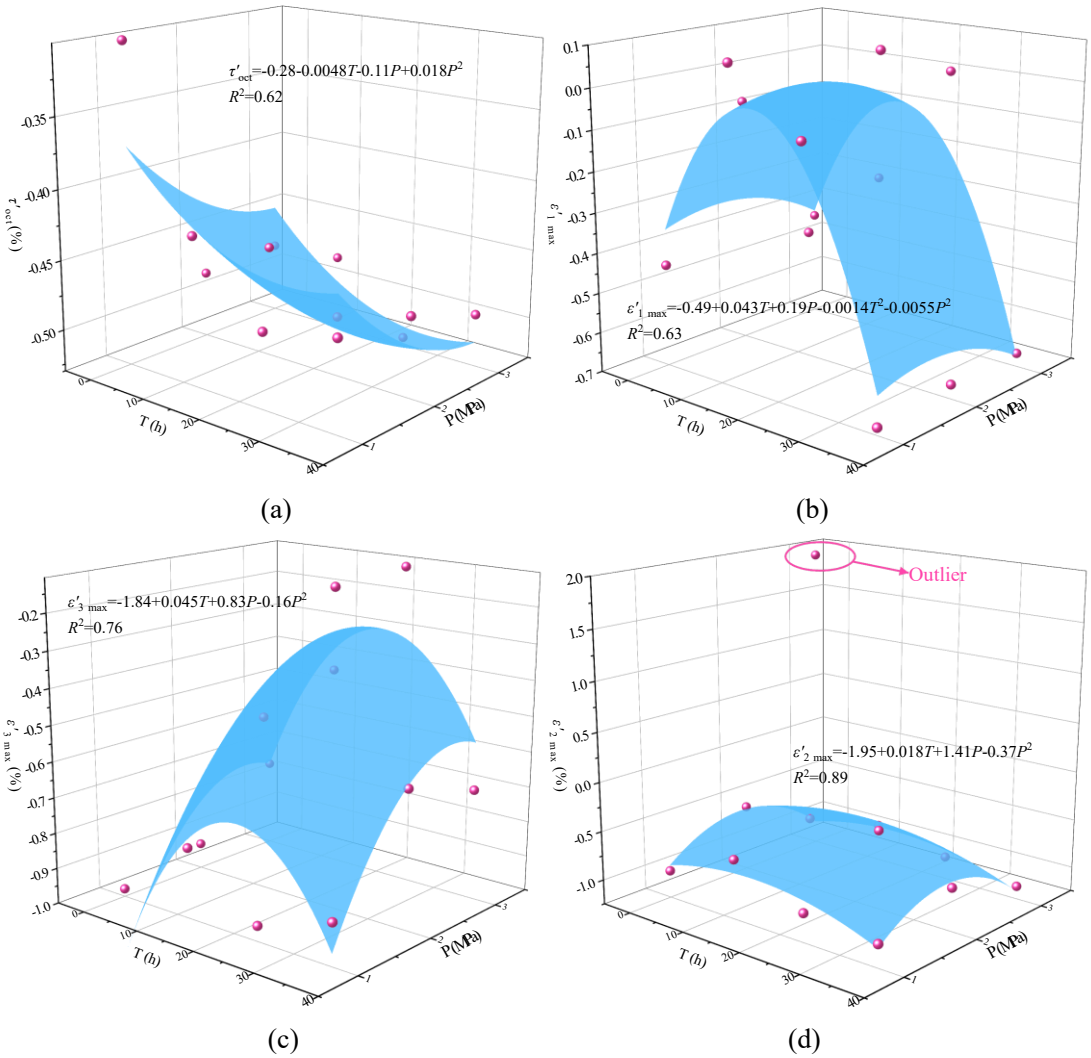

Fig. 5.26 Mechanical parameter curve of the samples under fatigue loading under different water pressure and water saturation duration. (a)τ'_{oct}. (b) $\varepsilon'_{1\,max}$. (c) $\varepsilon'_{2\,max}$. (d) $\varepsilon'_{3\,max}$.

$$\begin{cases} \tau'_{oct} = -0.28 - 0.0048T - 0.11P + 0.018P^2 \\ \varepsilon'_{1\,max} = -0.49 + 0.043T + 0.19P - 0.0014T^2 - 0.0055P^2 \\ \varepsilon'_{2\,max} = -1.95 + 0.018T + 1.41P - 0.37P^2 \\ \varepsilon'_{3\,max} = -1.84 + 0.045T + 0.83P - 0.16P^2 \end{cases} \tag{5.20}$$

As can be seen from Figure 5.26, after fatigue loading, the strength of the sample is significantly negatively correlated with the water pressure and water saturation duration. With the increase of water pressure and water saturation duration, the shear stress peak value of the sample decreases significantly after fatigue loading. The deformation characteristics of the sample showed a quadratic relationship with the water pressure and the water saturation duration, that is, the change rate of the deformation parameters of the sample increased first and then decreased with the increase of the water pressure and the water saturation duration.

By combining the peak shear stress data of the sample after fatigue loading with the damage characteristics and water flow characteristics during fatigue loading, a three-dimensional scatter diagram was drawn, as shown in Figure 5.27. It can be seen from Figure 5.27 that the damage degree of fatigue loading is roughly positively correlated with the rate of water flow. However, the strength of the sample under fatigue loading is negatively correlated with both.

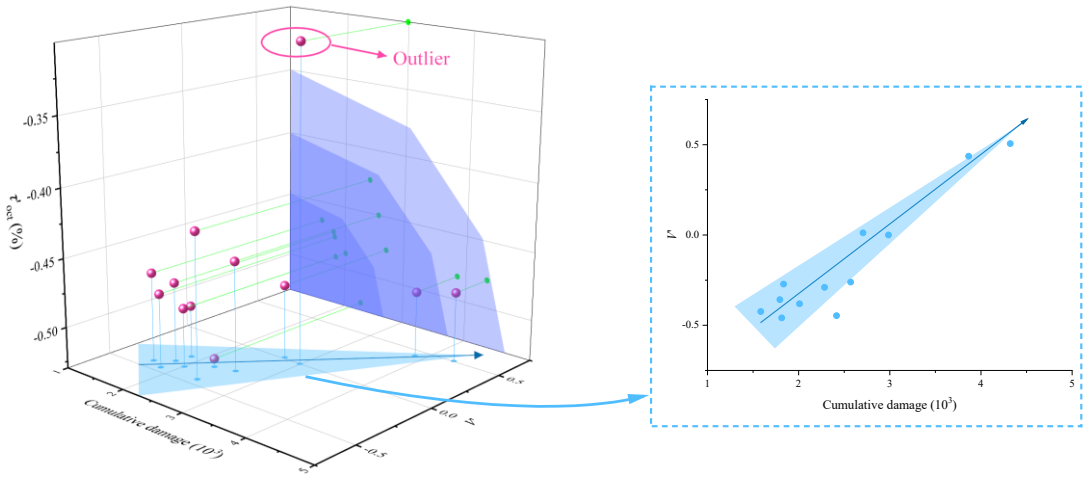

Fig. 5.27 Relationship between shear stress, water flow, and acoustic emission cumulative damage

To further analyze the deterioration mechanism of the mechanical properties of the sample under the coupling action of water pressure and water saturated, the fatigue damage function λ of the sample was established by combining the fatigue loading parameters with the mechanical parameters after fatigue loading:

$$\lambda \propto f(C'_{R-d}, C'_E, V', \tau'_{oct}, \varepsilon'_{1\,max}, \varepsilon'_{2\,max}, \varepsilon'_{3\,max}) \tag{5.20}$$

In Formula (5.20), C'_{R-d}, C'_E and V' are the parameters in the process of fatigue loading, $\tau'_{oct}, \varepsilon'_{1\,max}, \varepsilon'_{2\,max}$ and $\varepsilon'_{3\,max}$ are the parameters after fatigue loading, both are not in the same field parameters. To make the formula more scientific, the imaginary part j is introduced, i.e.:

$$\lambda \propto \{f(C'_{R-d}, C'_E, V') + j \cdot g(\tau'_{oct}, \varepsilon'_{1\,max}, \varepsilon'_{2\,max}, \varepsilon'_{3\,max})\} \tag{5.21}$$

The increase of cumulative Acoustic Emission parameters and water flow both represent the increase of sample damage, so:

$$\lambda \propto \{C'_{R-d}, C'_E, V'\} \tag{5.22}$$

Therefore, the real part function can be constructed as:

$$f(C'_{R-d}, C'_E, V') = C'_{R-d} + C'_E + V' \tag{5.23}$$

By substituting Formula (5.19) into Formula (5.23), we get:

$$f(C'_{R-d}, C'_E, V') = -0.19 - 0.124T + 0.66P - 0.075P^2 \tag{5.24}$$

The decrease of shear strength means the increase of sample damage, and the decrease of peak deformation means the decrease of sample deformation resistance. Therefore:

$$\begin{cases} \lambda \propto \frac{1}{\tau'_{oct}} \\ \lambda \propto \{\varepsilon'_{1\,max}, \varepsilon'_{2\,max}, \varepsilon'_{3\,max}\} \end{cases} \tag{5.25}$$

Therefore, the imaginary part function can be constructed as:

$$g(\tau'_{oct}, \varepsilon'_{1\,max}, \varepsilon'_{2\,max}, \varepsilon'_{3\,max}) = \frac{\varepsilon'_{1\,max}+\varepsilon'_{2\,max}+\varepsilon'_{3\,max}}{\tau'_{oct}} \tag{5.26}$$

By substituting Formula (5.20) into Formula (5.26), we get:

$$g(\tau'_{oct}, \varepsilon'_{1\,max}, \varepsilon'_{2\,max}, \varepsilon'_{3\,max}) = \frac{4.28-0.106T-2.16P+0.0014T^2+0.5175P^2}{0.28+0.0048T+0.11P-0.018P^2} \tag{5.27}$$

Therefore, the expression of the fatigue damage function is:

$$\lambda = -0.19 - 0.124T + 0.66P - 0.075P^2 + j \cdot \frac{4.28-0.106T-2.16P+0.0014T^2+0.5175P^2}{0.28+0.0048T+0.11P-0.018P^2} \tag{5.28}$$

where $P \in \{1, 2, 3\}$, $T \in \{0, 12, 24, 36\}$.

In Formula (5.28), the function of the real part represents the change of fatigue characteristics of the sample, the function of the imaginary part represents the change of mechanical properties of the sample after fatigue loading, and the module |λ| of the function represents the overall change degree of the sample under different water pressure and water saturation duration.

$$|\lambda| = \sqrt{(0.19 + 0.124T - 0.66P + 0.075P^2)^2 + \left(\frac{4.28-0.106T-2.16P+0.0014T^2+0.5175P^2}{0.28+0.0048T+0.11P-0.018P^2}\right)} \tag{5.29}$$

To plot the fatigue damage function in two dimensions, we introduce the function Date (n), defined as a function arranged in the order $\{\boldsymbol{T}^T \times \boldsymbol{P}\}$. Where $\boldsymbol{T}$ is a one-dimensional matrix [0, 12, 24, 36], and $\boldsymbol{P}$ is a one-dimensional matrix [1, 2, 3], namely:

$$\begin{cases} \text{Date}\ (1) = 0,1 \\ \text{Date}\ (2) = 0,2 \\ \quad \ldots \\ \text{Date}\ (12) = 36,1 \end{cases} \tag{5.30}$$

Substituting Date (n) into Equation (12) to replace the variables T and P allows for the plotting of the fatigue damage function of the samples in the complex plane, as illustrated in Figure 5.28. It can be clearly seen from Figure 5.25 that natural samples are most affected by water pressure. With the increase of fatigue damage during loading (the change of real part in

Figure 5.28), the mechanical properties of samples deteriorate sharply after fatigue damage, and the degree of deterioration of mechanical properties of natural samples is positively correlated with the degree of fatigue damage. The fatigue characteristics of the water saturated samples are also positively correlated with the water pressure, but the damage degree of samples during cyclic loading increases first and then decreases with the increase of water saturation duration. This shows that under true triaxial fatigue loading, the deterioration degree of mechanical properties of water saturated specimens is not linearly correlated with the fatigue damage characteristics of specimens during fatigue loading.

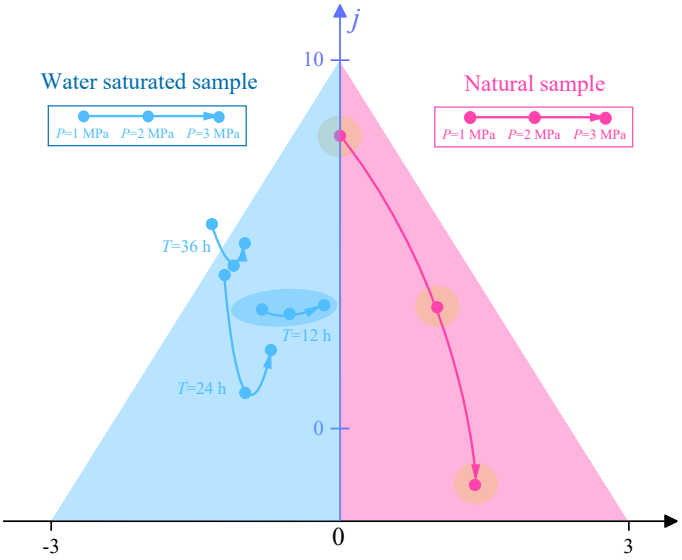

Fig. 5.28 Fatigue damage function of samples based on complex plane

5.3.2 Damage model extension based on neural network

In Section 5.4.1, the effects of water saturation duration and water pressure on the fatigue characteristics and the deterioration mechanism of the mechanical properties of the samples were analyzed in the complex plane, and the corresponding mathematical model was established. To increase the practicability of the model and further verify the accuracy of its results, this section adopts the neural network method to construct the model concretized based on Section 5.4.1. Figure 5.29 shows the neural network model based on multi-layer perceptron.

In Figure 5.29, the activation function of the model's hidden layer is the hyperbolic tangent (tanh x), and the weight calculation method for each input layer is detailed in Equations (4.1)-(4.9). Following these steps, the weights of all synapses in the model are determined. The model is then used to compute the mechanical parameters of the samples under different conditions after fatigue loading, as shown in Figure 5.30.

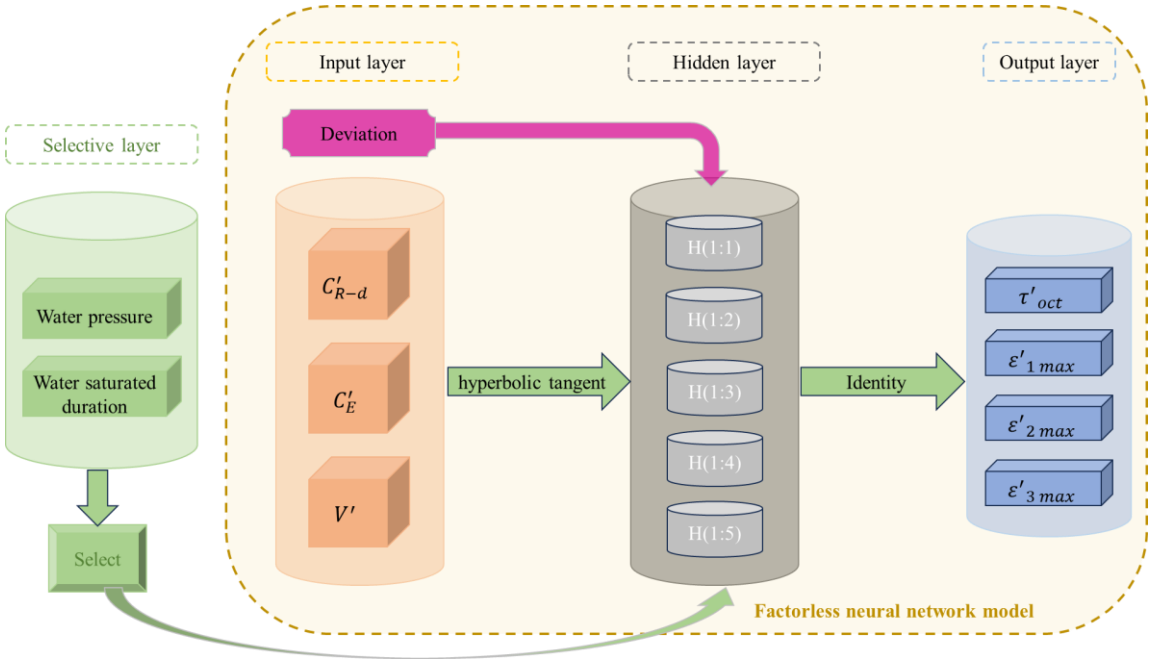

Fig. 5.29 A neural network model representing the relationship between {water saturation, water pressure}, {fatigue loading characteristics} and {post-fatigue mechanical properties}

From Figure 5.30, it can be observed that the overall error between the predicted values output by the model and the actual values is relatively small. Except for the significant error at date (1), the average error for the shear strength data points is approximately 1%, indicating good training performance. The prediction accuracy for strain is slightly lower than that for strength; however, with the exception of the two marked outlier points in the figure, the prediction accuracy for other values is high. These results demonstrate that the established neural network model exhibits good reliability.

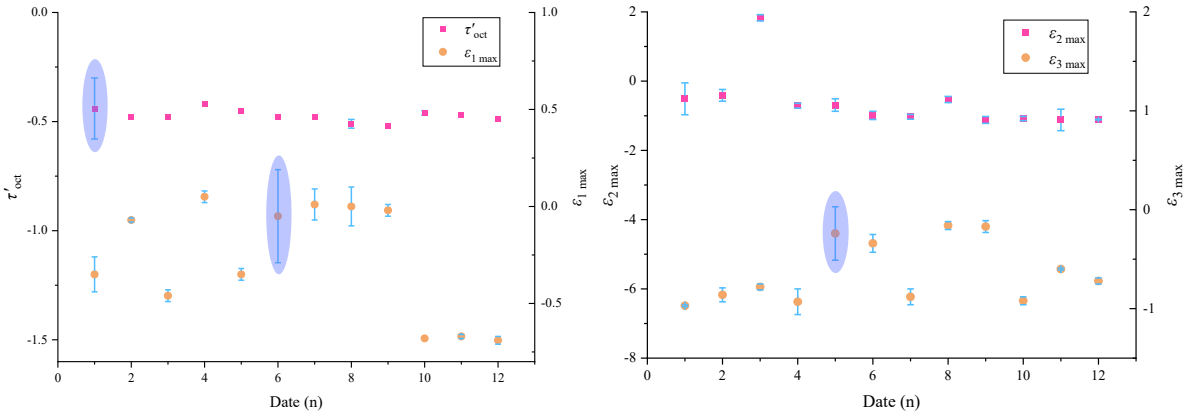

(a) (b)

Fig. 5.30 The error between the actual value of the mechanical parameters of the sample and the predicted value of the neural network. (a) τ'_{oct} and $\varepsilon'_{1\,max}$. (b) $\varepsilon'_{2\,max}$ and $\varepsilon'_{3\,max}$.

Using the established neural network model, the variables in the input layer are continuously processed by expanding the domain of the Date(n) function, introducing a new

function, New_Date(n), defined as the ordered arrangement of the $\{\boldsymbol{NT}^T \times \boldsymbol{P}\}$ function. Here, $\boldsymbol{NT}$ is a one-dimensional matrix [0,1,2,3, … ,36], and $\boldsymbol{P}$ is a one-dimensional matrix [1,2,3]. Thus, New_Date(n) can be expressed as follows:

$$\begin{cases} \text{New\_Date}\ (1) = 0,1 \\ \text{New\_Date}\ (2) = 0,2 \\ \text{New\_Date}\ (3) = 0,3 \\ \text{New\_Date}\ (4) = 1,1 \\ \quad \ldots \\ \text{New\_Date}\ (108) = 36,3 \end{cases} \tag{5.31}$$

By substituting the New_Date(n) function into the input layer and using the neural network model for predictive calculations, the complex plane representation of the influence coefficient λ is obtained, as illustrated in Figure 5.31.

Figure 5.31 shows that as the data becomes denser, the projections of the model's real and imaginary parts on the complex plane gradually approach a quadratic negative correlation. This method allows the patterns derived from limited laboratory experiments to be extended into a continuous domain space, thereby enhancing the practical utility of the model.

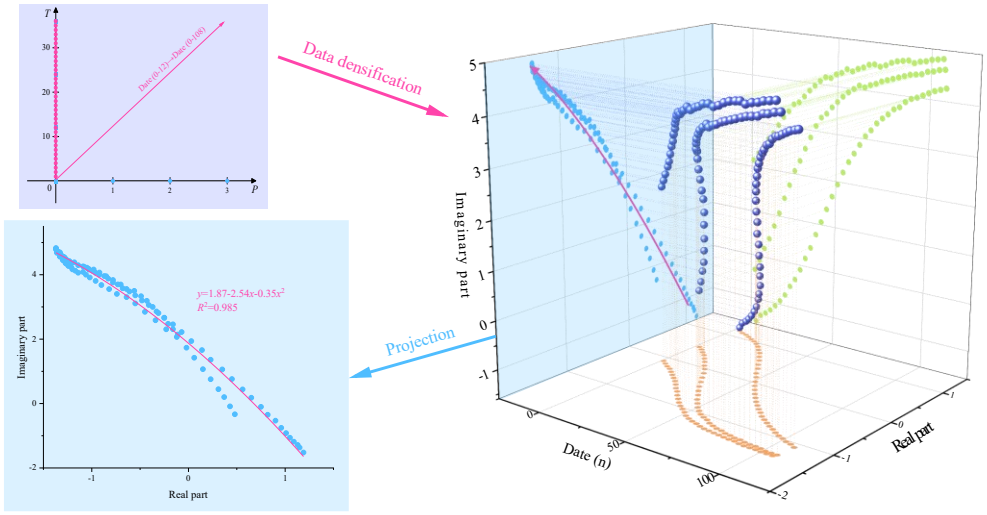

Fig. 5.31 Fatigue damage evolution model of sample based on neural network.

5.3.3 Model visualization based on Visual Basic

Visual Basic (VB) is an object-oriented programming language that features a graphical user interface and a rapid application development system. It allows for database connections using DAO, RDO, and ADO, enabling the generation of object-oriented applications. By programming the neural network model in VB, visualization of the established model can be achieved, allowing it to run directly on a computer for inputting experimental parameters and outputting results.

1) The first step involves data importation. A matrix $D[i,3]$ is created to store the values of three input vectors $\{C'_{R\text{-}d}, C'_E, V'\}$. Experimental data is imported into these matrices, and the

values of the matrices are sequentially input into the corresponding vectors within the program. Algorithm 1 provides the pseudocode for this method.

Algorithm 1. Data import

Input: $C'_{R\text{-}d}$, C'_E, V', Input matrix G, Number of data n
Output: Group *s0*
1: $\alpha \leftarrow 0$ and $\beta \leftarrow 0$
2: **for** $i \leftarrow 0$ to n-1 **do**
3: **for** $j \leftarrow 0$ to 2 **do**
4: **if** $G[i, j]$ is null **then**
5: Jump out of this loop
6: **else**
7: $C'_{R\text{-}d}[i] \leftarrow D[i, j]$
8: $C'_E[i] \leftarrow D[i, j]$
9: $V'[i] \leftarrow D[i, j]$
10: **end if**
11: **end for**
12: **end for**
13: **return** *s0*

2) After the data is imported, the model is trained for weights according to equations (3.1)-(3.9). Algorithm 2 provides a weight training method using τ_{oct} as an example.

Algorithm 2. Model training

Input: $C'_{R\text{-}d}$, C'_E, V', τ'_{oct}, Training number N
Output: Weight w_1, w_2, w_3
1: $w_1 \leftarrow 0.1$, $w_2 \leftarrow 0.1$, $w_3 \leftarrow 0.1$
2: **for** $i \leftarrow 0$ to N-1 **do**
3: $S \leftarrow w_1 C'_{R\text{-}d}[i] + w_2 C'_E[i] + w_3 V'[i]$
4: $Y \leftarrow (1\text{-}Exp(-2S))/(1+Exp(-2S))$
5: $r \leftarrow 0.1\,(1-Y^2)\cdot(\tau_{oct}[i]-Y)$
6: $w_1 \leftarrow w_1 + r \cdot C'_{R\text{-}d}[i]$
7: $w_2 \leftarrow w_2 + r \cdot C'_E[i]$
8: $w_3 \leftarrow w_3 + r \cdot V'[i]$
9: **end for**
10: **return** *s0*

3) After the model training is completed, the densified parameter data is imported into the program for prediction, with the data import method referenced in Algorithm 1.

Figure 5.32 shows a program that can run on the Windows system, visualizing the neural network model from Section 5.2.2 and adding functionalities for batch data import and export. It enables rapid input of parameters (saturation duration, water pressure) and fatigue characteristic parameters (C'_{R-d}, C'_E, V'), and allows for quick output of the prediction results to a [.txt] format file. This significantly enhances the efficiency of the model's application and promotion.

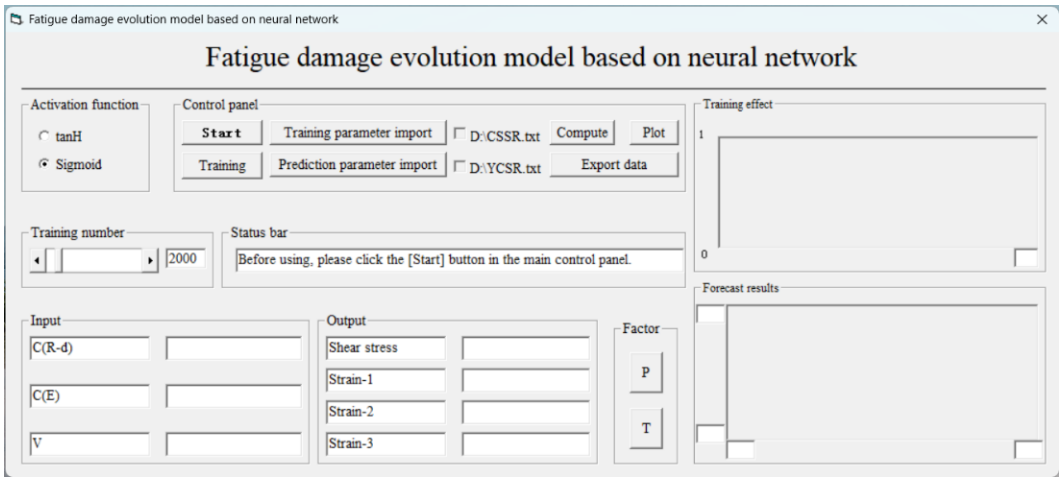

(a)

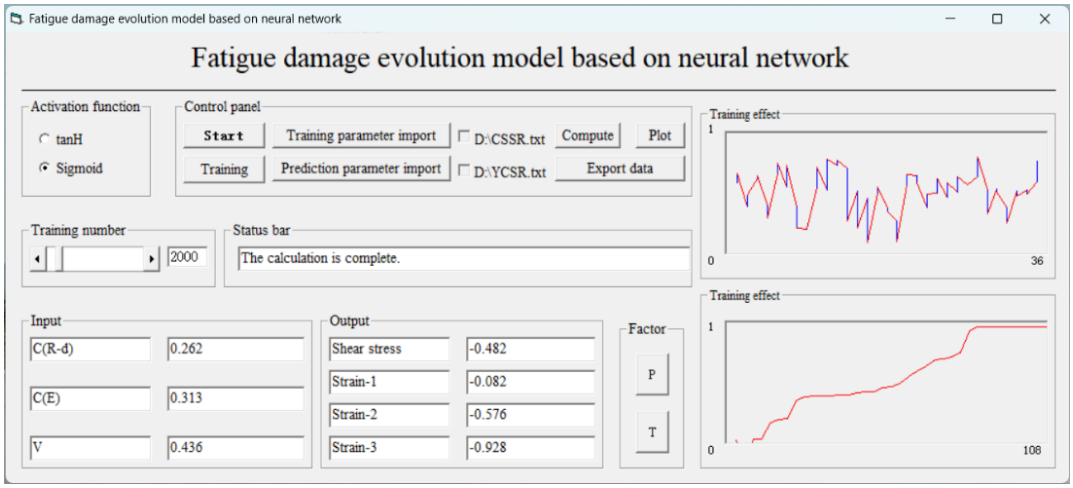

(b)

Fig. 5.32 Fatigue damage characteristic prediction software based on Visual Basic. (a) Software Interface. (b) Running Results.

5.3.4 Discussion of fatigue damage model results

From the results of the model shown in Figure 5.25, it is evident that under the same fatigue stress, the degradation mechanisms of the mechanical properties of natural samples and saturated water samples exhibit different trends. As illustrated in Figure 5.28, as the data volume increases, the real and imaginary parts of the model gradually approach a quadratic negative correlation in the complex plane, indicating that the mechanical performance degradation of saturated water samples initially increases and then decreases with the increase in fatigue damage. Here, we attempt to discuss the underlying reasons for this phenomenon from the perspective of the testing methods.

Compared to previous fatigue loading studies, the first advantage of this experimental method is that it measures the in-situ geostress at the sampling site through field tests, utilizes a true triaxial testing machine to apply loading to the geostress state, and then conducts fatigue loading tests. This approach better replicates the actual stress state compared to traditional uniaxial fatigue tests. According to previous research findings, the strength of samples

significantly decreases after water saturation under uniaxial compression [152]. However, under true triaxial conditions, although water saturation can lead to the deterioration of the mechanical properties of the samples, the presence of confining pressure prevents water from rapidly exuding from the sample surface after it fills the internal cracks, thereby enhancing the mechanical properties of the sample to varying degrees. Therefore, the sensitivity of peak strength to water saturation under true triaxial conditions is reduced [50].

The second advantage of this experimental method is that through multiple true triaxial fatigue tests and loading-unloading tests, it explores the mechanisms of mechanical performance degradation of samples under the combined effects of water saturation, water pressure, and fatigue stress. The mechanical properties of unsaturated samples (natural samples) are significantly correlated with fatigue damage characteristics. The greater the damage to the samples during the fatigue loading process, the poorer their mechanical properties post-fatigue loading [153, 154]. However, the water-saturated samples exhibit different phenomena. Based on experimental observations and the established mathematical model, the degree of damage during fatigue loading varies with different water saturation times. As T increases, the damage to the samples during fatigue loading first increases and then decreases. This indicates that water saturation damage and fatigue damage are not independent of each other, which is also the reason why the mathematical model results show that "the mechanical properties of the samples post-fatigue loading exhibit a trend of first weakening and then increasing with the increase in fatigue damage level." Considering the roles of water saturation and water pressure, the degree of damage from fatigue loading is no longer the sole factor determining the mechanical properties of the samples. Although the water saturation tests were completed before the fatigue loading tests, the influence of saturated water on the fatigue characteristics and mechanical properties of the samples persists.

The degradation curve of peak shear stress of the samples post-fatigue loading is illustrated in Figure 5.33. It can be seen that when T=24 h, the degree of degradation of the mechanical properties of the samples is maximized. This leads to the conclusion of a "maximum damage point" under the coupled effects of fatigue damage and water saturation damage, indicating that when T=24 h, the joint degradation effects of water saturation damage and fatigue damage on the mechanical properties of the samples are most pronounced. When $T \neq 24$ h, the joint degrading effect of water saturation on fatigue damage diminishes.

Simultaneously, the influence of water pressure on the mechanical properties of the samples is also affected by the water saturation time. Figure 5.33 shows that the mechanical properties of natural samples are positively correlated with significant water pressure damage characteristics during fatigue loading. The higher the water pressure, the greater the fatigue damage to the samples, which is consistent with previous results [50, 155]. However, while the degree of fatigue damage to the samples after water saturation is positively correlated with water pressure, the mechanical properties of the samples post-fatigue loading initially increase

and then decrease with the rise in water pressure. The above results indicate that the degradation mechanisms of the mechanical properties of the samples due to water saturation, water pressure, and fatigue loading are complex and interrelated. When exploring the fatigue characteristics of samples under the influence of water, it is essential to fully consider the coupling effects of various factors, rather than the mechanisms of a single factor on the mechanical properties of the samples. The findings are of significant reference value for studying the stability of water-rich surrounding rock under fatigue stress.

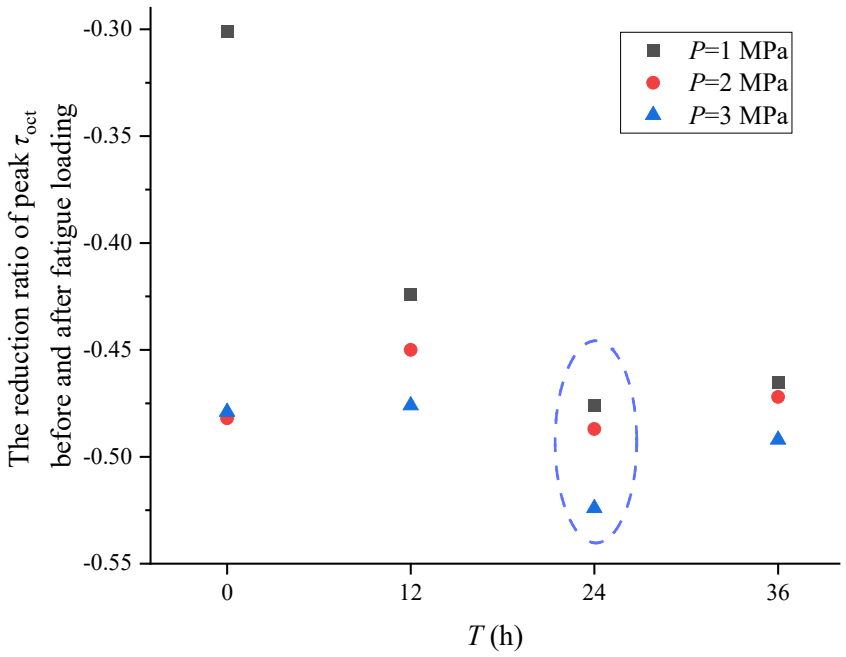

Fig. 5.33 The degradation curve of the peak shear stress of samples after fatigue loading

5.4 Summary

This chapter systematically reveals the mechanical response and permeability evolution of water-saturated shale under the coupled effects of hydraulic pressure and stress through true triaxial cyclic loading and seepage experiments. By integrating acoustic emission monitoring and neural network modeling, a multi-field coupling damage evaluation system is established. The main conclusions are as follows:

1. Regulation Mechanism of Water-Rock Interaction on Mechanical and Seepage Properties: The stress-strain curves of natural and water-saturated specimens exhibit significant differences. The localized expansion effect in water-saturated specimens enhances curve fluctuations, while the overall compression state after failure restricts the instantaneous increase in water flow. An increase in hydraulic pressure enhances the effective stress in the σ_1 direction, intensifies crack propagation, and reduces crack density in the σ_2 direction, thereby weakening the mechanical regulation effect of the intermediate principal stress. The permeability critical

point gradually disappears with prolonged water saturation time, indicating that water molecule infiltration reconstructs the fluid flow pathways within the fracture network.

2. Damage Evolution and Evaluation Methods under Cyclic Loading: During cyclic loading, the rate at which the hysteresis loop shifts to the right decreases with increasing water saturation time, reflecting the lubricating effect of water molecules in suppressing fatigue damage accumulation. Damage assessment based on cumulative acoustic emission counts indicates a positive correlation between hydraulic pressure and damage severity, while water saturation time is negatively correlated with damage severity. However, conventional formula-based methods have limitations in characterizing damage in water-saturated specimens. Pore water pressure evolution analysis shows that increasing hydraulic pressure elevates crack density in the σ_1 direction and alters the spatial distribution of fluid seepage pathways.

3. Failure Mode Transition under Multi-Field Coupling Effects: Natural specimens exhibit a distinct permeability threshold, with stress parameters increasing sharply after yielding. In contrast, water-saturated specimens experience mechanical degradation, leading to a wave-like fluctuation in the stress-time curve, with water flux variations lagging behind the yield point. Under true triaxial conditions, hydraulic pressure accelerates the transition into the steady strain phase while inducing repeated expansion-compression effects, ultimately causing a nonlinear surge in post-failure water flow.

4. Development of an Intelligent Damage Model and Engineering Applications: A fatigue damage model based on the complex plane is established, where the real part (fatigue damage) and the imaginary part (mechanical properties) exhibit a secondary negative correlation. By integrating neural network algorithms, the model is materialized. A developed visualization software (Windows platform) processes continuous variables to predict the mechanical parameter evolution under various hydraulic pressure-water saturation conditions, providing theoretical guidance for tunneling support in water-rich shale formations.

Chapter 6
Stability analysis and support scheme optimization of tunnels with saturated surrounding rock under cyclic stress disturbance

Chapter 4 and Chapter 5 analyze the impact of cyclic stress on the mechanical properties and permeability characteristics of saturated shale under both non-hydraulic and hydraulic conditions using laboratory experiments, theoretical analysis, and model development. To apply the laboratory experimental results to field scenarios and provide guidance for field construction, this chapter uses a Finite Difference 3D numerical model built with the FLAC3D software to simulate the excavation process of tunnels (Moysey et al., 2005; Zhang et al., 2017). The goal is to investigate the roof settlement, deformation of the tunnel walls, and the evolution of pore water pressure during excavation, and to provide support recommendations for saturated tunnels under cyclic stress disturbances.

Figure 6.1 shows the stress state of the surrounding rock during the tunnel excavation process, while Figure 6.2 presents the research roadmap for stability analysis and support scheme optimization of saturated surrounding rock under cyclic stress disturbances. As seen in Figure 6.2, the chapter first analyzes the stability of the tunnel excavation under natural conditions. Based on the results of the natural state analysis, the findings from Chapters 3 and 4 are incorporated into the model to analyze the excavation stability of both undrained and drained tunnels. Additionally, attempts are made to adjust the length and spacing of the anchor bolts to propose the most suitable support scheme for saturated tunnels under hydraulic disturbance.

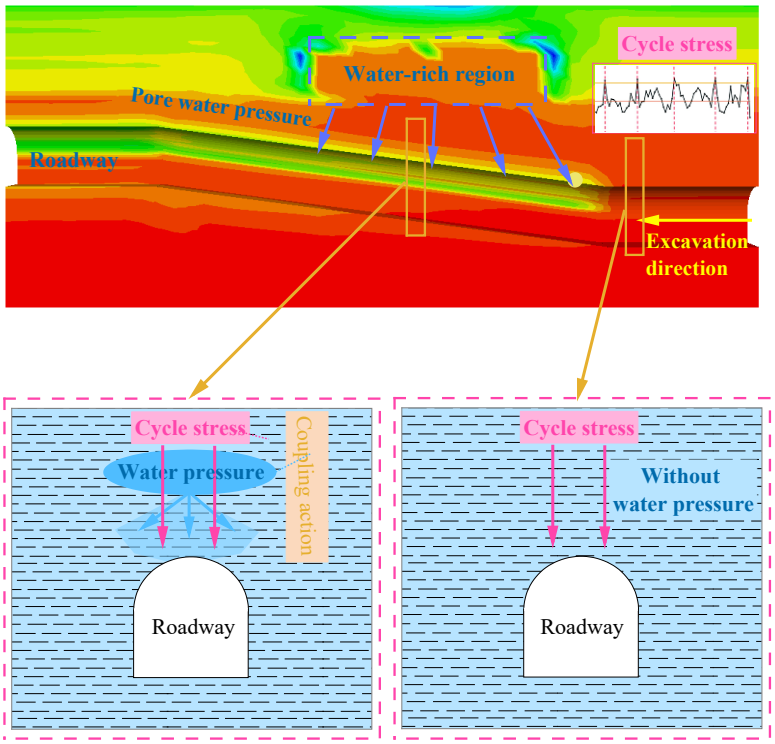

Fig. 6.1 Stress state of surrounding rock during tunnel excavation

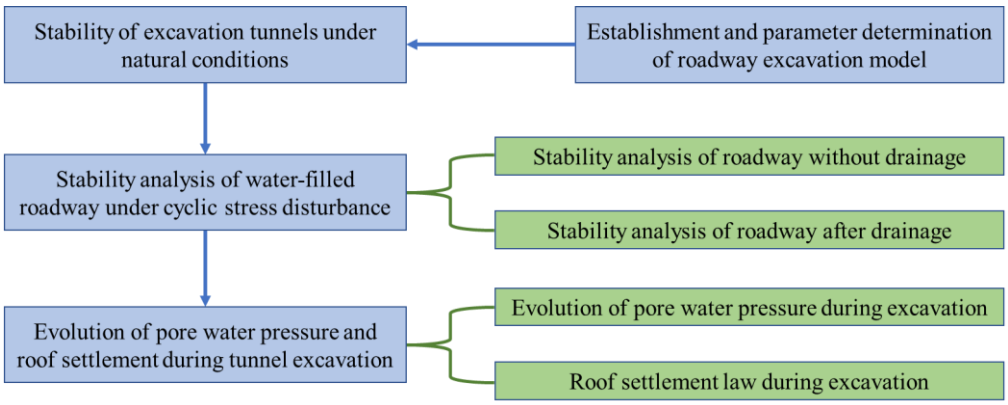

Fig. 6.2 Research roadmap of stability analysis and support scheme optimization of tunnel with saturated surrounding rock under cyclic stress disturbance

6.1 Establishment of tunnel excavation model and parameter determination

6.1.1 Basic principles of FLAC3D

FLAC3D software is primarily used for analyses and calculations related to underground engineering excavation, capable of simulating the stress and deformation processes of engineering structures within three-dimensional geological materials and other media. It is suitable for elastic-plastic analysis of materials, rheological predictions, and the simulation of geotechnical construction processes. In rapid Lagrangian analysis, FLAC3D employs a mixed discrete analysis method, dividing continuous media into hexahedral elements, with forces

concentrated at each node. During the computation, the stress and strain values of the hexahedral elements are obtained by volume-weighted averaging of their internal tetrahedra. For a tetrahedron with any point inside having a velocity component of u_i^0, the Gaussian formula gives:

$$\begin{cases} \iiint_V u_{i,j}^0 dV = \oiint_S u_i^0 n_j dS \\ u_{i,j} = -\frac{1}{3V}\sum_{l=1}^{4} u_i^l n_j^{(l)} S^{(l)} \end{cases} \tag{6.1}$$

where V is the volume of the tetrahedron, S is the surface area of the tetrahedron, n_j is the unit normal vector component of the outer surface, u_i^0 represents linear distribution, and n_j is constant on each face. The variable l is an index, with the superscript l indicating the variable at node l, and the superscript (l) indicating the variable at face l.

The three-dimensional rapid Lagrangian method focuses on nodes as computational objects, concentrating both force and mass at the nodes, and solving the motion equations in the time domain. The motion equation of the nodes can be expressed as follows:

$$\frac{\partial u_i^l}{\partial t} = \frac{F_i^l(t)}{m^l} \tag{6.2}$$

where $F_i^l(t)$ represents the unbalanced force component in the iii direction at node l at time t, and m^l is the concentrated mass at node l. For dynamic problems, concentrated mass is used, while for static problems, a virtual mass is applied to ensure numerical stability. For each tetrahedron, the virtual mass of its nodes is given by:

$$m^l = \frac{a_1}{9V}\max\left\{\left[n_i^{(i)} S^{(l)}\right]^2, i = 1,3\right\} \tag{6.3}$$

where $a_1 = K + \frac{4}{3G}$, Ks the bulk modulus and G is the shear modulus.

6.1.2 Anchor structure unit parameters

In FLAC3D software, the function of anchors is to provide localized resistance along joint surfaces, thereby preventing further expansion of separation [182]. The software includes a built-in Cable structure unit, which can generate shear resistance along its length, simulating the mechanical behavior of anchors in surrounding rock. The mechanical properties of the Cable structure unit are primarily influenced by factors such as its geometry and material.

The performance of the anchoring agent, as a critical element in the Cable structure unit, has a significant impact on the selection of parameters in numerical calculations and the resulting simulation outcomes. The main parameters include the bonding strength per unit length of the anchoring agent (c_g) and the stiffness per unit length of the agent (k_g). Based on the principles of the Cable structure unit, these two parameters can be calculated using equation (6.4):

$$\begin{cases} k_g = \frac{2\pi G}{10\ln\left(1+\frac{2l}{D}\right)} \\ c_g = \pi(D+2l)\tau_{peak} \end{cases} \tag{6.4}$$

where k_g is the stiffness of the anchoring agent per unit length (N/m^2); G is the shear modulus of the anchoring agent (GPa); D is the diameter of the anchor rod (m); l is the thickness of the anchoring agent (m), and τ_{peak} is the peak pull-out force (N) from the pull-out test.

In this study, the diameter of the anchor rod is 22 mm, with a maximum tensile breaking force of approximately 190 kN. According to field data and in-situ tests, when the anchorage length is 700 mm, the anchoring force is 168 kN, the elastic modulus of the anchoring agent is 13.5 GPa, the Poisson's ratio is 0.25, and the bonding strength per unit length of the anchoring agent is 2.5×10^5 N/m^2.

6.1.3 Introduction of water-force boundary condition and degradation model

The excavation of the tunnel is divided into two stages. The first stage introduces only the concepts of water saturation and cyclic stress. The implementation method is as follows: First, FISH language programming is used to define the function *va_1*, which incorporates a loop statement. Cyclic stress is applied to the roof of the first excavation stage, and the mechanical parameters of the water-saturated sample are imported into the first-stage model to achieve the combined effects of water saturation and cyclic stress. After the first-stage excavation is completed, a gradient water pressure (varying from 1–3 MPa, corresponding to Chapter 4) is applied to the rock mass above the second-stage excavation to realize the coupled effects of water saturation and cyclic stress under variable water pressure. The pseudocode for the FISH language is shown in Algorithm 5.1.

Algorithm 5.1

```
zone property {E_1, c_1, φ_1, etc.} range z @z_1-s, z_1-e
zone property {E_2, c_2, φ_2, etc.} range z @z_2-s, z_2-e
bound stress 0,P,0,0, ∇,0 range z @z_2-s, z_2-e y @y_zone
zone gridpoint initialize pore-pressure @P range z @z_2-s, z_2-e y @y_zone
define va_1
  β=0
  σ_cycle=σ_basic·math.sin(β·math.degrad)
  loop while β < 360
    command
      bound stress 0,@σ_cycle,0,0,0,0 range y @y_zone
      model cycle 10
    endcommand
    β=β+10
  endloop
end
@ va_1
```

In Algorithm 5.1, z_{n-s} (n=1,2) denotes the start of the nth stage, z_{n-e} (n=1,2) denotes the end of the nth stage, σ_{cycle} is the cyclic stress, y_{zone} is the range of cyclic stress

application, and *P* is the water pressure. The water pressure is applied with a gradient, i.e., $P = \rho g d_z$, which changes with excavation distance.

After introducing the hydro-mechanical boundary conditions, the FISH language is used to integrate the mechanical degradation model obtained in Chapter 4 into FLAC3D. The relationship between fatigue damage and the degradation of surrounding rock mechanical properties is utilized to determine the mechanical parameters of the surrounding rock. As shown in Figure 4.28, the fatigue characteristics of water-saturated samples are positively correlated with water pressure, but the damage degree during cyclic loading initially increases and then decreases with prolonged saturation. This indicates that water saturation and cyclic loading not only affect the mechanical properties of the sample but also influence each other's degradation effects. Under saturated conditions, the degradation of mechanical performance and fatigue damage are nonlinearly correlated. Therefore, the FISH language is employed to import the model results into FLAC3D, with specific details provided in Algorithm 5.2.

Algorithm 5.2

```
zone property {c_0, φ_0, etc.} range z @z_1, z_2
define va_2
  α=1
  loop while α<=n
    c_1 = λ^α c_0, φ_1 = λ^α φ_0
    [va_1]: (bound stress σ_cycle)
    command
    zone property {c_1, φ_1, etc.} range z @z_1, z_2
    endcommand
  α=α+1
  endloop
end
@ va_2
```

In Algorithm 5.2, λ is the degradation model exponent for shale, α is the number of cyclic loading cycles, *n* is the upper limit of cyclic loading cycles, and [*va_1*] refers to the cyclic stress application procedure in Algorithm 5.1. By combining Algorithm 5.1 and Algorithm 5.2, cyclic stress, water pressure, and the established degradation model can be integrated into FLAC3D to calculate the stability of the excavated tunnel.6.1.4 Establishment of tunnel excavation model based on FLAC3D

Based on the actual conditions of a mine site in Kunyang, a FLAC3D model was established to simulate the excavation process of a specific tunnel in the mine. The model monitors the evolution of the plastic zone in the surrounding rock and the settlement of the roof during excavation, as shown in Figure 6.3.

In Fig. 6.3, the total dimensions of the model are 50 × 20 × 20 m^3, and the tunnel width is 4 m. The bottom of the model is constrained by normal displacement, while the sides and top

are free boundaries. The model uses the Mohr-Coulomb criterion, and the excavation direction in the model is from right to left. According to the distribution of the mine's ore layers, the first section is set to be excavated horizontally, and the second section is excavated at a 15° angle to the horizontal. Anchor support is applied promptly after excavation, with a default spacing of 1.2 m between anchors along the excavation direction.

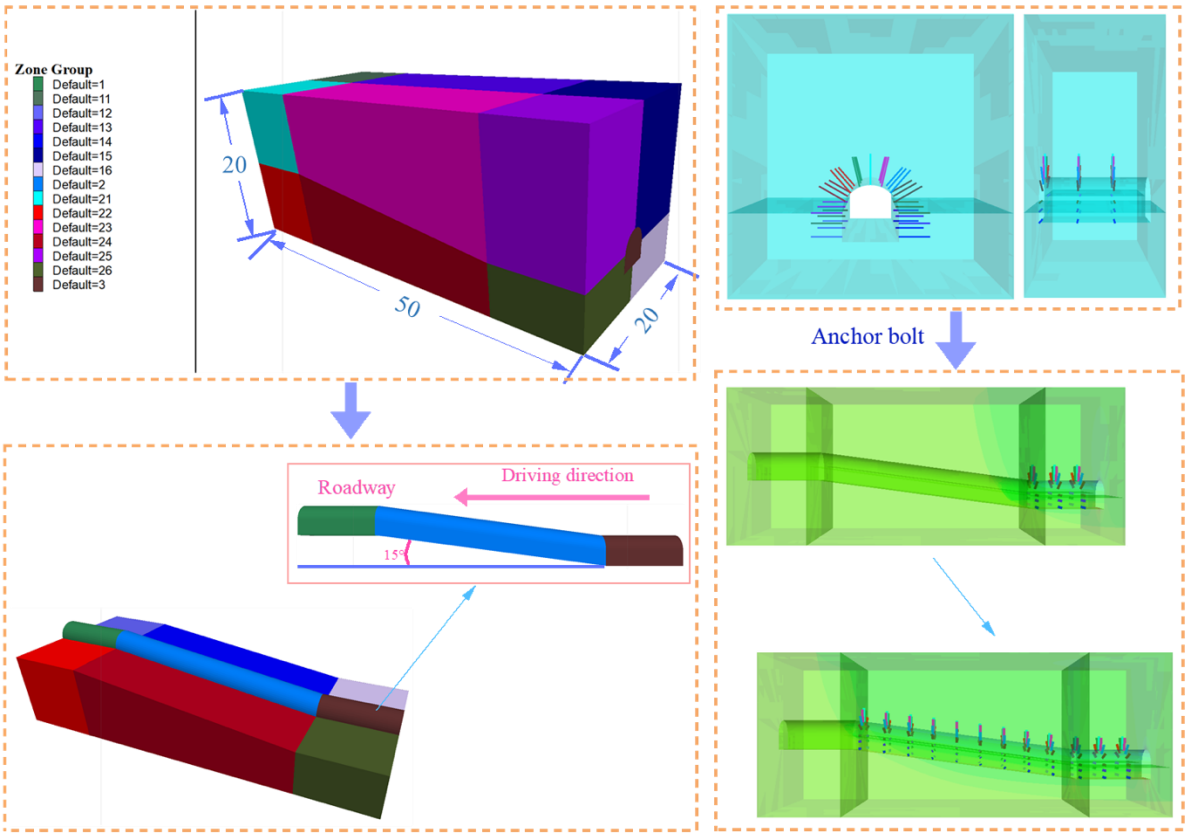

(a)

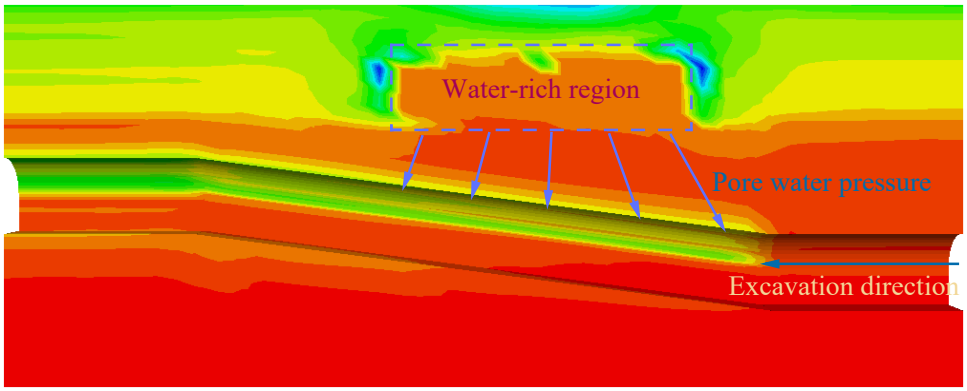

(b)

Fig. 6.3 Tunnel excavation model and bolt support diagram based on FLAC3D. (a) Model and bolt support scheme. (b) rock division and water-rich area.

6.1.5 Determination of mechanical parameters of the ore layer

Before model calculation, the mechanical parameters of the ore layer under natural and saturated conditions (vacuum-saturated for 48 hours) need to be determined. Figure 6.4 presents the conventional triaxial compression test stress-strain curves for phosphorite rock samples from the ore layer.

As shown in Figure 6.4, under all confining pressures, the strength of the natural samples is greater than that of the saturated samples, and the peak strain (the strain corresponding to peak strength) of the natural samples is also greater than that of the saturated samples. This indicates that after saturation, both the strength and deformation resistance of the samples significantly decrease.

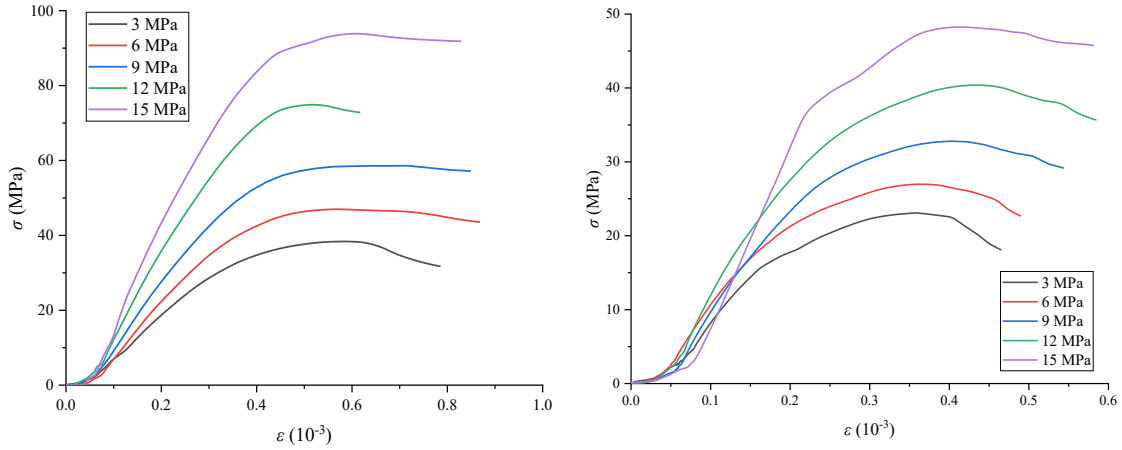

Fig. 6.4 Stress-strain curves of tunnel roof and floor samples under conventional triaxial compression test. (a) Natural samples.(b) Water saturated samples.

Both the peak strength and peak strain of the natural and saturated samples in triaxial compression show a clear positive correlation with confining pressure, consistent with the Mohr-Coulomb strength criterion. A scatter plot of peak strength versus confining pressure was obtained through regression, as shown in Figure 6.6. By substituting the intercept (uniaxial strength) and slope (confining pressure coefficient) from the fitted curve in Figure 6.5 into equations (3.12)–(3.15), the cohesion and internal friction angle of each set of samples were calculated.

$$\begin{cases} c = 4.86\ \text{MPa}, \varphi = 40.1° \text{ (Nature)} \\ c = 5.21\ MPa, \varphi = 21.2° \text{ (Water saturated)} \end{cases} \tag{6.5}$$

According to the Mohr-Coulomb criterion, the relationship between the sample strength parameters is as follows:

$$\begin{cases} \sigma_c = \frac{2c\ cos\varphi}{1-sin\varphi} \\ \sigma_t = \frac{2c\ cos\varphi}{1+sin\varphi} \end{cases} \tag{6.6}$$

According to equation (6.6), the mechanical parameters of the samples under different conditions can be obtained, as shown in Table 6.1.

Table 6.1 Mechanical parameters of tunnel roof and floor samples

Group	ρ (kg/m^3)	c (MPa)	φ (°)	σ_c (MPa)	σ_t (MPa)
Natural samples	2850	4.86	40.1	20.9	4.51
Water saturated samples	2960	7.14	21.2	30.3	7.14

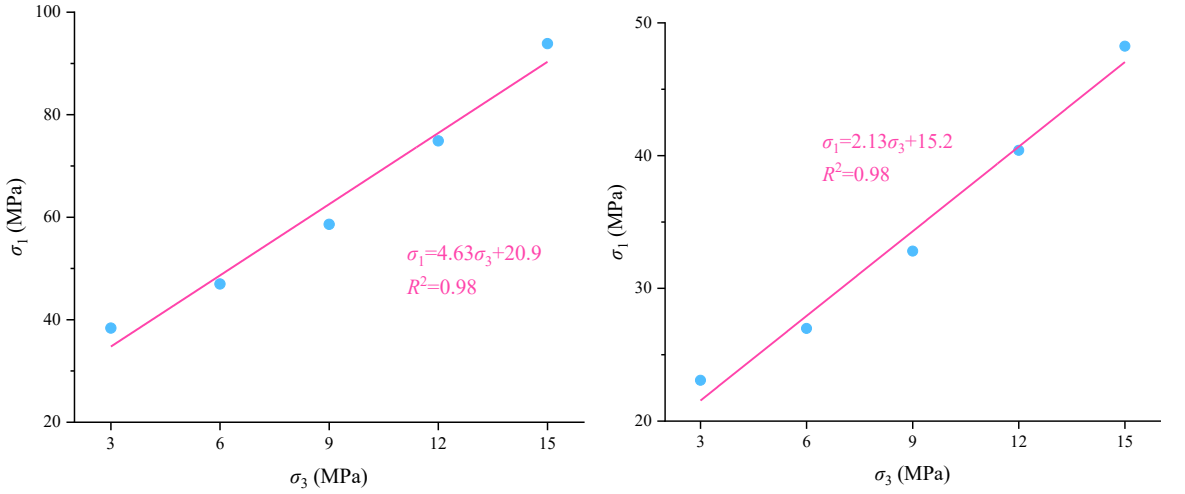

Fig. 6.5 Relationship between peak strength and confining pressure of samples. (a) Natural samples. (b) Water saturated samples.

6.1.6 Determination of mechanical parameters of shale in roof and floor under different conditions

Using the Mogi-Coulomb criterion, regression analysis was performed on the data from true triaxial tests in Chapter 4 to obtain the model parameters under natural, saturated, and "saturated + fatigue loading" conditions. In laboratory tests, true triaxial tests better simulate the process of rock mass transitioning from an in-situ stress state to post-failure under loading while considering the influence of the intermediate principal stress, yielding more accurate results than conventional triaxial tests. The Mogi-Coulomb criterion is used to calculate the mechanical parameters of samples under the coupling effect of saturation and fatigue stress, providing more precise mechanical parameters for numerical models.

The Mogi-Coulomb criterion describes a monotonically increasing relationship between octahedral shear stress and effective mean normal stress:

$$\begin{cases} \tau_{oct} = a + b\sigma_{m,2} \\ \tau_{oct} = \frac{1}{3}\sqrt{(\sigma_1-\sigma_3)^2+(\sigma_1-\sigma_2)^2+(\sigma_2-\sigma_3)^2} \\ \sigma_{m,2} = \frac{\sigma_1+\sigma_3}{2} \end{cases} \tag{6.7}$$

where τ_{oct} is the octahedral shear stress, $\sigma_{m,2}$ is the effective mean normal stress, a is the intercept of the Mogi-Coulomb criterion fitting line, and b is the slope of the line.

Equation (6.7) is used to calculate the values of τ_{oct} and $\sigma_{m,2}$ for samples under different conditions. A linear fitting method is used to derive the Mogi-Coulomb criterion equation for the samples, as shown in Figure 6.6.

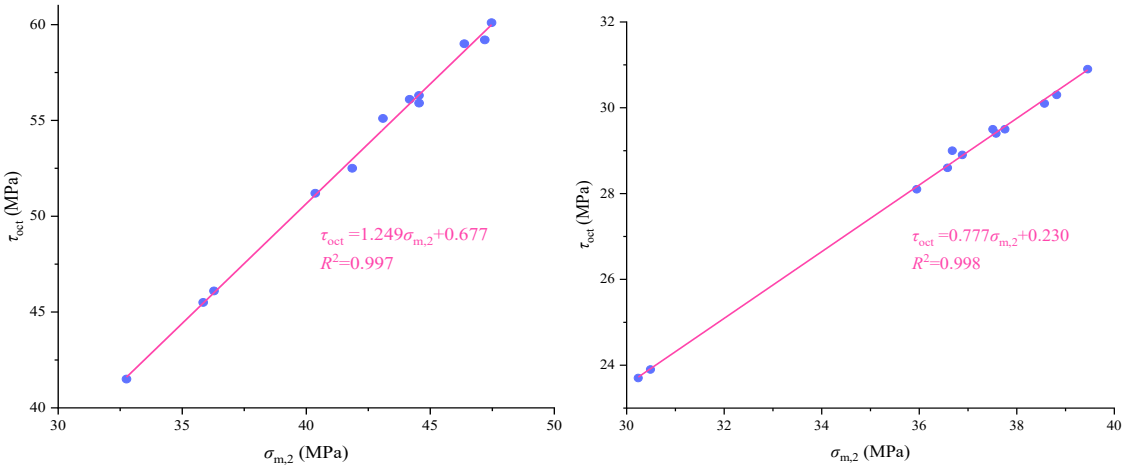

(a) (b)

Fig. 6.6 Mogi-Coulomb criteria were used to fit the curves of samples under different conditions. (a) Water saturated. (b) Water saturated + fatigue loading.

In Figure 6.6, the Mogi-Coulomb fitting equations for saturated and fatigue-saturated samples are:

$$\begin{cases} \tau_{oct} = 0.677 + 1.249\sigma_{m,2}\ (饱水) \\ \tau_{oct} = 0.230 + 0.777\sigma_{m,2}\ (疲劳饱水) \end{cases} \tag{6.8}$$

For the saturated samples, the Mogi-Coulomb parameters are {a=0.677, b=1.249} , and for the fatigue-saturated samples, the parameters are {a=0.230, b=0.777}.

The conversion formulas between the Mogi-Coulomb parameters and Mohr-Coulomb parameters are:

$$\begin{cases} a = \frac{2\sqrt{2}}{3}c\cos\varphi \\ b = \frac{2\sqrt{3}}{3}\sin\varphi \end{cases} \tag{6.9}$$

Substituting the Mogi-Coulomb parameters into Equation (6.9), the Mohr-Coulomb mechanical parameters for the two sets of samples are obtained as:

$$\begin{cases} c = 1.64\ \text{MPa}, \varphi = 35.87° \ (Water\ saturation) \\ c = 0.84\ \text{MPa}, \varphi = 11.50° \ (Water\ saturation\ and\ fatigue\ loading) \end{cases} \tag{6.10}$$

Similarly, according to the Mohr-Coulomb criterion, the relationship between the strength parameters is:

$$\begin{cases} \sigma_c = \frac{2c\cos\varphi}{1-\sin\varphi} \\ \sigma_t = \frac{2c\cos\varphi}{1+\sin\varphi} \end{cases} \tag{6.11}$$

By substituting Equation (6.10) into Equation (6.11), the uniaxial compressive strength and tensile strength parameters for the samples are obtained, as shown in Table 6.2.

Table 6.2 Mechanical parameters of shale under natural, water saturation and " water saturation + fatigue loading" conditions

Group	ρ (kg/m^3)	c (MPa)	φ (°)	σ_c (MPa)	σ_t (MPa)
Natural [50]	2679	15.3	34.9	58.6	16.0
Water saturated	2784	1.64	35.9	6.42	1.68
Water saturated + Fatigue loading	2784	0.84	11.5	2.05	1.37

6.2 Stability analysis of excavated tunnels under natural conditions

The mechanical parameters of the rock layers in their natural state from Tables 6.1 and 6.2 are imported into the model shown in Figure 6.3. The roof settlement and plastic zone characteristics of the excavated tunnel are calculated for two scenarios: without anchor support and with anchor support (with a bolt diameter of 22 mm, a length of 1800 mm, and a spacing of 1.2 m along the excavation direction), as illustrated in Figure 6.7 and Table 6.3.

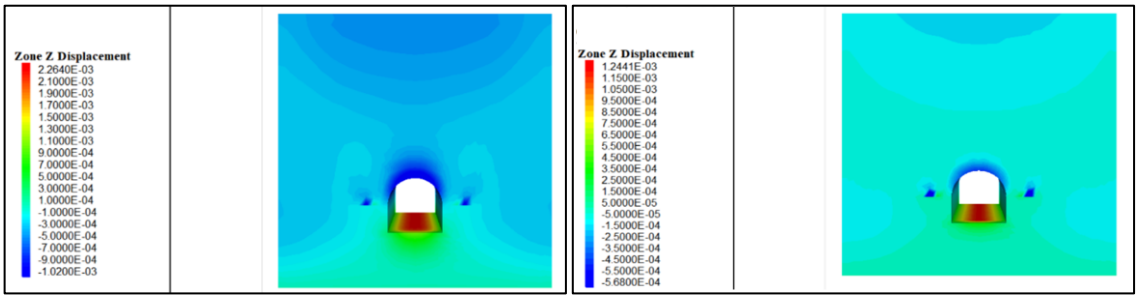

(a) (b)

Fig. 6.7 Roof settlement during the excavation of the first segment of the tunnel under natural conditions. (a) Without Support. (b) With Support.

As shown in Figure 6.7, without the use of anchor bolt support, the maximum roof settlement during the excavation of the first section of the tunnel under natural conditions is 1.020 mm. When anchor bolts are used for support, the maximum settlement is reduced to 0.568 mm, resulting in a 44.3% reduction in roof settlement. According to Table 6.3, without support, after the excavation of the first section under natural conditions, significant plastic zones appear

at section 1 of the tunnel, primarily manifested as shear failure. After the excavation of the second section, the plastic zones at section 2 develop more clearly, with shear failure extending from the sidewalls to the floor. After the completion of the second section excavation, the plastic failure area at section 3 further increases, extending from the sidewalls to the roof and floor of the tunnel. However, with anchor bolt support, the plastic zone in the sidewalls at the three sections is significantly reduced, and the stability of the sidewalls and roof is greatly improved.

This phenomenon indicates that the anchor bolts effectively control the deformation of the surrounding rock, reducing plastic failure, particularly in the sidewalls and roof areas. The anchor bolt support strengthens the surrounding rock, improving its shear resistance, inhibiting the expansion of the plastic zone, and ensuring the stability of the surrounding rock after excavation, thus reducing the extent of plastic failure during the excavation process. Based on the results from Figure 6.7 and Table 6.3, the anchor bolt support with a spacing of 1.2 meters plays a crucial role in the stability of the tunnel surrounding rock. Particularly in the early stages of excavation, the anchor bolt support helps ensure the stability of the surrounding rock by suppressing stress concentration and surrounding rock deformation.

Table 6.3 Plastic zone of surrounding rock during tunnel excavation under natural conditions

	Section 3	Section 2	Section 1
Unsupported	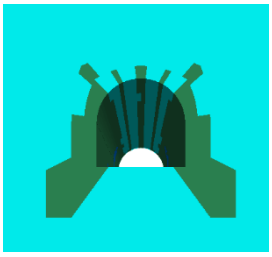	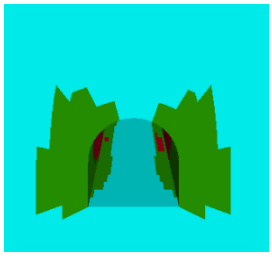	
Supported		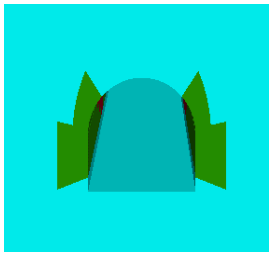	

Cross-Section Schematic	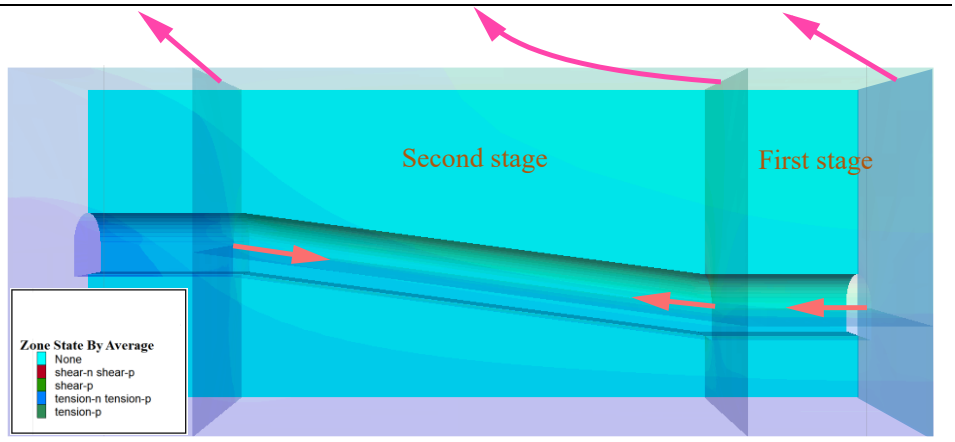

6.3 Stability analysis of fatigue-saturated tunnels

6.3.1 Stability analysis of fatigue-saturated tunnels without drainage

Figures 6.8 and 6.9 illustrate the roof settlement and plastic zone characteristics of the excavated tunnel before drainage. From Figure 6.8, it is evident that, without drainage, the maximum roof settlement during the excavation of the first segment of the fatigue-saturated tunnel reaches 5.009 mm, an increase of 3.989 mm compared to the natural tunnel (1.020 mm), representing a 391% increase. Figure 6.9 shows that under undrained conditions, significant plastic zones develop in the tunnel cross-section at all excavation stages. The fractured zones are uniformly and continuously distributed across the roof, floor, and walls of the tunnel, and under the influence of water pressure, numerous plastic damage regions also appear in the upper area of the tunnel.

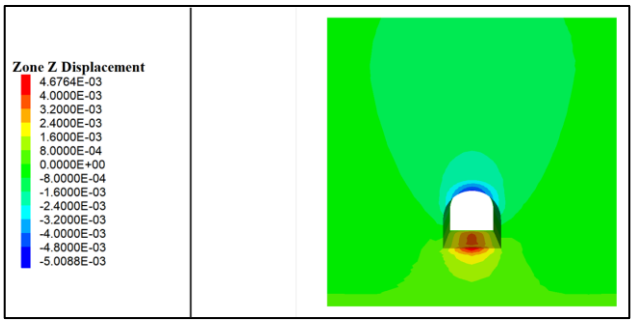

Fig. 6.8 Subsidence of roof during excavation of the first section of tunnel

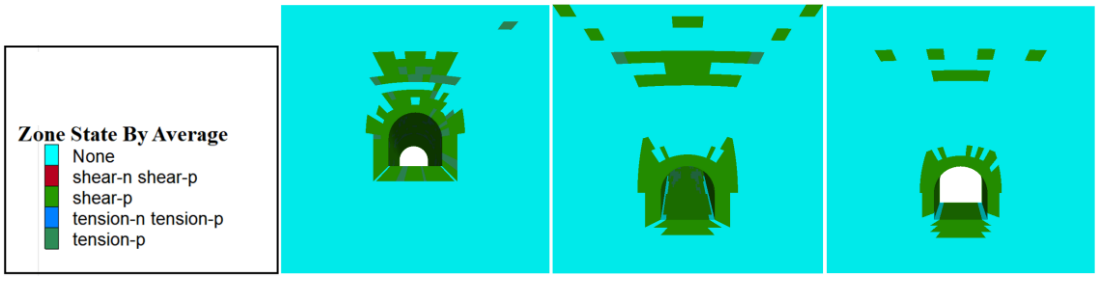

(a) (b) (c) (d)

Fig. 6.9 Plastic Zone Characteristics of the Surrounding Rock after Excavation of the Fatigue-Saturated Tunnel before Drainage. (a) Legend. (b) Section 3. (c) Section 2. (d) Section 1.

Figure 6.10 displays the evolution characteristics of pore water pressure in the water-rich zone above the second segment of the excavated tunnel before drainage. It can be observed from Figure 6.10 that after the excavation of both segments of the tunnel, the substantial subsidence of the roof causes the water in the water-rich zone to gradually extend downward with the excavation. The pore water pressure concentrates in the first segment and the front of the second segment of the tunnel, reaching a maximum value of approximately 1.5 MPa, indicating significant water pressure on the roof.

The above results indicate that the water pressure above the tunnel has a significant impact on the roof settlement and the development of plastic zones in the surrounding rock during excavation. To ensure the stability of the surrounding rock during the excavation process, it is necessary to conduct drainage of the tunnel roof before excavation.

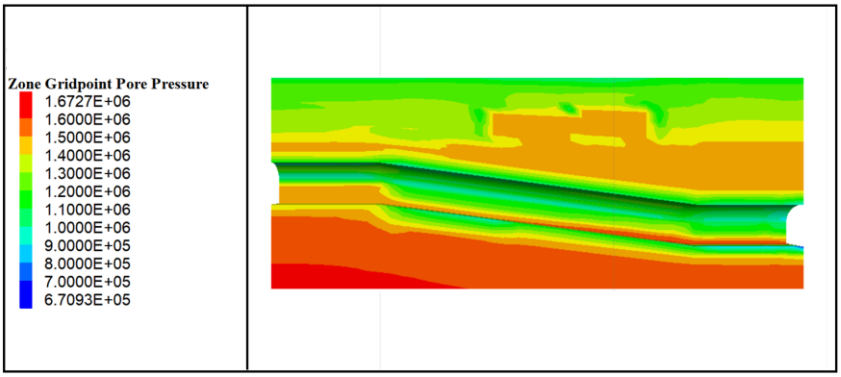

Fig. 6.10 Distribution of pore water pressure in rock mass after excavation of fatigued water-saturated tunnel before drainage.

6.3.2 Stability analysis of fatigue-saturated tunnels after drainage

As previously analyzed, the mechanical properties of the surrounding rock under fatigue-saturated conditions deteriorate, leading to a reduction in the stability of the surrounding rock after tunnel excavation. To maintain stability during excavation under fatigue-saturated conditions, drainage holes are first drilled in the tunnel roof, followed by the optimization of the support scheme in an attempt to propose a support solution suitable for fatigue-saturated tunnels.

The mechanical parameters of the surrounding rock in a fatigue-saturated state from Table 6.2 were incorporated into the model shown in Figure 6.3. Different support schemes were applied (with anchor lengths of 1800 mm, 2000 mm, and 2200 mm; and anchor spacings of 1.2 m, 1 m, and 0.8 m) to support the excavated tunnel, as illustrated in Figure 6.11.

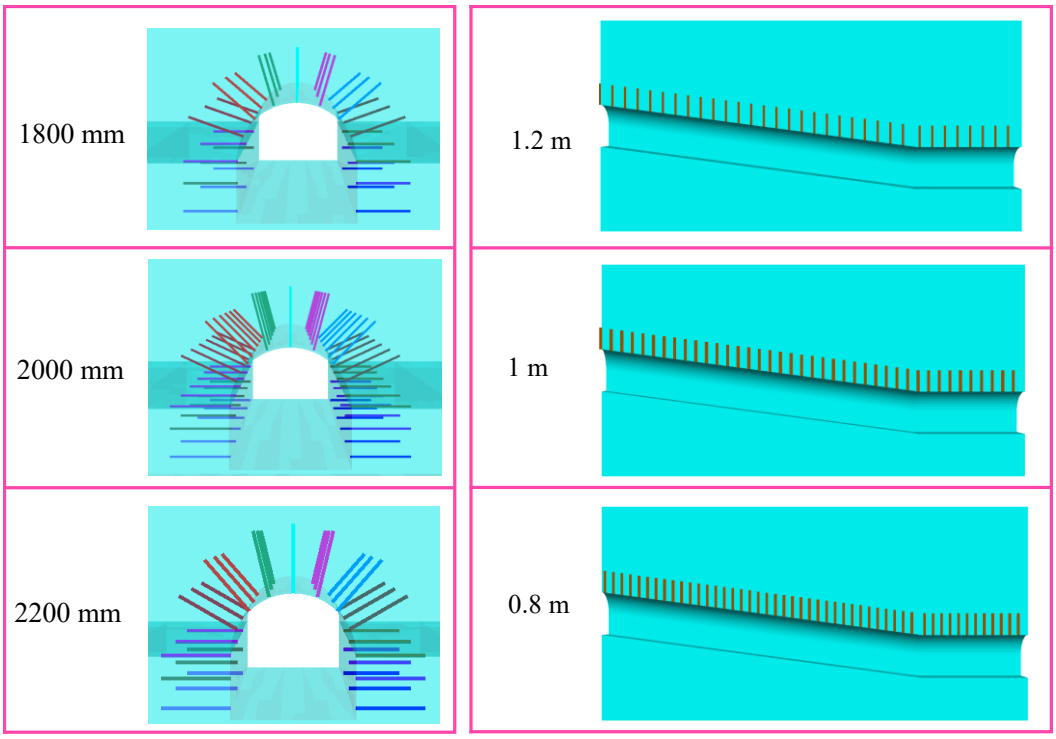

(a) (b)

Fig. 6.11 Bolt layout of tunnel under different bolt length and spacing schemes. (a) bolt length. (b) bolt spacing.

6.3.2.1 Influence of anchor length on tunnel stability

First, the impact of anchor length on the stability of the surrounding rock is analyzed. Figure 6.12 presents the development patterns of the plastic zones in the excavated tunnel sections for anchor lengths of 1800 mm, 2000 mm, and 2200 mm (with an anchor spacing of 1.2 m along the excavation direction). Figure 6.13 illustrates the roof settlement of the fatigue-saturated tunnel under different anchor lengths.

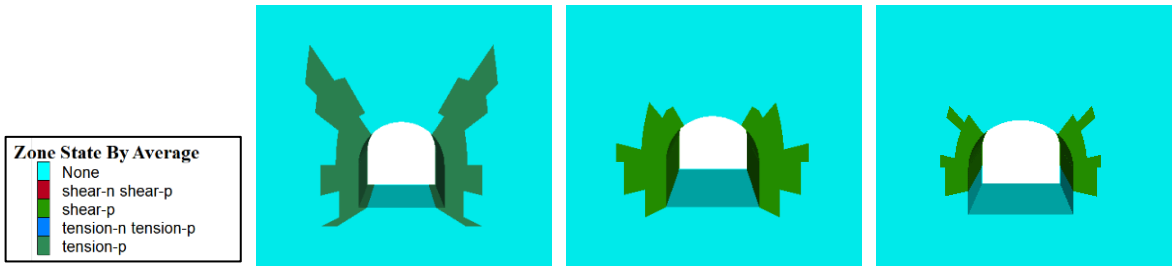

(a) (b) (c) (d)

Figure 6.12 Plastic zone characteristics of surrounding rock of water-saturated tunnel under different bolt length. (a) Legend. (b) Bolt length: 1800 mm. (c) bolt length: 2000 mm. (d) bolt length: 2200 mm.

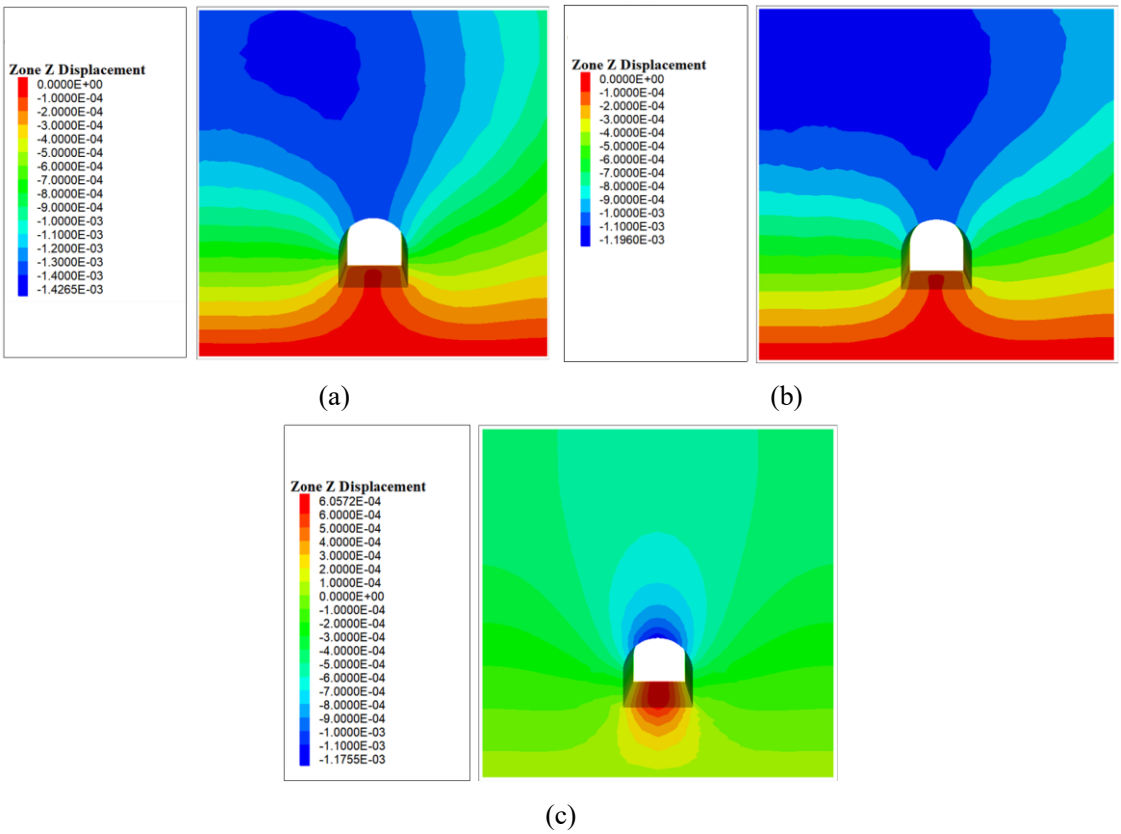

Fig. 6.13 Roof settlement of fatigue-saturated tunnel under different bolt length. (a) Bolt length: 1800 mm. (b) bolt length: 2000 mm. (c) bolt length: 2200 mm.

From Figures 6.12 and 6.13, it can be seen that when the anchor bolt length is 1800 mm, after the excavation of the tunnel, the plastic zone of the sidewalls and roof/floor is relatively large. The fracture zone of the sidewalls extends deeper into the sidewalls and the overlying rock layers, with an increasing affected area. The maximum settlement at the top of the tunnel reaches 1.43 mm. When the anchor bolt length is increased to 2000 mm and 2200 mm, the plastic zone of the sidewalls and roof/floor is significantly reduced after excavation. No significant plastic deformation is observed at the tunnel roof, and the maximum settlement at the top of the tunnel decreases to 1.20 mm and 1.18 mm, representing a reduction of 16.1% and 17.5%, respectively, compared to the 1800 mm anchor bolt length. This is because the main function of the anchor bolt is to provide tensile and shear resistance by restraining and supporting the surrounding rock, preventing excessive deformation. Shorter anchor bolts (such as 1800 mm) are unable to provide enough support force after excavation, leading to ineffective stress distribution and the expansion of the plastic zone and deformation. However, as the anchor bolt length increases, it can penetrate deeper into the surrounding rock and form effective contact, improving the surrounding rock's resistance to deformation and limiting the expansion of the plastic zone. Additionally, longer anchor bolts provide stronger support, effectively transmitting the localized stress generated during excavation to deeper surrounding rock, thereby alleviating stress concentration. By extending the length of the anchor bolts, the

overall stability of the surrounding rock is enhanced, and the plastic zone is reduced, especially in the roof and sidewall areas, where deformation is effectively controlled.

Figure 6.14 shows the evolution of pore water pressure in the water-rich zone above the second section of the saturated tunnel under cyclic stress disturbance for different anchor bolt lengths. From Figure 6.14, it is evident that with an anchor bolt length of 1800 mm, after excavation of the saturated fatigue tunnel, localized pore water pressure concentration zones appear above the roof of both the first and second sections of the tunnel, with a maximum pore water pressure of 0.67 MPa. When the anchor bolt length is 2000 mm, the pore water pressure concentration zone above the first section of the tunnel disappears, and the concentration zone above the second section is significantly reduced. With an anchor bolt length of 2200 mm, the pore water pressure distribution above the tunnel roof becomes more uniform, and the pore water pressure concentration zones above both sections of the tunnel disappear. The maximum pore water pressure decreases to approximately 0.5 MPa.

After excavation, the deformation of the surrounding rock causes water to infiltrate into the excavation face, forming pressure concentration zones in localized areas. Shorter anchor bolts (such as 1800 mm) fail to effectively suppress this water pressure concentration, resulting in higher and unevenly distributed pore water pressure. As the anchor bolt length increases, the stability of the surrounding rock is enhanced, and the infiltration path of the water is effectively restrained, leading to a more uniform distribution of pore water pressure. Particularly with 2200 mm anchor bolt support, the concentration of pore water pressure disappears, indicating that longer anchor bolts can effectively prevent water pressure concentration and reduce potential water-related hazards.

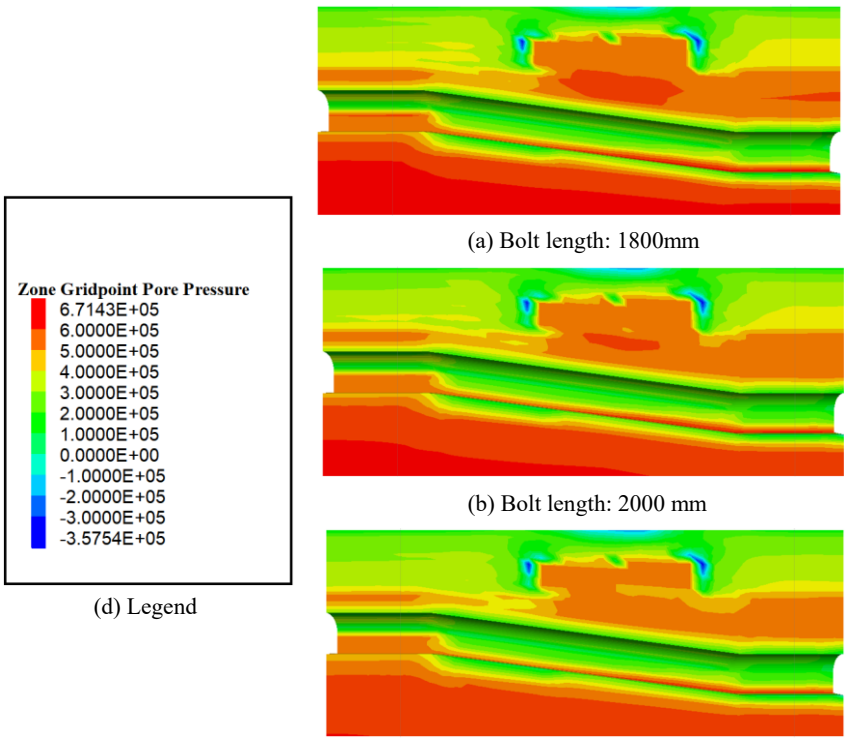

(a) Bolt length: 1800mm

(b) Bolt length: 2000 mm

(c) Bolt length: 2200 mm

(d) Legend

Fig. 6.14 Pore water pressure distribution of roof after excavation of fatigue-saturated tunnel under different bolt lengths.

After comprehensively comparing the distribution patterns of pore water pressure on the tunnel roof, roof settlement, and characteristics of the plastic zones, the support scheme with an anchor length of 2200 mm is selected for further analysis.

6.3.2.2 The impact of anchor spacing on tunnel stability during excavation

After setting the anchor length to 2000 mm, the development patterns of the plastic zones in the tunnel walls, roof, and floor were analyzed with anchor spacings of 1.2, 1, and 0.8 m. The findings are summarized in Table 6.4 and illustrated in Figure 6.15.

Table 6.4 Plastic zone characteristics of surrounding rock of water-saturated tunnel under different bolt layout spacing

	Section 3	Section 2	Section 1
Anchor rod spacing: 1.2 m	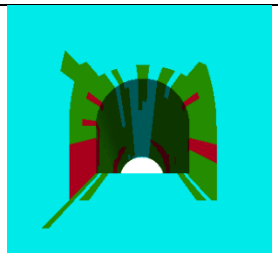	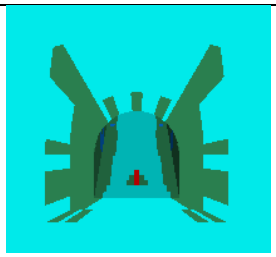	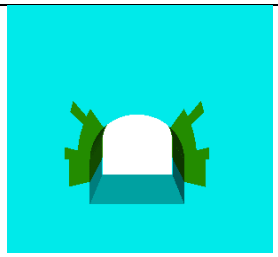

Anchor rod spacing: 1 m	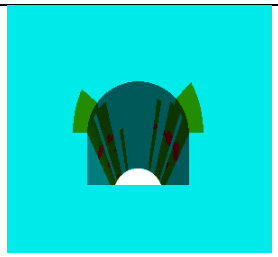	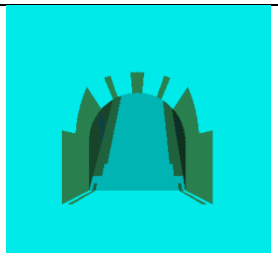	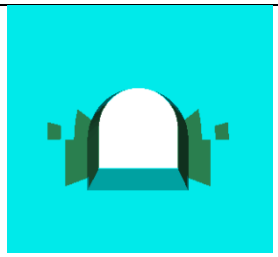
Anchor rod spacing: 0.8 m	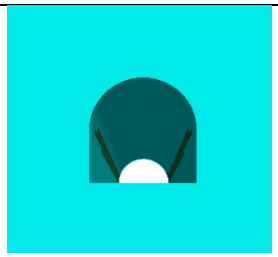		

From Table 6.4, it can be observed that with an anchor bolt spacing of 1.2 m, after the excavation of the first section of the tunnel, a distinct plastic zone appears at Section 1, manifesting as shear failure. After the excavation of the second section, the plastic zone at Section 2 gradually extends deeper into the sidewalls and overlying rock layers, with the affected area continuously expanding. After the completion of the second section excavation, the plastic zone at Section 3 further extends from the sidewalls to the roof and floor of the tunnel, gradually connecting, and the stability of the surrounding rock decreases further. This indicates that the support scheme with a 1.2 m anchor bolt spacing can no longer support the excavation stability of the saturated tunnel under cyclic stress disturbance. As the anchor bolt spacing decreases, the extent of the plastic zone at each section gradually becomes smaller, especially when the anchor bolt spacing is 0.8 m, where the plastic zone at the sidewalls of the excavated tunnel almost disappears, and the stability of the surrounding rock is significantly improved.

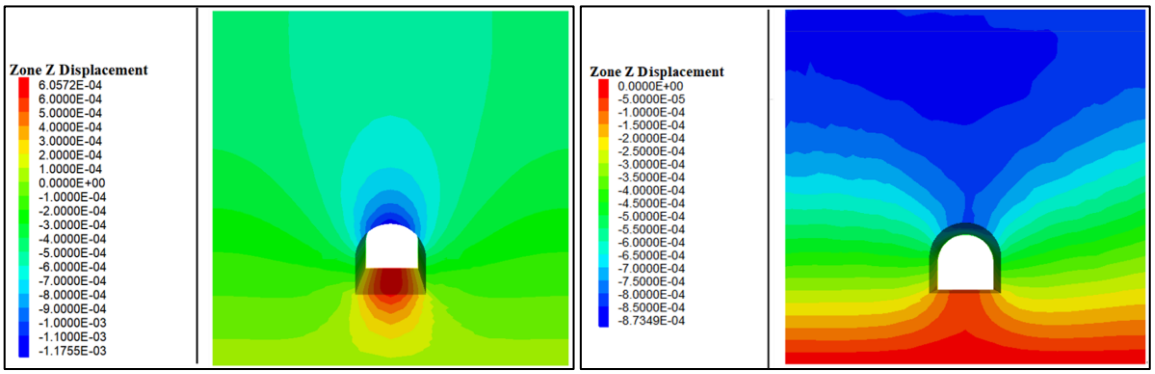

(a) (b)

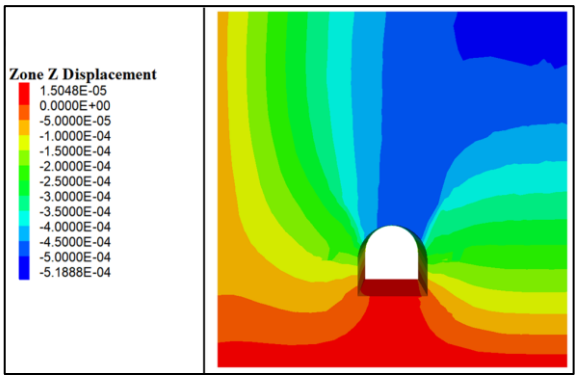

(c)

Fig. 6.15 Roof settlement of fatigue-saturated tunnel under different bolt layout spacing. (a) bolt spacing: 1.2 m. (b) bolt spacing: 1 m. (c) bolt spacing: 0.8 m.

At the same time, as shown in Figure 6.15, with an anchor bolt spacing of 1.2 m, the maximum settlement of the roof after the excavation of the first section is 1.196 mm. When the anchor bolt spacing is 1 m and 0.8 m, the settlement of the tunnel roof is reduced to 0.874 mm and 0.519 mm, representing a decrease of 26.9% and 56.6%, respectively. This demonstrates that as the anchor bolt spacing is reduced, the settlement of the tunnel roof decreases significantly.

The main function of the anchor bolt is to reinforce the surrounding rock, reducing deformation and preventing the expansion of the plastic zone. When the anchor bolt spacing is 1.2 m, the influence range of a single anchor bolt is relatively large, leading to insufficient support for the surrounding rock after excavation. Stress easily concentrates in localized areas, causing the expansion of the plastic zone. At this point, due to insufficient support force from the anchor bolts, the deformation of the surrounding rock is significant, leading to extensive shear failure in the sidewalls and roof/floor. When the anchor bolt spacing is reduced to 1 m and 0.8 m, the influence range of a single anchor bolt decreases, and the supporting force is enhanced. This allows better control over the deformation of the local surrounding rock, improving the overall stability of the surrounding rock and significantly reducing the extent of the plastic zone. Especially with a 0.8 m anchor bolt spacing, the plastic zone in the surrounding rock nearly disappears, showing a better support effect.

Figure 6.16 illustrates the evolution of pore water pressure in the water-rich zone above the second section of the tunnel for different anchor bolt spacings. From Figure 6.16, it is evident that compared to an anchor bolt spacing of 1.2 m (length: 2200 mm), when the spacing is reduced to 1 m, the pore water pressure above the roof of the first section of the tunnel decreases further, reducing to approximately 0.5 MPa. The region of concentrated pore water pressure above the second section also diminishes. When the anchor bolt spacing is reduced to 0.8 m, the pore water pressure decreases further after excavation, and with the continued reduction of the roof settlement and the further reduction in the development range of the plastic

zone, the pore water pressure above both sections of the tunnel reduces to approximately 0.4 MPa.

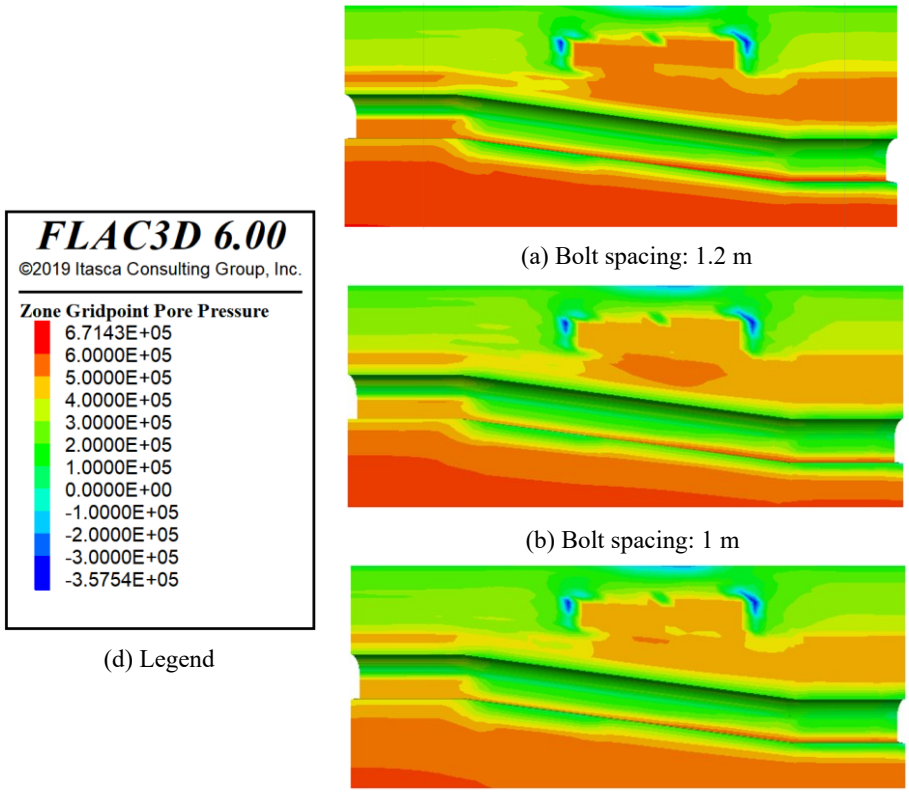

(a) Bolt spacing: 1.2 m

(b) Bolt spacing: 1 m

(c) Bolt spacing: 0.8 m

(d) Legend

Fig. 6.16 Pore water pressure distribution of roof after excavation of fatigue-saturated tunnel with different bolt spacing

The distribution of pore water pressure is closely related to the stability of the surrounding rock. Larger pore water pressure typically indicates strong water infiltration or water accumulation in the surrounding rock, which can lead to the instability of the surrounding rock. When the anchor bolt spacing is large, the support force distribution is sparse, and the pore water pressure in the surrounding rock is prone to concentrate in certain areas, causing localized pressure anomalies. As the anchor bolt spacing decreases, the support density increases, enabling a more uniform distribution of support force, inhibiting water accumulation, and making the pore water pressure distribution more uniform after excavation. The pressure value is significantly reduced.

Based on the analysis of the pore water pressure distribution, the surrounding plastic zone, and roof settlement, it can be concluded that the support scheme with a 0.8 m anchor bolt spacing is more suitable for the excavation support of a saturated tunnel under cyclic stress disturbance.

6.4 Evolution of pore water pressure and roof settlement during tunnel excavation

6.4.1 Evolution of pore water pressure in the roof during tunnel excavation

Figure 6.17 presents the evolution characteristics of pore water pressure in the roof during the excavation of a saturated tunnel under cyclic stress disturbance. From Figure 6.17, it can be observed that after applying the recommended support scheme (anchor bolt length of 2200 mm and spacing of 0.8 m), the evolution of pore water pressure in the roof gradually extends and concentrates towards the excavation direction, eventually spreading and dissipating.

In the early stages of the first section excavation, as the roof settlement increases, the original equilibrium of pore water pressure above the roof is disrupted. Water begins to infiltrate in the direction of the excavation, and the water pressure gradually extends towards the excavation, forming localized pressure concentration areas (see Excavation Phase 1-3). This occurs because, before excavation, the water above the roof is in a state of hydrostatic equilibrium, with the pore water pressure evenly distributed. After excavation, the settlement of the roof causes the imbalance of the original pore water pressure. The volume contraction of the rock skeleton increases the water pressure in the pore space near the excavation, leading to pressure concentration. After the completion of the first section excavation, due to the improved anchor bolt support scheme, the roof settlement rate is suppressed, and the range of water pressure concentration starts to decrease. After the model calculation reaches equilibrium, the water pressure distribution above the first section roof gradually becomes more uniform (see Excavation Phase 1-4).

After the excavation of the second section, the water pressure concentration areas above the roofs of both sections gradually split into two parts. As the second section continues to be excavated, the roof settlement displacement shifts mainly from the first section to the second section, causing the range of abnormal water pressure above the first section roof to gradually disappear (see Excavation Phase 2-1 to 3). As the roof settlement in the second section increases, the water in the saturated zone gradually infiltrates downward, and the pore water pressure is gradually released. After the completion of the second section excavation, due to the support effect, the roof settlement rate decreases, and after the model calculation reaches equilibrium, the stress concentration phenomenon in the roof disappears. The pore water pressure in the roof further decreases, and the abnormal pressure range above the roof also dissipates (see Excavation Phase 2-4 to 6). This phenomenon can be explained by the "stress-hydraulic coupling effect." As the second section is excavated, the settlement of the top rock mass in the second section induces a new stress concentration zone, causing the water pressure anomalies that were initially present in the first section to gradually disappear and form a new water pressure concentration zone in the second section.

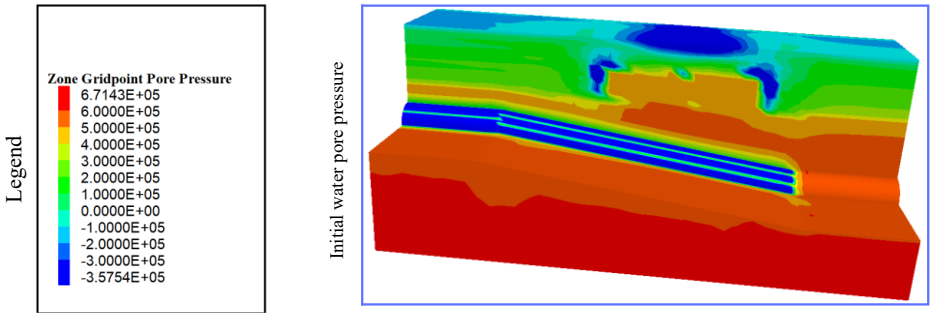

(a) Legend and initial pore pressure

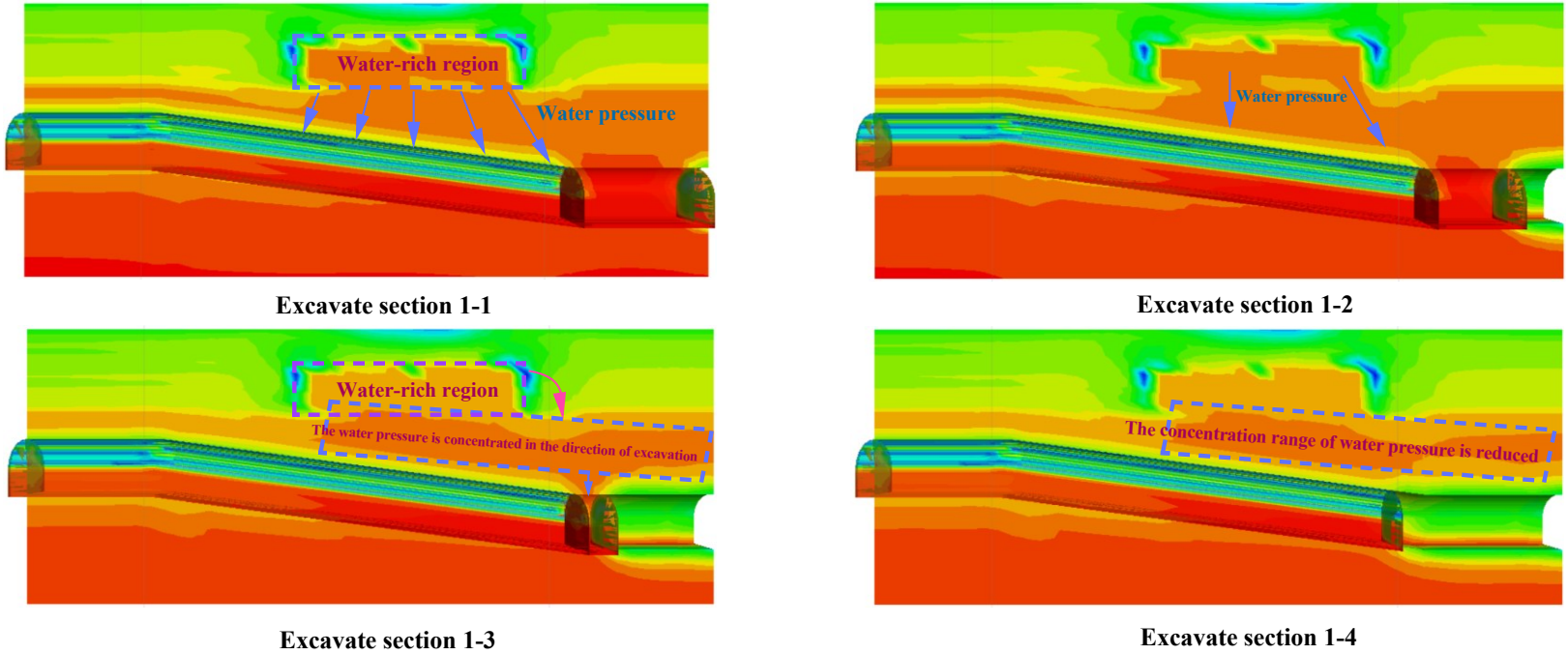

(b) Excavation of the first section

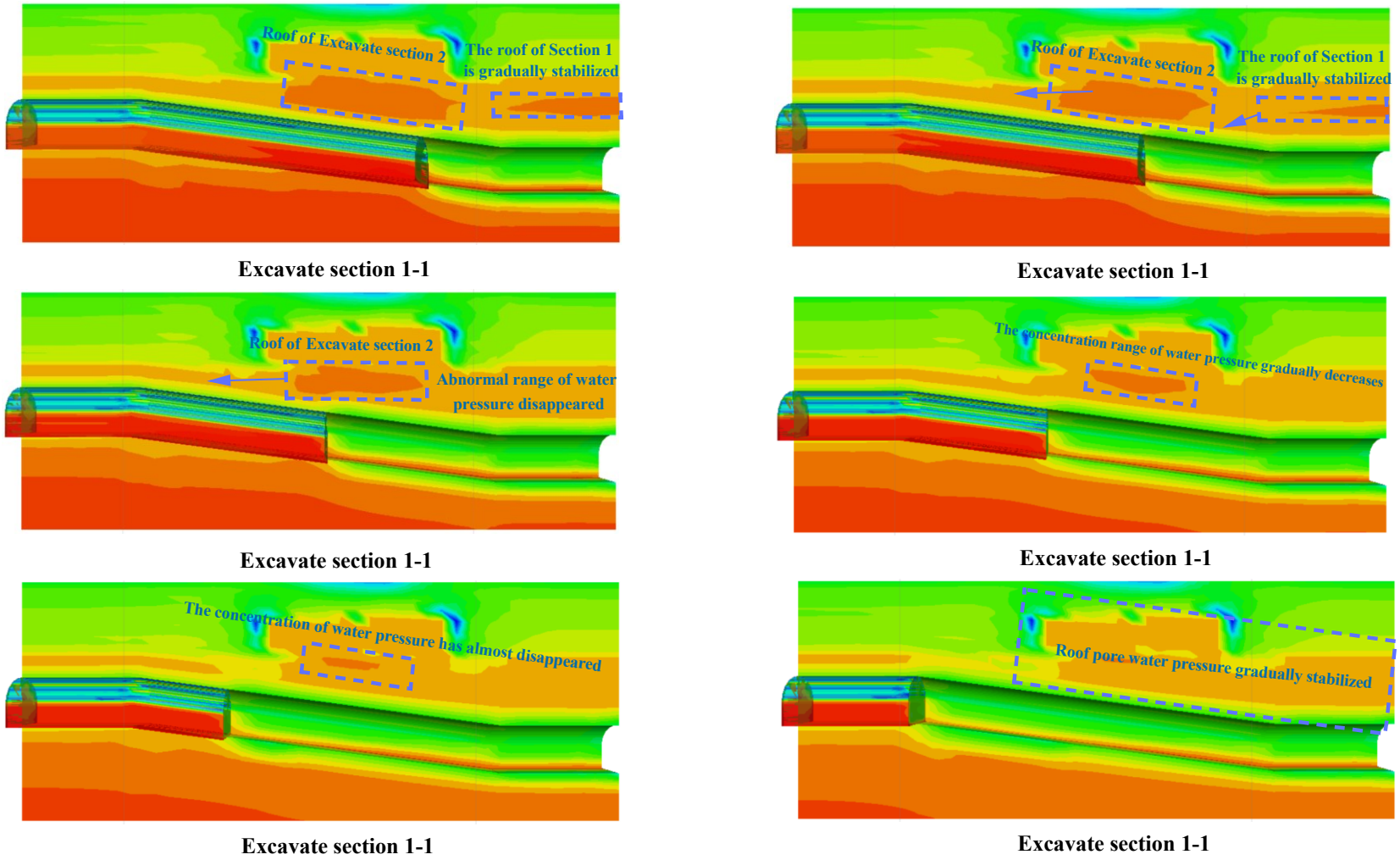

(c) Excavation of the second section

Fig. 6.17 Evolution of pore pressure in roof during tunnel excavation

The water gradually infiltrates downward from the saturated zone, and the release of pore water pressure causes the pressure concentration zone to expand. At the same time, as the support effect strengthens, the roof settlement rate decreases, the water pressure concentration phenomenon gradually disappears, and the pore water pressure further decreases.

This indicates that the support scheme for a saturated tunnel under cyclic stress disturbance not only reduces roof settlement but also effectively alleviates the water pressure concentration in the roof, maintaining the stability of the surrounding rock. Particularly in the later stages of excavation, the support effect ensures the stability of the roof pore water pressure, reducing the potential risk of damage due to pressure concentration.

The advantage of this support scheme also lies in its long-term stability. As the tunnel is gradually excavated, the deformation of the surrounding rock and the distribution of water pressure tend to stabilize, avoiding roof instability or crack development caused by excessive water pressure in the short term. This provides a more stable working environment for subsequent mining operations.

6.4.2 Settlement patterns of the roof during tunnel excavation

The support scheme using anchor bolts with a length of 2200 mm and a spacing of 0.8 m was applied to the excavation support of the saturated fatigue tunnel. Additionally, measurement points were arranged at the middle of both the first and second sections of the tunnel to monitor the roof settlement at these two locations in order to analyze the overall settlement variation pattern of the roof after the excavation of both sections in the "saturated fatigue" tunnel. The locations of the two measurement points and their corresponding roof settlement variation curves are shown in Figure 6.18.

From Figure 6.18, it can be seen that the roof settlement variation at Measurement Point 1 can be roughly divided into three stages:

1) From the beginning of the first section excavation to the excavation reaching Measurement Point 1: In this stage, as the tunnel is gradually excavated, the roof at Measurement Point 1 begins to settle gradually, with the settlement increasing as the excavation approaches. This is because, as the tunnel is excavated, the surrounding rock, which was previously compressed, begins to release stress, causing the roof rock mass to subside. During this process, the settlement rate of the roof is relatively slow, mainly because the surrounding rock has not yet reached the critical stage of large-scale deformation.

2) From the excavation reaching Measurement Point 1 to the completion of the first section excavation: In this stage, as the excavation progresses at Measurement Point 1, the roof settlement rapidly increases. As the tunnel nears Measurement Point 1, the deformation of the surrounding rock becomes more concentrated, especially at the roof, where the stress becomes more focused, leading to an acceleration of roof settlement. The intensified settlement in this stage indicates that the stress concentration effect ahead of the tunnel starts to take effect, and

the surrounding rock in the roof area may be in a critical state of elastic-plastic transition, leading to a rapid increase in settlement.

3) From the completion of the first section excavation to the completion of the second section excavation: In this stage, as the excavation of the tunnel gradually reaches equilibrium, the roof deformation gradually increases and tends to stabilize. By the end of the second section excavation, the maximum settlement at Measurement Point 1 reaches a peak of 0.519 mm. The stabilization of settlement in this stage indicates that the surrounding rock of the tunnel has undergone a certain degree of adaptive deformation. Through support measures such as anchor bolts, the settlement of the tunnel roof has been effectively controlled, and the deformation of the surrounding rock gradually stabilized.

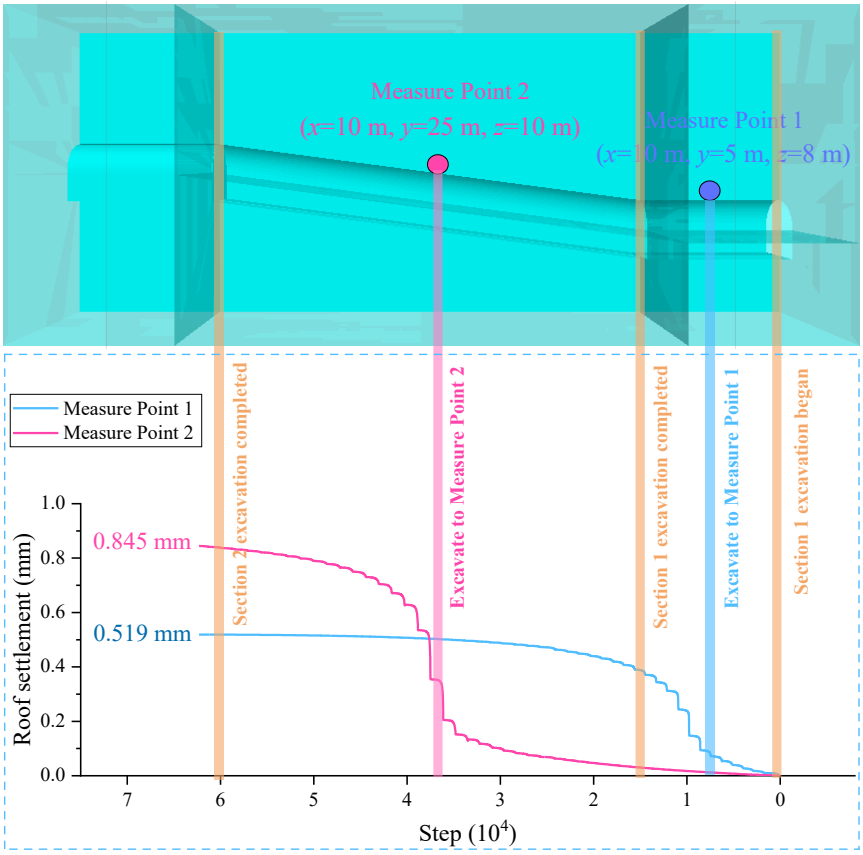

Fig. 6.18 The layout of the two measuring points and the monitoring curve of the roof settlement

The settlement variation at Measurement Point 2 is similar to that at Measurement Point 1, and can also be divided into the initial slow growth, rapid increase as the excavation reaches the point, and finally stabilization. The maximum roof settlement at Measurement Point 2 is 0.845 mm. This indicates that after the second section excavation, the settlement of the roof is mainly concentrated in the central part of the second section. Therefore, it is necessary to strengthen the monitoring and support of this section of the tunnel to ensure that the support structure can effectively control the settlement and deformation in this area.

6.5 Summary

This chapter reveals the evolution of surrounding rock stability in water-saturated tunnels under cyclic stress disturbance through numerical simulation. By integrating support parameter optimization and pore water pressure monitoring, an engineering prevention and control system under hydro-mechanical coupling is established. The key conclusions are as follows:

1. Differentiated Impact of Support Schemes on Surrounding Rock Stability: The default support scheme (Bolt diameter is 22 mm, length is 1800 mm, spacing along the excavation direction is 1.2 m) significantly improves the stability of natural tunnels, as evidenced by a substantial reduction in roof settlement and a noticeable shrinkage of the plastic zone on both sides. However, under undrained water-saturated conditions, cyclic stress disturbance leads to a sharp increase in roof settlement, a significant rise in peak pore water pressure, and the formation of a continuously distributed plastic damage zone around the tunnel. These findings confirm the necessity of pre-drainage measures to mitigate the disaster-inducing effects of water pressure.

2. Synergistic Optimization Effect of Drainage and Support: After drainage, pore water pressure decreases significantly. When combined with an optimized support scheme featuring increased bolt length and reduced spacing, both roof settlement and the extent of the plastic zone are substantially reduced, greatly enhancing surrounding rock stability. The results indicate that a "long anchoring + dense support" strategy can effectively suppress secondary damage induced by water pressure redistribution, providing a theoretical basis for the support design of water-saturated tunnels.

3. Spatiotemporal Evolution of Water Pressure and Deformation: The evolution of pore water pressure exhibits a pattern of convergence toward the excavation face, followed by gradient diffusion. The roof settlement process demonstrates a three-stage dynamic response: initial slow growth, rapid increase during excavation, and gradual stabilization in the later stage. During the second excavation phase, the central region of the roof shows a disproportionately high settlement ratio, highlighting the need for targeted monitoring and enhanced support measures.

Chapter 7
Field application of excavation and support optimization of water-filled tunnel

The optimized support scheme from Chapter 6 was applied to the excavation of the tunnel for testing. After the completion of the tunnel excavation support, multi-point displacement meters and roof separation meters were used to monitor the deformation of the tunnel sides and roof settlement. Pore water pressure was monitored to assess the pore water pressure of the tunnel roof and sides, aiming to investigate the stability of the surrounding rock and the evolution of pore water pressure during the excavation of a saturated tunnel under the recommended support scheme. Figure 6.1 shows the layout of the multi-point displacement meters, roof separation meters, and pore water pressure gauges in the excavated tunnel, while Figure 6.2 presents the equipment and structural diagrams.

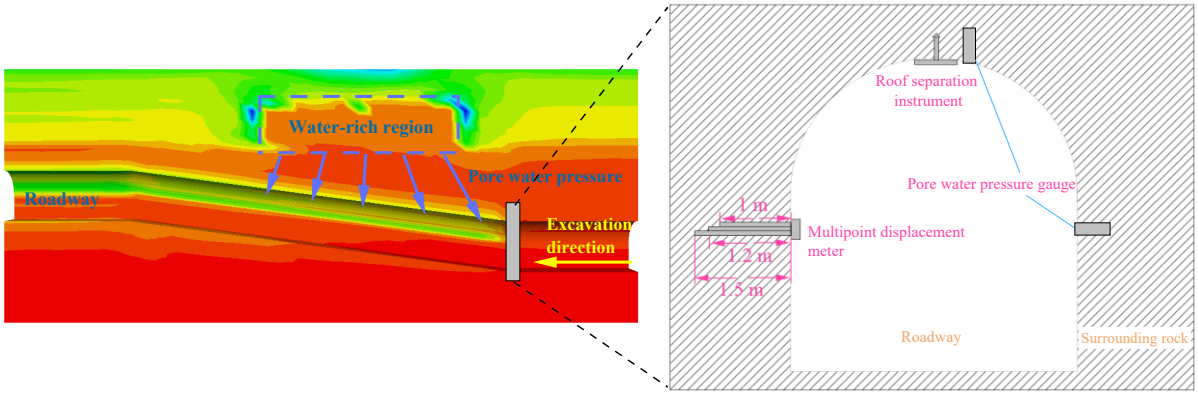

Fig. 7.1 Layout diagram of roof separation meter, multipoint displacement meter, and pore water pressure meter

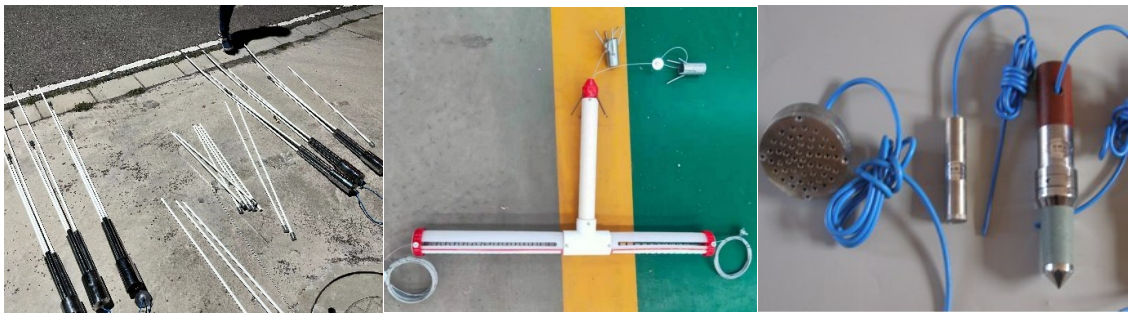

(a) (b) (c)

Fig. 7.2 Field monitoring equipment and its structure diagram. (a) Multipoint displacement meter. (b) Roof separation instrument. (c) Pore water pressure gauge.

7.1 Deformation monitoring of tunnel sidewalls

7.1.1 Principles and usage of multipoint displacement meters

A multipoint displacement meter is an instrument used to measure displacement signals through sensors placed on the object being monitored. When the object experiences displacement, the sensor detects the change and converts it into an electrical signal, which is transmitted to the data acquisition unit. Additionally, it enhances measurement accuracy and stability through signal amplification and filtering. The installation and usage of the multipoint displacement meter used in this study are as follows:

1) Drilling: According to the requirements of the multipoint displacement meter, first, a large hole of φ150×600 mm is drilled at the designated location, followed by drilling a smaller hole at the bottom of the larger one using a 100 mm diameter drill bit. The depth of the small hole should be 1 meter deeper than the deepest anchor head. The allowable error for the hole's position on the plane is 50 mm, with an angular deviation not exceeding ±1°.

2) Inserting the Measuring Rod: Place the assembled measuring rod of the multipoint displacement meter into the hole, install the analog sensor on the base sensor’s fixing rod, position the base according to the corresponding hole location, and reserve grouting and ventilation holes for grouting.

3) Grouting: After grouting, remove the analog sensor, install the multipoint displacement meter sensor on the base sensor’s fixing rod, and record the sensor’s corresponding rod number and anchor head position.

4) Data Collection: Connect the compatible data collector to the displacement meter's wire, take initial readings, and install the hole protection device.

After the installation of the multipoint displacement meter following these steps, the data collector is connected to the displacement meter's output cable, and the collector is used to read the frequency or modulus of the displacement meter. The method for calculating the data is as follows:

$$\begin{cases} L_1 = K\left(f_0{}^2 - f_x{}^2\right) \\ L_2 = K(f_0 - f_x) \end{cases} \tag{7.1}$$

where L_1 represents the displacement (frequency), L_2 represents the displacement (frequency modulus), K is the coefficient (provided by the manufacturer), f_0 is the initial value, and f_x is the real-time value.

7.1.2 Analysis of monitoring results of drift wall displacement

The JM-910 series multipoint displacement meter was used to monitor the sidewall displacement of the excavated tunnel after drainage. Four monitoring points were installed in the test section, numbered M1 to M4. The field arrangement of the multipoint displacement meter is shown in Figure 7.3.

(a) (b)

Fig. 7.3 Field arrangement and monitoring of multi-point displacement meter. (a) Field arrangement. (b) Field observation.

The monitoring data from the multipoint displacement meters were observed and recorded using a data collector. The deformation of the surrounding rock at different depths from each monitoring point was statistically analyzed, as shown in Table 7.1. Based on Table 7.1, the deformation curves for each monitoring point were plotted, as shown in Figure 7.4.

Table 7.1 The roof settlement of the tunnel

Time	M1 (mm)			M2 (mm)			M3 (mm)			M4 (mm)		
	1.5 m	1.2 m	1.0 m	1.5 m	1.2 m	1.0 m	1.5 m	1.2 m	1.0 m	1.5 m	1.2 m	1.0 m
0	0	0	0	0	0	0	0	0	0	0	0	0
1	0.034	0.042	0.053	0.027	0.034	0.042	0.02	0.025	0.032	0.027	0.036	0.044
3	0.082	0.103	0.134	0.065	0.082	0.107	0.042	0.052	0.061	0.068	0.081	0.092

13	0.173	0.198	0.212	0.134	0.157	0.17	0.094	0.112	0.117	0.141	0.158	0.165
14	0.189	0.206	0.218	0.152	0.165	0.174	0.118	0.125	0.13	0.152	0.168	0.174
16	0.201	0.212	0.221	0.154	0.166	0.174	0.121	0.127	0.131	0.153	0.169	0.175

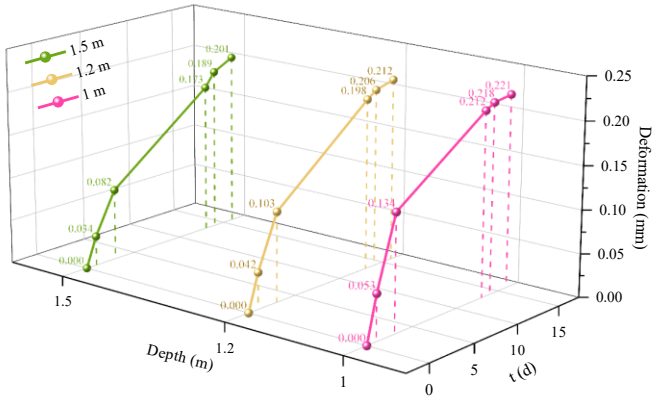

(a)

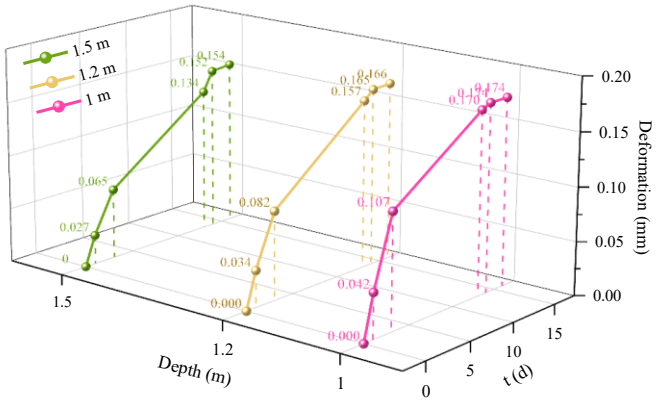

(b)

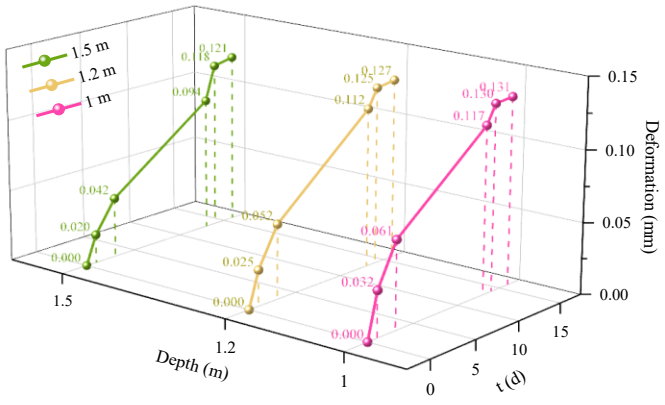

(c)

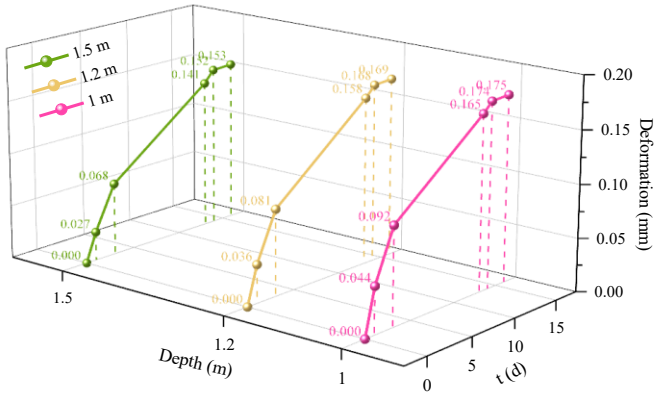

(d)

Fig. 7.4 Multi-point displacement meter monitoring results. (a) M1. (b) M2. (c) M3. (d) M4.

As shown in Figure 7.4, at a depth of 1 meter in the tunnel sidewall, the maximum deformation of the four monitoring points within 16 days was 0.221 mm, 0.174 mm, 0.131 mm, and 0.175 mm, with an average value of 0.173 mm. The average maximum deformation at depths of 1.2 meters and 1.5 meters was 0.169 mm and 0.157 mm, respectively. This indicates that as the monitoring depth increases, the deformation of the surrounding rock in the tunnel sidewall decreases. Additionally, as the monitoring period progresses, the rate of deformation increase at different depths gradually slows down, and the surrounding rock of the sidewall tends to stabilize. This demonstrates that the new support scheme effectively maintains the stability of the tunnel sidewall during excavation.

7.2 Roof subsidence monitoring

7.2.1 Principles and usage of the roof separation meter

The roof separation meter monitors and records roof subsidence by tracking changes in multiple fixed points within roof boreholes, allowing the assessment of roof stability and the effectiveness of the rock bolt support. The roof separation meter has two measurement points (as shown in Figure 7.1d): one fixed to the stable deep rock layer (deep base point) and the other fixed to the surrounding rock at the same depth as the rock bolt end (shallow base point). By measuring the relative displacement between the two base points and the roof surface, the total roof separation value can be obtained. The specific installation method of the roof separation meter is as follows:

1) Use a 28 mm diameter rock bolt drill to create an 8-meter deep borehole in the roof.

2) Open the anchor claws on the roof separation meter and use the installation rod to push the deep base anchor claw to the bottom of the hole; the installation depths for the shallow base anchor claws are 1 m, 1.5 m, 2.0 m, 2.5 m, and 3 m, respectively.

3) Push the anchor claws of the base anchor heads into the borehole, and fix the steel wire rope to the valves on both sides of the roof separation meter using fixing screws. Install the casing and firmly connect the lower end of the casing to the waterproof board, with the bottom

edge of the waterproof board approximately 35 mm from the roof. Then, connect the deep anchor head measuring rope to the inner tube, and the shallow anchor head measuring rope to the outer measuring tube. Align the zero point of the outer measuring tube with the bottom edge of the casing, and align the zero point of the inner measuring tube with the bottom edge of the outer measuring tube.

After installing the roof separation meter according to the above method, record the readings of the outer measuring tube scale on the roof bolt at regular intervals, and perform statistical analysis. The roof subsidence at the monitoring point can be calculated using the following formula:

$$S = S_1 + S_2 \tag{7.2}$$

where S is the total roof separation value, S_1 is the reading of the roof separation meter inner measuring tube within the rock bolt anchor range, and S_2 is the reading of the roof separation meter outer measuring tube within the rock bolt anchor range.

7.2.2 Analysis of roof subsidence results

The roof subsidence of the excavated tunnel after drainage was monitored using the roof separation meter, as shown in Figure 7.5.

(a) (b) (c)

Fig. 7.5 The installation process of the roof separation instrument. (a) Drilling. (b) Installation. (c) Post-installation effect diagram.

Four monitoring points were arranged along the tunnel, with shallow reference points installed at depths of 1 m, 1.5 m, 2.0 m, 2.5 m, and 3 m at each monitoring location to observe the separation of shallow rock layers at different depths. The monitoring data from the roof separation meters were observed and recorded, as shown in Table 7.2.

Table 7.2 The roof settlement of the tunnel

时间	M1			M2			M3			M4		
	S_1 (mm)	S_2 (mm)	S (mm)	S_1 (mm)	S_2 (mm)	S (mm)	S_1 (mm)	S_2 (mm)	S (mm)	S_1 (mm)	S_2 (mm)	S (mm)

1	0.2	0	0.2	0.2	0	0.2	0	0	0	0	0	0
3	0.3	0.1	0.4	0.3	0.1	0.4	0.1	0	0.1	0.1	0	0.1
13	0.5	0.1	0.6	0.3	0.1	0.4	0.1	0.1	0.2	0.3	0.1	0.4
14	0.5	0.1	0.6	0.3	0.2	0.5	0.2	0.1	0.3	0.3	0.2	0.5
16	0.6	0.1	0.7	0.3	0.2	0.5	0.2	0.1	0.3	0.3	0.2	0.5

Using equation (7.2), the monitoring data from the roof separation meter were calculated, and the variation in roof subsidence over the monitoring period was plotted, as shown in Figure 7.6.

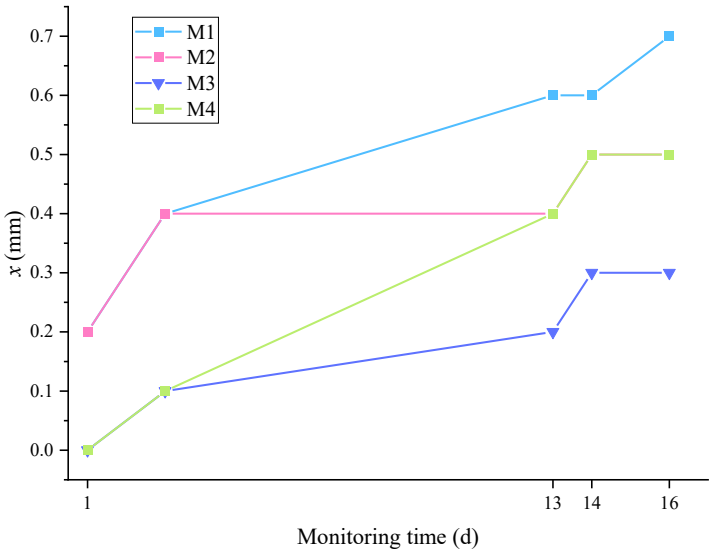

Fig. 7.6 Monitoring results of tunnel roof settlement

From Figure 7.6, it can be seen that the maximum roof subsidence at the four monitoring points within 16 days was 0.7 mm, 0.3 mm, 0.3 mm, and 0.5 mm, with an average value of 0.45 mm, which is slightly smaller than the numerical simulation results. Additionally, except for M1, the monitoring results for the other points stabilized by day 14. This indicates that the new support scheme has a good stabilizing effect on the water-saturated tunnel.

7.3 Pore water pressure monitoring

7.3.1 Principles and usage of the pore water pressure gauge

1) Drill a hole at the location where the pore water pressure gauge is to be installed. Mark the cable according to the predetermined installation depth of the pressure gauge, and then embed the top end of the installation rod into the bottom of the drill rod.

2) Place the pre-boiled pressure gauge into the protective tube, ensuring that the threading holes in the protective tube align with the opening on the installation rod. Then, insert the protective tube into the installation rod.

3) Pass the installation rope through the threading hole and fix it to the end of the protective tube. Lower the drill rod at a constant speed, ensuring that the pore water pressure gauge is lowered at a steady rate under the protection of the installation rod until it reaches the predetermined depth in the borehole.

After installing the pore water pressure gauge according to the above method, the measured pore water pressure is calculated using the following formula:

$$P = K \times (Fx^2 - F0^2) \tag{7.3}$$

where, P is the measured pore water pressure value (MPa); K is the sensitivity coefficient of the pore water pressure gauge; Fx is the working frequency value of the pore water pressure gauge; $F0$ is the initial frequency value of the pore water pressure gauge.

7.3.2 Analysis of pore water pressure results

Pore water pressure in the roof and sidewalls of the tunnel after drainage was monitored using the pore water pressure gauges. Four monitoring points were arranged along the tunnel, with the pore water pressure gauges in the roof numbered X1 and X2, and those in the sidewalls numbered X3 and X4, as shown in Figure 7.7. The monitoring data from the pore water pressure gauges were observed and recorded, as shown in Tables 7.3-7.4.

(a) (b)

Fig.7.7 Layout and field monitoring of pore water pressure gauges. (a) Arrangement. (b) Data Monitoring.

The variation in pore water pressure at different monitoring points in the tunnel roof and sidewalls over time was plotted based on Tables 7.3-7.4, as shown in Figure 7.8.

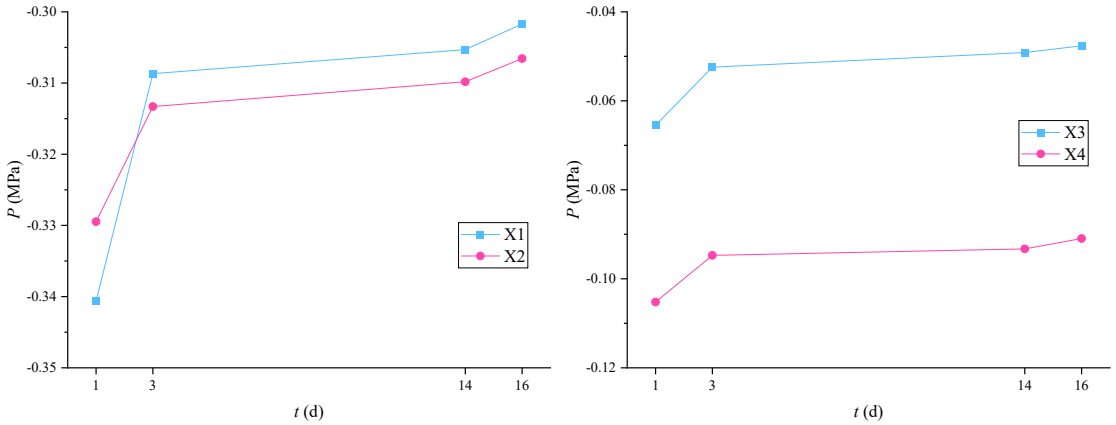

(a) (b)

Fig. 7.8 Monitoring results of pore water pressure in roof and two sides of tunnel. (a) Roof. (b) Sidewalls.

From Figure 7.8, it can be observed that the absolute values of pore water pressure at the four monitoring points exhibit a decreasing trend over time. This indicates that during the excavation of the tunnel, as water is discharged from the sidewalls, the pore water pressure in the sidewalls gradually decreases and tends toward stability. On day 16, the absolute values of pore water pressure at the four monitoring points were 0.302 MPa, 0.307 MPa, 0.048 MPa, and 0.091 MPa, all of which were less than 0.5 MPa. This suggests that the new support scheme not only maintains the stability of the surrounding rock in the water-saturated tunnel but also effectively alleviates the concentration of water pressure in the tunnel roof and sidewalls.

Table 7.3 Statistics of monitoring results of pore water pressure at X1 and X2 measuring points

Measurement Point	Time (d)	K (Coefficient)	F_0 (Initial Value)	F_x (Real-time Value)	P (MPa)
X1	1	6.78E-07	1788	1641.5	-0.341
	3	6.78E-07	1788	1655.8	-0.309
	14	6.78E-07	1788	1657.3	-0.305
	16	6.78E-07	1788	1658.9	-0.302
X2	1	7.52E-07	1778	1650.2	-0.329
	3	7.52E-07	1778	1656.7	-0.313
	14	7.52E-07	1778	1658.1	-0.310
	16	7.52E-07	1778	1659.4	-0.307

Table. 7.4 Statistics of monitoring results of pore water pressure at X3 and X4 measuring points

Measurement Point	Time (d)	K (Coefficient)	F_0 (Initial Value)	F_x (Real-time Value)	P (MPa)

X3	1	7.16E-07	1779	1753.1	-0.066
	3	7.16E-07	1779	1758.3	-0.052
	14	7.16E-07	1779	1759.6	-0.049
	16	7.16E-07	1779	1760.2	-0.048
X4	1	8.34E-07	1780	1744.2	-0.105
	3	8.34E-07	1780	1747.8	-0.095
	14	8.34E-07	1780	1748.3	-0.093
	16	8.34E-07	1780	1749.1	-0.091

7.4 Summary

This chapter systematically evaluates the engineering effectiveness of a new support scheme in controlling the stability of water-saturated tunnel surrounding rock through field monitoring and data analysis. By integrating multi-point displacement meters, roof separation monitors, and pore water pressure gauges, the regulatory mechanism of the support system on hydro-mechanical coupling is revealed. The main conclusions are as follows:

1. Spatiotemporal Evolution of Surrounding Rock Deformation: The deformation of tunnel sidewalls exhibits a gradient decrease with increasing monitoring depth (0.173 mm at 1 m depth → 0.157 mm at 1.5 m depth), and the deformation rate gradually converges over time, indicating that the support structure effectively inhibits the propagation of shallow rock mass damage. The roof settlement stabilizes at 0.45 mm during the 16-day monitoring period, entering a deformation stagnation phase after the 14th day, confirming the support system's role in preventing roof separation development.

2. Dynamic Response Characteristics of Pore Water Pressure: The pore water pressure in the tunnel roof and sidewalls continuously decreases as excavation progresses, and the phenomenon of water pressure concentration is significantly alleviated after support implementation. Monitoring data indicate a positive correlation between the rate of water pressure attenuation and the drainage efficiency of the tunnel, validating the optimization effect of the support-drainage synergy on seepage pathways.

3. Comprehensive Performance Evaluation of the Support System: Coupled analysis of deformation and water pressure monitoring data reveals that the new support scheme achieves a synergistic mechanism of rigid support (suppressing deformation) and flexible water

conduction (reducing water pressure), enabling the water-saturated tunnel surrounding rock to reach a dual stability state of mechanics and seepage within 16 days. This provides empirical evidence for similar engineering applications.

Chapter 8
Conclusions and outlook

8.1 Summary of the main conclusions

This study focused on a water-rich tunnel in a phosphate mine in Yunnan, employing in-situ experiments, laboratory tests, model construction, numerical simulations, and field monitoring. Field tests were conducted to investigate the water pressures and the geostatic stresses at the site. Thanks to the collection of samples of shale, standard cylindrical and cubic specimens were prepared for laboratory testing. Based on the stress and hydrological environment during the excavation of the tunnel, research was carried out on the damage characteristics of water-saturated shale under cyclic stress disturbance and the mechanical-seepage coupling characteristics. The effects of saturation, water pressure, and cyclic stresses on the mechanical properties and permeability of the samples were explored, leading to the identification of the degradation mechanism of the mechanical properties and the evolution law of permeability under hydro-mechanical coupling. Based on this, a 3D Finite Difference numerical model was used to simulate the excavation process of the water-saturated tunnel under cyclic stress disturbance, analyzing the deformation and pore water pressure evolution of the excavated tunnel under different support schemes after drainage, followed by field monitoring and verification. The main research conclusions can be summarised as follows.

1) Determination of the engineering geological characteristics of the rock mass surrounding the water-saturated tunnel. Based on engineering geological field surveys and stressmeter testing, the engineering geological characteristics and geostatic stress field distribution of the target mining area in the Yunnan phosphate mine were systematically revealed. The surrounding rock is of poor rock mass quality. Transient electromagnetic detection revealed three zones of low-resistance anomalies ahead of the working face: a water-rich anomaly body developed within a 0-8 m range, and fractured water channel anomalies were detected in the 25-40 m range on both sides. Water pressure monitoring indicated that the pore water pressure stabilized after the 14^{th} day of excavation (average 1.42 MPa, fluctuation < 4.2%). Geostatic stress testing data showed that the maximum principal stress (σ_1 = 15.68 MPa) and the intermediate principal stress (σ_2 = 7.32 MPa) were nearly horizontal, while the minimum principal

stress (σ_3 = 4.98 MPa) was close to vertical. The water pressure and geostatic stress test results provide a basis for the formulation of true triaxial test plans.

2) Damage characteristics of water-saturated shale under cyclic stress disturbance. Through water saturation and cyclic loading experiments, the mechanical response characteristics of shale under the coupled effects of water saturation duration and cyclic stress were systematically investigated. Combining acoustic emission monitoring and damage variable analysis, the synergistic degradation mechanism of water-rock interaction and fatigue damage was revealed. Cyclic loading promotes the expansion of primary fractures and the initiation of new cracks, while long-term vacuum saturation exacerbates the softening effect of cracks through moisture penetration. This leads to multiple fluctuations in the stress-strain curve of the "cyclic loading + water saturation" group after the peak, with significant enhancement of plastic characteristics. The failure mode of the specimen evolves from shear failure in the natural state to heavy shear or through-failure, with a multi-stage fracture zone expansion pattern. As the water saturation time increases, the compressive strength of the specimens decreases by 11.0% to 46.1%, and the stress-strain curve transitions from smooth brittle elasticity to stepped plasticity. The cyclic stress degradation effect exhibits nonlinear decay with increased water saturation time, indicating a significant dynamic coupling relationship. The damage variable-time curve shows a high correlation with stress evolution during the compaction and elastic stages, with a higher contribution rate of damage during the initial cyclic loading stage. The level of acoustic emission response is positively correlated with the accumulated plastic strain, and after water saturation, the acoustic emission response during the loading process gradually decreases, indicating that moisture penetration inhibits the rapid expansion of new cracks. A fatigue damage model revealed a coupling threshold point (t_w = 24 h), with fatigue damage dominating the mechanical degradation when t_w < 24 h. After t_w > 24 h, water-rock chemical interactions become the dominant factor, reducing the specimen's sensitivity to cyclic stress. The model predicts changes in the mechanical parameters of water-saturated samples after cyclic loading using acoustic emission parameters and plastic strain as dual indicators.

3) Mechanical-seepage coupling characteristics and model construction of water-saturated shale under cyclic stress disturbance. Through coupled cyclic loading and seepage experiments, the mechanical response and permeability evolution of water-saturated shale under water pressure-stress synergy were systematically revealed. Combining acoustic emission monitoring and neural network modeling, a multi-field coupled damage evaluation system was established. The stress-strain curves of natural and water-saturated samples show significant differences. The water-saturated samples experience enhanced curve fluctuations due to local expansion effects, and after failure,

the overall compression state limits the instantaneous increase in water flow. An increase in water pressure raises the effective stress in the σ_1 direction, exacerbating crack propagation and reducing crack density in the σ_2 direction, while weakening the mechanical regulation of the intermediate principal stress. The critical permeability point gradually disappears with increasing water saturation time, indicating that moisture penetration restructures the flow paths in the fracture network. During cyclic loading, longer water saturation time causes a decrease in the rate of rightward shifting of the hysteresis loop, reflecting the moisture lubrication effect that suppresses fatigue damage accumulation. Damage assessment based on accumulated acoustic emission counts shows a positive correlation between water pressure and damage extent and a negative correlation between saturation time and damage extent. However, the formula method for characterizing the damage of water-saturated samples has limitations. The evolution of pore water pressure analysis shows that an increase in water pressure leads to higher crack density in the σ_1 direction and alters the distribution of the seepage direction of water. Natural samples have a clear permeability point, with stress parameters sharply increasing after yielding, whereas water-saturated samples exhibit a wave-like fluctuation in the stress-time curve due to mechanical degradation, and water flux changes lag behind the yield point. Under true triaxial conditions, water pressure accelerates the specimen's entry into the stable strain phase, inducing repeated expansion-compression effects, leading to a nonlinear surge in total water flow after failure. A mechanical-seepage coupling model based on the complex plane reveals that the real part (fatigue damage) and imaginary part (mechanical performance) are secondarily negatively correlated, and the model is realized using a neural network algorithm. The developed visualization software (Windows platform) can predict the evolution of mechanical parameters under different water pressure-saturation conditions, providing theoretical reference for excavation and support in water-rich shale tunnels.

4) Stability analysis of the water-saturated rock mass surrounding the tunnel under cyclic stress disturbance. Three dimensional numerical simulations conducted revealed that the stability evolution of water-saturated rock mass surrounding the tunnel under cyclic stress disturbance is significantly improved by the default support scheme (Bolt diameter is 22 mm, length is 1800 mm, spacing along the excavation direction is 1.2 m), as evidenced by a large reduction in roof settlement and a noticeable reduction in the extent of plastic zones on both sides. However, under unsaturated water conditions, cyclic stress disturbance leads to a sharp increase in roof settlement and a significant rise in pore water pressures, generating a continuously distributed plastic damage zone around the tunnel. This confirms the need for pre-drainage measures to control water pressure-induced damages. After drainage, the pore water pressure decreases significantly, and an optimized scheme combining increased anchor length and reduced

spacing greatly reduces roof settlement and the extent of plastic zones, significantly improving the surrounding rock stability conditions. The results show that the "long anchorage + dense support" strategy can effectively inhibit secondary damage induced by water pressure redistribution, providing a theoretical basis for the design of supports in water-saturated tunnels. The spatiotemporal evolution of water pressure-deformation during excavation reveals that pore water pressure evolves with a characteristic gradient diffusion towards the excavation face, and the roof settlement process displays a three-phase dynamic response: initial slow growth, rapid increase during excavation, and gradual stabilization in the later stages. During the second excavation phase, the settlement of the roof's central area is prominent, requiring targeted monitoring and support.

5) Mining pressure monitoring and engineering application in water-saturated tunnels. Through field monitoring and data analysis, the engineering effectiveness of a new support scheme for controlling the stability of surrounding rock in water-saturated tunnels was systematically evaluated. Sidewall deformation decreases with monitoring depth, showing a gradient reduction (0.173 mm at 1 m → 0.157 mm at 1.5 m depth), and the deformation rate gradually converges over time, indicating that the support structure effectively suppresses the propagation of shallow rock mass damage. Roof settlement stabilized at 0.45 mm during the 16-day monitoring period, entering a deformation stagnation phase after the 14^{th} day, confirming the support system's ability to prevent roof separation development. The pore water pressure in the tunnel roof and sidewalls decreases continuously with excavation, and the phenomenon of water pressure concentration was significantly alleviated after the support was implemented. Monitoring data show that the rate of water pressure attenuation is positively correlated with the drainage efficiency of the tunnel, validating the optimization effect of the support-drainage synergy on seepage pathways. Coupled analysis of deformation and water pressure monitoring data shows that the new support scheme achieves a dual stability state of mechanics and seepage in the water-saturated surrounding rock within 16 days, providing empirical evidence for similar engineering applications.

8.2 Main innovations

The main innovations can be summarised as follows.

1) Multi-field Coupling Damage Threshold Model and Intelligent Prediction Technology. A dual-parameter coupling model based on the complex plane theory ("fatigue damage-mechanical properties") has been established. By introducing a dynamic correlation mechanism between acoustic emission signals and plastic strain rate, the model predicts the attenuation of mechanical parameters of water-saturated shale under cyclic stress disturbance.

2) Fracture Water Pressure-Stress Coupling Damage Mechanism. Multi-scale experiments reveal the coupling damage mechanism of "cyclic stress disturbance-water corrosion-water pressure effect" in water-saturated shale. A critical water saturation threshold (tw = 24 hours) is identified, explaining the mechanism of stress corrosion at the crack tip caused by water molecule infiltration, providing theoretical reference for deep water-rich tunnel stability research.
3) Water-Pressure Synergistic Control Support Optimization System. A graded prevention and control technology of "pre-drainage-long anchoring-dense support" is proposed, along with dynamic support sequencing standards. Through the optimization of anchor bolt parameters and the synergistic effect of pre-drainage, the stability of the water-saturated tunnel is effectively maintained, overcoming the problem of traditional support failure in a seepage-stress coupling environment. The spatial and temporal evolution of pore water pressure from "convergence to excavation face → gradient diffusion" is revealed, providing a theoretical basis for the support of surrounding rock in water-rich tunnels.

8.3 Outlook

This study has achieved staged results in the water-pressure coupling damage mechanism and stability control of surrounding rock in water-saturated shale tunnels. However, due to limitations in experimental conditions, theoretical depth, and engineering complexity, future research can be expanded in the following directions.

1) Expansion of Experimental Methods and Multi-field Coupling Effects
   The current research focuses on water pressure-stress dual-field coupling. Future studies can introduce additional physical fields, such as temperature fields (geothermal gradients) and chemical fields (ion migration in groundwater), to reveal the rock mass damage evolution under the synergistic effects of thermal-water-pressure-chemical coupling. Simulating complex deep mining environments, the enhanced effect of clay mineral hydration expansion on fracture propagation under high-temperature conditions can also be explored.
2) Upgrading of Intelligent Models and Dynamic Control Technologies
   Although the complex plane damage model has been established and visualization software has been developed, there is still room for improvement in real-time prediction and adaptive control. Future research could integrate digital twin technology to create an integrated platform for dynamic monitoring, simulation, and early warning of tunnel surrounding rock stability. This would incorporate fiber-optic sensing, micro-seismic monitoring, and machine learning algorithms to achieve minute-level dynamic inversion of damage evolution. Additionally, exploring engineering data-sharing mechanisms

based on blockchain technology could facilitate the universal validation of models across different mines and geological conditions.

References

Alishaev M., Abdulagatov I., Abdulagatova Z. (2012). Effective thermal conductivity of fluid-saturated rocks Experiment and modeling. Engineering Geology. (2012). 135, 24-39.

Aras, A., Ozsen, H., and Dursun, A. (2020). Using artificial neural networks for the prediction of bond work index from rock mechanics properties. Mineral Process. Extr. Metallurgy Rev. 41 (3), 145–152.

Arora K., Chakraborty T., Rao K., et al. (2019) Experimental study on stiffness degradation of rock under uniaxial cyclic sinusoidal compression loading. Rock Mechanics and Rock Engineering. 52(11): 4785-4797.

Cai X., Zhou Z., Zang H., Song Z. (2020). Water saturation effects on dynamic behavior and microstructure damage of sandstone: Phenomena and mechanisms. Engineering Geology. 276, 105760.

Cao K., Ma L., Wu Y., Spearing A., Khan N., Hussain S., Rehman F. (2022). Statistical damage model for dry and saturated rock under uniaxial loading based on infrared radiation for possible stress prediction. Engineering Fracture Mechanics. 260, 108134.

Cao K., Ma L., Wu Y., et al. (2021) Cyclic fatigue characteristics of rock failure using infrared radiation as precursor to violent failure: Experimental insights from loading and unloading response. Fatigue & Fracture of Engineering Materials & Structures. 44(2),584-594.

Cao M., Ye J., Creep-stress-time four parameters mathematical model of calcareous sand in South China Sea. Rock and Soil Mechanics. 2019, 40 (5): 1771-1777.

Caselle C, Baud P, Kushnir A, Reuschlé T, Bonetto S, 2022, Influence of water on deformation and failure of gypsum rock. Journal of Structural Geology, 163: 104722.

Caselle C., Baud P., Kushnir A., Reuschlé T., Bonetto S. (2022). Influence of water on deformation and failure of gypsum rock. Journal of Structural Geology. 163.

Chang S., Wang W., Liu K., Yuan R., Zhang S., Li D., Li H., Kang Y. 2022. Energy dissipation characteristics of water saturated coal samples under true triaxial dynamicand static combined loading. Journal of China Coal Society. 47(05):2011-2026.

Chen Cancan. 2021. Experimental study on aging characteristics and deformation localization of rock under triaxial loading under water-rock coupling. Chongqing University.

Chen J., Ye Y., Pu Y., Xu W., Mengli D., 2022. Experimental study on uniaxial compression failure modes and acoustic emission characteristics of fissured sandstone under water saturation. Theoretical and Applied Fracture Mechanics.119. https://doi.org/10.1016/j.tafmec.2022.103359.

Chen M., Yang L., Zang C., et al. (2023) Study on mechanical behavior and failure mechanism of specimens with single joint subjected to dynamic cyclical loading. Fatigue & Fracture of Engineering Materials & Structures. 46(8), 2878-2894.

Chen T., Feng X., Cui G., Tan Y., Pan Z., 2019. Experimental study of permeability change of organic-rich gas shales under high effective stress. Journal of natural gas science and engineering. 64:1-14. https://doi.org/10.1016/j.jngse.2019.01.014.

Chen X., Peter E., Jon E., Thomas A., 2019. Effect of Water on Fracture Mechanical Properties of Shales. Journal of Geophysical Research: Solid Earth. 124(3):2428-2444.

Chen Y., Ni J., Shao W., Zhou Y., Javadi A., Azzam R. (2012). Coalescence of fractures under uni-axial compression and fatigue loading. Rock Mechanics and Rock Engineering. 45(2), 241-249.

Chen Y., Wang Y., Zhang Q. (2014). Coupled seepage-elastoplastic-damage analysis of saturated porous media and its application to water conveyance tunnel. Tunnelling and Underground Space Technology. 44, 80-87.

Cheng P., Yu Q., 2019, Experimental study on the relationship between the matric potential and methane breakthrough pressure of partially water-saturated shale fractures. Journal of Hydrology. 578.

Cheng P., Zhang C., Ma Z., et al. (2021) Experimental study of micromechanical properties alterations of shale matrix treated by ScCO2-Water saturation using nanoindentation tests. Energy. 242:0360-5442.

Dai F., Zhang Q., Liu Y., Du H., Yan Z. (2022). Experimental evaluation of sandstone under cyclic coupled compression-shear loading: fatigue mechanical response and failure behavior. Acta Geotechnica. 17(8), 3315-3336.

Dou F., Wang J., Leung C., Ma Z., 2021.The alterations of critical pore water pressure and micro-cracking morphology with near-wellbore fractures in hydraulic fracturing of shale reservoirs. Engineering Fracture Mechanics. 242. https://doi.org/10.1016/j.engfracmech.2020.107481.

Du K., Li X., Yang C., Zhou J., Chen S., Manoj K., 2020, Experimental investigations on mechanical performance of rocks under fatigue loads and biaxial confinements. Journal of Central South University. 27(10), 2985-2998.

Du K., Sun Y., Zhou J., Wang S., Tao M., Yang C., Khandelwal M, 2021, Low amplitude fatigue performance of sandstone, marble, and granite under high static stress. Geomechanics and Geophysics for Geo-Energy and Geo-Resources. 7(3).

Fang P., Chen J., Liu Z. (2021). Study on the regularity of ore pressure in intelligent working face with large mining height. Coal science and technology. 45 (2), 36-40.

Feng F., Chen S., Wang Q., ROSTAMI J., KHORESHOK AA. Sheng S., Bian Z., Ding Y.2022.Experimental study on failure characteristics of natural and saturated sandstone under true triaxial unloading and dynamic disturbance condition. Chinese Journal of Rock Mechanics and Engineering.

Ghanbarzadeh S., Hesse M., Prodanovic M., Gardner J. (2016). Deformation-assisted fluid percolation in rock salt. Science. 350(6264), 1069-1072.

Grab M., Quintal B., Caspari E., Deuber C., Maurer H., Greenhalgh S. (2017). The effect of boiling on seismic properties of water-saturated fractured rock. Journal of Geophysical Research-Solid Earth. 122(11), 9228-9252.

Gu H., Lai X., Tao M., Cao W., Yang Z. (2023). The role of porosity in the dynamic disturbance resistance of water-saturated coal. International Journal of Rock Mechanics and Mining Sciences. 166, 105388.

He J., Li X., Yin C., Zhang Y., Lin C., 2020. Propagation and characterization of the micro cracks induced by hydraulic fracturing in shale. Energy.191. https://doi.org/10.1016/j.energy.2019.116449.

He M., Li N., Zhu C., Chen Y., Wu H. (2019). Experimental investigation and damage modeling of salt rock subjected to fatigue loading. International Journal of Rock Mechanics and Mining Sciences. 114, 17-23.

He M., Li N., Zhu C., Chen Y., Wu H. (2019). Experimental investigation and damage modeling of salt rock subjected to fatigue loading. International Journal of Rock Mechanics and Mining Sciences. 114, 17-23.

Hu B., Wang J., 2022. A lattice Boltzmann simulation on the gas flow in fractal organic matter of shale gas reservoirs. Journal of Petroleum Science and Engineering. 210. https://doi.org/10.1016/j.petrol.2021.110048.

Hu P., Liu S., Du Z., Wang B., Wu J., Li C., 2023. A calculation model for Shale reservoir matrix apparent permeability considering different Shale lithofacies through 2D digital core. Journal of Petroleum Science and Engineering. https://doi.org/10.1080/10916466.2022.2150216.

Huang Z., Zhang W., Zhang H., et al. (2023) Study on the fatigue properties and constitutive model of siltstone under the coupled action of dry–wet cycles and cyclic loads. Soil Dynamics and Earthquake Engineering. 171: 107990..

Jia P, Wang X, Wang D, 2023, Full water fracture rock deformation of freezing and thawing characteristic study. Rock and soil mechanics, 44 (02): 345-354.

Jiang Y., Luo Y., Lu Y., Qin C., Liu H., 2016. Effects of supercritical CO2 treatment time, pressure, and temperature on microstructure of shale. Energy. 97, 173-181.

Kuang L., Zhou G., Wang J., Zhu K., Shang X., Oblique cutting soil stress release method governance coal rooting well tower deflection study [J]. Rock and soil mechanics, 2018, 33 (4) 6:1422-1430.

Li C., Gao C., Li N. (2020). Experimental investigation of anisotropic fatigue characteristics of shale under uniaxial cyclic loading. International Journal of Rock Mechanics and Mining Sciences. 130, 104314.

Li C., Gao C., Li N. (2020). Experimental investigation of anisotropic fatigue characteristics of shale under uniaxial cyclic loading. International Journal of Rock Mechanics and Mining Sciences. 130, 104314.

Li D., Jiang F., Chen Y., et al. Study on mechanism of rock burst induced by "dynamic and static" stress effect of water-rich working face in deep well [J]. Journal of geotechnical engineering, 2018, 40 (9): 1714-1722.

Li D., Wong L., Liu G., et al. (2012) Influence of water content and anisotropy on the strength and deformability of low porosity meta-sedimentary rocks under triaxial compression. Engineering Geology. 126: 46-66.

Li H, Qiao Y, He M, Shen R, Gu Z, Tai C, Xiao Y, and Tang Jie, 2023, Effect of water saturation on dynamic behavior of sandstone after wetting-drying cycle treatment. Engineering Geology, 107105.

Li M, Yin G, Xu J, Cao J, Song Z (2016a) Permeability evolution of shale under anisotropic true triaxial stress conditions. Int J Coal Geol 165:142–148. https:/doi.org/10.1016/j.coal.2016.08.017.

Li M, Yin G, Xu J, Li W, Song Z, Jiang C (2016b) A novel true triaxial apparatus to study the geomechanical and fluid flow aspects of energy exploitations in geological formations. Rock Mech Rock Eng 49(12):4647–4659.

Li M., Yin G., Xu J., Cao J., Song Z., 2016. Permeability evolution of shale under anisotropic true triaxial stress conditions. International Journal of Coal Geology.165: 142-148. https://doi.org/10.1016/j.coal.2016.08.017.

Li R., Zhu J., Qu H., et al. (2022) An experimental investigation on fatigue characteristics of granite under repeated dynamic tensions. International Journal of Rock Mechanics and Mining Sciences. 158: 105185..

Li S., Wang C., Zhang D., Wang M., Zhou F., Pan Y. (2023b). Deterioration mechanism of mechanical properties of phosphorite under different saturation duration.Frontiers in Earth Science.

Li S., Wang H., Wang C., Zhang B., Zhang D. (2023a). Deterioration mechanismof physical and mechanical properties of phosphate rock under seismic disturbanceand saturation.Frontiers in Earth Science.

Li S., Zheng M., Qu D., Kuang Z., Wang G., Qiu S. Wireless stress measuring system based on borehole deformation method and test analysis [J]. Journal of rock mechanics and engineering, 2021, 40 (S1) : 2841-2850.

Li Y., Zhai C., Xu J., Yu X., Sun Y., Cong Y., Tang W., Zheng Y., 2023, Effects of steam treatment on the internal moisture and physicochemical structure of coal and their implications for coalbed methane recovery. Energy. 270.

Li Z, Suo J, Fan J, Marion F, Jiang D, Daniel N, 2023, Damage evolution of rock salt under multilevel amplitude creep–fatigue loading with acoustic emission monitoring. International Journal of Rock Mechanics and Mining Sciences, 164: 105346.

Li Z., Suo J., Fan J., Fourmeau M., Jiang D., Nelias D. (2023). Damage evolution of rock salt under multilevel amplitude creep-fatigue loading with Acoustic Emission monitoring. International Journal of Rock Mechanics and Mining Sciences. 164, 105346.

Liang L., Ding Y., Liu X., et al. (2019) Evaluation and mechanical influence of clay shale hydration using acoustic time-frequency domain characteristics. Journal of Geophysics and Engineering. 16(3): 493–508, .

Liang M., Wang Z., Zhang Y., Greenwell C., Li H., Yu Y., Liu S., 2021. Experimental investigation on gas permeability in bedding shale with brittle and semi-brittle deformations under triaxial compression. Journal of Petroleum Science and Engineering. 196. https://doi.org/10.1016/j.petrol.2020.108049.

Liu A., Liu S., Zhang R., Sang G., Xia K., (2023). Cyclical water vapor sorption-induced structural alterations of mine roof shale. International Journal of Coal Geology. 273, 104267.

Liu C., Yin G., Li M., Deng B., Song Z., Liu Y., Yin S., 2019. Shale permeability model considering bedding effect under true triaxial stress conditions. Journal of Natural Gas Science and Engineering. 68. https://doi.org/10.1016/j.jngse.2019.102908.

Liu D, Hu P, Zhao L, 2022, Experimental study on the influence of saturation on mechanical properties of rocks in red bed areas. Water Transport Engineering, 4: 166-171, 179.

Liu D., Hu P., Zhao L. (2022) Experimental study on the effect of water saturation on the mechanical properties of rocks in red bed area. Port & Waterway Engineering. 179 (4):166-171.

Liu F., Liu Y., Yang T., et al. (2021) Fine-grained Evaluation of Mine Rock Mass Quality Based on Core Image Deep Learning. Journal of Geotechnical Engineering, 43(05): 968-974.

Liu J., Zhang H. (2017) Water Content Influence on Properties of Red-Layers in Guangzhou Metro Line, China. Advances in Materials Science and Engineering. 2017, 4808909.

Liu S, Li X, 2023a. Experimental study on the efect of cold soaking with liquid nitrogen on the coal chemical and microstructural characteristics. Environmental Science and Pollution Research. 30(3):36080–36097.

Liu S, Sun H, Zhang D, (2023) Nuclear magnetic resonance study on the influence of liquid nitrogen cold soaking on the pore structure of different coals. Physics of Fluids. 35(1), 012009.

Liu S, Sun H, Zhang D, (2023) Experimental study of effect of liquid nitrogen cold soaking on coal pore structure and fractal characteristics. Energy, 275(7): 127470.

Liu W., Ma L., Zhao Z. (2023) Fracture Precursor Recognition and Damage Quantitative Characterization of Stressed Rock Using Infrared Radiation. Rock Mechanics and Rock Engineering. 56(8), 5567-5584.

Liu Y., Yin G., Li M., Zhang D., Huang G., Liu P., Liu C., Zhao H., Yu B. (2019). Mechanical properties and failure behavior of dry and water-saturated anisotropic coal under true-triaxial loading conditions. Rock Mechanics and Rock Engineering. 53(11), 4799-4818.

Liu Z, Cao P, Zhao Q, Cao R, Wang F, (2022) Deformation and damage properties of rock-like materials subjected to multi-level loading-unloading cycles. Journal of Rock Mechanics and Geotechnical Engineering.

Luo D., Su G., He B. (2019) Experimental study on true triaxial rock burst of granite with different saturation degree. Rock and Soil Mechanics.

Luo K, Bai Y, Zhao S, Xia D, Wu C, Jia Y, (2022) Experimental study on the influence of saturation time on acoustic emission characteristics of clay-bearing rock minerals. Mining Engineering Research, 37(2): 26-36.

Luo K., Bai Y., Zhao S., et al. (2022) Experimental study on the effect of water saturation time on acoustic emission characteristics of clay mineral rocks. Mineral Engineering Research. 37(2): 26-36. https://doi.org/10.13582/j.cnki.1674-5876.2022.02.004.

Luo Y. (2020) Influence of water on mechanical behavior of surrounding rock in hard-rock tunnels: An experimental simulation. Engineering Geology. 277:105816 .

Lyu Q., Shi J., Tan J., Dick J., Kang X. (2022) Effects of shale swelling and water-blocking on shale permeability. Journal of Petroleum Science and Engineering. 212. https://doi.org/10.1016/j.petrol.2022.110276.

Ma L, Huang C, Meints C (2020) A full-scale case study on the leaching process of acid rock drainage in waste rock piles and the net infiltration through cover systems. Water Air and Soil Pollution. 231(6), 305.

Ma L., Wang Y., Wang M., et al. (2021) Mechanical properties of rock salt under combined creep and fatigue. International Journal of Rock Mechanics and Mining Sciences. 141: 104654.

Ma L., Wu J., Wang M., Dong L., Wei H. (2020). Dynamic compressive properties of dry and saturated coral rocks at high strain rates. Engineering Geology. 272, 105615.

Mazars J. (1986). A description of microscale and macroscale damage of concrete structures. Engineering Fracture Mechanics, 25(5): 729-737.

Meng J., Lyu C., Wang L, et al. (2023) Effect of cyclic load on mechanical properties and failure mechanisms of different rank coals. Energy. 278: 0360-5442.

Moore D., Lockner D., (2004). Crystallographic controls on the frictional behavior of dry and water-saturated sheet structure minerals. Journal of Geophysical Research-Solid Earth. 109(B3).

Moussas, V., and Diamantis, K. (2021). Predicting uniaxial compressive strength of serpentinites through physical, dynamic and mechanical properties using neural networks. J. Rock Mech. Geotechnical Eng. 13 (1), 167–175.

Moysey S., Singha K., Knight R. (2005). A framework for inferring field-scale rock physics relationships through numerical simulation. Geophysical Research Letters. 32(8), L08304.

Ni H, Wang R, Zhang Y, 2005, Numerical simulation study on rock breaking mechanism and process under high pressure water jet. Applied Mathematics and Mechanics-English Edition. 26(12), 1595-1604.

Peng S., Wang Z., Xu J., et al.2018. Experimental study on loading rate effect of water-filled rock after failure under triaxial compression. Rock and Soil Mechanics.

Priest J., Abbas M., Hayley J. (2021). The change in geomechanical properties of gas saturated methane hydrate-bearing sand resulting from water saturation. Journal of Geophysical Research-Solid Earth. 126(9).

Qin Y., Tang H., Wu Z., Ge X. 3D ground stress calculation method of deep shale based on local wall stress relief method of drilling [J]. Journal of rock mechanics and engineering, 2018,5(6):1468-1480.

Ramsay J (1980) Crack-seal mechanism of rock deformation. Nature. 284(5752):135–139.

Roshan H., Ehsani S., Marjo C., Andersen M., Acworth R., 2015. Mechanisms of water adsorption into partially saturated fractured shales: An experimental study. Fuel. 159:628-637. https://doi.org/10.1016/j.fuel.2015.07.015.

Sang Q., Zhang S., Li Y., et al. (2019) Determination of organic and inorganic hydrocarbon saturations and effective porosities in shale using vacuum-imbibition method. International Journal of Coal Geology. 200, 123-134.

Shen R, Li T, Li H, He S, Zhao E, Hou Z, Chen T, 2021, Study on the effect of water on electromagnetic radiation characteristics of fractured sandstone under load. Environmental Earth Sciences. 80(3).

Shi Z., Li J., Wang M., Chen J., et al. (2023) Fatigue fracture behaviour and constitutive model of freeze-thaw sandstone under multilevel fatigue loads. Bulletin of Engineering Geology and The Environment. 82(8),319.

Siddiqui M., Roshan H. (2022). Thermodynamic characterization of chemical damage in variably saturated water-active shales. Rock Mechanics and Rock Engineering. 55(8), 5259-5284.

Song Z., Liu H., Zheng F., Chen Y., Sun Y., Song W.2023.Mechanical behavior and failure response characteristics of hard sandstones considering bedding dip angles. Coal Geology & Exploration.

Song Z., Wang C., Zhao Y., et al. (2023) Effect of frequency on rock's mechanical responses under multi-level compressive cyclic loading: an experimental investigation. Bulletin of Engineering Geology and The Environment. 82(6), 224.

Song Z., Wang Y., Konietzky H., Cai X., (2021). Mechanical behavior of marble exposed to freeze-thaw-fatigue loading. International Journal of Rock Mechanics and Mining Sciences. 138, 104648.

Sui Y., Lin T., Liu X., Dong C., Cheng W., Zhang G., Liao Z. 2020.Numerical simulation for the effect of cyclic stress on microstructure and mechanical properties of reservoir rocks during operations of gas storage. Journal of China University of Petroleum(Edition of Natural Science).

Sun B., Zhu Z., Luo Z. (2017). Dynamic mechanical behavior and fatigue damage evolution of sandstone under cyclic loading. International Journal of Rock Mechanics and Mining Sciences. 94, 82-89.

Tan J., Hu C., Lyu Q., et al. (2019) Multi-fractal analysis for the AE energy dissipation of CO2 and CO2+ brine/water treated low-clay shales under uniaxial compressive tests. Fuel. 246:330-339.

Tan Y., Zhang S., Tang S., Cui G., Ma Y., Sun M., Pan Z., 2021. Impact of water saturation on gas permeability in shale: Experimental and modelling. Journal of Natural Gas Science and Engineering. https://doi.org/10.1016/j.jngse.2021.104062.

Tang C., Zhou W., Chen Z., Wei J., 2023. Numerical simulation of CO2 sequestration in shale gas reservoirs at reservoir scale coupled with enhanced gas recovery. Energy. 277.

Tang X., Teng J., Zhang C., Liu S. 2018.Experimental study on creep characteristics of layered water-bearing shale. Rock and Soil Mechanics.

Thongraksa A., Punya-in Y., Jongpradist P., Kim H., Jamsawang P. (2021). Failure behaviors of rock masses around highly pressurized cavern: Initiation and modes of failure. Tunnelling and Underground Space Technology. 115, 104058.

Vaneghi R., Ferdosi B., Okoth A., Kuek B. (2018). Strength degradation of sandstone and granodiorite under uniaxial cyclic loading. Journal of Rock Mechanics and Geotechnical Engineering. 10(1), 117-126.

Wang C., Wei S., Pan Y., Zhang S., (2022) Experimental study on fatigue life of gypsumlike rock under uniaxial compression with different loading frequencies. Pure and Applied Geophysics, 179.

Wang C, Wei S, Zhang D, Yang Y, Yu B, Pan Y, (2023), Physical properties and tensile strength evolution of gypsum materials under different water content conditions. Construction and Building Materials. 364,129865.

Wang C, Zhang D, Yu B, Li S, (2023), Deformation and seepage characteristics of coal under true triaxial loading-unloading. Rock Mechanics and Rock Engineering. 56, 2673–2695.

Wang C., (2021) Study on low-frequency dynamic physico-mechanical properties of gypsum rocks, Henan Polytechnic University. MSc Thesis. pp12-15.

Wang C., Liu C., Liu D. 2019. Experimental study on volume effect of saturated fractured sandstone under uniaxial compression. Chinese Journal of Underground Space and Engineering.

Wang C., Study on low-frequency dynamic physico-mechanical properties of gypsum rocks. [D]. Henan Polytechnic University, 2021. MSc Thesis, pp13-14.

Wang C., Wang Y., Han Z., Wang C., Wang J., Hu S. Vertical hole stress release method testing technology and application [J]. Rock and soil mechanics, the lancet, 2022 (5) : 1412-1421.

Wang C., Wei S., Wang M., Xu C., Zhang S. (2022b). Rockburst characteristics of gypsum-like rocks after fatigue cyclic loading. Arabian Journal of Geosciences .15 (15).

Wang C., Zhang D., Liu C., et al. (2023a) Deformation and seepage characteristics of water-saturated shale under true triaxial stress. Energy. 284: 129191.

Wang J, Li J, Shi Z, Chen J, 2022a, Fatigue damage and fracture evolution characteristics of sandstone under multistage intermittent cyclic loading. Theoretical and Applied Fracture Mechanics, 119: 103375.

Wang J, Zhang Q, Song Z, Liu X, Wang X, Zhang Y, 2022b, Microstructural variations and damage evolvement of salt rock under cyclic loading. International Journal of Rock Mechanics and Mining Sciences, 152: 105078.

Wang J., Li J., Shi Z. (2022a) Deformation damage and acoustic emission characteristics of red sandstone under fatigue–creep interaction. Theoretical and Applied Fracture Mechanics. 117: 103192.

Wang J., Li J., Shi Z., (2021) Crack evolution law and failure mode of red sandstone under fatigue-creep interaction. Fatigue & Fracture of Engineering Materials & Structures. 45(1), 270-284.

Wang J., Li J., Shi Z., et al. (2022b) Fatigue damage and fracture evolution characteristics of sandstone under multistage intermittent cyclic loading. Theoretical and Applied Fracture Mechanics. 119: 103375.

Wang J., Takahashi E., Xiong X., Chen L., Li L., Suzuki T., Walter M. (2020). The Water-Saturated Solidus and Second Critical Endpoint of Peridotite: Implications for Magma Genesis Within the Mantle Wedge. Journal of Geophysical Research-Solid Earth. 125(8).

Wang P, Yin T, Hu B. 2020, Dynamic tensile strength and failure mechanisms of thermally treated sandstone under dry and water-saturated conditions. Transactions of Nonferrous Metals Society of China. 30(8): 2217-2238 .

Wang Y., Feng W., Hu R., Li C. (2020). Fracture Evolution and Energy Characteristics During Marble Failure Under Triaxial Fatigue Cyclic and Confining Pressure Unloading (FC-CPU) Conditions. Rock Mechanics and Rock Engineering. 54(2), 799-818.

Wang Y., Jing H., Chen K., Wei L. Pingdingshan mining area zoning of in-situ stress distribution rule and space. Journal of rock mechanics and engineering, 2014 (S1) : 2620-2627.

Wang Y., Li C., Han J., (2020) On the effect of stress amplitude on fracture and energy evolution of pre-flawed granite under uniaxial increasing-amplitude fatigue loads. Engineering Fracture Mechanics. 240, 107366.

Wei C. 2020. Mechanism of stress path and water cut on shale deformation and energy evolution. Chongqing University.

Wei S., Wang C., Yang Y., Wang M., Physical and mechanical properties of gypsum-like rock materials, Advances in Civil Engineering (2020) 1–17, .

Wen M., Xiong H., Xu J. (2022). Thermo-hydro-mechanical response of a partially sealed circular tunnel in saturated rock under inner water pressure. Tunnelling and Underground Space Technology. 126, 104552.

Wood J, 2015, Crushed-rock vs. full-diameter core samples for water-saturation determination in a tight-gas siltstone play. Spe Reservoir Evaluation & Engineering. 18(3), 407-416.

Wu W., Gong F., Jiang Q. (2023). Influence of water on rockburst of surrounding rock in deep circular tunnels under triaxial internal unloading conditions. Tunnelling and Underground Space Technology. 138, 105165.

Xu H., Liu H., Bie P., (2022) Study on stress-strain response characteristics of different types of rocks under triaxial multi-stage cyclic loading. Nonferrous Metals (Mining Section). 74(2):61-68.

Xu T., Fu M., Yang S., Heap M., Zhou G. (2021). A Numerical Meso-Scale Elasto-Plastic Damage Model for Modeling the Deformation and Fracturing of Sandstone Under Cyclic Loading. Rock Mechanics and Rock Engineering. 54(9), 4569-4591.

Yang K., Zhou J., Xian X., Zhou L., Zhang C., Tian S., Lu Z., Zhang F., 2022. Chemical-mechanical coupling effects on the permeability of shale subjected to supercritical CO2-water exposure. Energy. 248, 123591.

Yang S., Yin P., Xu S., 2021. Permeability Evolution Characteristics of Intact and Fractured Shale Specimens. Rock Mechanics and Rock Engineering. 54: 6057–6076. https://doi.org/10.1007/s00603-021-02603-y.

Yin T., Yin J., Wu Y., et al. (2022) Water saturation effects on the mechanical characteristics and fracture evolution of sandstone containing pre-existing flaws. Theoretical and Applied Fracture Mechanics. 122: 103605.

Yun H., Moon S., Seo Y. (2022). Effects of breccia and water contents on the mechanical properties of fault-core-zone materials. Scientific Reports. 12(1), 7093.

Zaima K., Katayama I. (2018). Evolution of Elastic Wave Velocities and Amplitudes During Triaxial Deformation of Aji Granite Under Dry and Water-Saturated Conditions. Journal of Geophysical Research-Solid Earth. 123(11), 9601-9614.

Zeng X., Sun J., Yan W., Cui R., Yuan W., Yan W., Xu D., 2020. New Insight into the Petrophysical Characterization of Shales with Different Fluid Saturation States Based on Nuclear Magnetic Resonance Experiments. Energy and Fuels. 34(5): 5599-5610.

Zhai M., Xue L., Bu F., Yang B., Huang X., Liang N., Ding H., 2022. Effects of bedding planes on progressive failure of shales under uniaxial compression: Insights from acoustic emission characteristics. Theoretical and Applied Fracture Mechanics.119. https://doi.org/10.1016/j.tafmec.2022.103343.

Zhang Q., Zhang X., Wang Z., Wen X., Xue J. (2017). Failure mechanism and numerical simulation of zonal disintegration around a deep tunnel under high stress. International Journal of Rock Mechanics and Mining Sciences. 93, 344-355.

Zhang S., Sheng J., 2018. Effect of Water Imbibition on Fracture Generation in Mancos Shale under Isotropic and Anisotropic Stress Conditions. Journal of Geotechnical and Geoenvironmental Engineering. 144(2). https://doi.org/10.1061/(ASCE)GT.1943-5606.0001832.

Zhang W., Klein B., Randolph M., Puzrin A. (2021). Upslope Failure Mechanisms and Criteria in Submarine Landslides: Shear Band Propagation, Slab Failure and Retrogression. Journal of Geophysical Research-Solid Earth. 126(9).

Zhang W., Zhao J., Zhang D., 2022, Construction and validation of the upscaling model of organic-rich shale by considering water-sensitivity effects. Journal of Petroleum Science and Engineering. 2022.

Zhang Y., Jiang P., Li C., Zhao Z., Gao S., Yao S., Sui H., Huang J., 2023. Evolution Law of Porosity and Permeability in In-Situ Pyrolysis Zone of Oil Shale. International Journal of Heat and Technology. I41(1): 224-230. https://doi.org/10.18280/ijht.410124.

Zhang Y., Yang Z., Yao X., et al. Experimental research on rock burst warning method based on acoustic emission signal cluster analysis and neural network recognition. Rock and Soil Mechanics.2017, 38 (S2): 89-98. https://doi.org/10.16285/j.rsm.2017.S2.012.

Zhao B., Xu T., Yang S., Fu T. 2021.Experimental and numerical study of fatigue damage of highly stressed rocks under cyclic loading. Journal of Central South University(Science and Technology).

Zhao K., Li H., Ma H., et al. (2022) Creep-fatigue characteristics of rock salt under different loading paths. Journal of Petroleum Science and Engineering. 218: 111036..

Zhao K., Ma H., Yang C., Chen X., Liu Y., Liang X., Cai R. (2021). Damage evolution and deformation of rock salt under creep-fatigue loading. Rock Mechanics and Rock Engineering. 54(4), 1985-1997.

Zhao L, 2022, Experimental study on mechanical property softening of saturated sandstone. Chinese Journal of Underground Space and Engineering, 18(01): 154-162.

Zhao S., Gao G., Wang C., Zhang N., Liu Y., Hou Z., Liu X. Small aperture cone hole bottom set of core stress release method and experimental study [J]. Journal of coal, 2021 46-48 (S1) : 74-83.

Zhao Y., Ding L., Wang X., et al. Acoustic emission and charge signal response characteristics in the process of fault stick-slip instability. Rock and Soil Mechanics. 2024,45(4): 973-990. https://doi.org/10.16285/j.rsm.2023.0534.

Zhao Y., Liu S., Zhao G., Elsworth D., Jiang Y., Han J. (2014). Failure mechanisms in coal: Dependence on strain rate and microstructure. Journal of Geophysical Research-Solid Earth. 119(9), 6924-6935.

Zheng C., Yao Q., Li X. (2023). Evolution law of ultrasonic characteristics and its relationship with coal-measure sandstone mechanical properties during saturation and desaturation. Journal of Building Engineering. 75, 106909.

Zheng G., Xu J., Wang P., Fang X., Wang H. 2017.Dynamic and static mechanical tests of red sandstone with different saturation. Journal of Air Force Engineering University.

Zheng G., Xu J., Wang P., et al. (2017) Dynamic and static mechanical tests of red sandstone under different water saturation. Journal of Air Force Engineering University. 18(1): 99-104.

Zheng Y, Kong L, A B (2020) Strength theory and numerical limit analysis, vol 3. Science Press, pp 49–50. ISBN: 978-7-03-064464-0.

Zhong Z., Li Y., Huang D. (2022). Prestress Loss Mechanism and Constitutive Model of an Anchored Joint Rock Mass Under Low-frequency Fatigue Loading. Rock Mechanics and Rock Engineering. 56I(2), 1517-1535.

Zhu L, Shen W, He M, Shao J, 2022, Contribution of atomistic study to better understand water saturation effect on mechanical behavior of clayey rocks in triaxial compression. Computers and Geotechnics, 146: 104738.

Zhu L., Shen W., He M., et al. (2022) Contribution of atomistic study to better understand water saturation effect on mechanical behavior of clayey rocks in triaxial compression. Computers and Geotechnics. 146: 104738.

Zhu Z., Guo J., Sun F., Zhang H. 2023.Experimental study on acoustic emission and crack propagation of fractured sandstone with different water content. Chinese Journal of High-Pressure Physics.

Zhuang L., Kim K., Diaz M., et al. (2020) Evaluation of water saturation effect on mechanical properties and hydraulic fracturing behavior of granite. International Journal of Rock Mechanics and Mining Sciences. 130: 104321.

Zuo Y., Sun W., Wu Z., et al.2018.Permeability test of shale under osmotic pressure-stress coupling. Rock and Soil Mechanics.

Appendix
Achievements during the doctoral studies

A. Academic papers published

A1 (First author or corresponding author)

[1] **Wang CY**, Zhang DM* Xiong ZY, et al. Acoustic emission noise reduction: a case of a uniaxial compression test of gypsum-like rock. *International Journal of Rock Mechanics and Mining Sciences*. 2024(178), 105781. https://doi.org/10.1016/j.ijrmms.2024.105781. (SCI, Q1, Top)

[2] **Wang CY**, Zhang DM*, Yu BC, et al. Deformation and seepage characteristics of coal under true triaxial loading-unloading. *Rock Mechanics and Rock Engineering*. 2023(56), 2673-2695. https://doi.org/10.1007/s00603-022-03207-w. (SCI, Q1, Top)

[3] **Wang CY**, Zhang DM*, Liu CX, et al. Deformation and seepage characteristics of water-saturated shale under true triaxial stress. *Energy*. 2023(284), 129191. https://doi.org/10.1016/j.energy.2023.129191. (SCI, Q1, Top)

[4] **Wang CY**, Wei SJ, Zhang DM*, et al. Physical properties and tensile strength evolution of gypsum materials under different water content conditions. *Construction and Building Materials*. 2023(364), 129865. https://doi.org/10.1016/j.conbuildmat.2022.129865. (SCI, Q1, Top)

[5] **Wang CY,** Zhang DM, Liu CX. Fatigue damage characteristic and degradation mechanism of mechanical properties in shale under different water saturation duration. *Physics of Fluids*. 2025(37), 026622. https://doi.org/10.1063/5.0254759. (SCI, Q1)

[6] **Wang CY**, Wei SJ*, Ren FK, et al. Effects of $CaCO_3$ and SiO_2 contents on mechanical and acoustic emission properties of gypsum materials. *Physics of Fluids*. (2025.03.15, SCI, **Q1**; Accepted)

[7] **Wang CY**, Wei SJ*, Pan YS, et al. Experimental study on fatigue life of gypsum-like rock under uniaxial compression with different loading frequencies. *Pure and Applied Geophysics*, 2022(179), 1225-1239. https://doi.org/10.1007/s00024-022-02966-5. (SCI, Q2)

[8] **Wang CY**, Wei SJ, Zhang DM*, et al. Evolution of mechanical and rockburst parameters of gypsum-like rock under fatigue stress disturbance. *Rock Mechanics Bulletin*. 2024, 100171. https://doi.org/10.1016/j.rockmb.2024.100171. (SCI, Q2)

[9] **Wang CY**, Pan YS, Zhang DM*, et al. CO_2 seepage behavior in coal under different stress and water content conditions. *Quarterly Journal of Engineering Geology and Hydrogeology*. (2025.03.19, Accepted; SCI, Q3)

[10] **Wang CY**, Wei SJ*, Wang M, et al. Rockburst characteristics of gypsum-like rocks after fatigue cyclic loading. *Arabian Journal of Geosciences*, 2022.15,1342. https://doi.org/10.1007/s12517-022-10636-y. (SCI, Q3)

[11] **Wang CY**, Wei SJ*, Zhai LW et al. Experimental study on physical and mechanical properties of coal and rock composite samples based on gypsum rocks. Journal of Henan Polytechnic University (Natural Science Edition), 2022, 41(06), 36-44. https://doi.org/10.16186/j.cnki.1673-9787.2021020019. (Peking University Chinese core)

[12] Ren FK, Yang H, **Wang CY* (corresponding author)**, et al. Impact of High-Pressure Liquid on CO_2 Gas Behavior in Coal Seam Gas-Liquid Combined Fracturing. *Rock Mechanics and Rock Engineering*. (2025.03.30, SCI, Q1; Accepted)

[13] Ren FK, **Wang CY* (corresponding author)**, Li J, et al. Gas drainage interception technology for tunnel between coal seams passing through geological abnormal areas. *Geomechanics and Geoengineering.* 2025. 1–20. https://doi.org/10.1080/17486025.2025.2456554. (SCI, Q3)

[14] Ren FK, **Wang CY* (corresponding author)**, Pan YS, et al. The impact of temperature and pressures on the efficiency of CH_4 replacement in CO_2-injected coal. *Journal of Energy Engineering*. (2025.01.03, Accepted; SCI, Q3)

[15] Ren FK, **Wang CY* (corresponding author)**, Pan YS, et al. The correlation between the fluid injection pressure and the unit fluid injection quantity during hydraulic fracturing. *Archives of Mining Sciences*. (2025.03.16, Accepted; SCI, Q3)

[16] Pan YS, **Wang CY* (corresponding author)**, Wang ZZ, et al. The influence and forecast of three industries and energy structure on regional carbon emission. *Energy Sources, Part A: Recovery, Utilization, and Environmental Effects*. 2024, 4078-4094. https://doi.org/10.1080/15567036.2024.2323157. (SCI, Q3)

[17] Pan YS, **Wang CY* (corresponding author)**, Wang YD. Study on mechanical degradation mechanism of rock under seismic disturbance stress. *Quarterly Journal of Engineering Geology and Hydrogeology*. 2022(55). https://doi.org/10.1144/qjegh2022-007. (SCI, Q3)

[18] Li SJ, **Wang CY* (corresponding author)**, Zhang DM, et al. Deterioration mechanism of mechanical properties of phosphorite under different saturation duration. *Frontiers in Earth Science (Environmental Informatics and Remote Sensing)*. 2023.06.23. https://doi.org/10.3389/feart.2023.1227742. (SCI, Q2)

[19] Li SJ, Wang H, **Wang CY* (corresponding author)**, et al. Deterioration mechanism of physical and mechanical properties of phosphate rock under seismic disturbance and saturation. *Frontiers in Earth Science (Geohazards and Georisks).* 2023.06.15. https://doi.org/10.3389/feart.2023.1211314. (SCI, Q2)

[20] Li SJ, Pan YS, **Wang CY* (corresponding author)**, et al. Stability Analysis of a Water-Rich Slope under Seismic Disturbance. *Advances in Civil Engineering*. 2024.14. https://doi.org/10.1155/2024/8894948. (SCI, Q3)

A2 (Co-author)

[21] Pan YS, Zhang HB, **Wang CY**, Zhou YD, Impact of land use change on regional carbon sink capacity: Evidence from Sanmenxia, China. *Ecological Indicators*. 2023(156), 111189. https://doi.org/10.1016/j.ecolind.2023.111189. (SCI, Q1, Top)

[22] Ren FK, Zhang DM, **Wang CY**; Lu XT, Wang PP, Zhang Y. Influence of liquid CO2 phase transition blasting on hydraulic fracturing in combined fracturing conditions. In: *Physics Of Fluids*. 2025. Accepted. (SCI, Q1)

[23] Yu BC, Zhang DM, Xu B, Liu YB, Zhao HG, **Wang CY**. Modeling of true triaxial strength of rocks based on optimized genetic programming. *Applied Soft Computing*. 2022(129), 109601. https://doi.org/10.1016/j.asoc.2022.109601. (SCI, Q1, Top)

[24] Wang CY, Zhang DM, Tan DJ, Ye JH, Wang XL, **Wang CY**, Li QL. Study on the evolution of limestone damage and permeability under the tunnel driving stress path. *Construction and Building Materials*. 2024(425), 136050. https://doi.org/10.1016/j.conbuildmat.2024.136050. (SCI, Q1, Top)

[25] Wang XL, Zhang DM, Geng JB, Jin ZH, **Wang CY**, Ren KD. Effects of CO_2 intrusion on pore structure characteristics of mineral-bearing coal: Implication for CO_2 injection pressure. *Journal of Natural Gas Science and Engineering*. 2022(108), 104808. https://doi.org/10.1016/j.jngse.2022.104808. (SCI, Q1, Top)

[26] Yu BC, Zhang DM, Zhao K, Xu B, Geng JB, **Wang CY**, Chen Y. Experimental study on stress and permeability response with gas depletion in coal seams. *Journal of Natural Gas Science and Engineering.* 2022(108), 104824. https://doi.org/10.1016/j.jngse.2022.104824. (SCI, Q1, Top)

[27] Yu BC, Zhang DM, Xu B, Xiao WJ, **Wang CY**, Du WH. Experimental Study of Desorption and Seepage Characteristics of Single Gas and CO_2–CH_4 Gas Mixture in Coal. *Natural Resources Research*. 2022(31), 2715–2730. https://doi.org/10. 1007/s11053-022-10077-0. (SCI, Q1)

[28] Li SJ, **Wang CY**, Zhang DM, Yu BC, Ren KD. Failure and deformation characteristics of shale subject to true triaxial stress loading and unloading under water retention and seepage. *Royal Society Open Science*. 2022. https://doi.org/10.1098/rsos.220530. (SCI, Q2)

[29] Wang CY, Zhang DM, Li SJ, Chen Y, **Wang CY**, Ren KD. Study on in situ stress testing method based on Kaiser effect of acoustic emission and COMSOL simulation. *Frontiers of Earth Science*. 2023(17), 818–831. https://doi.org/10.1007/s11707-022-1034-x. (SCI, Q3)

[30] Zhang JG, Wang M, Zhou HW, Zhang DM, Yu BC, **Wang CY**, Wang YJ. Coal and rock dynamic disaster prevention and control technology in the large mining face of a deep outburst mine. *Frontiers of Earth Science*. 2023(17), 701–712. https://doi.org/10.1007/s11707-022-1060-8. (SCI, Q3)

[31] Li HT, Yu G, Fang YZ, Chen YR, **Wang CY**, Zhang DM, Gas production prediction and risk quantification of shale gas reservoirs in Sichuan Basin based on Gauss prediction model and Monte Carlo probability method. *Frontiers in Earth Science*. 2022(10). https://doi.org/10.3389/feart.2022.977200. (SCI, Q2)

[32] Li HT, Yu G, Li C, Xie Z, Liu CX, Zhang DM, **Wang CY**. Prediction Model and Risk Quantification of Natural Gas Peak Production in Central Sichuan Paleo-Uplift Gas Reservoirs. *Geofluids*. 2023, 4858118. https://doi.org/10.1155/2023/4858118. (SCI, Q2)

B. Participation to research projects

[1] Zhang DM, **Wang CY**, Lin Y, et al. Research on Rock Mechanics Analysis and Stope Stability in the Nadan Potash Mining Area of Laos, 2023. (Supervisor first, student second)

[2] Zhang DM, **Wang CY**, Liu CX, et al. Study on the Evolution of the Fracture Field and Groundwater Infiltration Under True Triaxial Stress Conditions, 2023. (Supervisor first, student second)

[3] Zhang DM, **Wang CY**, Chen Y, et al. Research on Big Data Analysis and Prediction Models for Gas Reservoir Recovery Rates, 2022. (Supervisor first, student second)

[4] Zhang DM, **Wang CY**, Chen Y, et al. Construction and Application of Production Peak Models in the Sichuan Basin Under Multiple Boundaries, 2022. (Supervisor first, student second)

[5] Zhang DM, Chen Y, **Wang CY**, et al. Cluster Analysis and Recovery Rate Prediction Model Study for the Carboniferous Gas Reservoirs in Eastern Sichuan, 2022.

[6] Zhang DM, Chen Y, **Wang CY**, et al. Research on the Prediction Method System for Natural Gas Production Development Targets, 2023.

[7] Wang H, Zhang DM, **Wang CY**, et al. Study on the Fracture Mechanisms of Surrounding Rock in the Second Mine of the Kunyang Phosphate Mine Under Seismic Loading, 2022.

C. Patents applied

[1] Zhang DM, Yu BC, **Wang CY**, et al. Axial Endface Coal and Gas Outburst Simulation Experiment System Under Multi-field Coupling Conditions [P]. Chongqing: CN116183864A, 2023-05-30. (Invention authorized)

[2] Zhang DM, Yu BC, **Wang CY**, et al. True Triaxial Testing Method for Full-process Visualization of Soft Rock Deformation Under High-temperature Stress Environment [P]. Chongqing: CN202211668265.X, 2024-06-25. (Invention authorized)

[3] Wei SJ, Wang Meng, **Wang CY**, et al. Testing Device and Method for Free Expansion Volume During the Hydration of Expansive Rock [P]. Henan: CN201910456429.4, 2024-04-26. (Invention authorized)

[4] Wei SJ, Guo Min, **Wang CY**, et al. Testing Device and Method for Confined Expansion Force During the Hydration of Expansive Rock [P]. Henan: CN201910456146.X, 2024-01-30. (Invention authorized)

[5] Zhang DM, Yu BC, Du WH, **Wang CY**, et al. Experiment Method for Inducing Coal and Gas Outburst Under Gradational Dynamic Loading [P]. Chongqing: CN116087457A, 2023-05-09. (Invention authorized)

[6] Zhang DM, Yu BC, Wang H, **Wang CY**, et al. Gas Outburst Experiment System for Deep-buried Coal Seams [P]. Chongqing: CN116087458A, 2023-05-09. (Invention authorized)

[7] Zhang DM, Yu BC, Du WH, **Wang CY**, et al. Liquid Carbon Dioxide Perforation-induced Fracturing Simulation Experiment System for Coal Seams [P]. Chongqing: CN116087459A, 2023-05-09. (Invention authorized)

[8] Yu BC, Zhang DM, Chen Y, **Wang CY**, et al. Physical Simulation Method for Hydraulic Connectivity in VHSD Vertical Horizontal Wells for Heavy Oil Reservoirs [P]. Chongqing: CN115977621A, 2023-04-18. (Invention authorized)

[9] Yu BC, Zhang DM, Chen Y, **Wang CY**, et al. Box Module for Large-scale Heavy Oil Extraction Test Specimens [P]. Chongqing: CN202211669449.8, 2024-05-07. (Invention authorized)

[10] Zhang DM, Yu BC, Du WH, **Wang CY**, et al. Gas Outburst Simulation Experiment System Capable of Monitoring Stress, Temperature, and Gas Pressure [P]. Chongqing: CN116298175A, 2023-06-23. (Invention authorized)

[11] Zhang DM, Yu BC, Wang H, **Wang CY**, et al. Comprehensive Test Method for Oil Sand Strength, Strain, and Permeability Under High-temperature Stress Environment [P]. Chongqing: CN116087468A, 2023-05-09. (Invention authorized)

[12] Wei SJ, Wu YF, Cui F, Li H, **Wang CY**, et al. Similar Simulation Experiment Device Capable of Applying Controllable Impact Loads [P]. Henan: CN201811318330.X, 2024-03-26. (Invention authorized)

D. Awards and honors for scientific and technological achievements

[1] November 2024: The Second Prize of Science and Technology Progress Award of China Work Safety Association (**Ranked fifth**)

[2] October 2024: Baosteel Outstanding Student Scholarship (Only 5 students, 5/50000)

[3] November 2024: National Scholarship **(National Level)**

[4] July 2023: National Scholarship for Overseas Study by the China Scholarship Council **(National Level)**

[5] July 2023: Excellent Micro-video Award for "Understanding China" by the Ministry of Education **(National Level)**

[6] January 2024: Third Prize in the Chongqing College Students Safety and Emergency Skills Competition **(Provincial and Ministerial Level)**

[7] June 2023: Advanced Individual in Chongqing Volunteer Service Activities **(Provincial and Ministerial Level)**

[8] December 2022: First Prize in the Chongqing Graduate Essay Competition **(Provincial and Ministerial Level)**

[9] December 2023: Top Ten Students of School of Resources and Safety Engineering, Chongqing University

[10] December 2023: The TuBoShi Scholarship of Chongqing University

[11] May 2022: Advanced Individual as One of the Top Ten Young Volunteers at Chongqing University

[12] May 2023: Advanced Individual in Cultural and Artistic Achievements as One of the Top Ten Students at Chongqing University

[13] September 2023: Excellent Student at Chongqing University

[14] September 2024: Outstanding Graduate of Chongqing University

[15] May 2024: Outstanding Communist Youth League Member of Chongqing University

[16] October 2023: Sunshine League Member of Chongqing University **(Nominated as one of the Top Ten Communist Youth League Members of Chongqing University)**

[17] April 2022: Outstanding Individual in the "Hundred Students Work Placement Program" at Chongqing University

[18] February 2023: Third Prize in the Chongqing Public Document Writing Competition

E. Copyrights obtained

[1] **Wang CY**, Ren FK. Software for Planning Analysis and Evaluation of Coal Mine Disaster Management Programs [P]. 2023SR0610869, June 9, 2023.

[2] Ren FK, **Wang CY**. Software for Schedule Management of Coal Mine Disaster Management Projects [P]. 2023SR0611855, June 9, 2023.

[3] Ren FK, **Wang CY**. Software for Detection and Evaluation of Coal Mine Disaster Management Effects [P]. 2023SR0610868, June 9, 2023.

[4] Pan YS, **Wang CY**, Ren FK. Software for Identification and Assessment of Land Use Change Influencing Factors [P]. 2023SR1509678, August 25, 2023.